

Tumour progression in metastatic breast cancer cell lines: engineered *in vitro* models

A thesis submitted to The University of Manchester for the degree of

Doctor of Philosophy

in the Faculty of Biology, Medicine & Health

2022

Lekha V Shah

School of Health Sciences

Division of Pharmacy & Optometry

Table of contents

| | |
|---|-----------|
| Table of contents | 2 |
| List of figures | 8 |
| List of Tables | 9 |
| List of Abbreviations | 10 |
| Abstract | 15 |
| Declaration | 16 |
| Copyright statement | 16 |
| Acknowledgements | 17 |
| Rationale for alternative format | 18 |
| Thesis summary – Manuscript organisation | 19 |
| Contribution of authors | 23 |
| Chapter 1. Engineered <i>in vitro</i> Models: Mimicking <i>in vivo</i> Physiology. | 26 |
| Abstract | 27 |
| Overview..... | 28 |
| 1. The tissue microenvironment..... | 29 |
| 1.1 Cellular components | 30 |
| 1.1.1 Epithelial tissue..... | 30 |
| 1.1.2 Connective tissue | 31 |
| 1.1.3 Muscular tissue | 32 |
| 1.1.4 Central and peripheral nervous tissue | 32 |
| 1.1.5 Stem cells and progenitors | 34 |
| 1.2 Biochemical factors | 35 |
| 1.2.1 Peptide..... | 36 |
| 1.2.2 Steroid | 36 |
| 1.2.3 Neurotransmitters..... | 37 |
| 1.3 Biophysical components | 38 |
| 1.3.1 Extracellular matrix composition and mechanical stiffness | 38 |
| 1.3.2 Partial pressure of O ₂ (pO ₂) | 40 |

| | |
|---|----|
| 1.3.3 pH and tissue buffering | 41 |
| 1.3.4 Ions and small molecules | 41 |
| 1.3.5 Interstitial fluid flow and blood flow | 42 |
| 1.4 Functional tissue unit | 43 |
| 2. Traditional <i>in vitro</i> models: 2D tissue culture | 46 |
| 2.1 Regulation and qualification of materials used in cell culture..... | 49 |
| 2.2 Limitations of traditional <i>in vitro</i> models | 50 |
| 3. Three-dimensional (3D) cultures | 52 |
| 3.1 Spheroids..... | 52 |
| 3.1.1 Hanging drop method | 53 |
| 3.1.2 Low adhesion TCP plate method..... | 53 |
| 3.1.3 Device assisted culture method (Bioreactors)..... | 54 |
| Efficacy of spheroid culture..... | 55 |
| 3.2 Scaffold-based 3D culture..... | 56 |
| 3.2.1 Hydrogels as soft and hydrated scaffolds | 57 |
| 3.2.2 3D Polymeric scaffolds..... | 58 |
| 3.3 Additive manufacturing of 3D scaffolds..... | 59 |
| 3.3.1 Additive manufacturing of hard scaffolds | 60 |
| 3.3.2 Additive manufacturing of soft scaffolds | 60 |
| 3.3.3 3D Bioprinting | 61 |
| 3.4 Properties of scaffold for <i>in vitro</i> models. | 62 |
| 3.4.1 Mechanical properties..... | 62 |
| 3.4.2 Pore size and porosity | 63 |
| 3.4.3 Provision of nutrients..... | 64 |
| 3.4.4 Stability and degradation. | 65 |
| 3.4.5 Biocompatibility. | 66 |
| 3.4.6 Biosampling and bioanalysis | 66 |
| 3.5 Organoids | 69 |
| 3.5.1 Tissue organoids | 70 |
| 3.5.2 Multicellular organoids..... | 70 |
| 3.6 Organ-on-a-chip..... | 71 |

| | |
|---|------------|
| 3.6.1 Fluid dynamics..... | 72 |
| 3.6.2 Organised patterning of cell types | 72 |
| 3.6.3 Control over mechanical stimuli..... | 73 |
| 3.6.4 Sensors to detect physiological parameters | 73 |
| 3.6.5 Example of Lung-on-a-chip..... | 73 |
| 3.7 State-of-the-art 3D breast cancer models..... | 75 |
| 4. Regulation for good practices within <i>in vitro</i> models..... | 78 |
| 5. Conclusions..... | 80 |
| Chapter 2. Role of stiffness and physico-chemical properties of tumour microenvironment on breast cancer cell stemness | 105 |
| Abstract..... | 106 |
| 1. Introduction..... | 106 |
| 2. Materials and methods | 109 |
| 2.1 Alginate-gelatin hydrogel preparation | 109 |
| 2.2 Unconfined compression tests: hydrogel stiffness..... | 110 |
| 2.3 Cell culture..... | 111 |
| 2.3.3 3D dynamic model: Quasi vivo system | 112 |
| 2.4 Cell proliferation and viability..... | 113 |
| 2.6 B-CSCs and EMT Marker expression: Flow cytometry..... | 113 |
| 2.7 ALDH expression: Aldefluor assay | 115 |
| 2.8 Analysis of cell aggregates: size and shape | 115 |
| 2.9 Principal component analysis | 116 |
| 2.10 Image acquisition and analysis | 116 |
| 2.11 Statistical analysis..... | 116 |
| 3. Results..... | 116 |
| 3.1 Modelling biophysical and chemical cues <i>in vitro</i> | 117 |
| 3.2 MDA-MB-231 proliferation is less sensitive to varying biophysical cues than MCF-7 .. | 120 |
| 3.3 Lower stiffness and perfusion permits for higher aggregate sizes in both cell lines | 123 |
| 3.4 E-CSCs and M-CSCs marker expression in MDA-MB-231 | 127 |
| 3.5 E-CSC and M-CSC marker expression in MCF-7..... | 130 |
| 3.6 Principal component analysis (PCA) of B-CSC markers | 132 |

| | |
|--|------------|
| 4. Discussion..... | 134 |
| 5. Conclusions..... | 139 |
| Acknowledgements..... | 140 |
| Supplementary information | 149 |
| Chapter 3. Additively manufactured BaTiO₃ composite scaffolds: A novel strategy for load bearing bone tissue engineering applications..... | 161 |
| Abstract..... | 162 |
| 1. Introduction..... | 163 |
| 2. Materials and methods | 166 |
| 2.1 Design and manufacturing of 3D scaffolds..... | 166 |
| 2.2 Physicochemical characterisation and mechanical properties evaluation | 168 |
| 2.2.1 Attenuated Total Reflectance Fourier Transform Infrared Spectroscopy (ATR-FTIR) | 168 |
| 2.2.2 Thermogravimetric analysis (TGA)..... | 168 |
| 2.2.3 Imaging: Scanning Electron Microscopy (SEM) and Micro-Computed Tomography (micro-CT) | 168 |
| 2.2.4 Mechanical properties..... | 169 |
| 2.3 Dielectric and piezoelectric properties..... | 169 |
| 2.4 <i>In vitro</i> cell studies..... | 169 |
| 2.4.1 Cell culture..... | 169 |
| 2.4.2 Scaffold cell seeding and mineralisation protocol..... | 170 |
| 2.4.3 Proliferation assay..... | 170 |
| 2.4.4 Alkaline phosphatase activity (ALP) assay | 171 |
| 2.4.5 Alizarin-red staining and deposited calcium quantification | 171 |
| 2.4.6 Immunofluorescence staining and image acquisition..... | 172 |
| 2.5 Statistical Analysis..... | 173 |
| 3. Results and Discussion | 173 |
| 3.1 Physicochemical and mechanical characterisation | 173 |
| 3.2 Electroactive properties..... | 180 |
| 3.3 <i>In vitro</i> evaluation of the 3D printed scaffolds | 182 |
| 3.3.1 Cytocompatibility..... | 182 |
| 3.3.2 Osteogenic potential and mineralisation | 184 |

| | |
|---|------------|
| 4. Conclusions | 187 |
| Acknowledgements | 188 |
| References | 189 |
| Chapter 4. Invasion and Secondary site colonisation as a function of <i>in vitro</i> primary tumour matrix stiffness | 198 |
| Abstract | 199 |
| Keywords | 199 |
| 1. Introduction | 200 |
| 2. Methodology | 202 |
| 2.1 General Cell culture | 202 |
| 2.2 3D cell culture: encapsulation in alginate-gelatin hydrogel beads | 203 |
| 2.2.1 Preparation of hydrogel precursors and crosslinking solutions | 203 |
| 2.2.2 3D breast cancer models: alginate-gelatin hydrogels | 204 |
| 2.2.3 Cell recovery: hydrogels dissolution | 204 |
| 2.3 3D bone models: PCL-based scaffold..... | 205 |
| 2.3.1 PCL scaffolds: bone scaffold | 205 |
| 2.3.2 Decellularization of PCL scaffolds: biohybrid bone scaffolds | 206 |
| 2.4 Alginate-gelatin hydrogels and PCL scaffold: breast to bone model | 206 |
| 2.4.1 Indirect migration model..... | 206 |
| 2.4.2 Direct migration model | 207 |
| 2.5 Cell proliferation assay | 207 |
| 2.6 Adhesion/ Cell spreading assay | 209 |
| 2.7 Scratch assay | 209 |
| 2.8 Invasion assay | 210 |
| 2.10 PThrP expression | 210 |
| 2.11 IL-6 release quantification | 211 |
| 2.12 Image acquisition and analysis | 211 |
| 2.13 Statistical analysis..... | 212 |
| 3. Results and Discussion | 212 |
| 3.1 Conditioning MDA-MB 231 with high stiffness leads to increased migratory and invasive phenotype..... | 212 |

| | |
|--|-----|
| 3.2 Decellularized PCL scaffolds to mimic bone ECM..... | 217 |
| 3.3 Indirect migration of MDA-MB 231 and MDA-IV cells in biohybrid scaffolds | 221 |
| 3.4 Direct migration of MDA-MB 231 and MDA-IV from hydrogels to biohybrid scaffolds | 225 |
| 3.5 Response of MDA-IV cells in ‘Direct’ and ‘Indirect’ model..... | 226 |
| Supplementary information | 235 |
| Final discussion and conclusions | 245 |
| Future work and perspective | 249 |

Total word count: 52,469 words

List of figures

| | |
|--|-----|
| Figure 1. Graphical abstract of the thesis..... | 19 |
| Figure 1-1. General representation of cell types found in breast tissue microenvironment.. | 33 |
| Figure 1-2. General representation of biochemical factors in breast tissue microenvironment..... | 37 |
| Figure 1-3. General representation of biomechanical factors in breast tissue microenvironment.... | 43 |
| Figure 1-4. Breast ductal microenvironment as a combination of cellular, biochemical and biophysical factors that define tissue functionality | 45 |
| Figure 1-5 Properties of <i>in vitro</i> models for tissue engineering applications..... | 68 |
| Figure 1-6. Examples of stomach organoid structure..... | 71 |
| Figure 1-7. Schematic representation of Lung-on-a-chip..... | 75 |
| Figure 2-1: Representation of independent cues included in the 3D models..... | 119 |
| Figure 2-2: Breast cancer proliferation in varying TME cues..... | 122 |
| Figure 2-3. Breast cancer cell aggregates in varying TME cues..... | 124 |
| Figure 2-4: Breast cancer cell circularity with varying TME cues..... | 126 |
| Figure 2-5: Flow cytometry analysis of CSC markers in MDA-MB231. | 129 |
| Figure 2-6: Flow cytometry analysis of CSC markers in MCF-7 cells..... | 131 |
| Figure 2-7: Principal component analysis (PCA) of B-CSC marker expression..... | 133 |
| Figure 3-1. Manufacturing of polymeric and composite scaffolds | 167 |
| Figure 3-2. FTIR spectra..... | 174 |
| Figure 3-3. Thermal characterization of the samples after extrusion:..... | 175 |
| Figure 3-4. SEM morphological evaluation of the 3D printed scaffolds at different magnifications | 176 |
| Figure 3-5. Micro-CT reconstruction of PCL | 177 |
| Figure 3-6. Porosity values derived from micro-CT scans..... | 178 |
| Figure 3-7. Dielectric response of scaffolds | 181 |
| Figure 3-8. Proliferation assay of Saos-2 cell lines when cultured in PCL (black), PCL/HA (red) and PCL/BaTiO ₃ (blue) scaffolds. | 183 |
| Figure 3-9. Osteogenic activity of Saos-2 cells in PCL, PCL/HA and PCL/BaTiO ₃ scaffolds..... | 186 |
| Figure 3-10. Collagen and osteocalcein deposition by Saos-2 cells in PCL, PCL/HA and PCL/BaTiO ₃ scaffolds | 187 |
| Figure 4-1: Schematic layout of experimental plan for indirect (A) and direct migration (B)..... | 208 |
| Figure 4-2. Cellular adhesion on stiffness conditioned cells..... | 215 |
| Figure 4-3. Migration assay of stiffness conditioned cells.. | 216 |
| Figure 4-4. Invasion assay of stiffness conditioned cells..... | 217 |
| Figure 4-5. Biohybrid PCL scaffolds..... | 220 |
| Figure 4-6. PTHrP expression and IL-6 release in indirect migration assay.. | 224 |
| Figure 4-7. PTHrP and IL-6 quantification in Direct Migration model.. | 227 |

List of Tables

| | |
|---|------------|
| Table 1-1. Factors used in regular cell culture and their characteristics..... | 47 |
| Table 1-2. Advantages and disadvantages of scaffold free methods for generating spheroids | 54 |
| Table 2-1. Alginate-based hydrogels composition..... | 111 |
| Table 2-2. Antibody dilutions for isotype control, primary antibodies and secondary antibody for various markers..... | 114 |
| Table 2-3. Adhesion ligand density, polymer concentration and stiffness of the four selected hydrogel groups..... | 117 |
| Table 3-1. Summary of processing conditions used to fabricate polymeric PCL scaffolds, PCL/HA and PCL/BaTiO3 composite scaffolds..... | 167 |
| Table 4-1. Final concentrations of Alginate, gelatin and calcium chloride in preparation of Alginate- gelatin gels..... | 204 |
| Table 4-2. Optimised printing parameters for 3D scaffolds | 205 |
| Table 4-3. Hydrogel composition of the four selected alginate-gelatin hydrogels varying compressive moduli (stiffness) and concentration of gelatin (adhesion ligand content)..... | 213 |

List of Abbreviations

2D – Two Dimensional

3D – Three Dimensional

3Rs – Reduction, refinement and replacement

AFM – Atomic Force Microscopy

ALDH – Aldehyde Dehydrogenase

ALP – Alkaline Phosphatase

AM – Additive Manufacturing

A β – Amyloid Beta

ANOVA – One-way Analysis of Variance

ATR-FTIR – Attenuated Total Reflectance Fourier Transform Infrared Spectroscopy

BAAA – Bodipy-aminoacetaldehyde

BaTiO₃ – Barium Titanate

B-CSCs – Breast Cancer Stem Cells

BM – Basement Membrane

BSC – Biosafety Cabinets

BSE – Back Scattered Electron

CAAT – Centre for Alternatives to Animal Testing

CAD – Computer Aided Design

CCLs – C-C motif ligands

CNS – Central Nervous System

CoA – Certificate of Analysis

CSF – Colony Stimulating Factor

DAPI – 4',6-diamidino-2-phenylindole

DCIS – Ductal Carcinoma in Situ

DMEM – Dulbecco's Modified Eagle Medium

ECACC – European Collection of Authenticated Cell Cultures

ECM – Extracellular Matrix

E-CSCs – Epithelial type Cancer Stem Cells

ECVAM – European Centre for the Validation of Alternative Methods

EGF – Epithelial Growth Factor

ER – Estrogen Receptor

FBS – Fetal Bovine Serum

FDA – Food and Drug Administration

FDM – Fused Deposition modelling

FGF – Fibroblast Growth Factor

GABA – Gamma aminobutyric acid

GAG – Glycosaminoglycans

GCCP – Good Cell Culture Practices

GIVIMP – The Good In Vitro Method Practices

GIVReSt – Good In Vitro Reporting standards

GLP – Good Laboratory Practices

GMP – Good Manufacturing Practise

HA – Hydroxyapatite

HA – Hyaluronic acid

HBS – Hapes Buffered Saline

HEPA - High Efficiency Particulate Air

HSCs – Haematopoietic stem cells

HTS - High throughput Screening

HTERT - human telomerase reverse transcriptase

HUVECs – Human Umbilical Vein Endothelial Cells

IATA – Integrated approaches to testing and assessment

ICH – International Conference of Harmonization

IDC – Invasive Ductal Carcinoma
IL-6 – Interleukin-6
IL – Interleukin
IM – Interstitial matrix
iPSCs – induced Pluripotent Stem cells
ISO – International Organization for Standardization
L – Litre
m – Metre
M – Molarity
M-CSCs – Mesenchymal type cancer stem cells
MFI – Median fluorescence intensity
Micro-CT – Micro computed tomography
MMP-9 – Matrix metalloproteinases
MSCs – Mesenchymal stem cells
MW – Multi-well
NOG – Noggin
OCR – Oxygen Consumption Rate
OCED – Organization for Economic Co-operation and Development
OOC – Organ on a chip
Pa – Pascal
PBS – Phosphate buffered saline
PCA – Principal component analysis
PCL – Polycaprolactone
PDMS – Polydimethylsiloxane
PDX – Patient derived xenografts
P-E – Polarisation electric field
PEG – Poly (ethylene glycol)

PES – Polyethersulfone
PFA – Paraformaldehyde
pHe – extracellular pH
PLA – Poly Lactic acid
PLGA – poly-(lactic-co-glycolic acid)
PLLA – Poly-(l-lactic acid)
PMDA – Pharmaceuticals and Medical Devices Agency
PMSF – Phenylmethylsulfonyl fluoride
pO₂ – partial pressure of oxygen
Poly-HEMA – poly 2-hydroxyethyl methacrylate
PR – Progesterone Receptor
PTHrP – Parathyroid Hormone related Protein
PtO₂ – Tissue partial pressure of oxygen
PVDF – Polyvinylidene Difluoride
RANKL – Receptor Activator of Nuclear factor Kappa-B Ligand
RFU – Relative fluorescence units
RS – Reference standards
RT – Room temperature
SD – Standard deviation
SEM – Scanning electron microscopy
SLS – Selective Laser Sintering
SLA – Stereolithography
SrHA – Strontium HA
TCP – Tissue culture plates
TCP – Tricalcium phosphate
TEB – Terminal end bud
TGA – Thermogravimetric analysis

TGA – Therapeutic Goods Administration

TGF – Transforming growth factor

TME – Tumour Microenvironment

TNBC – Triple negative breast cancer

USP – United states Pharmacopeia

WHO – World Health Organization

ZEB-1 – Zinc finger E-box-binding homeobox-1

Abstract

Breast tumour progression is a multifactorial phenomenon in which the tumour cells share a dynamic relationship with the tumour micro-environment (TME). TME is a complex combination of both cellular (fibroblasts, immune cells, endothelial cells) and non-cellular components (extracellular matrix (ECM), tissue architecture, signalling molecules, interstitial fluid, etc). The TME gets altered by the surrounding tumour and its dysregulation in turn affects tumour progression. Dysregulation of non-cellular TME cues such as ECM, extracellular pH, and interstitial fluid flow are correlated to breast cancer progression but their direct impact on breast cancer phenotypes has not been examined yet. Traditional preclinical models, like 2D cell culture *in vitro* systems, fail to mimic such cell-TME interactions, whereas use of animal models for such studies renders it difficult to control and decouple the TME variables. Hence the aim of this thesis was to engineer 3D *in vitro* models that could precisely mimic these TME changes and decouple them to understand their individual as well as collective contribution to breast cancer progression. Breast cancer cells were cultured in alginate-gelatin hydrogels used to mimic normal (1-2 kPa) and tumour (6-10 kPa) breast tissue stiffness. These were further cultured in a perfusion system (500 $\mu\text{L}/\text{min}$) to mimic interstitial fluid flow with media of different pH (pH 7.4 and 6.5). The *in vitro* model effectively decoupled these cues and captured their distinctive effect on two breast cancer cell lines' (MDA-MB 231 and MCF-7) proliferation, morphology, and cancer stem cell population. Overall, we observed that high stiffness and acidic pH are the main factors involved in increasing stem cell content of both the breast cancer cell lines. With metastasis sharing a major burden of breast cancer related deaths, impact of matrix stiffness on migration, invasion and bone metastasis was also probed using *in vitro* techniques. Bone microenvironment was mimicked by using "biohybrid" poly- ϵ -caprolactone (PCL) scaffolds that mimicked bone stiffness (45-55 MPa), porosity (~40-50%), and contained bone-ECM deposited by osteoblasts. Alginate hydrogels of different stiffness were combined with PCL scaffolds to model the "breast to bone metastasis", where high primary tumour matrix stiffness was found to be associated with increased migration, invasion and expression of osteolytic factors (PTHrP and IL-6) in metastatic breast cancer cell line MDA-MB 231. This thesis effectively explored primary tumour TME factors and the far-reaching implication they can have on metastasis and tumour progression. Additionally, these 3D *in vitro* models present themselves as future platforms for disease prognosis and drug efficacy studies in presence of relevant TME cues.

Declaration

The work in this thesis was carried out at The University of Manchester between September 2017 and May 2021 under the supervision of Dr Annalisa Tirella, Prof Kaye J. Williams and Dr Ayşe Latif. All of the work is my own, with contributions from collaborators acknowledged throughout. No portion of the work referred to in the thesis has been submitted in support of an application for another degree or qualification of this or any other university or other institute of learning.

Copyright statement

I. The author of this thesis (including any appendices and/or schedules to this thesis) owns certain copyright or related rights in it (the “Copyright”) and s/he has given the University of Manchester certain rights to use such Copyright, including for administrative purposes.

II. Copies of this thesis, either in full or in extracts and whether in hard or electronic copy, may be made only in accordance with the Copyright, Designs and Patents Act 1988 (as amended) and regulations issued under it or, where appropriate, in accordance with licensing agreements which the University has from time to time. This page must form part of any such copies made.

III. The ownership of certain Copyright, patents, designs, trademarks and other intellectual property (the “Intellectual Property”) and any reproductions of copyright works in the thesis, for example graphs and tables (“Reproductions”), which may be described in this thesis, may not be owned by the author and may be owned by third parties. Such Intellectual Property and Reproductions cannot and must not be made available for use without the prior written permission of the owner(s) of the relevant Intellectual Property and/or Reproductions.

IV. Further information on the conditions under which disclosure, publication and commercialisation of this thesis, the Copyright and any Intellectual Property and/or Reproductions described in it may take place is available in the University IP Policy (see <http://documents.manchester.ac.uk/DocuInfo.aspx?DocID=24420>), in any relevant Thesis restriction declarations deposited in the University Library, the University Library’s regulations (see <http://www.library.manchester.ac.uk/about/regulations/>) and in the University’s policy on Presentation of Theses.

Acknowledgements

“She stood in the storm, and when the wind did not blow her way, she adjusted her sails”- Elizabeth Edwards.

Much like this quote my PhD journey has been about finding, introspecting, failing, and coming up with solutions again. It has been nothing less of a cathartic and at the same time exhaustive experience. Fortunately, there were a lot of people that got me through and without whom this journey would have never been complete.

Firstly, I would like to express my gratitude to my supervisor Dr Annalisa Tirella for providing me the opportunity to work on this project and for her guidance during the same. Thank you for being the kindest person and helping me with all the big and especially the little things during this journey. Special thanks to both my co-supervisors Dr Ayşe Latif and Prof Kaye Williams for all their suggestions and guidance for the project. I am thankful to President’s doctoral scholarship (PDS) for funding the project.

I am grateful to all lab members of ‘Bioengineered systems lab’ group and ‘Experimental oncology’ group for being the best lab-mates and companions. Especially thankful to Wia and Chen for our lab chatter and fun outings. To Chen for recommending some of the best food I have tasted and being co-companion in making and complaining about Alginate based gels. To Siriwat, Xue, Khalsa, Iwan and Bushra for being there and helping around the lab.

Most importantly, I am so thankful for my big Indian family. Just all your memories were enough to get me through dark times. To my parents, uncles, and aunts for supporting my journey right from the beginning. I would like to thank my sister Pooja for her immense help and support and for the happy times we had together. My cousins, Yash and Yukta for being there and supporting me. Lastly, I would like to thank Vijay, my partner in everything, from beginning our journey together in Manchester and to getting through our PhDs.

Rationale for alternative format

The research undertaken during this PhD has resulted in three *in vitro* studies that collectively aim to model various aspects of breast cancer progression and bone metastasis. The research performed in this thesis is a coherent study, the results are arranged to obtain three independent research manuscripts and a book chapter to be used for publications to international peer-reviewed journals. **Chapter 1** is published as a chapter in the peer reviewed book “Biomedical Product and Materials Evaluation (Editor: P.V. Mohanan), **Chapter 3** is a published journal article in the peer reviewed “Materials Science and Engineering: C”, whereas **Chapter 2** and **Chapter 4** are written in journal format with the intention to be submitted to “Acta Biomaterialia”.

Thesis summary – Manuscript organisation

Engineered 3D *in vitro* models have the potential to model tissue pathophysiology and understand disease mechanisms, aiming to replace and/or reduce existing animal models. In the context of this thesis, aspects of breast cancer progression were modelled using a combination of biomaterials and tissue engineering approaches. Non-cellular components which are a major and a complex part of the tumour microenvironment (TME) are dysregulated during development and progression of the pathology, being recognised to have a key role in homeostatic disruption and extracellular matrix (ECM) remodelling. However, with the current models (2D *in vitro* models and animal models) it is difficult to 1) precisely control cancer associated ECM dysregulation and 2) decouple properties of the ECM to understand effect of its individual components on cancer cell phenotypes. Hence this research firstly focused on the development of 3D *in vitro* models able to mimic and decouple physical and chemical properties of normal and cancer associated ECM (mentioned as inputs, Figure 1), and secondly on understanding the effect of ECM variations on breast cancer phenotypes (mentioned as outputs, Figure 1).

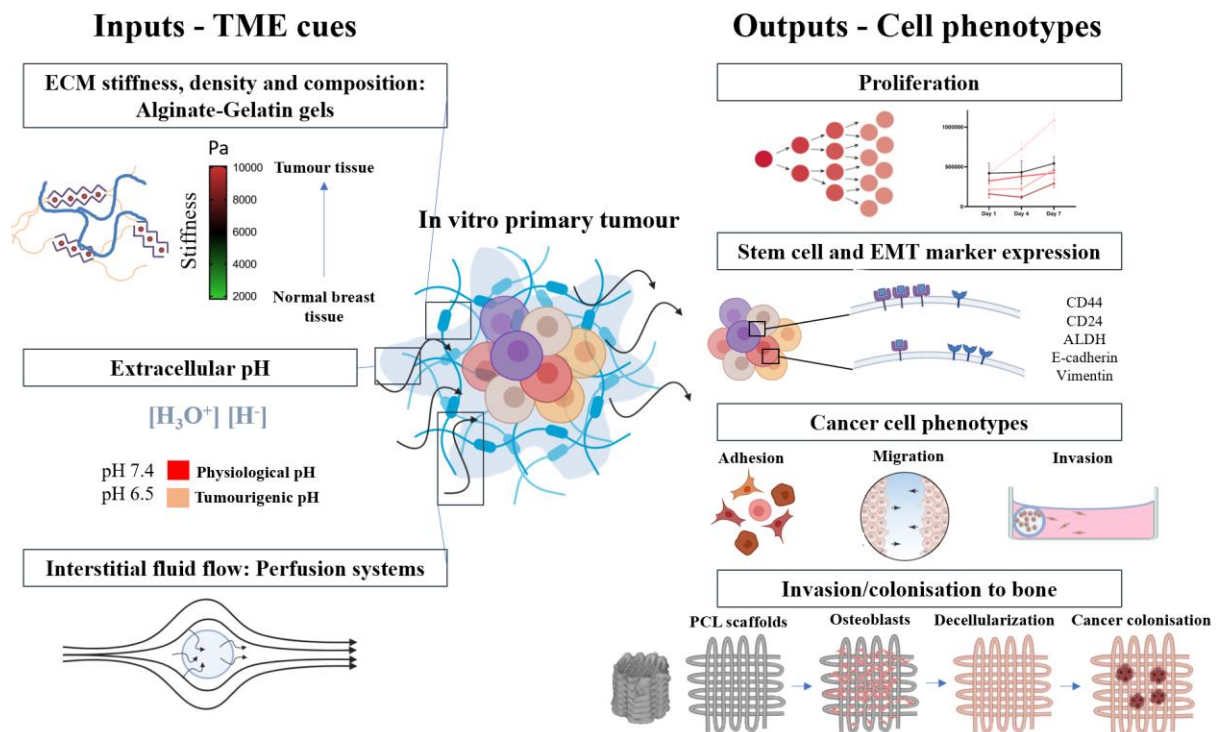


Figure 1. Graphical abstract of the thesis: Inputs defined by TME cues of ECM stiffness, density and composition, extracellular pH and interstitial flow. Outputs defined by cell proliferation, stem cell markers, migratory and invasive phenotype, and colonisation to a secondary site

With that in mind **Chapter 1** was written as an introduction to *in vitro* models and their required design criteria for mimicking better *in vivo* tissue physiology. This chapter illustrates important components (cellular, biophysical, and biochemical) of the tissue microenvironment that define its structure and function. It then elucidates several tissue engineering approaches used to incorporate these components in a single system with the aim to model tissue like structure and function. The chapter provides a comprehensive review of state-of-the-art *in vitro* models, with insights on their usage along with their advantages and disadvantages. Ultimately the main aim of this chapter is to introduce the reader to terms and concepts that will be used throughout the thesis.

TME properties like ECM composition, density, stiffness, extracellular pH and interstitial fluid flow are known to be highly altered during cancer progression. For example, increased collagen deposition and density of crosslinks is associated with primary tumour growth, promoting matrix stiffening and increased cells adhesion motifs. Increased cellular metabolism leads to acidic extracellular pH, whereas increased tumour mass causes increment of both interstitial pressure and fluid flow. To that end, **Chapter 2** focusses on engineering these TME changes in a single system, where matrix stiffness, density and composition was controlled by using alginate-gelatin hydrogels, extracellular pH (pHe) varied with cell culture media and a perfusion system allowed for mimicking interstitial fluid flow as in TME. With these models it was possible to decouple effects of matrix stiffness, matrix composition, extracellular pH and fluid flow and study their effect on cultured cells. Two breast cancer cell lines (i.e. MCF-7 and MDA-MB 231) were selected as representative of low grade luminal subtype and high grade basal subtype. Cells were cultured in selected TME cues and primary tumour breast cancer phenotypes of proliferation, cell cluster morphology and cancer stem cell (CSC) population were analysed. We found key differences in growth and morphology of less invasive, luminal cell type MCF-7 compared to more invasive, basal type MDA-MB 231. MCF-7's growth significantly decreased in higher stiffness and acidic pHe, whereas MDA-MB 231 sustained their growth in all microenvironments showcasing their aggressiveness. MDA-MB 231 showed increased irregularity in shapes of formed cell aggregates only in presence of high gelatin content and without correlation with matrix stiffness. On the contrary, MCF-7 showed similar spherical shaped cell aggregates in all microenvironments tested.

Most importantly we examined effects of these cues on two stem cell populations: mesenchymal CSCs (M-CSCs) and epithelial CSCs (E-CSCs). When the only variable was hydrogel's stiffness, this promoted increased E-CSCs population in MDA-MB 231 cells. The combination of higher stiffness and acidic pH_e caused increase of both types of CSC populations. Similar results were observed with MCF-7, where the combination of stiff matrix and acidic pH_e increased proportion of stem cells. These experiments are the first one to suggest that high stiffness and acidic pH_e, which are known hallmarks of tumour progression, further increase stemness in breast cancer cell population.

While these cues were found to be influential in cancer phenotypes at the primary site, the next step was to understand if invasion and metastasis to a secondary site are also affected. For the purpose of this thesis, we only examined breast to bone metastasis as it accounts ~60% of breast metastasis in patients. Similar to what describe in **Chapter 2** for breast tissue, bone tissue was also engineered *in vitro* using polymeric composite scaffolds. **Chapter 3** is a study performed in collaboration with Dr Elena Mancuso (Ulster University) and Dr Hamideh Khanbareh (University of Bath) that characterize few composite poly-ε-caprolactone (PCL) printed scaffolds as support for growing human osteoblasts and inducing ECM mineralisation. PCL was used as dispersion phase with inclusion of either hydroxyapatite (HA) or barium titanate (BaTiO₃) ceramic particles to mimic bone composition. Scaffolds were 3D printed superimposing a geometry able to mimic bone porosity. The addition of BaTiO₃ improved mechanical performance (stiffness) of scaffolds and improved dielectric permittivity, an important property to maintain bone-phenotype. Importantly, PCL BaTiO₃ increased cell proliferation and alkaline phosphatase activity supporting its role in maturation of osteoblast culture. Both HA and BaTiO₃ inclusion led to increased calcium and mineralised matrix deposition by osteoblasts, supporting the use of composite PCL scaffolds for bone tissue engineering purposes.

Following the reports of use on decellularized PCL scaffolds which are able to retain ECM secreted by cells post decellularization, **Chapter 4** described the possibility to use decellularized composite PCL scaffolds as bone secondary site. Composite PCL (i.e. PCL HA, PCL BaTiO₃ and PCL Strontium-HA) and pristine PCL scaffolds were used to culture osteoblasts, assessing 1) deposition of mineralised matrix after 21 days of culture and 2) decellularization methods to retain deposited bone ECM. Criteria for selection of a specific scaffold in further studies was their capability to

retain deposited ECM: PCL HA was found to be the one with highest mineralised matrix. The ‘biohybrid’ PCL HA scaffold was further used as bone model to study secondary breast metastasis *in vitro*. In the second part of **Chapter 4**, the effects of primary tumour matrix stiffness and composition on migration, invasion and secondary site response was studied. MDA-MB 231 cells were selected because of their high invasive potential and pre-cultured in alginate-gelatin hydrogels, previously used in **Chapter 2**. It was observed that culture in high stiffness increased migratory and invasive phenotype of MDA-MB 231 cells. Essentially, cells pre-cultured in high matrix stiffness also have increased expression of osteolytic factors, parathyroid hormone related protein (PTHrP) and Interleukin- 6 (IL-6), when cultured in bone scaffolds. We found in these experiments that high stiffness, more than high gelatin content, was important in driving metastatic behaviour of these cells.

Overall, the thesis elucidates direct effects of TME cues on various aspects of breast cancer progression and metastasis to bone. This study sets precedence for use of *in vitro* models that can mimic and decouple components of TME for further studies to better understand disease mechanism, with direct impact on the design and testing of therapeutic modalities.

Contribution of authors

Chapter 1. Engineered in vitro Models: Mimicking in vivo Physiology. Lekha Shah (LS) and Annalisa Tirella (AT). *Woodhead Publishing Series in Biomaterials*, Biomedical Product and Materials Evaluation (Editor: P.V. Mohanan), Pages 555-609 (2022).

LS (First author): Conceptualised the structure and wrote the original draft of the book chapter.

AT (Corresponding author): Guided in the organisation of the chapter, critically revised manuscript and approved the final version for publication.

Chapter 2. Role of stiffness & physico-chemical properties of tumour microenvironment on breast cancer cell stemness. Lekha Shah, Ayşe Latif (AL), Kaye J. Williams (KJW) and Annalisa Tirella. *Manuscript in preparation*

LS (First author): Conceived hypothesis and research objectives, contributed to planning, execution and data analysis of all the experiments in the manuscript, wrote the original draft and revised for final version.

AL (Contributor): Conceived hypothesis and research objectives, provided supervision and inputs on progress of the study, critically revised manuscript and approved the final version for thesis

KJW (Contributor): Conceived hypothesis and research objectives, provided supervision and inputs on progress of the study, critically revised manuscript and approved the final version for thesis

AT (Corresponding author): Conceived hypothesis and research objectives, designed experiments, provided supervision and inputs on progress of the study, critically revised manuscript and approved the final version for thesis.

Chapter 3. Additively manufactured BaTiO₃ composite scaffolds: A novel strategy for load bearing bone tissue engineering applications. Elena Mancuso (EM), Lekha Shah, Swati Jindal (SJ), Cecile Serenelli (CS), Zois Michail Tsikriteas (ZMT), Hamideh Khanbareh (HM) and Annalisa Tirella. *Mater. Sci. Eng. C* **126**, 112192 (2021). DoI: 10.1016/j.msec.2021.112192

EM: *Conceived hypothesis and research objectives, contributed to planning and execution of designing and manufacturing the scaffolds, provided supervision, drafted and critically revised the manuscript, and approved the final version.*

LS: *Conceived hypothesis and research objectives, contributed to planning and execution of in vitro cell studies including cytocompatibility and osteogenic potential investigations (Section 3.3), drafted the original manuscript and approved the final version.*

SJ, CS: *Contributed to planning and execution of designing, manufacturing, and mechanical and physiochemical characterisation of scaffolds (Section 3.1), drafted the original manuscript and approved the final version.*

ZMT: *Contributed to planning and execution of characterisation of electroactive properties of scaffolds (Section 3.2), drafted the original manuscript and approved the final version.*

HM: *Conceived hypothesis and research objectives, provided supervision, drafted and critically revised manuscript and approved the final version.*

AT: *Conceived hypothesis and research objectives, provided supervision, drafted and critically revised manuscript and approved the final version.*

Chapter 4. Invasion and Secondary site colonisation as a function of in vitro primary tumour matrix stiffness. Lekha Shah, Ayşe Latif, Kaye J. Williams, Elena Mancuso and Annalisa Tirella. *Manuscript in preparation.*

LS (First author): *Conceived hypothesis and research objectives, contributed to planning, execution and data analysis of all the experiments in the manuscript, wrote the original draft and revised for final version.*

AL (Contributor): *Conceived hypothesis and research objectives, provided supervision and inputs on progress of the study, critically revised manuscript and approved the final version for thesis*

KJW (Contributor): *Conceived hypothesis and research objectives, provided supervision and inputs on progress of the study, critically revised manuscript and approved the final version for thesis*

AT (Corresponding author): *Conceived hypothesis and research objectives, designed experiments, provided supervision and inputs on progress of the study, critically revised manuscript and approved the final version for thesis.*

Thesis context – Chapter 1

Chapter 1- “Engineered *in vitro* models: Mimicking *in vivo* physiology”, originally a book chapter, was written as an introduction to development of *in vitro* models. It explores important components of the *in vivo* tissue microenvironment (namely cellular, biophysical and biochemical) that form the template for establishment of *in vitro* models. Some of these components have been used further in the thesis to build ‘breast’ and ‘bone’ *in vitro* microenvironment. Additionally, this chapter advocates the need for 3D *in vitro* models and compares different types of tissue engineering techniques involved in their development. This includes both, a broad description of all the major techniques used generally in *in vitro* models, and also state-of-the-art breast cancer models. The terminologies and concepts used in this chapter serve as an introduction and rationalisation for the experimental design used to study breast cancer and bone metastasis later in the thesis.

Chapter 1. Engineered *in vitro* Models: Mimicking *in vivo* Physiology.

Lekha Shah¹, Annalisa Tirella^{1,*}

¹ Division of Pharmacy and Optometry, Faculty of Biology, Medicine and Health, University of Manchester, Oxford Road, M13 9PL, Manchester, United Kingdom

Woodhead Publishing Series in Biomaterials, Biomedical Product and Materials Evaluation

(Editor: P.V. Mohanan), (2022), Pages 555-609

DoI: 10.1016/B978-0-12-823966-7.00002-5

*Corresponding author: Division of Pharmacy and Optometry, Faculty of Biology, Medicine and Health, University of Manchester, Oxford Road, M13 9PL, Manchester, United Kingdom; annalisa.tirella@manchester.ac.uk

Abstract

Human tissues are all characterised by an intrinsic complexity, rendering them difficult to model. Animal models often do not resemble human characteristics and involve strict ethical regulation for their use in research. For these and many other reasons, there is an increasing need for preclinical *in vitro* models to replace and reduce the use of animals in research and to study human cellular and tissue functionality. Current bioengineering strategies aim to advance three-dimensional (3D) *in vitro* models and mimic *in vivo* complexity as well as to study functional and systemic responses. Advancements in 3D *in vitro* technologies will provide the opportunity to study biological processes, additionally enabling high-throughput drugs testing and efficacy. This chapter focuses on bioengineering tools, including biomaterial development and tissue engineering techniques that define tissue microenvironment and functionality, with an emphasis on their inclusion as established emerging *in vitro* technologies. The chapter further illustrates the development of different *in vitro* models and compares a variety of strategies used to achieve *in vivo*-like functionalities. Last, it explores current regulations for validation of *in vitro* models and harmonisation of practices for their use, providing insightful guidelines for future research.

Keywords

In vitro models, Spheroids, Organoids, Organ-on-the-chip, Biomaterials, Bio-fabrication techniques, 3D printing, Validation and harmonisation of *in vitro* models.

Overview

Over past decades, there has been an open debate among scientists on the most appropriate models to study biological processes as well as to understand physiological and pathological phenomena. What we know is that animal models can be engineered and genetically modified to replicate certain aspects of human diseases, preserving all systemic biochemical signals and organs/tissues crosstalk. In these models, complex and systemic responses are naturally included allowing a more holistic interrogation of biological processes. However, there are two main drawbacks in using animal models: the first is the lack of representation of the exact human physiology, the second is ethical concerns with their usage.

It is important to consider that it is difficult to entirely engineer, map, and replicate human physiology and diseases in animal models. Among the most used animal models, some are known to lack important components of the studied biological process, or factors involved in the disease; for example, there are several transgenic animal models used for cancer research which are able to spontaneously form tumour masses, however these do not mimic the human tumour progression¹. On the other hand, tumour xenograft mouse models, implanted with human tumour cells, strictly require to be immune-compromised and as a result are unable to mimic interactions of immune cells with tumour mass². Diseased conditions such as Alzheimer's are age dependent and evolve slowly by steady and sustained release of Amyloid Beta (A β) peptides. Such slow evolution process has not been replicated yet in animal models³.

Another critical aspect to consider are the strict ethical regulations for the use of animals in research, which have been increased across countries and include not only restrictive use of certain animals for experiments but also introduce the 3Rs principles (reduction, refinement and replacement) for the use of animals in research^{4,5}. While reduction and refinement ensures optimum use of animals in procedures, replacement has motivated innovation in development of alternatives such as *in vitro* models⁵. For example, the UK has strictest regulation compared to other countries for the use of animal models as included under the Animal Scientific Procedure Act (ASPA) 1986. Along with restrictive use of dogs, cats, monkeys and horses, additional practices like cost-benefit analysis of every procedure is mandatory under the ASPA act^{6,7}. Similarly, centres like UK's National centre for replacement, refinement and reduction (3Rs) of

animal research follow and encourage ideals conceptualised on ‘Principles of Humane experimental techniques’ by Russell and Burch ⁸.

In this perspective, engineered *in vitro* models can offer two main advantages: the use of primary human cells to better model human physiology and also bypass most of the ethical issues that are linked with use of animals in research. Ethical approval and consent, as well as easier access to biobanks and human samples, has incredibly simplified the use of human-derived materials donated for research. With guidelines for replacement of animal models, like 3Rs ⁹, and the considerable development of biomedical sciences, *in vitro* models hold an exceptional potential to recapitulate the human biology/physiology and address the research question in a more relevant manner.

This chapter will focus on the design of *in vitro* models and cover essential criteria to consider in mimicking *in vivo* physiology. First, it will illustrate the most important elements of the tissue microenvironment that are known to orchestrate human physiological functions, followed by bioengineering solutions for the incorporation of such microenvironmental factors into *in vitro* models. Finally, emerging regulations around the use of biomaterials and development and validation of *in vitro* models will be discussed.

1. The tissue microenvironment

The physiological microenvironment of any tissue can be seen as the combination of cellular, biophysical and biochemical components. The combination, as well as the temporal and spatial location of each component, are finely controlled at a micro scale or at a cellular level and their synergy provides the tissue with its three-dimensional (3D) structure and characteristic function(s) ¹⁰. In other words, the functional heterogeneity of each tissue and organ is attributed to the distinctive and tissue-specific microenvironment. With the perspective to engineer and/or regenerate a tissue, there are two intrinsic challenges: identify the key properties of the microenvironment directly linked to tissue-specific functionality, and establish standard guidelines for the design of microenvironments that can be then used to model tissues or organs ¹⁰⁻¹².

Animal models have been used in the past decades as the only alternative to human in many research fields. Although useful and essential in many studies, animal models often fail in

providing relevant information on human specific tissue interactions. As consequence, many studies may still be inconclusive, e.g. prediction of drug efficacy and translation to therapies. The dilemma yet is to identify unique methods to characterise human tissue microenvironment and inform bioengineers and regulatory bodies on the most appropriate models to be used. This is key to overcome ethical issues involved with *in vivo* studies and also have a better clinical prediction with possibility for personalised therapeutics as well as for capturing variations in human diseases due to its high throughput nature. Moreover, to increase the complexity of the problem, it is essential to understand the dynamic and interdependent nature of microenvironment's components and identify the key factor(s) essential to control and direct tissue physiology. Once all these factors are uniquely identified, tissue engineering approaches could be used to mimic these cues and develop novel and relevant *in vitro* models to represent *in vivo* physiology.

In this section we briefly introduce the cellular, biochemical and biophysical components of the breast tissue microenvironment that play a role in normal as well as tumour conditions, ultimately affecting tissue functionality and disease physiology (Figs 1-3)

1.1 Cellular components

Organs are functional and structural combination of two or more tissue types. In turn, each tissue is comprised of cell types that control its function (Fig. 1). This section will focus on different cells of the four tissue types found in human anatomy: epithelial, connective, muscle and nervous tissue. Particularly, breast tissue is a fibro-glandular tissue that consists of glands/ducts for milk secretion which are lined by epithelial tissue and surrounded by fibrous connective tissue (Fig 1). Although nervous and muscle tissue are also present, dysfunction of epithelial and connective tissue is the most involved in breast cancers.

1.1.1 Epithelial tissue

The epithelial tissue comprises of epithelial cells forming a uniform and homogeneous layer that cover the inner and the outer lining of the organs. These cells have a wide variety of functions that includes tissue protection, secretion, absorption, sensing and transport of nutrients. Due to their important structural function of lining the tissues, they are often interconnected to neighbouring cells via anchoring junctions, tight junctions or gap junctions ¹³.

Depending on the function, epithelial cells have different spatial arrangements, specialized structures or activities. For instance, endothelial cells lining the capillaries have flat single cell layer called simple squamous epithelium which facilitates exchange of nutrients and growth factors. Whereas, stratified squamous cell epithelium consists of multicellular layer that functions to protect the tissue underneath located in linings of the skin, mouth, oesophagus, vagina, urethra etc. For some tissues like the lining of the respiratory tract and fallopian tubes, specialised structures called cilia are present on the apical surface of epithelial cells to facilitate movement of particulate matter and germ cells respectively ¹³.

Specialised activities, like synthesis and secretion of biochemicals, essential for organ's function are also carried out by epithelial cells in distinctive structures called glands. Endocrine glands like anterior pituitary gland and pancreas consist of a group of cells that release hormones in the blood stream directly; whereas exocrine glands such as epithelial cells of breast lobules release milk in isolated tubular ducts ¹³.

1.1.2 Connective tissue

Connective tissue consists of cells that function to connect, protect and insulate tissue contents and are also involved in transport of fluids and nutrients. Connective tissue has a wide range of classification that depends on function, cell types and structure of extracellular matrix (ECM) secreted by them. Unlike epithelial cells, these cell types are mostly surrounded by their own ECM and have little direct cell-cell connections ^{14,15}. The role of ECM and its composition will be discussed later in this chapter, whereas this section will focus on cell types of connective tissue.

Stromal connective tissue, or simply connective tissue, provides structural support to tissue contents. It has resident cells like fibroblasts that are primarily responsible for the release of ECM and adipocytes that store fat globules to insulate the contents of the tissue. Together they protect tissue from thermal and mechanical shock ^{14,15}.

Special connective tissues include blood, bone and cartilage. Blood, also known as fluid connective tissue, consists of erythrocytes, platelets, leucocytes and other immune cells that are responsible for transport of nutrients and immune protection throughout the body. Immune cells like macrophages, mast cells and lymphocytes can migrate to stromal connective tissue and help in tissue remodelling in response to pathogens, wound healing, or tissue development ^{14,15}.

Bone and cartilage are supportive connective tissues. Osteoblasts are the cellular component in bone responsible for secreting bone matrix and bone mineralization. To regulate bone homeostasis, osteoclasts are also a part of this connective tissue and are responsible for bone resorption. Chondrocytes are present in cartilage and are responsible for its ECM structure ¹⁵.

1.1.3 Muscular tissue

Muscle tissue is mainly responsible for contractile functions that enable the movement of joints or contractions of specific organs ¹⁶. Muscle cells have special structural modification to facilitate quick transfer of contractile signals ^{16,17}.

Skeletal muscles, responsible for body's voluntary movements like locomotion, are composed of myocytes. In this tissue type, several myoblasts can fuse and form multinucleated long muscle fibres with actinomyosin chains forming along the fiber to relay contractile signals. Due to the actinomyosin chains they appear striated under the microscope ^{16,17}.

By contrast, involuntary movements (e.g., cardiac muscles) are initiated by branched cardiomyocytes that have specialised intercellular junctions called intercalated disc to relay electrochemical signals. Smooth muscle tissues are involved in involuntary movement of tissues and organs and have cells that are characterised by absence of striations and appear spindle shaped ^{16,17}.

1.1.4 Central and peripheral nervous tissue

Neurons are responsible for generation and transfer of electrochemical information in the nervous tissue. Neurons are biochemically linked through neurotransmitters to coordinate information transfer in the brain and also to other organs ¹⁸. As a consequence of their function neurons have a distinctive morphology with two types of protoplasmic processes extending from the cell body: axons and dendrites. Neurons are classified as unipolar, bipolar and multipolar neurons based on the structure of these processes ^{19,20}. The most common type of structure found in the central nervous system (CNS) are the multipolar neurons, which have one axon and several dendrites. Whereas bipolar neurons have one axon and one dendrite extending on the opposite side of the cell body. These are rare and mostly found in sensory organs like in the retina of eyes and the olfactory mucosa.

Based on the function in the peripheral nervous system, neurons are classified as sensory which convey sensory inputs to the CNS and motor neurons which send information to muscles and organs from the CNS. Interneurons are the ones that transfer signals among the sensory and motor neurons to regulate their signals ²⁰.

Multipolar neurons in CNS are also classified based on the neurotransmitters they secrete, for example GABAergic or dopaminergic neurons that release gamma aminobutyric acid (GABA) or dopamine respectively ¹⁹.

Other cell types called neuroglia in the nervous tissue are responsible for development and moderation of the neuron's function. These include astrocytes, microglial cells, Schwann cells and satellite cells ^{18,20}.

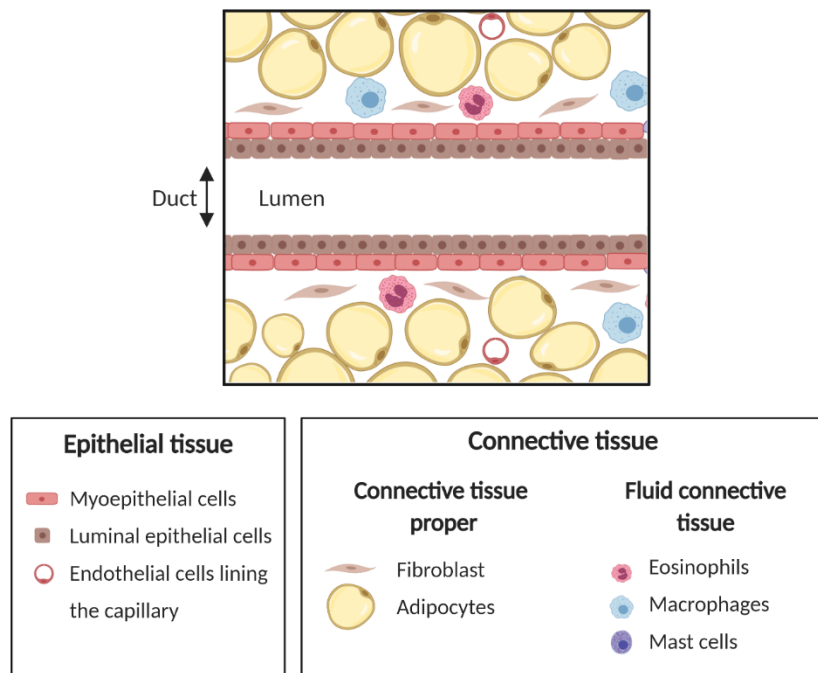


Figure 1. **General representation of cell types found in breast tissue microenvironment.** Mammary ducts are present in breast tissue to transport milk secretion and are lined with layers of epithelial cells. The epithelial structure is surrounded by connective tissue or stromal tissue containing fibroblasts and adipocytes. The connective tissue is interspersed with blood capillaries lined by endothelial cells. Immune cells like macrophages and eosinophils are recruited from blood capillaries to the connective tissue region. Created with BioRender.com.

1.1.5 Stem cells and progenitors

Stem cells, a pool of undifferentiated and unspecialised cells, are known to divide asymmetrically to maintain their original population as well as to produce varying levels of differentiated cells in the tissues. Human stem cells are capable of differentiating into multiple cell types; hence they hold a tremendous potential for development of relevant *in vitro* models and be used in regenerative medicine application. Human stem cells are classified as a function of their potency (or the ability) to create different types of cells ²¹. Totipotent stem cells have the potential to differentiate into all cell types, such as zygote which is involved in development of an organism forming embryonic and extra-embryonic tissues. Pluripotent stem cells, like embryonic stem cells (ESCs), can differentiate into embryonic tissues only. Multipotent cells have the ability to differentiate into several types of a specific lineage, like hematopoietic stem cells (HSCs) present in the bone marrow create blood cells. On the other hand, oligopotent stem cells, like myeloid cells, have a narrower potency, becoming only white blood cells. Unipotent stem cells, by definition, can make only one type of cell, an example are dermatocytes that differentiate into skin cells ²¹.

Adult human stem cells that are present post developmental stage in humans are mostly multipotent or less. They produce tissue specific, terminally differentiated cells and are involved in tissue homeostasis and repair ²². Examples of these include; hematopoietic stems cells, neural stem cells, prostate gland stem cells, intestinal stem cells and mammary gland stem cells ²². The fate of these stem cells is determined by their *niche*, or the extracellular microenvironment ²³. The so-called *niche* is a specialised and transient microenvironment, responsible to direct cell-cell interactions, and includes specific signalling molecules or matrix proteins ^{24,25}. Much research has been performed in the past years to understand the main factors directing stem cell differentiation. Since early 2000s, tissue engineering approaches have been used to better understand these differentiation mechanisms, analysing single and combinations of physico-chemical stimuli in engineered *in vitro* models ^{26,27}.

Although useful, applications of adult stem cells have limitations to consider like difficulties in isolation, amplification and long-term culture. Similarly with ESCs, there are current ethical and regulatory concerns that restrict their usage within the range of '14-day limit' and inhibits usage past the stage of primitive streak emergence ^{28,29}. As a potential candidate, another type of stem

cell has been created in laboratories known as the induced pluripotent stem cells (iPSCs). iPSCs are basically adult somatic cells, such as skin biopsy derived fibroblasts, that undergo nuclear reprogramming to change potency by inducing transcription of a combination of four factors: Oct4, Sox2, Klf4 and c-Myc³⁰. Due to their abundant nature, ease of isolation and less regulatory concerns, the number of research models using iPSCs is much higher than the ones using adult stem cells and ESCs³¹. The main advantage of iPSCs, when compared to ESCs, is being patient-specific which reinforces their use and clinical relevance in personalised treatments^{32,33}.

Nonetheless, both ESCs and iPSCs have been shown to differentiate into various cell types *in vitro* by using varied methods like chemical engineered culture medium, engineered stem cell niche as well as introducing mechanical, electrical and perfusion engineering³⁴. However, a detailed description of potential uses of ESCs and iPSCs is beyond the scope of this chapter.

1.2 Biochemical factors

Biochemical factors include secreted signalling biomolecules responsible for several processes and linked to specific tissue functions. The effect of a secreted factor is determined by its biochemical structure and its resultant interaction with cellular signalling (Fig. 2). Biochemical factors are categorised based on their mode of signalling: endocrine, paracrine and autocrine³⁵. Insulin is one example of a factor involved in endocrine signalling, with direct impact on tissue function at distant sites from its secretion. The signal is distributed systemically by direct release and transported in the blood vessels. On the contrary, paracrine signalling involves factors that act on neighbouring cells, such as the release of neurotransmitters in the synaptic junction of neurons. Autocrine factors, instead, cause a response on the same cell that secretes the factor, such as macrophages secreting interleukin-1 beta (IL-1 β) in response to microbial invasion that use the factor to stimulate themselves and trigger the release of other cytokines directing macrophage recruiting and polarisation.

Another classification method used for biochemical factors is based on their chemical nature. In the perspective of tissue engineering, this classification method enables an easier identification of required concentration profiles and purity for regulation guidelines. As an example, the previously mentioned cytokine IL-1 β or IFN- γ is dosed to macrophages at a concentration of 20 ng/ml³⁶ and 100 ng/ml³⁷ respectively to induce inflammatory response. Based on chemical structure,

biochemical factors are grouped as: peptides, steroids and neurotransmitters³⁵. Both peptide and steroid biochemical factors have been found to be important in breast duct elongation and bifurcation, which is a well-regulated process for mammary morphogenesis during puberty and lactation (Fig 2)³⁸. Dysregulation of these hormones such as estrogen and growth factors like GF, HGF and EGF has been linked to breast tumour formation and progression^{39,40}.

1.2.1 Peptide

This factors consists of chain of amino acids which can be in the form of small peptides (2 – 50 amino acids) or large proteins^{35,41}. In most of the cases, peptide hormones signal target cells by binding to their specific receptors on the cell surface³⁵.

Examples of factors belonging to this group are insulin and glucagon, both secreted by islet cells in pancreas and involved in endocrine regulation of glucose metabolism. Another well-known example include growth hormone, thyroid stimulating hormone, follicle stimulating hormone which are secreted from the pituitary gland⁴¹.

A large variety of paracrine signalling growth factors like epidermal growth factor (EGF), fibroblast growth factor (FGF), transforming growth factors (TGF) which are involved in cell proliferation and differentiation belong to this group. All these factors play an essential role in tissue development and repair^{42,43}.

A wide range of factors important in immune response with functions such as immune cell recruitment, pro- and anti-inflammatory effects to regulate cell proliferation, apoptosis and differentiation are included in this group⁴⁴. Among these, the most important are cytokines, like interferon family and interleukins family (IL), as well as chemo-attractants, for example the colony stimulating factor (CSF) and the C-C motif ligands (CCLs).

1.2.2 Steroid

Steroid hormones are hydrophobic molecules synthesized from cholesterol that are able to diffuse through the plasma membrane^{35,45}.

Examples of this group are sex hormones such as testosterone, estrogen, progesterone; as well as thyroid hormone such as glucocorticoids and vitamin D. Overall these hormones have functions

in many important processes like metabolism, survival in stress, sexual characteristics development, inflammation and immune functions ⁴⁵.

1.2.3 Neurotransmitters

Neurotransmitters are soluble biomolecules released by neurons in response to action potential responsible for transmitting information between neurons ^{35,46}.

Some examples of these factors include serotonin, dopamine, acetylcholine, glutamate, glycine ⁴⁶. Similar to peptide hormones, neurotransmitters also have receptors on post synaptic neurons (receptor neuron) to transmit the signal ⁴⁶.

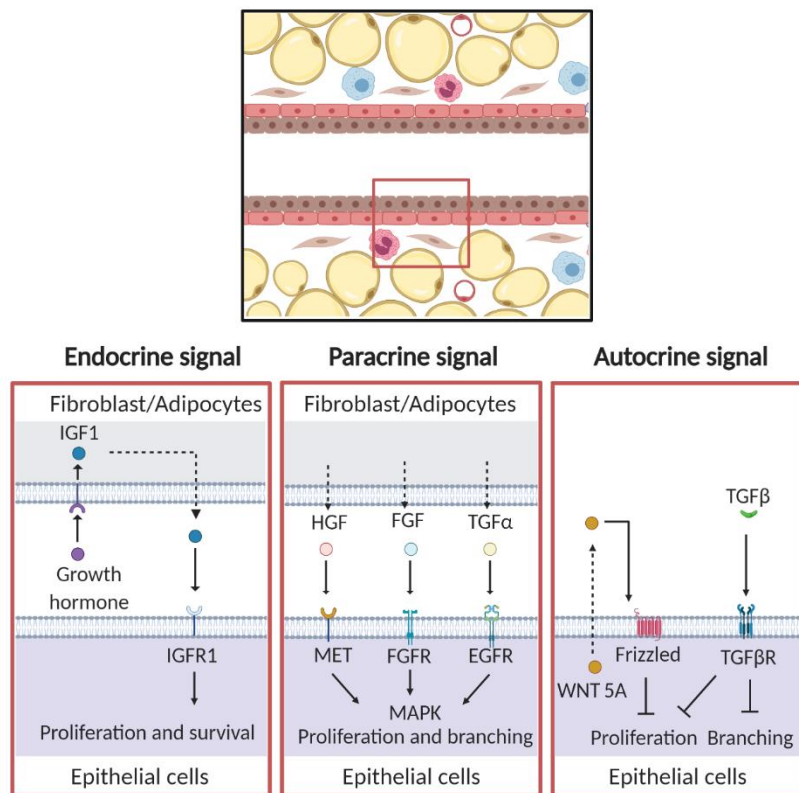


Figure 2. **General representation of biochemical factors in breast tissue microenvironment.** Biochemical factors regulate tissue dynamics like mammary duct elongation, bifurcation or lateral branching via paracrine, autocrine and endocrine signals. Endocrine signalling of growth hormone by pituitary gland acts to induce epithelial cell proliferation. Paracrine signals of growth factors like HGF, FGF and TGF- α from stromal cells can induce both proliferation and branching of the duct epithelial cells. Autocrine signalling of TGF- β secreted by epithelial cells acts as a negative feedback loop to inhibit duct

proliferation and branching. *FGF*, fibroblast growth factor; *HGF*, hepatocyte growth factor; *TGF- α* , transforming growth factor- α ; *TGF- β* , transforming growth factor- β . Modified from Gjorevski N, Nelson CM. Integrated morphodynamic signalling of the mammary gland. *Nat Rev Mol Cell Biol.* 2011;12(9):581-593. Created with BioRender.com

1.3 Biophysical components

1.3.1 Extracellular matrix composition and mechanical stiffness

The extracellular matrix (ECM) is a major non-cellular component of the breast microenvironment and consists of fibrous proteins and proteoglycans secreted by cells that provide physical support, mechanical strength, hydration, and buffering capacities to the tissue. Apart from being integral to biomechanical cues, ECM components are also known to contribute to biochemical signalling with impact on biological processes like cell growth, differentiation, migration, survival and metabolism ⁴⁷.

Proteoglycans are a heterogenous group characterised by a protein covalently linked with one or more chains of glycosaminoglycan (GAG) and are typically responsible for hydration and resistance to compressive mechanical loads (Fig. 3). The key component of proteoglycans are GAGs, polysaccharide chains of repeating disaccharide units ⁴⁷. Different types of GAGs are classified depending on the chemical modifications present, typical examples are sulphated GAGs (e.g. heparin sulphate, chondroitin sulphate) and non-sulphated GAGs (e.g. hyaluronic acid, HA). Multiple GAGs are then linked to the protein core to form small leucine rich proteoglycans (SLRP) like decorin or large proteoglycans like aggrecan, versican and neurocan. With their capacity to bind to water and other ECM proteins like collagen, proteoglycans in interstitial matrix and basement membrane in breast tissue are important for ECM hydration and mechanical stiffness. Furthermore, high mammographic density and tissue stiffness is linked with increased proteoglycan deposition of aggrecan, versican and prelecan which increases breast cancer risk ⁴⁸. Elevated stromal versican is also associated with increased rate of relapse in breast cancer patients ⁴⁹. Additionally, proteoglycans are involved in signalling pathways affecting cell adhesion, migration and proliferation. For instance, SLRP regulates EGF and TGF- β signalling by providing cells with an accessible repository via binding of these factors ⁵⁰. One such example is

decorin which is known to inhibit multiple receptor tyrosine kinases and hence showing anti-cancer, anti-metastatic activity ⁵¹.

Among the protein components of the ECM, collagen and elastin are principal fibrous proteins. Collagen, considered the most abundant fibrous protein of the ECM, has about 28 known types in vertebrates and has a signature triple helix structure made up of three alpha-polypeptide chains. Collagen types are classified based on their alpha-chain composition and supramolecular structure formed by crosslinked collagen helix, both of which are largely dictated by the mechanical function of the tissue ⁵². For example, collagen type I is found in various connective tissues like bones, tendons and skin. In tendons, these collagen fibrils form thick parallel bundles to complement unidirectional tensile strength; whereas in skin these fibrils are loose wavy structures to accommodate multidirectional forces ^{52,53}. The second type of collagen prevalent in ECM is collagen IV. It is found in basement membranes of epithelial cells and has a mesh-like structure to facilitate their anchoring to the underlying connective tissue (Fig. 3). Similar to proteoglycans, increased collagen deposition and linear alignment of collagen fibrils in breast tissue is linked with high tissue stiffness and higher grade of tumours in patients ⁵⁴. Other fibrous proteins found in ECM include elastin, fibronectin, laminin, fibrillin play a critical role in crosslinking fibrous proteins and their content varies significantly between tissues with active contribution to mechanical properties and control over stromal cell behaviour ⁴⁷. In fact, all these proteins have specific cell adhesion domains involved in cellular mechano-transduction and ECM sensing. Fibronectin and laminins are such proteins that are recognised by cells through membrane proteins called integrins which ultimately have pleiotropic effects on cellular proliferation and migration, having association with tumorigenic phenotype (Fig. 3) ⁴⁷. The interaction of all these matrix components provide the characteristic tensile strength or stiffness to each tissue that could range from 10^3 Pa (breast) to $10^6 - 10^9$ Pa (bone), preventing mechanical ruptures and allowing deformations typical of repetitive movements ⁵².

ECM dynamics: Dynamics and consequent remodelling of the ECM is one of the most important factors to consider when looking at tissue function. ECM dynamics is associated with many biological processes such as wound healing, immune response, and tissue development like mammary gland morphogenesis. Each tissue has a characteristic population of enzymes that regulates the ECM composition (with both degradation and synthesis of new components) and the

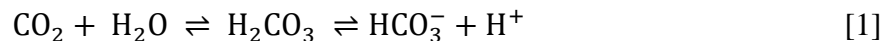
mechanical response. Typical examples are matrix metallo-proteases (MMPs), serine and cysteine proteases, mainly responsible for the degradation of specific ECM domains (i.e. fibrillar proteins) and orchestrating ECM homeostasis. On the other hand, ECM sensing by integrins is responsible for deposition of fibronectins and laminins that leads to a cascade of deposition of other required ECM components^{47,55}. Further, enzymes such as Lox and transglutaminase crosslink collagen fibrils which can increase tissue stiffness⁵⁶. The interplay of ECM degradation, deposition and crosslinking also leads to changes in mechanical properties of the tissue, hence making tissue stiffness a dynamic and temporal property. In case of breast cancer, ECM remodelling by proteases, increased ECM crosslinking and deposition ultimately increases tissue stiffness and is responsible for tissue ductal invasion and duct bifurcation^{38,56} (Fig. 4).

1.3.2 Partial pressure of O₂ (pO₂)

Oxygen is a key element in maintaining the biological function as its consumption in aerobic respiration is an important energy source for all cellular activities. Oxygen is actively transported in the blood stream, with initial sourcing in the lungs where oxygen binds and is carried by haemoglobin through arteries, and then diffuses to tissues through capillaries. The transport and diffusion of oxygen to tissues is driven by: (1) the gradient of oxygen's partial pressure, (2) the local tissue metabolic demand, (3) available surface area for its exchange, and (4) permeability of diffusion barriers (e.g., epithelial layer). A peculiar characteristic of tissues, both in normal and diseased state, is the tissue partial pressure of oxygen (PtO₂). This value is regulated by the tissue consumption rate, blood flow and the availability of oxygen; for example, average PtO₂ of nervous tissue in the brain is in the upper range of 30 – 48 mm Hg as it depends on constant supply of oxygen from the blood. Relatively high oxygen content is required also in skeletal muscles, but as the tissue is tolerant to hypoxia, typical oxygenation is described by PtO₂ values ranging from 7.5 to 31 mm Hg⁵⁷. Even within the same tissue type PtO₂ values can change due to diseased conditions such as cancer where hypoxia is present in tumour core due to increased local tissue metabolic demand. Normal breast median PtO₂ is around 65 mmHg, whereas median PtO₂ in breast cancer tissue can reach 10 mmHg⁵⁸.

1.3.3 pH and tissue buffering

Each tissue and organ have an acid-base balance where typical physiological pH is kept towards slightly basic values of 7.35 to 7.45. The homeostasis of pH values is essential to various cellular biochemical reactions, and also contributes to the maintenance of protein structure and function, like oxygen transport by haemoglobin ⁵⁹. There are exceptions to the typical physiological pH value, like in compartments of the gastro-intestinal tract and in intracellular organelles. In the first example, stomach and intestine's lumen have acidic pH values varying between 1.5 and 7 to facilitate the degradation of lipids, fats and carbohydrates for digestion ⁶⁰. When looking at intracellular organelles (e.g. endosomes, lysosomes), the pH values are regulated between 5.0 and 6.5 to ensure protein degradation ⁶¹. In case of diseases, pH homeostasis is dysregulated and shifted to more acidic values, like cancer and inflammatory states display pH values in the range of 6.5 to 7. pH regulation is closely linked with metabolism and respiration. Basically, carbon dioxide released by cellular metabolism in any tissue, reacts with water to form carbonic acid that further dissociates as bicarbonate and hydrogen ion ⁶². This reaction is the primary buffer system of the interstitial space in the tissue microenvironment and remains in equilibrium to maintain the pH.



Other local buffer systems also include phosphate buffers as well certain proteins that help maintain intracellular pH.

1.3.4 Ions and small molecules

Other ions important in physiological functions are sodium (Na^+), potassium (K^+), calcium (Ca^{2+}), phosphate (PO_4^{3-}), iron (Fe^{2+}), magnesium (Mg^{2+}) chloride (Cl^-) and copper ions ⁶³. Sodium and potassium are principal cations important in maintaining cellular osmotic balance and in propagating action potentials in cells of nervous and cardiac tissues ^{63,64}. Calcium is involved in normal muscle and cardiac muscle contraction, blood coagulation, as well as acts as an enzyme activator and secondary messenger for hormones ⁶⁵. Between all the functions of calcium, the most important one is the formation of bone tissue (performed along with phosphate). Phosphate ions are additionally important in intracellular ATP and nucleic acid synthesis ⁶⁶. Additionally, gas

molecules like nitrogen oxide (NO) and carbon mono-oxide (CO) are involved in blood vessel dilation and work on endothelial cells in response to acetylcholine released by neurons ⁶⁷.

1.3.5 Interstitial fluid flow and blood flow

Soluble factors and fluids are free to move within the ECM to guarantee their provision and removal from the microenvironment. Interstitial fluid flows through the ECM around the cells, transporting mixtures of plasma nutrients from surrounding blood capillaries and removing cellular waste to the nearest lymphatic capillaries. This fluid flow is driven by hydrostatic and osmotic pressure differences between capillaries and it is regulated by lymphatic drainage, blood flow and other movements typical of arterial pulsation and respiration ⁶⁸. Although there is a debate over the measurement and interpretation of the velocity of interstitial fluid flow, technological advancements and more precise experiments suggest that typical interstitial fluid velocities are in the range of $0.1 - 2 \mu\text{m sec}^{-1}$ ⁶⁹. The interstitial flow can transmit mechanical shear stress onto the cell membrane, as well as effect cellular processes with non-mechanical stimuli such as altering spatial distribution and local concentration of secreted soluble factors (e.g., signalling molecules). Together these mechanisms are important in directing cell migration and differentiation, promoting processes such as development and tissue organisation, tissue repair and immune response ⁶⁸. An example of the importance of interstitial flow was exhibited in an *in vitro* skin regeneration model, where lymphatic capillaries failed to self-organise with reduced fluid flow demonstrating that fluid flow is correlated with lymphatic cell proliferation and organisation ⁷⁰. Diseased states such as cancer, fibrosis and inflammation are known to have dysregulated interstitial flow values ⁷¹. *In vitro* models culturing lung fibroblasts in collagen gels showed increased ECM deposition and differentiation of cells into myofibroblasts in response to increased fluid flow to values of $4 - 10 \mu\text{m sec}^{-1}$ ⁷².

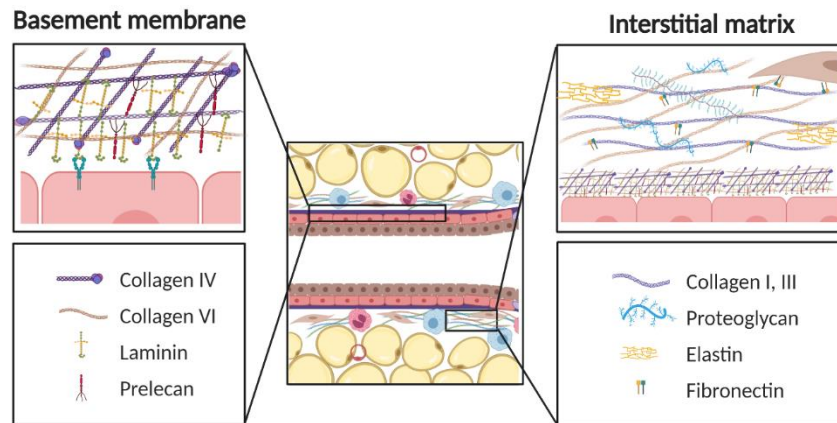


Figure 3. **General representation of biomechanical factors in breast tissue microenvironment.** Epithelial cells are aligned on the mammary duct and sit on a self-secreted basement membrane important for adhesion and signal transmission. The basement membrane forms a mesh like structure that anchors and separates the epithelial cells from the underlying stromal tissues. It is predominantly constituted of collagen IV and laminin, wherein laminin associated with differentiation and maintenance of the polarity of epithelial cells. The interstitial matrix has a high collagen content, which along with proteoglycans and fibronectin serves the purpose to physically support the ductal structure and contributing to the tissue stiffness. Modified from Gjorevski N, Nelson CM. Integrated morphodynamic signalling of the mammary gland. *Nat Rev Mol Cell Biol.* 2011;12(9):581-593. Created with BioRender.com.

1.4 Functional tissue unit

A functional tissue unit consists of the heterogeneous combination of all the above-mentioned factors at a 3D microscale: cells, biophysical and biochemical components. The characteristic architecture and composition convey the specific function to each tissue, with functional tissue units also being responsible for tissue homeostasis and dynamics. For example, mammary glands made up of milk producing lobules and drained by lactiferous ducts are constituted of cellular, biochemical and biophysical factor that regulate milk secretion at a micro scale (Fig. 4) ^{38,73}.

The enlarged snapshot of the breast ductal microenvironment (Fig.4) shows the cross section of a duct ending in a terminal end bud (TEB) at the microscale, which branches and extends in the adipose stroma throughout puberty and during lactation. The ducts are lined by a luminal epithelial layer on the inner side that will differentiate into milk producing alveoli when matured; the myoepithelial cell layer on the outer side has the function to trigger contractions for milk secretion

³⁸. The bulbous TEB is lined by cap cells that are thought of as pool of mammary stem cells, able to differentiate into myoepithelium and luminal epithelial cells ⁷⁴. The duct is covered by connective tissue cells called fibroblasts responsible for ECM homeostasis around the duct, and adipocytes, forming the mechanical insulation of the connective stroma. Small blood capillaries within the adipose stroma have the function to transport oxygen and nutrients ³⁸. These capillaries also serve as a passage for recruitment of immune cells like eosinophils, macrophages and mast cells that play an important role in the remodelling of the tissue ³⁸.

Mammary duct development is regulated by distinctive biochemical signalling at each stage (typically age and gender dependent); paracrine, autocrine and endocrine signals are all involved from mammary duct morphogenesis to lactation. Factors such as estrogen, fibroblast growth factor (FGF) and transforming growth factor- α (TGF- α) can induce proliferation, branching, and differentiation of epithelial cell layer in milk producing alveolar cells. Other signals include interactions of immune cells with epithelial cells for tissue remodelling via proteases and ECM deposition.

Mechanical signalling and ECM composition also play an important role in ductal branching and elongation. Along the duct, thick basement membrane (BM) and highly collagenous interstitial matrix (IM) is present whereas at the TEB, BM and IM are thinner to facilitate invasion ^{38,75}. One of the potential mechanisms by which ECM signals for invasion is through integrin signalling. High mechanical stress at TEB can potentially expose encrypted sites in the ECM that are recognised by integrins and induces its signalling ^{38,76}. This further leads to branching or invasion in the fibro-adipose tissue. Aging and pathological states, such as breast cancer, are processes linked to a gradual ECM stiffening that affects cellular invasion via the same pathway; such ECM stiffening is linked with disease outcome ^{77,78}.

All these factors are important in tissue organisation and function. Hence, measurement of these factors and engineering controlling over them at micro scale is essential in mimicking the *in vivo* physiology to model desired function *in vitro*. Such models can be further used to study effects of variations or of inclusion of known external stimuli, for example toxicology, pharmacology and therapeutic efficacy.

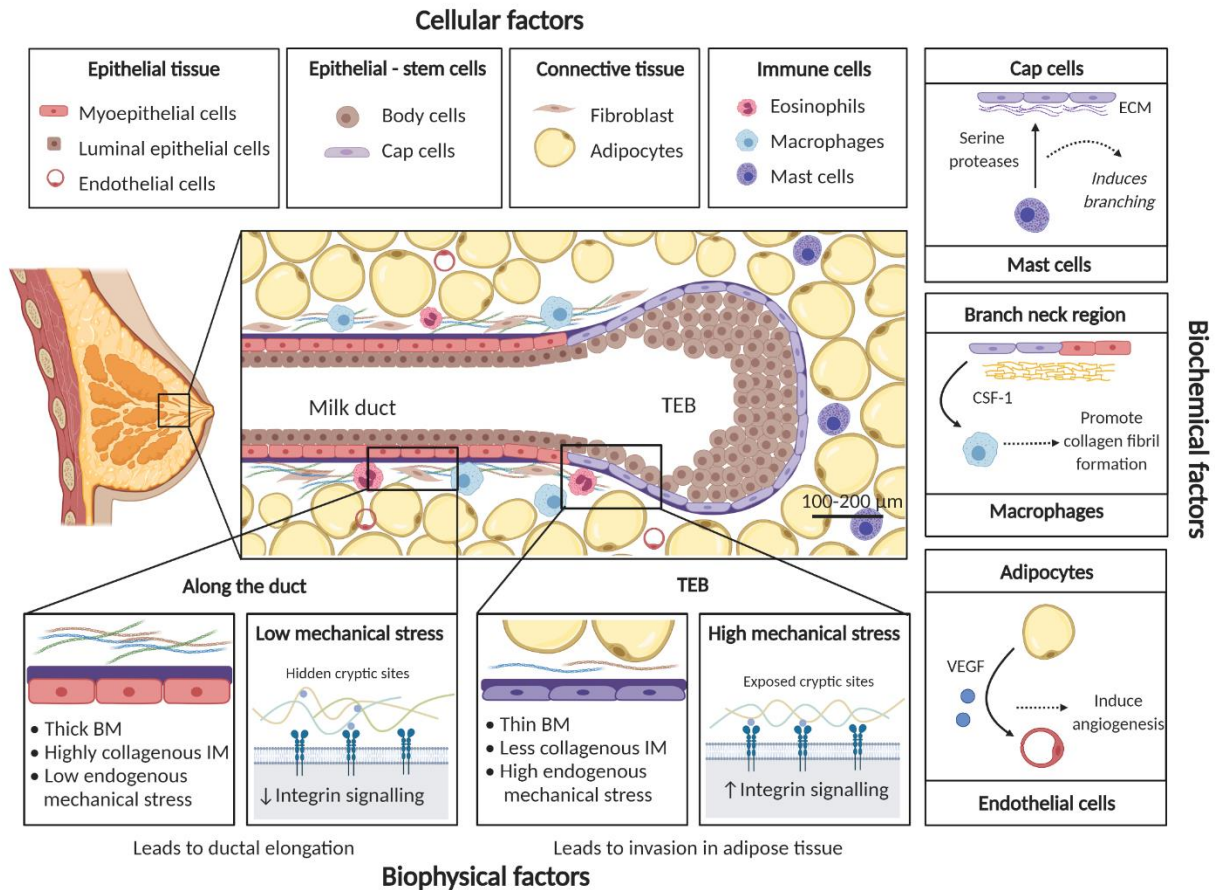


Figure 4. **Breast ductal microenvironment as a combination of cellular, biochemical and biophysical factors that define tissue functionality.** Cellular factors consist of epithelial cells responsible for milk secretion and connective tissue cells controlling ECM homeostasis around the duct. Adipocytes secrete VEGF to induce angiogenesis and promote the formation of new blood vessels. Biochemical factors promote interactions and crosstalk between different cell types. The release of serine proteases by mast cells induces bifurcation at TEB, in parallel the release of CSF-1 by epithelial cells promotes the recruitment of macrophages and consequent ECM remodelling by collagen fibril formation at the neck region of the branch. Biophysical factors, such as differences in mechanical stresses at duct compared to TEB, are responsible for its invasion and ductal elongation. *CSF-1* Colony stimulating factor; *TEB*, Terminal end bud; *VEGF*, vascular endothelial growth factor. Modified from Gjorevski N, Nelson CM. Integrated morphodynamic signalling of the mammary gland. *Nat Rev Mol Cell Biol.* 2011;12(9):581-593. Created with BioRender.com

2. Traditional *in vitro* models: 2D tissue culture

Wilhelm Roux first showed that it was possible to culture living cells outside the body in 1885 when he cultured neural plate of chick embryos in saline buffer solution for a few days⁷⁹. In 1907 Harrison Ford developed the sterile hanging drop method for growing explanted frog embryonic tissue in lymph solution for up to 5 weeks, with successful observation of nerve fibre growth^{79,80}. Burrow and Carel in 1910 took it a step further and introduced specialised media that included fresh plasma from the tissue source, with varying concentrations of salt and serum in the solution. These were probably the first examples demonstrating the idea of ‘tissue culture’: culturing cells in complex media and cell culture flasks made up of Pyrex (or borosilicate) glass^{79,81,82}. Further improvement to this idea was proposed by Rous by using a trypsin solution for chemical disintegration of tissue to obtain a single cell culture⁸³.

Initial *in vitro* studies were performed with primary cell cultures, with cells obtained directly from the donor tissues: these studies consisted of mixed types of cell populations that would grow for a limited period of time (typically few weeks). Only with the establishment of subculture technique, it was possible to obtain single cell lines and grow them further. In 1951, the first human cell line was derived from cervical cancer tissue of a patient; Henrietta Lacks, also known as HeLa cells (established by George Gey)^{84,85}. Then Hayflick reported that normal human cell lines doubled a finite number of times as opposed to cancer cells that divided indefinitely⁸⁶. On this basis, different studies were performed on normal cells with the aim to create cell line repositories that can be stored and used indefinitely for long term studies. One of the first studies involved oncogenic transformation by viral oncogenes such as large T antigen from SV40 or E6, E7 gene from human papillomavirus^{79,87}. Recent advances include genetic overexpression of human telomerase reverse transcriptase (hTERT) that increase the stability of chromosomes by elongating the telomeres rendering the cells able to divide indefinitely⁸⁷. However the immortalization procedure and the indefinite growth *in vitro* can result in cells with significant changes to their genetic and phenotypic composition when compared to their primary cell counterpart⁸⁸⁻⁹⁰. From this perspective, while established immortalized cell lines do have an advantage such as ease of access, well established culture conditions and indefinite growth, primary cells are preferred for the more accurate *in vivo* representation.

In recent years and thanks to recent medical and technological advances, an increase in access to biobanks, repository of human samples from patients after their consent, was recorded to develop more relevant *in vitro* models using directly primary cells from patients. Although research involving human tissue requires ethical approval (for example, Human Tissue Act, 2004, UK) ⁹¹, access to the biobanks is fairly easy when compared to the ethical regulations, and extensive cost and benefit analysis involved with animal models.

The increased number of *in vitro* models is also linked to the establishment and improvement of reagents, instruments and analytical methods ⁷⁹. This determines continuous improvement in culturing and maintaining cells in culture, sometimes achieved simply by the provision of basic physiochemical factors. Typical factors nowadays used in traditional *in vitro* models are summarised in Table 1.

Table 1: Factors used in regular cell culture and their characteristics⁷⁹

| <i>Factors</i> | Characteristics |
|-----------------------------|--|
| <i>Attachment substrate</i> | Adherent cells need a substrate for attachment and growth. Glass and polystyrene have been used in the past. Currently, polystyrene treated by gas plasma to make it more hydrophilic and cell attachment friendly is most commonly used ⁹² . To add additional functionality to surfaces, extracted ECM components like collagen and fibronectin are also used as a thin coating on polystyrene for certain cell lines to enhance adhesion ⁹³ . |
| <i>Media</i> | Media is a mixture of complex salts like D-PBS or HBSS with supplements including vitamins, amino acids, carbohydrates, ions and trace elements. Distinctive formulations are used to provide specific nutrients to cells, as well as to maintain osmolality and pH ^{79,94} through use of buffering components (see below). |

| | |
|---|---|
| <i>Serum</i> | For sustained cell growth, media is supplemented with serum. Serum is a complex mixture of proteins and lipids that includes growth factors, inhibitors and hormones. Due to the complexity of mixture, the cheapest and easiest way to obtain serum for cell culture is through extraction from blood of bovine or horse origin ⁹⁴ . |
| <i>pH and buffer</i> | Addition of sodium bicarbonate in the media as a buffer system is the most common choice to maintain pH values in the physiological range of 7.0 – 7.4. To balance the bicarbonate ions (Eq. 1) and obtain the desired pH, cell culture incubators are provided with 5 – 10% CO ₂ . Other efficient buffer systems like HEPES and PIPES are also used in certain media composition ⁹⁵ . |
| <i>Temperature, humidity and oxygen</i> | Cell culture incubators have built-in temperature and humidity control. The temperature is maintained at physiological temperature of 37°C for most mammalian cell lines. The relative humidity is adjusted to approximately 90 – 95% to avoid media evaporation. CO ₂ sensors are used to guarantee control over the environment and mimic <i>in vivo</i> conditions. Optional oxygen availability allows precise control of the culture environment by simulating specific physiological conditions ⁹⁶ . |
| <i>Sterility</i> | Biology safety cabinets (BSC) have filtered air flow via ventilation through high efficiency particulate air (HEPA) to culture cells in sterile environment. Mostly, laminar flow cabinets are designed to have ISO 14644 class 5 cleanliness (less 3,520 particles at or below 0.5 µm within the clean air). |

| | |
|--|--|
| | There are three types of BSC: Class I, Class II and Class III dependent on the hazard groups of the cultured cells ⁹⁷ . |
|--|--|

2.1 Regulation and qualification of materials used in cell culture

Although no specific regulations are defined for cell culture protocols and methods, quality management guidelines for the use of the above-mentioned materials in non-clinical *in vitro* applications are generally defined by manufacturers. For example, the International Organization for Standardization (ISO) 9000 and 9001 series describes quality management principles that are required for efficient quality system, although not specific to any particular industry or product ^{98,99}.

The raw materials used during clinical applications like cell therapy or vaccine production, that are not used in the final product are called ancillary materials. In the case of ancillary materials, the International Conference of Harmonization (ICH) provides specific guidelines on qualification of these products; examples are ICH Q5A/D (quality of biotechnological products), ICH Q6B (Test procedures and acceptance criteria for biotechnological/biological products) and ICH Q7 (Good manufacturing practice Guide for Active Pharmaceutical Ingredients) ^{100,101}. On this line, the World Health Organization (WHO) also details quality assurance guidelines and procedures for the use of biological products ¹⁰².

In addition to international guidelines, more commonly followed are the national regulations such as United States' Food and Drug Administration (FDA) and US Pharmacopeia (USP). FDA has quality systems associated specifically with biologics such as 21 CFR 610.15 (General biologics products standards) and 21 CFR 1271.210 (Human cells, tissues supplies and cellular and tissue-based products: supplies and reagents) ^{100,103}. On the other hand, USP has published a risk based approach for qualification of ancillary materials in USP <1043>, where a low risk material such as therapeutic drug made with Good Manufacturing Practice (GMP) will require less stringent risk reduction activity than a high risk material that was not intended for cell research or not made in compliance with GMP ¹⁰⁴. Building on <1043> information, there are further specific chapters in USP that define quality attributes of specific biological materials, such as animal derived fetal

bovine serum <90>, growth factors and cytokine <92>, and cellular/tissue-based products <1046> which are used as ancillary materials. USP also reports reference standards (USP RS) of biological materials which can be used by manufacturers to calibrate their own products and comply to consistent standards. For example, a cell-based assay was used to assign specific activity for the cytokine IL-4 to form its USP RS ¹⁰⁴. Although USP is US centric, its guidelines are generally adopted globally. Other examples of local regulations on the use of biological derived materials are the United Kingdom and the European Union, with British Standards Institution (PAS 83:2012 Guidance on codes of practice, standardised methods and regulations for cell-based therapeutics) and Eudralex Vol 4 (Good Manufacturing Practices) respectively. Another example is the Therapeutic Goods Administration (TGA) that governs the manufacture of cellular therapy products within Australia, whereas Japan follows guidelines released by the Pharmaceuticals and Medical Devices Agency (PMDA) ¹⁰⁰. For the ancillary materials, most manufactures supply a Certificate of Analysis (CoA) that illustrates information on source, purity, safety and suitability of the product, as well as declaration of compliance with the regulations listed above and for each country they apply to. However, final decision is on the end-users, who have to decide whether further qualification may be required based on the intended use in the final clinical stage of the product ¹⁰⁰.

2.2 Limitations of traditional *in vitro* models

As was illustrated in the first half of the chapter, cellular and tissue function are directly linked and dependent by their interactions with the microenvironment and its properties. Breakthrough in biology and understanding of many biological processes was achieved thanks to the first *in vitro* models leading to the traditional growth of cells on tissue culture treated polystyrene (TCP) petri dishes (i.e. 2D *in vitro* model – Fig. 5A). Although these models led to the understanding of various cellular processes, the absence of other physiological factors raised the awareness of lack of relevance of such system to model cellular response *in vivo*. A simple example of this debate is on the mechanical properties of materials: the elastic modulus of polystyrene is in the range of 10^9 Pa (GPa), whereas most of body tissues have elastic moduli between 10^2 Pa (0.1 kPa, soft tissues) and 10^5 Pa (0.1 MPa, skeletal tissue). Brain and lungs are the most soft tissues having low elastic moduli, 70 Pa and 200 Pa respectively; whereas bone tissue has the highest stiffness, starting from and greater than 2 GPa ¹⁰⁵. Differences in mechanical properties are proven to impact on cell

proliferation, adhesion, cell morphology and differentiation¹⁰⁶. As an example, adult neural stem cells favour neuronal differentiation on softer substrates (1 kPa) whereas on stiffer substrates (> 7 kPa) they favour oligodendrocyte differentiation and astrocyte were observed only on medium stiffness (1 kPa – 3.5 kPa)¹⁰⁷. This effect will not have been possible to decipher in a traditional *in vitro* setting

The lack of a volumetric distribution is another major limitation of traditional *in vitro* models. In fact, the presence of a two-dimensional (2D) substrate imposes cell adhesion only on the ventral surface of cells leading to a flat morphology: as consequence, an imbalance of traction forces could impact on the study of cell-cell and cell-matrix interactions (Fig. 5A). Different cell-cell, cell-ECM interactions are also lost when cultured on a flat monolayer surface and cells receive an even distribution of nutrients available from media unlike in normal physiological conditions. Most importantly, not only the physical characteristics but also the genomic expression of cells was demonstrated to be altered between cell populations cultured in 2D *in vitro* models compared to the *in vivo* scenario¹⁰⁸.

Similar considerations apply to oxygen exchange. The oxygen provision in 2D *in vitro* models is affected by the rate of oxygen diffusion, the free diffusion distance and also oxygen consumption rate (OCR) of the cell types¹⁰⁹. As discussed earlier, a capillary system *in vivo* guarantees free diffusion limit of oxygen transport within 30 – 200 μm only¹¹⁰. Whereas in a TCP plate, oxygen must diffuse freely through the media by a few millimetres to reach the cells attached to the plate. Additionally, due to low oxygen solubility of media, oxygen equilibrium throughout the flask might take as long as 100 minutes¹¹¹. Both these factors can lead to reduced oxygen flux for the cells at the bottom of the flask especially if oxygen consumption rate (OCR) of the cell type is high or if the cells are confluent¹⁰⁹. Steps like supplying with bare minimum of media volume in the flask and constant stirring of media can overcome some of these issues. However, 2D *in vitro* cell culture instruments and practices do not actively involve regulating these factors.

The lack of relevance and mismatch with properties typical of the *in vivo* microenvironment may affect research output. Examples are the lack of predictability of most pharmacological studies (e.g. cancer therapies that began with traditional 2D *in vitro* models using cell lines, with the ambition to predict results on animals (*in vivo*) and hence humans. However, drug efficacy and side effects are often underestimated with a high percentage of drugs failing to pass to human

testing, mostly because preclinical models lack the complexity and heterogeneity found in the actual disease. In fact, only 5% of tested compounds able to show anticancer activity *in vitro* are used for medical treatment after passing phase-III in clinical trials¹¹². This is just one example that drives the development of *in vitro* models to better replicate the *in vivo* scenario.

3. Three-dimensional (3D) cultures

As was discussed in the previous section, there is a clear need to develop *in vitro* models that can better mimic the human *in vivo* physiology and with more translatability of findings to the clinical setting. In the past decades, 3D *in vitro* models were developed to resolve specific disadvantages identified in traditional 2D *in vitro* models. With this aim, 3D *in vitro* models try to recapitulate elements of the physiological complexity by condensing and controlling several key parameters such as cell-cell and cell-microenvironment interactions.

Based on the design and methodology, 3D *in vitro* models are commonly categorised as scaffold-based or scaffold-free systems. Scaffold-based models use natural or synthetic biomaterials that provide a porous 3D architecture to support cell-matrix interaction with cell attachment and proliferation. Scaffold-free models involve substrate contact inhibitions to promote cell aggregation and growth with cell-cell interactions only. Using either of these two or a mixture of both, 3D *in vitro* models like spheroids, organoids and tissue-on-a-chip have been successfully developed, recapitulating elements of physiological and diseased states.

3.1 Spheroids

Spheroids are cluster of cells that aggregate together in a volume from a culture of either single cell type or multiple cell types^{113–115}. Many primary cells like cardiomyocytes, chondrocytes, hepatocytes as well as cancer cell lines like MCF7 (breast cancer), HeLa (cervical cancer), HepG2 (hepatocellular carcinoma) have been successfully used to form spheroid^{113,116}. After the initial cell-cell contact in a suspension of dispersed cells, expression of cell junctions like E-cadherins reinforces cell-cell interaction and leads to compaction of the spheroid¹¹³. The spheroid culture is more organotypic compared to a 2D monolayer as it mimics multicellularity as well as 3D cell-cell interactions^{113,114} (Fig. 5B). In addition, the distribution of nutrients, growth factors and oxygen distributions are not uniform throughout the spheroids^{117,118}. Spheroids that have diameter

more than 200 μm develop gradients of nutrients and oxygen thus creating heterogeneous cell populations with an outer layer of normoxic, proliferating cells and an inner mass of hypoxic and quiescent cells ^{118,119}. This characteristic makes spheroids particularly helpful when assessing drug delivery and/or efficacy in diseases like tumours: in a more *in vivo* like context tumour microenvironments are known to have a hypoxic mass in the core of the tumour mass ¹¹⁹.

Spheroids generated by scaffold free methods are formed through cellular aggregation, generally by inhibiting contact with the substrate/surrounding material. Each approach has its own pros and cons, and the selection usually depends on cell type and nature of the experiment (Table 2) ¹¹³.

3.1.1 Hanging drop method

This method was designed to culture a single cell suspension in a small drop of media hanging from the lid of a cell culture plate ¹¹⁴. The plate is filled with media to maintain a humidified atmosphere and prevent evaporation of the drop. The cells naturally aggregate with each other in the absence of a substrate and form a 3D cellular mass ^{114,120}. Initial cell concentration determines the size of the spheroids so formed. In early stages of its development, disadvantages of this method were lack of control over handling small liquid volumes which impacted consistency in outcomes of spheroid size and assay handling. Although, commercial development and dedicated design of hanging drop plates have enhanced the control over final products, allowing long term culture while also obtaining uniformly sized spheroids ^{121,122}.

3.1.2 Low adhesion TCP plate method

This method is more recent and, as the name suggests, uses material with poor cellular adhesion properties to culture cells and promote cell-cell interactions, rather than adhesion. Ultralow adhesion plates are produced using low adherent materials, examples of such materials are PDMS material ¹²³ or poly 2-hydroxyethyl methacrylate (poly-HEMA) polystyrene coated plates ¹²⁴. Improvements on spheroid formation and control over its dimensions were obtained changing the well shape; a tapered or round bottom define the position and the size of generated spheroids ¹²⁰. This method has an advantage over hanging drop as further assays can be performed directly on the same plate, avoiding disruption of formed spheroids.

3.1.3 Device assisted culture method (Bioreactors)

Several devices previously designed to control the fluid dynamics of *in vitro* cell culture have been repurposed to maintain cells in suspension and promote their aggregation into spheroids. Systems like spinner flask bioreactors have been successfully used to promote spheroid aggregation, as well as control their growth, size and cell number using different cell lines ^{115,125}. The culture of cells in such bioreactors prevent their settlement, hence adhesion, to the bottom of the flask. Another example of this type of bioreactor is the rotational bioreactor developed by the National Aeronautics and Space Administration (NASA) and named microgravity bioreactor, which uses a self-rotating container to keep cells in suspension ^{126,127}. Although both devices are known for large scale production of spheroids and high amplification efficiency, they may be also associated with cellular damage caused by fluid shear stress and cell collision during culture. To avoid such issues, a different approach was proposed with the use of magnetic levitation and proven to trigger cell aggregation by levitating cells that were incubated with a mixture of hydrogel containing magnetic nanoparticles. The magnetic field was shown to be sufficient to lift the cells from the bottom of the well and towards the media-air interface and promote cell-cell interactions required to effectively form spheroids ¹²⁸.

Table 2. Advantages and disadvantages of scaffold free methods for generating spheroids ¹¹³:

| <i>Methods for generating spheroids</i> | Advantages | Disadvantages |
|---|---|--|
| <i>Hanging drop method</i> ¹²¹ | <ul style="list-style-type: none"> • Uniform sized spheroids; • High reproducibility and controlled environment; • Compliant with high throughput screening. | <ul style="list-style-type: none"> • Cannot change media during culture; • Needs spheroid transfer to perform an assay; • Small sized spheroids cannot be used for analysis like immuno-histochemistry; |

| | | |
|---|--|---|
| | | <ul style="list-style-type: none"> • Difficult for mass amplification of spheroids. |
| <i>Low adhesion plates</i> ¹²⁹ | <ul style="list-style-type: none"> • Inexpensive; • Simple and accessible procedure. | <ul style="list-style-type: none"> • Non-uniform sized spheroids; • Labour intensive (but could be automated). |
| <i>Magnetic levitation</i> ¹²⁸ | <ul style="list-style-type: none"> • Rapid spheroid formation; • Controlled size of spheroids; • Applicable to variety of cells. | <ul style="list-style-type: none"> • Possible loss of spheroid integrity after removal of magnetic field; • Damage to cell morphology due to extra stresses/shears. |
| <i>Bioreactors</i> ^{125,127} | <ul style="list-style-type: none"> • High amplification from initial culture; • Mixing of nutrient and oxygen; • Long term culture. | <ul style="list-style-type: none"> • Non-uniform spheroid sizes; • Possible shear damage. |

Efficacy of spheroid culture

The most suitable properties and characteristics of spheroids are still debated across scientists, with no general consensus on the most appropriate method for the formation and growth of spheroids. It is however possible to determine quality or efficacy criteria for the classification of the spheroids generated by the above-mentioned methods. Various factors such as uniformity in spheroid size and shape are generally recognised by many scientists with use of high throughput image analysis

for objective evaluation ¹³⁰. Further, cell viability, metabolism assays and marker expression to assess cell proliferation and apoptosis have been useful to assess functionality of the spheroids generated ¹³¹, but these are more subject to the type of study to be performed.

It is not an easy task to identify a unique and reliable method that can be adopted across all experiments. Spheroids present themselves as a simple 3D model that can be adopted by laboratories to replace 2D monolayers and better recapitulate the *in vivo* physiology; cancer models are the very first example of successful use of spheroids ¹³². There are still several practical challenges associated with spheroid culture when making it compliant with high throughput screening (HTS) including the development and maintenance of spheroids of uniform size and their assay development. Integration with techniques like assay automation ¹²², microfluidics ¹³³, high throughput microscopy and biohybrid sensors ¹³⁴ (bioelectric array to measure spheroid surface impedance) can aid use of multicellular spheroids for HTS ¹³⁵.

3.2 Scaffold-based 3D culture

Various scaffolds (and scaffolding materials) have been designed and developed to emulate the ECM of human tissues (or some of its properties). Scaffolds are biomaterials described as polymeric networks with nano-pores (obtained by intrinsic polymeric chain interactions) or micropores (obtained by various fabrication methods like particulate leaching, additive manufacturing as described later in the chapter). These interactions are directed by physical entanglement and/or chemical crosslinks that can be permanent or reversible, e.g. covalent and electrostatic interactions respectively. Scaffolds combine physical properties such as porosity, stiffness and microarchitecture, as well as chemical cues such as adhesive motifs and signalling factors (all summarised in Fig. 5C and D) that mimic the tissue of interest ^{114,120}. These scaffold properties influence cellular behaviour and impact on cell aggregation, proliferation or migration ^{120,136}. Hence, in addition to cell-cell interaction, scaffold-based cell culture is also required to model cell-matrix interaction. There are innumerable types and shapes of scaffolds developed over the years. In the following sections we report their classification based on the chemical composition.

3.2.1 Hydrogels as soft and hydrated scaffolds

Hydrogels are one class of biomaterial widely used to model physiological systems. Several macromolecules can form hydrogels, with protein, carbohydrates, and glycosaminoglycans being the most commonly used. As discussed in Section 1.3.1, all of these are present in different proportions within the ECM. Other synthetic biomolecules that have high affinity with water can also form hydrogels. In essence, hydrogels are composed of a 3D highly hydrated network made by interactions (intermolecular and interfibrillar crosslinks) of hydrophilic polymer chains that are capable of holding water in their structure^{114,137} (Figs. 4 and 5C) Hydrogels have been extensively used in biomedical applications due to their various properties like biocompatibility, mechanics resembling soft tissue ECM and their hydrophilic nature¹³⁶.

As was mentioned earlier in the chapter, hydrogels are formed from both natural and synthetic sources, as well as from mixtures of both. Natural materials used to form hydrogels include native ECM polymeric components (Section 1.3.1) that have been sourced from microbes, animal or plant tissues. These include collagen, gelatin, laminin, fibrin, hyaluronic acid, alginate, agarose, chitosan, silk fibrils as well as ECM-derivative formulations obtained from mouse sarcoma like Matrigel^{120,137}. Many naturally derived polymers are also bioactive, hence communicate with cultured cells via cell-matrix interactions, as consequence cells present phenotypes similar to the ones found *in vivo*, like cell polarisation, regulated proliferation and differentiation. For example, cells cultured within collagen hydrogels adhere to the matrix through adhesive motifs that promote integrin mediated cell signalling and consequent cell-matrix dynamics¹³⁷. Mammary epithelial cells grown in Matrigel (a hydrated and 3D setting) are found to develop a healthy spherical acini-like structure; on contrary, this is not observed when cultured as monolayers on TCP where epithelial cells display flat morphology and increased growth rate¹³⁸. However, using animal derived material like Matrigel has limitations such as the unknown biochemical composition and batch-to-batch variations^{139,140}. The variability between Matrigel batches impacts on accurate modelling of biochemical composition and the mechanical properties of the scaffold, limiting our understanding of cause-effect relationships between different signals and cell function¹³⁷.

Synthetic hydrogels for 3D *in vitro* models are mainly obtained using modified polymers and peptides. Poly-(ethylene glycol) (PEG), polyacrylamides or poly ethers are the most used polymers, and allow researchers to finely control parameters such as stiffness, pore size or

degradation kinetics (discussed later in this section) through controlled polymerisation and crosslinking ¹⁴¹. Characterisation and testing of synthetic polymers and peptides is nowadays straightforward, with guidelines ¹⁴² as well as external services ¹⁴³ helping to draft certificates of analysis. This enables researchers to link cause-effect relationships between cell behaviour and material interactions to specific properties of the material being used. Unfunctionalized synthetic hydrogels permit cell growth by providing 3D substrate and mechanical support, however they are not bioactive, meaning they lack interactive moieties (for adhesion, degradation/proteolysis etc) which could impact on cell-matrix interaction ^{120,137}. To promote cell adhesion and interaction with the ECM mimicking material, most synthetic polymers are functionalised with adhesive moieties as well as proteolytic sites to increase their bioactivity. For example, adhesion polypeptide GRGDS, containing the RGD motif that binds to integrins, was included in N-isopropylacrylamide gels to increase cellular adhesion ¹⁴⁴.

Composite materials can also be used, combining both natural and synthetic materials and designed to provide a spectrum of mechanical and chemical support ^{141,145}. One example is the hybrid hydrogel formulated with poly-(lactic-co-glycolic acid) (PLGA)-gelatin/chondroitin/hyaluronate and used for differentiation of MSCs into chondrocytes for cartilage regeneration ¹⁴⁶. Another study by Xu et al. reports how modification of hyaluronic acid and its photo-crosslink with poly-(Nε-acryloyl l-lysine) synthetic polymer could increase the hydrogel mechanical properties and overcome lack of structural integrity in HA hydrogels. In this study, as in many others reported in literature, is suggested that the degree of HA modification could be used to control other physical properties like crosslinks, swelling and viscoelasticity, hence to match properties of the tissue of interest ¹⁴⁷.

3.2.2 3D Polymeric scaffolds

Solid polymeric 3D scaffolds are designed to provide a volumetric temporary porous structure with controlled physical properties, such as porosity and interconnectivity, to allow cell adhesion and growth. Pore size of such structures is often controlled to match the typical values of tissues, such as cancellous bone or cortical bone have a pore size in the range of 300 – 500 µm and 10 – 50 µm respectively ¹⁴⁸. Furthermore, interconnected porosity is required in such type of scaffolds

as it ensures provision of nutrients and mechanical support to promote tissue regeneration ^{115,149} (Fig. 5D).

Several classes of materials can be used for the manufacturing of such scaffolds such as polymeric materials and their blends with inclusion of bioactive particles or fillers in form of ceramics and glasses. Polylactic-co-glycolic acid (PLGA), polycaprolactone (PCL), poly-L-lactic acid (PLLA) are the most used scaffolding materials for tissue engineering and regenerative medicine ^{114,149}, used to model both normal and diseased states of target tissues ^{150,151}. Polymers, ceramics and metals selected for these applications are typically FDA approved materials, with a number of biomedical applications regulated by local authorities; this is a big advantage for a rapid approval of their use following regulatory requirements. From a regulatory perspective, fabrication methods that do not alter the properties of these raw materials are always preferable. Fabrication methods used to manufacture scaffolds with interconnected porosity are: solvent casting, particulate leaching ¹⁵², freeze drying ¹⁵³, gas foaming ¹⁵⁴, electrospinning ¹⁵⁵ and 3D printing ¹⁵⁶. Methods such as particulate leaching, solvent casting and freeze drying, rely on the controlled removal of solvents or dissolution of sacrificial materials to control porosity and pore size. Techniques like electrospinning and 3D printing (discussed in Section 3.3), have a different approach based on the design of filament deposition with known dimension to control the resultant pore size and porosity ^{115,157}.

3.3 Additive manufacturing of 3D scaffolds

Additive manufacturing processes are typically used to produce objects with precise control over geometry and size, translating the design of a model to physical 3D scaffold via computer aided software using a layer-by-layer deposition to form the volumetric shape with the required spatial resolution ^{158,159}. In recent years, additive manufacturing technologies (or 3D printing technologies) have been used to fabricate scaffolds for tissue engineering and regenerative medicine applications, allowing the control over physical properties such as pore size, porosity, scaffold shape and stiffness. In this section we discuss the 3D printing of different biomaterials for the fabrication of three types of scaffolds: (1) polymeric (hard), (2) hydrogel (soft), and (3) cell-laden hydrogel.

3.3.1 Additive manufacturing of hard scaffolds

The manufacturing process of hard scaffolds has been optimised over the past decades, allowing high fidelity and reproducibility of manufactured products¹⁵⁹. FDA approved polymers are mostly used in 3D printing either in the form of fused filament or in solution with organic solvents¹⁵⁹. Powder-based 3D printing is a successful method for the manufacturing of polymeric hard scaffolds: this method uses dispensing systems of adhesive liquid and low viscosity solutions on a powder bed to promote the fusion of the polymeric powder into filaments¹⁵⁷. Alternatively, Selective Laser Sintering (SLS) systems are used for promoting fusion of powders by a local increase of temperature and melding into filaments with the aid of a high energy laser^{157,158}. Of note, many other biocompatible and bioactive materials can be used with additive manufacturing technologies (e.g. metals, ceramics), however their use may not be always compatible with the presence of cells and biological components due to the high temperature generated in the process¹⁵⁷. In this case, cells are seeded post printing on the surface of such scaffolds.

Fused deposition modelling is yet another highly popular ink based technology that uses a temperature controlled nozzle able to change the state of the material/ink and control its viscosity during printing^{157,160}. As soon as ejected through the nozzle, the temperature of the material is lowered allowing transition to the solid state and the formation of a shaped filament. Synthetic polymers like PCL, PLA and PLGA are most commonly 3D printed by this method, with temperature and printing speed being the key parameters to control the size of the deposited filaments.

3.3.2 Additive manufacturing of soft scaffolds

Liquid and low viscosity biomaterials are used to manufacture soft scaffolds, generally using water-based *inks*. Typical examples of water-based *inks* are solutions of alginate, collagen, gelatin and silk. These materials are formulated as hydrogel precursors, which undergo almost instantaneous gelation (or crosslinking) immediately after printing and in order to retain the shape and dimensions¹⁶¹.

Direct ink-writing, as the name suggests, is an extrusion based additive manufacturing technique that ejects low viscosity suspensions through a nozzle operating at ambient temperature hence avoiding exposure to high energy sources¹⁶². In this way, water-based and biologically derived

materials are directly printed onto a surface with crosslinking reagents, these processes are designed to avoid any degradation or other undesired effects on printed materials. Indirect ink writing methods could also be used with water-based *inks*, in this case the *ink* is dispensed into a negative mold (made of supporting and sacrificial material) and cast out of the mold post polymerisation ¹⁶³.

One of the other strategies used to promote shape retention after printing is the photopolymerisation or stereolithography (SLA) printing ¹⁶⁴. In this case, the *ink* is formulated to include photo-sensitive elements; a low power light beam is controlled and moved to promote photopolymerisation and fix the 3D shape, a process that happens almost instantaneously ^{157,164}. Typically, a UV light source is used to initiate polymer chain reaction in a photo-responsive liquid polymer, where the laser beam dimension determines the final resolution of the 3D printed structure. Two-photon polymerisation is another such method recently developed that uses a near infrared laser beam to polymerase hydrogel precursors like gelatin modified with methacrylamide moieties ¹⁵⁷.

3.3.3 3D Bioprinting

In recent years, development of different *bioinks* (printable water-based and viscous formulations with encapsulated single cell suspension culture, microtissues and/or spheroids) has paved the way for 3D bioprinting. 3D bioprinters allow direct printing of *bioinks* in physiological and sterile conditions; tuning the viscosity, nozzle diameter and flow rates required to avoid high shear stresses and preserve cells viability after printing ¹⁶⁵. In this approach, all the technologies discussed in paragraph 3.3.2 can be used to process *bioinks* and the manufacturing method used to fabricate such scaffolds is called bioprinting.

Bioprinting not only gives the possibility to control the spatial location of cells and their density, but also allows the control size, shape and volumetric position of biomaterials with the possibility to obtain tissue-like structure after a certain culturing time ¹⁵⁸. 3D bioprinted scaffolds have a great advantage over scaffold-based models: not only they offer control over high cell seeding densities (in most of the cases above 0.5 million cells/mL), but also allow precise layering of cells and biomaterials to recapitulate the structure of the tissue of interest. Nonetheless, bioprinting is automated and allows high-throughput fabrication of scaffolds ¹⁶⁶.

Continuous improvements have been implemented in bioprinting technologies to better control the manufacturing process and add functionalities to printed cell-containing scaffolds, yet there are still many technical challenges involved to form a functional tissue. One of the main issues to be solved to be able to 3D bioprinting organs is to promote an effective vascularisation of the printed objects. For all details on various types, advantages and disadvantages of printing methods, the reader is directed to review papers solely focused on this topic ^{156,158,159}.

3.4 Properties of scaffold for *in vitro* models.

As discussed in previous paragraphs, there are many ways to modify biomaterials and refine the control over physico-chemical and mechanical properties of 3D scaffolds. Properties such as substrate stiffness, pore size, (bio)degradability, permeability and nutrient transport are among the most important to be defined and then designed into the model according to experimental need. Additionally, biocompatibility, ease of sampling and suitable analysis are other crucial factors to design into the scaffold and obtain functional 3D *in vitro* model.

In the following paragraphs the principal properties of scaffolds to mimic native tissue properties will be discussed.

3.4.1 Mechanical properties.

The response of material to external forces is typically described by the elastic modulus. Depending on the direction of the force, the elastic modulus of a material can be reported as Young's modulus (E, unit Pa) or shear modulus (G', unit Pa). In the case of the Young's modulus, the force is applied perpendicularly to a surface of the tested material; whereas in the case of the shear modulus, the applied force acts parallel to the surface. According to their behaviour, materials are typically classified as elastic, plastic and viscoelastic. However, when it comes to the discussion of the response to external forces of more complex and heterogenous materials/structures (like tissues), another concept needs to be introduced: 'stiffness'. In fact, when referring to a heterogeneous and 3D structure composed of several biomaterials and cells, the mechanical response to external forces is generally defined as stiffness. The mechanical response, hence the stiffness, varies across tissue types *in vivo* and it is known to impact on several tissue functions, such as mechano-transduction ^{105,106}.

The mechanical properties of materials, and the resultant stiffness of scaffolds, provides mechanical stimuli and impact on many biological processes. It therefore essential to set stiffness as one of the design criteria to be considered in the designing of relevant *in vitro* models. One example of the importance of stiffness is reported for mESCs: they were able to preserve their self-renewal phenotype (high Oct4 and Nanog expression) for longer when they were cultured on mechanically soft substrates (0.6 kPa) rather than conventional rigid plastic surfaces ¹⁶⁷. This was one of the first studies to support the importance of stiffness in cell/tissue development. Other studies reported on the importance of cell culture substrate stiffness were on testing drug efficacy *in vitro*. Nguyen et al. reported that sorafenib has shown reduced efficacy against breast cancer cell lines cultured when these were cultured on stiffer and collagen-rich substrates, proposing to consider more representative models of breast tumour tissue stiffness when testing drug efficacy ¹⁶⁸.

3.4.2 Pore size and porosity

Pore size of tissues *in vivo* ranges from anywhere between nanopores to large micropores, for example breast tissue is nanoporous (100-1000 nm) ¹⁶⁹ whereas bone is a microporous tissue (100-400 μm) ¹⁴⁸. Pore size is known to affect cellular characteristics in several ways, such as by determining the biochemical presentation of adhesive ligands. Hence *in vitro*, pore size and scaffold porosity are known to play an important role in promoting cell adhesion and proliferation ¹⁷⁰. Hydrogels have a mesh with intrinsic nanometre sized pores that engages the whole cell surface with substrates' adhesive moieties/ligands, which can faithfully represent tissues like breast, brain or liver etc ^{136,145}. Additionally, larger pores with size of more than 100 μm can be designed into polymeric and fibre scaffolds and controlled via manufacturing (Section 3.2.2, Section 3.3) for tissues like bone and bone marrow. Such micropores can act as curved 2D surfaces leading to partial cell-substrate and cell-cell interactions (Fig. 5C and D).

Within such microporous scaffolds, there is an optimum average pore size and density specific to the cell type being studied. As demonstrated by Zeltinger et al., both pore size and pore density impact on adhesion and cellular interactions of vascular smooth muscle cells and endothelial cells ¹⁷¹. Both tested cells were found to prefer higher pore density, but vascular muscle cells form a uniform layer when cultured within scaffolds of pore sizes > 100 μm whereas endothelial cells

preferred to grow on surfaces with pore sizes $< 38 \mu\text{m}$ ¹⁷¹. Similarly, osteoblasts prefer a pore size ranging from 100-700 μm for optimal growth as this range is closer to *in vivo* bone tissue¹⁷². Many other studies reported in literature, show how porosity and pore size can better represent the actual *in vivo* situation and promote cellular responses to form functional tissues.

Porosity or the density of pores within scaffolds also affects pores interconnectivity within the scaffolds. This property has been demonstrated critical and affect cell spreading, migration and functionality. Examples are methacrylic terpolymer fibrous scaffolds, in which low void space/porosity enhanced cell spreading and enzymatic activity in HUVECs (human umbilical vein endothelial cells)¹⁷³. Whereas high porosity of PLLA fibrous scaffolds are reported to enhanced migration capacity of lymphatic endothelial cells on PLLA fibres¹⁷⁴.

3.4.3 Provision of nutrients

Nutrients that include small molecules like glucose, as well as amino acids and macromolecules like growth factors, are fundamental to preserve cell viability and phenotype. As such, it is recommended to consider all the factors that could impact on diffusion of nutrients and other soluble factors across the 3D scaffold to ensure adequate macromolecular transport for required biological processes. Nutrients are typically soluble in water and can diffuse through hydrogels with intrinsic nanometre pores. The diffusion rate of each molecule depends on its chemical characteristics, as well as the hydrodynamic diameter. Hydrogel pore size (proportional to crosslinks type and density) is another factor to consider for the diffusion of such molecules, with smaller pore size reported to limit nutrient flux¹⁷⁵; as an example, the diffusion rate of high molecular weight molecules like albumin is hampered by increased crosslinking density in calcium crosslinked alginate microspheres¹⁷⁶ and glutaraldehyde crosslinked chitosan gels¹⁷⁷. Diffusion of nutrients, as well as other by-products, is also influenced by the number, the metabolic activity and distribution of cells across the 3D scaffold.

Scaffold pore size and porosity influence the volumetric diffusion and perfusion of soluble factors and nutrients. In the case of hard microporous scaffolds, these molecules follow diffusion rates as previously discussed. Thanks to pores interconnectivity, the cell culture could flow through the pores and guarantee homogeneous distribution of soluble factors. In the case of advanced 3D

models, such perfusion can also be facilitated by the use of a peristaltic pump that can promote unidirectional flow of media within the scaffolds at known shear rates ¹⁷⁸.

3.4.4 Stability and degradation.

Physiological conditions are known to promote hydrolysis and degradation of many materials, mainly due to the relatively high temperature and high content of oxygen in a water-based environment compared to standard storage condition (specified by national/international stability requirements). Degradation studies, and corresponding kinetic profiles, are required to verify material/scaffold stability for *in vitro* and *in vivo* conditions, hence determine their suitability for approval to their preclinical application ^{136,175}. In the specific case of *in vitro* models, a criterion for scaffold acceptance relies on its ability to provide mechanical strength for the duration of the study, as well as allow gradual remodelling of the microenvironment by cellular ECM deposition. As previously discussed, variation of surface and mechanical properties of scaffolds affect cell stretching, proliferation and cellular fate. In a study with enzymatically degradable alginate hydrogels, it was observed that neuronal progenitors were able to expand and proliferate better than in their non-degradable counterpart ¹⁷⁹. Whereas, in case of enzymatically degradable HA hydrogels (steady degradation from day 2 to day 14), cultured hMSCs showed enhanced cell traction and favoured osteogenesis when compared to slowly degrading (stable for 14 days) HA hydrogels, hMSCs favoured adipogenesis ¹⁸⁰. To conclude, it is necessary to verify and certify that specific/required degradation profiles are designed into the scaffold and serve the purpose of the experiment/application.

There are several methods to be implemented to achieve a known degradation kinetics of scaffolds. The main degradation mechanisms for polymeric scaffolds maintained in physiological conditions are: hydrolysis, enzymatic cleavage and dissolution ¹⁷⁵. Some synthetic hydrogels are designed with domains susceptible to hydrolysis, like ester linkages. Whereas natural polymers scaffolds (e.g. collagen) have enzymatic sites that can be degraded following biological processes by proteases secreted directly by cells. A strategy often used to control degradation kinetics is by tuning the amount of the groups that are hydrolytically/enzymatically cleaved ^{181,182}. For instance synthetic polymers are functionalized with oligopeptides that have enzymatic cleavage sites and by controlling the amount of oligopeptides as well as enzyme concentration, the degradation

kinetics are controlled ¹⁸². Recently, photodegradable hydrogels have been engineered to degrade based on UV light exposure and paved the way for different strategies over synthetic polymer degradation ¹⁸³.

3.4.5 Biocompatibility.

Material interaction with biological components is pivotal when designing a scaffold for biomedical applications. Biocompatibility describes the ability of being compatible with cells and allowing for normal cell functions. There are several assays to assess material and scaffolds biocompatibility, such as cellular viability, proliferation or adhesion. Lack of cell viability can be linked to scaffold toxicity, whereas reduced cell proliferation and adhesion can assess whether the scaffold is able to promote or assist the normal functioning of the cells ¹⁷⁵. As discussed in the previous sections, many synthetic polymers (e.g. PLGA, PLLA, PEG) are FDA approved for *in vivo* purposes and hence are a popular choice for scaffolds used in *in vitro* models ¹⁸⁴. Most of the natural (or naturally derived) polymers are non-toxic, however not all are able to promote cells growth. Collagen and Matrigel are the most used natural biomaterials supporting cell growth as they naturally include adhesion domains. For all the other biomaterials, being natural or synthetic, inclusion of adhesive motifs ¹⁸⁵, growth factors ¹⁸⁶ or proteolytic sites ¹⁸² is necessary to promote cell adhesion and proliferation.

3.4.6 Biosampling and bioanalysis

Isolation of cells or cellular materials from within scaffolds is required for further propagation or molecular and cellular analysis ¹³⁶. Sample isolation is technically challenging from many scaffolds, and in some cases, this could cause degradation of biological products e.g. DNA, protein. This factor should be taken into account during model design, material selection and experimental planning. Depending on the type of scaffolds and cellular material to be retrieved, isolation techniques can vary. Enzymatic degradation of the scaffolds and cells can be used to retrieve DNA or RNA from the cells. Whereas gentle approaches have to be used if live cells are to be retrieved from the scaffolds. For instance, calcium sequestering solution can dissolve calcium crosslinked alginate gels and is gentle enough to retrieve live cells ¹⁸⁷.

Investigation of model evolution and quantification of dynamic variation in a system is a desirable requirement to be included in engineered *in vitro* models. Typical investigation of a biological system requires the use of microscopes to assess cellular functions and monitoring properties such as cellular morphology and organisation, as well as intracellular protein localisation. Many hydrogels are optically transparent, allowing not only optical but also fluorescence investigation through microscopy¹³⁶. The use of high-resolution microscopy could be challenging for the investigation of some 3D models which mainly depends on the thickness and optical density of the sample/model. In fact, many solid scaffolds are made with opaque materials, e.g. synthetic polymers, allowing investigation only of exposed surfaces and specific/accessible area such as through macro-pores. Recently, and with the trend to miniaturize biological models, microfluidic devices and tissue-on-a-chip (Section 3.4) allow culture of thin 3D models in optically transparent slides, with possibility to be investigated using high resolution microscopy¹⁸⁸. Other emerging technologies report on the inclusion of self-reporting scaffolds (e.g. coupled with pH sensing nanoparticles) to report on local pH variation and real time detection of metabolic activity^{189,190}. Invasive microscopic techniques like histology can be applied to 3D models and cell-laden hydrogel scaffolds with methodology adapted for the investigation of tissues, however some technical challenges have not been solved like maintaining hydrogel architecture and having proper sections¹³⁶.



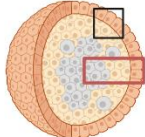
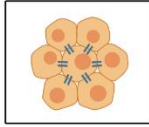

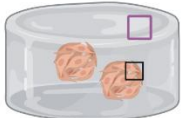
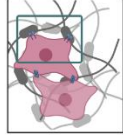

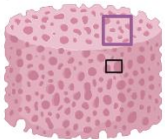
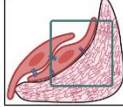

| | Cell surface engagement | Exposure to soluble factors | Mechanical factors (stiffness) | Microarchitecture Porosity | Degradation/ Remodelling | |
|----------------------------------|--|--|---|--|---|---|
| A 2D TCP models |  |  | Uniform distribution - free diffusion through media | (GPa) Cannot be altered | Not available | Not available |
| B Scaffold-free Spheroid |  |  | Non-uniform distribution  $D_H < D_S$ | Cannot be altered | Not available | Cells can deposit matrix |
| C Hydrogel scaffold |  |  | Non-uniform distribution $D_H < D_S$ | (Pa- kPa) Can be designed and modified | nanoporosity  | Designable matrix degradation and active remodelling by cells |
| D Microporous scaffold |  |  | D_p (Interlinked porosity) | (kPa- MPa) Can be designed and modified | Interlinked microporosity  | Designable matrix degradation and active remodelling |

Figure 5 Properties of *in vitro* models for tissue engineering applications. **A)** 2D models and TCP plate: The ventral cell surface has membrane receptors engaged with the flat 2D substrate in TCP plates imposing flat morphology. Minimal possibility to modulate properties of the adhesion substrate. **B)** Scaffold free spheroid: Cells growth as scaffold free spheroids have 3D surface interactions with other cell's receptors. No possibility to modulate the model, cells can deposit their own ECM. **C)** Hydrogels scaffold: Cells in hydrogel have 3D receptor ligand interactions with the material (mimic ECM properties), as well as other cells. Mechanical and architectural properties of the biomaterials can be controlled, cells can deposit their own ECM. **D)** Polymeric microporous scaffolds: Cells in microporous scaffolds have interactions with curved 2D substrate of adhesive biomaterials and cells also have 3D multicellular connections. Mechanical and architectural properties of the biomaterials can be controlled, cells can deposit their own ECM. Created with BioRender.com

3.5 Organoids

Organoids are 3D cell aggregates reported to mimic the *in vivo* physiology more closely than spheroids. Organoids are derived from a combination of organ specific stem cells, tissue progenitors and primary tissue cells. Strategies for growing organoids are mostly tissue specific, with a general approach that a soft physical support for cell growth is provided, together with biochemical factors for differentiation^{114,115,191}. As the development of organoids is a relatively new and promising research area to study human biological processes, technical challenges are mostly linked to their formation and maintenance for long-term in culture. The main strategy used to form organoids is to provide minimal differentiation or growth information to cells, and then rely on their self-organisation capacity to create organ-like structures¹⁹². Organ developmental and tissue homeostatic studies from a combination of *in vivo* and *in vitro* models have helped in recognising these biochemical and biophysical factors that drive the self-organisation. This, together with the advent and recognition of stem cells, made possible to isolate and engineer their niche to drive tissue development *in vitro*^{191,193}. Since the driving force of organoid development is their self-organisation and self-renewal capacity which can better recreate the human tissue complexity, the main intrinsic disadvantage resides in the longer culture time required for their complete formation, for instance stomach organoids require 34 days to form a tissue like organisation (Fig. 6)¹⁹¹. On the other hand, spheroids lack tissue like organisation but are formed in few hours as they rely only on cell-cell adhesion^{191,193}. Identification of requirements for the development of organoids is essential to establish standardised ways hence reduce variability, optimise research outputs and make organoids suitable for HTS.

Recently combinations of scaffold and scaffold-free techniques have been explored to develop organoids^{114,115}. The first reported method consists of growing stem cells / progenitor cells on ECM coated surfaces or on the top of a layer of feeder cells that provide biochemical factors for self-renewal or differentiation. The second approach foresees the provision of mechanical support to grow organoids either in the form of Matrigel / scaffold embedding or by introduction of interfaces, for example air-liquid interfaces for growth of keratinocytes. The third methodology reported to form organoids is similar to the techniques used to form spheroids, such as hanging drop method or use of low adhesion plates to encourage the formation of embryoid-like aggregates.

3.5.1 Tissue organoids

Tissue organoids usually consist of epithelial structures only and without the stromal component^{114,115}. As the epithelial organisation most often represents a tissue-like structure, these organoids are called tissue organoids. For example, stomach organoids created by Lgr5+ adult stem cells of pyloric stomach tissue, display characteristics of adult stomach epithelium¹⁹¹. As briefly mentioned in the previous paragraph, Matrigel embedding with a cocktail of biochemical factors that consists of Wnt3a, R-spondin, noggin (NOG), FGF and EGF ligand with TGF β inhibitors has been used to develop these stomach organoids¹⁹⁴. These cultures mimic the epithelial gland base with a centrally enclosed lumen but lack a supportive stromal component and hence the epithelial-stromal interactions^{191,194}. This type of tissue organoid is represented in Fig. 6.

3.5.2 Multicellular organoids

Pluripotent stem cell organoid/ multicellular organoids are generated from ESCs or iPSCs and mostly consist of both epithelial and mesenchymal/stromal components. Taking the same example of stomach organoids, contrary to the one step ASC protocol, a step wise differentiation protocol of PSCs is performed here. Briefly, PSCs are first differentiated into definitive endoderm by activin that is followed by Wnt, FGF and noggin treatment to prevent the intestinal fate¹⁹⁵. This organoid is then embedded in Matrigel with retinoic acid and EGF rich media to create and maintain a stomach organoid that consists of all cell types present in the antrum, a posterior stomach region (Fig. 6)¹⁹⁵.

To date, several organoid models have been successfully derived from ESCs, iPSCs and ASCs/progenitors to form organoid structures from pancreas, liver, intestine, thymus, kidney, retina and heart. Apart from cell viability, the efficacy of the organoid formation has also been assessed by their organotypic features including tissue-like morphology and function. For instance, intestinal¹⁹⁶ and stomach organoids¹⁹⁵ from PSCs were able to form tissue mimicking epithelial and stromal tissue components whereas thyroid organoids derived from mESCs showed tissue functionality of iodide organification and the potential to release thyroid hormones *in vivo*¹⁹⁷.

This type of organoids, in addition to including multiple cell types, also have the capacity to develop tissue-like polarity, architecture of epithelial and stromal components as well as tissue

functionality. Yet, these organoids present some inadequacies to the *in vivo* complexity such as the lack of vasculature, making them not able to recreate a complete organ development ¹¹⁵. Nonetheless, engineering approaches are likely to be part of continuing attempts to grow organoids that are both increasingly complex and yet better controlled.

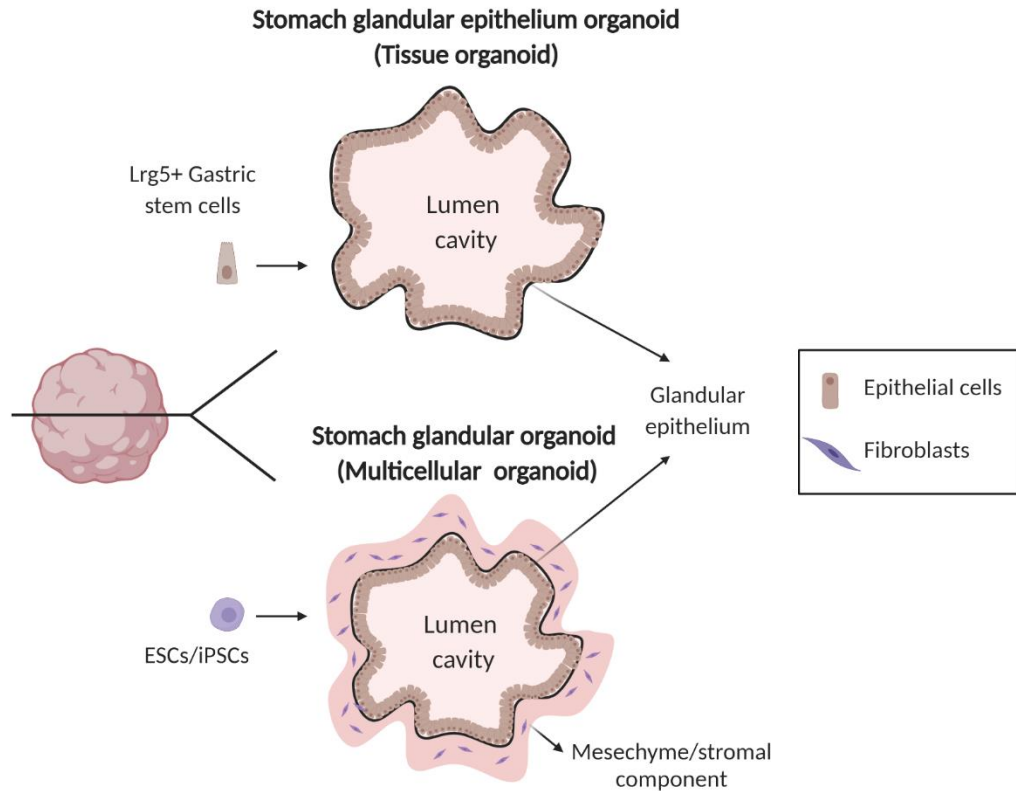


Figure 6. **Examples of stomach organoid structure.** Structure of tissue organoid by adult gastric stem cells ¹⁹¹ and multicellular organoid by ESCs/iPSCs ¹⁹⁵. *ESCs*, Embryonic stem cells; *iPSCs*, induced pluripotent stem cells; *LGR5*, Leucine-rich repeat-containing G-protein coupled receptor. Created with BioRender.com

3.6 Organ-on-a-chip

Over the past two decades, a novel approach to model tissue physiology called ‘organ-on-a-chip’ (OOC) has been developed. This engineering approach is inspired from ‘lab-on-a-chip’ techniques that use micro-channels etched on a chip (with typical dimension in the range of 10 – 100 μm) to precisely control and manipulate microvolumes of fluids. The structure, size and

compartmentalisation of these channels forms the basis of integrating or separating samples as well as carrying out operations like reactions or detection^{198,199}. Similarly, ‘organ-on-a-chip’ or OOC consists of channels (ranging from few μm to mm) compartmentalised or separated by semipermeable membrane that ambitiously aim to recreate the complexity of human organs physiology and functionality. More realistically, such micro-devices can be used to recreate the complexity of human tissues and are generally used to co-culture cells and perfused them with known flow values of media and nutrients composition. As said, such microfluidic channels interconnect different cell types on a micro/milli-scale level thus reducing not just the number of cells used but also the volumes of cell culture medium, biochemical factors and drugs^{199,200}. In order to recreate the complexity of tissues, OOC are designed including one or several key components^{199,200}, as described and reviewed in the following paragraphs.

3.6.1 Fluid dynamics

The inclusion of fluid flow allows to control shear stresses acting on cell membranes cultured *in vitro*, as well as maintain cells in a dynamic culture to exchange secreted factors and recreate cross-talks typical of physiological states of tissues. As mentioned in section 1.3.5, interstitial fluid flow not only produces shear stresses on cells but also impacts on cellular phenotypes. In OOC device, the microfluidic channels are connected to controlled pumps in a closed loop to simulate the fluid flow present in different body compartments, also allowing for the continuous provision of nutrients and removal of waste metabolic products. Through programmable software speed, direction and type (e.g. unidirectional vs pulsatile) the fluid speed, pressure and resultant shear stresses can be finely tuned and varied on demand. In fact, by altering the flow velocity or channel structure, these devices can also account for gradients of biochemical factors as seen *in vivo*¹⁹⁹.

3.6.2 Organised patterning of cell types

Tissue compartmentalisation and channel geometry can spatially define cell location in multicellular co-culture in OOC. While organoids rely on self-organisation of cell types, OOC engineers their guided spatial confinement to generate reproducibility in terms of cellular structures created²⁰¹. As shown in Fig. 1, *in vivo* cell types are arranged in precise geometries and have imposed adhesion surfaces, e.g., apical side of luminal epithelial cells face the lumen, whereas the basal side rests on myoepithelial cells. To reproduce this tissue-like barrier among cell

types, OOC incorporate microfluidic membranes made up of biomaterials with known additional features such as semi-permeability, porosity and mechanical properties to mimic the physiological function^{202,203}. 3D printing techniques can also add in to this feature of OOC by creating cell laden scaffolds precisely within the microfluidic chamber^{204,205}.

3.6.3 Control over mechanical stimuli

Various organs undergo dynamic pressure changes for their functions. For example, the lung alveoli surface is mechanically stretched while breathing or skeletal muscle cells undergo contraction while in movement. Such mechanical stimuli are recognised to be important in maintaining tissue function. As mentioned in the last section, with the use of elastic membranes and external force, periodic mechanical stresses can be simulated within the microfluidic chambers. Other external stimulus includes electrical stimulation or environmental control of nutrients, pH, O₂ and CO₂²⁰⁰.

3.6.4 Sensors to detect physiological parameters

The inclusion of sensing elements does not necessarily add information to the biomimetic features of *in vitro* models; however, they allow direct measures (e.g., pH, oxygen concentration) to study tissue functions and/or drug efficacy. This component can include features like harnessing chip material, geometry and thickness for better optical readouts²⁰⁶ or it can also integrate sensing units within the model, like the use of multi-electrode arrays in chips to read transepithelial electrical resistance to understand vascular permeability in endothelial cells²⁰⁷.

3.6.5 Example of Lung-on-a-chip

A lung-on-a-chip was developed by Huh et al. to mimic lung tissue physiology and assess lung function²⁰⁸. Alveoli, the functional unit of lungs, have simple squamous epithelium lining the air-tissue interface that exchanges gases. The stroma/parenchyma beneath this epithelial layer have endothelium lined blood capillaries that provide nutrition to the epithelium, as well as receive oxygen that is to be circulated throughout the body. Hence, this interface of epithelial alveolar cells and endothelium cells forms the basis of lung tissue function. Worth noting that during breathing the alveoli expands periodically when the air is inspired, this leads to the stretching of epithelial cells as well as endothelial cells beneath them. To model this biological process, Huh et

al. developed a microsystem that reconstituted the functional alveolar-capillary interface of the lung²⁰⁸ (Fig. 7). For this, a microfluidic chip consisting of two apposed channels separated by a porous polydimethylsiloxane (PDMS) elastic membrane was assembled. Human alveolar epithelial cells and human pulmonary endothelial cells were cultured on the opposite sides of the membrane. Air was introduced into the alveolar channel with the epithelial cells to create an air-tissue interface, whereas the endothelial layer was perfused with media to mimic a blood capillary transporting nutrients. The elastic PDMS membrane was periodically stretched along with the cells in response to an external mechanical stimulus of vacuum. This periodic mechanical stretching at 0.2 Hz mimicked breathing pattern. With the air-tissue-liquid interface under periodic mechanical stimulus, a better cell alignment was observed, and tissue barrier integrity as measured by protein permeability was of similar values retrieved by *in vivo* measurements.

Tissue pathophysiology can also be mimicked by OOC models. In the same model described by Huh et al., pulmonary inflammation was mimicked by inclusion of blood-borne immune cells in the vascular channel fluid flow. Living *Escherichia coli* bacteria introduced into the alveolar epithelium channel, activated the underlying endothelial cells by increasing expression of ICAM. The circulating neutrophils were observed to adhere to the activated endothelial cells only, which further led to transmigration of neutrophils via the porous membrane into the alveolar channel. Once on the apical surface of alveolar epithelial cells, the neutrophils were able to engulf the bacteria mimicking the *in vivo* immune response.

Over the past year there was an increased development of single OOC models, reported to successfully mimic tissues like heart, liver, kidney, gut, blood-brain barrier, skin, as well as diseased conditions like cancer (with most of the models reviewed by Ronaldson-Bouchard and Vunjak-Novakovic²⁰⁹). As OOC models aim to recapitulate minimal *in vivo* functionality, a way to assess the efficacy of such models is to check on tissue functionality: a heart-on-a-chip model derived from iPSCs was assessed on heart muscle function of contractility, beat rate and excitation threshold for the cells²¹⁰.

To summaries, OOC uses organised spatial confinement, fluid flow and external stimuli to mimic basic tissue physiology. These models can further be developed to model pathology, with direct use and impact on drug screening and efficacy studies. Although they still lack the whole complexity of tissue, for example absence of stromal cells, there are new avenues to combine other

techniques like 3D printing to engineer the *in vivo* biological complexity as well as maintaining reproducibility across *in vitro* models.

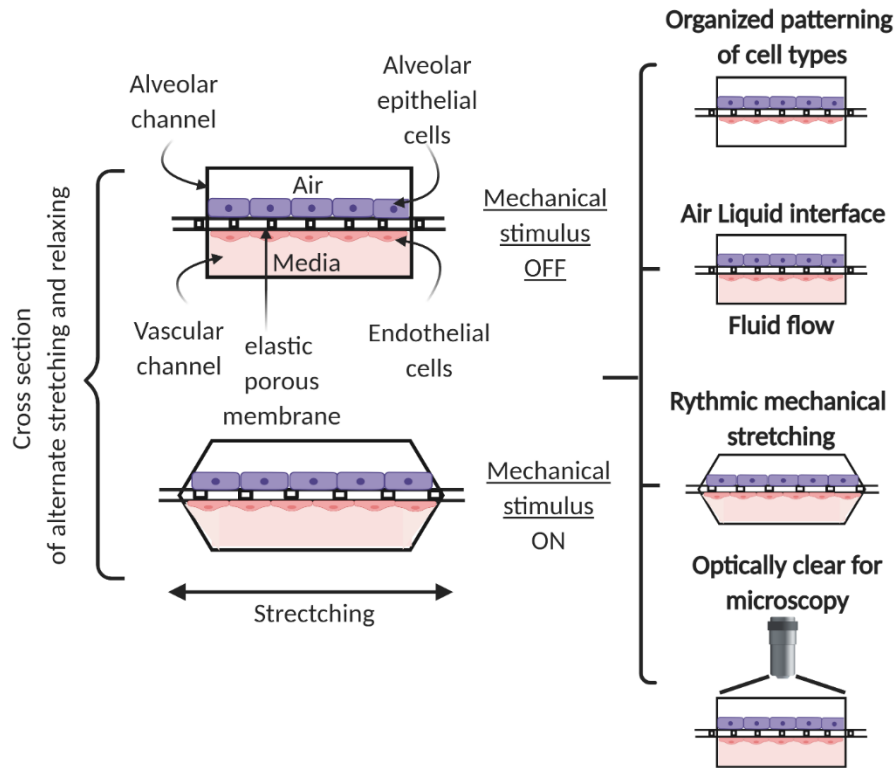


Figure 7. **Schematic representation of Lung-on-a-chip.** The proposed OOC model has organised layout of alveolar epithelial and endothelial cells with an air-liquid interface. The model includes additional rhythmic stretching (i.e. mechanical stimulus) to mimic the physiological breathing movements. The OOC chip is designed to be optically clear for ease real-time imaging of dynamic functions. Modified from Huh D, Matthews BD, Mammoto A, Montoya-Zavala M, Yuan Hsin H, Ingber DE. Reconstituting organ-level lung functions on a chip. *Science*. 2010;328(5986):1662-1668. Created with BioRender.com

3.7 State-of-the-art 3D breast cancer models

Multiple tissue engineering techniques have been applied to engineer various aspects of breast cancer progression. The simplest models include unicellular or multicellular spheroids that rely on 3D aggregation of cells via scaffold free techniques. MDA-MB 231 cells, a triple negative breast cancer (TNBC) cell line, was used to form spheroids of size 300-500 μm by hanging drop method²¹¹. Such spheroids were able to demonstrate increased necrosis and hypoxia induced gene

expression in cells at day 6 mimicking *in vivo* tumour physiology of increased hypoxia. Hanging drop method when combined with 3D printing technique and customised plate design was able to produce a precise and high throughput 384 well plate assay that can be assessed for drug efficacy studies and 3D migration in the same plate ²¹². Such models provide a valid alternative to 2D models for preclinical studies, as there is less variability within samples, and they can be performed on a large scale. However, not all cell types, especially patient derived cells, can successfully produce spheroids using this method. For example, in a hanging drop based study, only 27 out of 31 breast cancer patient derived cells formed spheroids successfully ²¹³. Other techniques like magnetic levitation used to form multicellular spheroids of breast cancer cells and fibroblasts have added advantages. Due to magnet assisted spheroid compaction, most cell types form spheroids with this method and also in shorter time period of around 24 hours, as compared to an interval of 6 - 20 days with other methods ²¹⁴. Such techniques if combined with high throughput platforms can be ideal for personalised therapeutics because of scalability and shorter assay period.

While scaffold free based spheroids are simplistic with high reproducibility, they still lack important cues such as ECM that are well known to play a part in cancer progression ²¹⁵. To overcome this, scaffold-based techniques involve encapsulation of cancer cells in natural or synthetic substitutes of ECM. Hydrogel-based scaffolds are typically preferred owing to the possibility of tailoring their mechanical properties to closely mimic the tumour ECM. For instance, MCF-7 cells (luminal breast cancer subtype) cultured in collagen-alginate hydrogels of varying stiffness exhibited differential response to doxorubicin depending on the matrix stiffness, hence concluding that ECM properties can affect therapeutic efficacy ²¹⁶. Inclusion of synthetic hydrogels can bring more reproducibility and possibility for performing high throughput assays as synthetic hydrogel composition and mechanics are better controlled ²¹⁵. Nguyen et al., developed polyethylene glycol- phosphorylcholine (PEG-PC) hydrogel based high throughput assay for studying stiffness mediated phenotypes. MDA-MB 231 cultured on top of stiff (20-30kPa) hydrogels showed lower response to Sorafenib, a Raf kinase inhibitor. Instead, JNK and β 1 integrin mediate resistance to sorafenib in high stiffness hydrogel, hence combination of Sorafenib and JNK inhibitor works better in high stiffness hydrogels ¹⁶⁸. Inclusion of such cues can inform on better therapeutic options in the preclinical phase. Different peptides resembling ECM components, and protease sites for controlled degradation in hydrogels can also be included to better mimic ECM composition and dynamics. For instance, PEG based hydrogels were

functionalised with collagen (GFOGER), fibronectin (RGDS), and laminin (IKVAV) peptides ²¹⁷. Consistent with *in vivo* observations of collagen-rich ECMs of increased stiffness correlating with cancer progression, collagen peptides along with high stiffness exhibited increased growth rate of MDA-MB 231 spheroids. Whereas fibronectin/RGDS was shown to be involved in increased cell spreading and irregular spheroid shape indicating separate roles for ECM components in cancer phenotypes ²¹⁷. Additional advantage of scaffold-based model is that cell types can be segregated within the model unlike multicellular spheroids which have no designed cell pattern. For instance, multicellular spheroid of TNBC cells and human mammary fibroblasts showcased that active CXCL-12 (secreted by fibroblast) and CXCR-4 (receptors on cancer cell) signalling is involved in increased metabolic activity of cancer cells ²¹⁸. However, in a scaffold-based model, segregation of these cells can be achieved where breast cancer spheroids were embedded in collagen gel containing dispersed fibroblasts ²¹⁹. This mimics native tumours where stromal cells such as fibroblasts are dispersed within the matrix bordering the mass of cancer cells. With such model it was possible to mimic invasion of cancer cells into fibroblast containing ECM. Additionally, CXCL-12 and CXCR-4 axis was also found to be involved in this invasion and therapeutic interventions like AMD3100 inhibited this interaction as well as the invasion ²¹⁹. Hence scaffold-based models are more organotypic than scaffold free ones, but due to increased complexity they have less scalability and reproducibility, and longer culture periods. Techniques like 3D bioprinting can improve reproducibility of scaffold-based models. For instance, MDA-MB 231 and fibroblasts were encapsulated in alginate-gelatin hydrogels and 3D printed to achieve consistent placement of cells for standardised cancer models which can be used for high throughput assays ²²⁰.

Microfluidic devices and tissue-on-a-chip models can provide both complexity as well as scalability and consistency within their model. As mentioned in Section 3.6, microfluidic devices have designed chambers with porous membranes that helps in customised cell patterning. One such study developed micro-sized chips of consistent size and shape, with collagen embedded MDA-MB-231 central channel flanked by channels of fibroblasts embedded collagen ²²¹. In this model, real time imaging and precise quantification of cancer cell invasion within fibroblast containing collagen gel was possible due to thin, compartmentalised and optically transparent microfluidic chambers. Additionally, tissue-on-a-chip models are able to mimic complex tumour related processes, like intravasation and extravasation, due to integrated fluid flow within the

model. Nagaraju et al. developed a three-channel microfluidic system consisting of a stromal ECM situated between 3D breast cancer cell channel and an endothelium lined channel ²²². Fluid flow was designed to be directed from the cancer channel through the stromal ECM and finally leaving through the endothelium lined channel. This system mimicked *in vivo* process of stromal invasion followed by intravasation within the outer vasculature, providing a platform for studying therapeutic efficacy on these specific processes. Additionally, the conditioned media collected through the endothelium lined channel provided information on potential therapeutic targets involved in intravasation ²²². On the other hand, Bersini et al. developed a microfluidic model for breast cancer extravasation to bone microenvironment ²²³. With a similar methodology, the two-channel device consisted of an endothelium lined channel and a 3D bone microenvironment channel (osteoblasts and osteoclasts embedded in collagen). MDA-MB 231 that were introduced in the endothelial channel with the media flow successfully extravasated to the bone microenvironment and formed micro-metastasis. With this device it was possible to validate and/or screen for molecules that inhibited extravasation, such as inhibitors for CXCL2 and CXCR2 signalling which is implicated in breast cancer extravasation *in vivo* ²²³. Another important component, tumour-immune cells interactions, are difficult to model because of their complexity. However, role of certain circulatory immune cells such as macrophages can be modelled within microfluidic devices due to compartmentalisation of the endothelium lined fluid channel which mimics a hollow vascular lumen. It was observed in an intravasation microfluidic model that cancer cells intravasate to the apical layer of endothelium only when macrophages are introduced in the channel ²²⁴. In summary, microfluidic models present themselves as a platform for mimicking complex cancer phenotypes. Although recent 3D breast cancer *in vitro* models have paved the way for incorporating many aspects of tumour complexity, they are still a long way from being standardised preclinical models. Model validation and regulations for standardisation of these models could be the key for their inclusion in preclinical studies and personalised medicine options.

4. Regulation for good practices within *in vitro* models

As described in this Chapter, the increased use of *in vitro* models has been paralleled by an increased need for regulations to control performances, report standards, guarantee reproducibility, introduce quality management, and finally validate models. In the past decades, attempts to

develop such guidelines and regulations have been made. One of the first, *Good Cell Culture Practices* (GCCP), was conceptualised in 1999 but only developed as a guidance document in 2005 by Coecke et al.²²⁵. The guidance includes the need for documentation of origin of cells and tissues with corresponding details on their maintenance and storage. It also guides on details to be included in publications relating to materials and methods for easy reproducibility and proper evaluation of the work²²⁵. Although the initial drafts or GCCP 1.0 were mostly based on traditional *in vitro* models, with the advent of microphysical systems like organoids and OOC, separate regulatory guidelines were required. On this basis, the aim of GCCP 2.0 was to include recommendations that covers stem cell based models, organoids as well as OOC^{226,227}.

GCCP 2.0 elucidates guidelines for documenting establishment, maintenance as well as materials and methodology used with primary human cells and human PSCs that includes iPSCs. It advocates provision of adequate training and compliance with ethical and legal regulations involved with stem cells. With microphysical systems, GCCP recommendation outlined the need for use of quality assured raw materials and documentation of protocols, SOPs, experimental design, test procedure and its acceptance criteria along with data collection and analysis. Further it recommends scientific reports to include statement of compliance with GCCP principles, elucidating the extent to which the study adheres in terms of relevant standards and regulations with proper safety and quality assured procedures²²⁷.

The *Good In Vitro Method Practices* (GIVIMP) is another guidance document established by European validation body EURL ECVAM and Organization for Economic Co-operation and Development (OCED)²²⁸. It was planned as a joint activity between OCED's established Good Laboratory Practices (GLP) and its National Coordinators of the Test Guidelines program (WNT). The objective of GIVIMP is to give guidance for reducing uncertainties within *in vitro* model based predictions by increasing the reliability and robustness of *in vitro* methods. While GCCP guides on documentation, GIVIMP guidelines are related to *in vitro* method development, standardisation and harmonisation that would further help in validation and acceptance of *in vitro* safety measures by regulatory agencies. The guidelines cover quality considerations of apparatus, materials and facilities as well as SOPs, test systems and reference items, performance of the method and reporting of results²²⁸.

While many *in vitro* models are being developed, regulatory bodies like ECVAM (European Centre for the Validation of Alternative Methods) exists to approve and validate their use for a particular application^{229,230}. Adherence to the above-mentioned guidelines like GIVIMP or GCCP is considered positive factor for the validation application. ECVAM along with its scientific advisory committee sends the positive validated outcomes to OCED that further develops a test guideline for the appropriate and safe use of the model worldwide²³⁰. These guidelines are not legally binding but are generally followed by industry and academia while developing *in vitro* models to speed up the preclinical outputs.

There are also other initiative in progress like Centre for Alternatives to Animal Testing (CAAT)'s *Good In Vitro Reporting standards* (GIVReSt), which aims to control uncertainty arising from reporting data, and in particular when combined with big data²³¹. For instance, the guidelines would emphasise on *in silico* methods, data processing and statistical consideration among others.

As the field of *in vitro* models is still evolving with new methods and models being established, the regulatory environment will likely have to modify, predict and accommodate future changes and challenges. For example, many *in vitro* models have complex endpoints or efficacy assessment that rely on multiple tests called 'Integrated approaches to testing and assessment' (IATA). Same model can be assessed through different combination of efficacy studies and current regulation has yet to be developed that can accommodate various integrated approaches²³⁰.

5. Conclusions

This chapter discusses the design criteria and the requirements to consider when engineering *in vitro* models to mimic *in vivo* microenvironmental factors, and with the ultimate aim of recapitulating and controlling *in vivo* physiology. While the intention for *in vitro* models to replace and/or reduce animal models has been clear across various research fields, yet their use in research area such as toxicity screening and drug efficacy studies, as well as delineating fundamental physiological processes is still limited. As illustrated in the chapter, various approaches have been used and refined across the past decades to develop multifunctional *in vitro* models. In our opinion, there are two considerations that prevent the widespread use of engineered *in vitro* models: 1) lack of regulation over biological materials and methods and 2) definition of required balance between the complexity of a model and its accuracy/efficacy in

mimicking *in vivo* physiology. On this last point, the debate over the use of *in vitro* models like spheroids (simple and more reproducible) and organoids (more holistic and complex, intrinsically heterogenous but less reproducible) is still on going. Similar considerations were discussed on the use of OOC: the use of mechanical and chemical engineering methods to model the *in vivo* like functionality would guarantee the reproducibility and accuracy required by regulatory bodies. The increasing number of engineered models used arises the necessity to define precise regulations and properties to harmonise research across disciplines. We believe that specific design criteria and higher control over outputs generated by developed models is required; and this would help to make an informed decision for the use of engineered *in vitro* models as per the application requirements. For this reason, collaboration between academics, industry and regulatory bodies is necessary to identify requirements for the components included and processing methods to obtain *in vitro* models.

References

1. Ruggeri BA, Camp F, Miknyoczki S. Animal models of disease: pre-clinical animal models of cancer and their applications and utility in drug discovery. *Biochem Pharmacol.* 2014;87(1):150-161. doi:10.1016/j.bcp.2013.06.020
2. Simons BW, Brayton C. Challenges and limitations of mouse xenograft models of cancer. In: *Patient Derived Tumor Xenograft Models: Promise, Potential and Practice*. Elsevier Inc.; 2017:25-36. doi:10.1016/B978-0-12-804010-2.00003-5
3. Drummond E, Wisniewski T. Alzheimer's disease: experimental models and reality. *Acta Neuropathol.* 2017;133(2):155-175. doi:10.1007/s00401-016-1662-x
4. (US) I of M, (US) NRC. The Evolving Regulatory Environment. 2012.
5. Ferdowsian HR, Beck N. Ethical and Scientific Considerations Regarding Animal Testing and Research. MacCallum CJ, ed. *PLoS One.* 2011;6(9):e24059. doi:10.1371/journal.pone.0024059
6. Animal testing and research - GOV.UK. <https://www.gov.uk/guidance/research-and-testing-using-animals>. Accessed April 21, 2020.
7. Animal Research Regulations in the UK – Speaking of Research. <https://speakingofresearch.com/facts/animal-research-regulations-in-the-uk/>. Accessed April 21, 2020.
8. Russell W, Burch R. *The Principles of Humane Experimental Technique.*; 1959. [http://117.239.25.194:7000/jspui/bitstream/123456789/1342/1/PRILIMINERY AND CONTENTS.pdf](http://117.239.25.194:7000/jspui/bitstream/123456789/1342/1/PRILIMINERY_AND_CONTENTS.pdf). Accessed August 23, 2020.
9. The 3Rs | NC3Rs. <https://www.nc3rs.org.uk/the-3rs>. Accessed May 13, 2020.
10. Rijal G, Li W. Native-mimicking in vitro microenvironment: An elusive and seductive future for tumor modeling and tissue engineering. *J Biol Eng.* 2018;12(1). doi:10.1186/s13036-018-0114-7
11. Barthes J, Özçelik H, Hindié M, Ndreu-Halili A, Hasan A, Engin Vrana N. Cell Microenvironment Engineering and Monitoring for Tissue Engineering and Regenerative Medicine: The Recent Advances. 2014. doi:10.1155/2014/921905

12. Sakolish CM, Esch MB, Hickman JJ, Shuler ML, Mahler GJ. Modeling Barrier Tissues In Vitro: Methods, Achievements, and Challenges. *EBioMedicine*. 2016;5:30-39. doi:10.1016/j.ebiom.2016.02.023
13. J. Gordon Betts, Kelly A. Young, James A. Wise, Eddie Johnson, Brandon Poe, Dean H. Kruse, Oksana Korol, Jody E. Johnson, Mark Womble PD. Chapter 4.2: Epithelial tissue. In: *Anatomy and Physiology*. OpenStax; 2013.
14. Tissues C, Matrix C. Connective Tissues (Chapter 32). *Cell Biol*. January 2017:308-319. doi:10.1016/B978-0-323-34126-4.00032-3
15. J. Gordon Betts, Kelly A. Young, James A. Wise, Eddie Johnson, Brandon Poe, Dean H. Kruse, Oksana Korol, Jody E. Johnson, Mark Womble PD. Chapter 4.3: Connective tissue supports and protects. In: *Anatomy and Physiology*. OpenStax; 2013.
16. J. Gordon Betts, Kelly A. Young, James A. Wise, Eddie Johnson, Brandon Poe, Dean H. Kruse, Oksana Korol, Jody E. Johnson, Mark Womble PD. Chapter 4.4: Muscle tissue and motion. In: *Anatomy and Physiology*. OpenStax; 2013.
17. Muscle - Muscle types | Britannica. <https://www.britannica.com/science/muscle/Muscle-types#ref58934>. Accessed April 6, 2020.
18. J. Gordon Betts, Kelly A. Young, James A. Wise, Eddie Johnson, Brandon Poe, Dean H. Kruse, Oksana Korol, Jody E. Johnson, Mark Womble PD. Chapter 4.6: Nervous Tissue Mediates Perception and Response. In: *Anatomy and Physiology*. OpenStax; 2013.
19. Types of neurons - Queensland Brain Institute - University of Queensland. <https://qbi.uq.edu.au/brain/brain-anatomy/types-neurons>. Accessed April 6, 2020.
20. Marieb EN, Hoehn K. *Human Anatomy & Physiology, Global Edition*. Vol Tenth edit. Pearson; 2015. <http://search.ebscohost.com/login.aspx?direct=true&db=nlebk&AN=1419600&site=ehost-live>. Accessed April 6, 2020.
21. Zakrzewski W, Dobrzyński M, Szymonowicz M, Rybak Z. Stem cells: Past, present, and future. *Stem Cell Res Ther*. 2019;10(1):68. doi:10.1186/s13287-019-1165-5
22. Tweedell KS. The adaptability of somatic stem cells: A review. *J Stem Cells Regen Med*. 2017;13(1):3-13.

23. Rezza A, Sennett R, Rendl M. Adult Stem Cell Niches. Cellular and Molecular Components. In: *Current Topics in Developmental Biology*. Vol 107. Academic Press Inc.; 2014:333-372. doi:10.1016/B978-0-12-416022-4.00012-3
24. Pennings S, Liu KJ, Qian H. Editorial The Stem Cell Niche: Interactions between Stem Cells and Their Environment. *Stem Cells Int*. 2018;2018. doi:10.1155/2018/4879379
25. Morrison SJ, Spradling AC. Stem Cells and Niches: Mechanisms That Promote Stem Cell Maintenance throughout Life. *Cell*. 2008;132(4):598-611. doi:10.1016/j.cell.2008.01.038
26. Titushkin I, Sun S, Shin J, Cho M. Physicochemical Control of Adult Stem Cell Differentiation: Shedding Light on Potential Molecular Mechanisms. *J Biomed Biotechnol*. 2010;2010:14. doi:10.1155/2010/743476
27. Snykers S, De Kock J, Rogiers V, Vanhaecke T. In Vitro Differentiation of Embryonic and Adult Stem Cells into Hepatocytes: State of the Art. *Stem Cells*. 2009;27(3):577-605. doi:10.1634/stemcells.2008-0963
28. Of stem cells and ethics. *Nat Cell Biol*. 2017;19(12):1381. doi:10.1038/ncb3652
29. Regulation of stem cell research in the United Kingdom | Eurostemcell. <https://www.eurostemcell.org/regulation-stem-cell-research-united-kingdom>. Accessed March 26, 2020.
30. Takahashi K, Yamanaka S. Induction of Pluripotent Stem Cells from Mouse Embryonic and Adult Fibroblast Cultures by Defined Factors. *Cell*. 2006;126(4):663-676. doi:10.1016/j.cell.2006.07.024
31. Yu J, Thomson JA. Induced Pluripotent Stem Cells. In: *Principles of Tissue Engineering: Fourth Edition*. Elsevier Inc.; 2013:581-594. doi:10.1016/B978-0-12-398358-9.00030-6
32. Doss MX, Sachinidis A. Current Challenges of iPSC-Based Disease Modeling and Therapeutic Implications. *Cells*. 2019;8(5):403. doi:10.3390/cells8050403
33. Ebert AD, Liang P, Wu JC. Induced pluripotent stem cells as a disease modeling and drug screening platform. *J Cardiovasc Pharmacol*. 2012;60(4):408-416. doi:10.1097/FJC.0b013e318247f642
34. Verfaillie C, Terryn J, Tricot T, Gajjar M. Recent advances in lineage differentiation from

- stem cells: Hurdles and opportunities? *F1000Research*. 2018;7. doi:10.12688/f1000research.12596.1
35. Cooper GM. Signaling Molecules and Their Receptors. 2000.
 36. Rios de la Rosa JM, Tirella A, Gennari A, Stratford IJ, Tirelli N. The CD44-Mediated Uptake of Hyaluronic Acid-Based Carriers in Macrophages. *Adv Healthc Mater*. 2017;6(4):1601012. doi:10.1002/adhm.201601012
 37. Wang F, Zhang S, Jeon R, et al. Interferon Gamma Induces Reversible Metabolic Reprogramming of M1 Macrophages to Sustain Cell Viability and Pro-Inflammatory Activity. *EBioMedicine*. 2018;30:303-316. doi:10.1016/j.ebiom.2018.02.009
 38. Gjorevski N, Nelson CM. Integrated morphodynamic signalling of the mammary gland. *Nat Rev Mol Cell Biol*. 2011;12(9):581-593. doi:10.1038/nrm3168
 39. Vella V, De Francesco EM, Lappano R, et al. Microenvironmental Determinants of Breast Cancer Metastasis: Focus on the Crucial Interplay Between Estrogen and Insulin/Insulin-Like Growth Factor Signaling. *Front Cell Dev Biol*. 2020;8:1458. doi:10.3389/FCELL.2020.608412/BIBTEX
 40. Russo J, Russo IH. The role of estrogen in the initiation of breast cancer. *J Steroid Biochem Mol Biol*. 2006;102(1-5):89-96. doi:10.1016/J.JSBMB.2006.09.004
 41. Litwack G. Polypeptide Hormones. In: *Human Biochemistry*. Elsevier; 2018:427-465. doi:10.1016/B978-0-12-383864-3.00015-6
 42. Bafico A, Aaronson SA. Classification of Growth Factors and Their Receptors. 2003.
 43. Deuel TF, Chang Y. Growth Factors. In: *Principles of Tissue Engineering: Fourth Edition*. Elsevier Inc.; 2013:291-308. doi:10.1016/B978-0-12-398358-9.00016-1
 44. Chung KF. Cytokines. In: *Asthma and COPD*. Elsevier Ltd; 2009:327-341. doi:10.1016/B978-0-12-374001-4.00027-4
 45. Litwack G. Steroid Hormones. In: *Human Biochemistry*. Elsevier; 2018:467-506. doi:10.1016/B978-0-12-383864-3.00016-8
 46. Miller SL, Yeh HH. Neurotransmitters and Neurotransmission in the Developing and Adult Nervous System. In: *Conn's Translational Neuroscience*. Elsevier Inc.; 2017:49-84.

doi:10.1016/B978-0-12-802381-5.00004-X

47. Frantz C, Stewart KM, Weaver VM. The extracellular matrix at a glance. *J Cell Sci.* 2010;123(24):4195-4200. doi:10.1242/jcs.023820
48. Shawky MS, Ricciardelli C, Lord M, et al. Proteoglycans: Potential Agents in Mammographic Density and the Associated Breast Cancer Risk. *J Mammary Gland Biol Neoplasia.* 2015;20(3-4):121-131. doi:10.1007/S10911-015-9346-Z
49. Suwihat S, Ricciardelli C, Tammi R, et al. Expression of extracellular matrix components versican, chondroitin sulfate, tenascin, and hyaluronan, and their association with disease outcome in node-negative breast cancer. *Clin Cancer Res.* 2004;10(7):2491-2498. doi:10.1158/1078-0432.CCR-03-0146
50. Schaefer L, Schaefer RM. Proteoglycans: From structural compounds to signaling molecules. *Cell Tissue Res.* 2010;339(1):237-246. doi:10.1007/s00441-009-0821-y
51. Neill T, Schaefer L, Iozzo R V. Decorin as a multivalent therapeutic agent against cancer. *Adv Drug Deliv Rev.* 2016;97:174-185. doi:10.1016/J.ADDR.2015.10.016
52. Muiznieks LD, Keeley FW. Molecular assembly and mechanical properties of the extracellular matrix: A fibrous protein perspective. *Biochim Biophys Acta - Mol Basis Dis.* 2013;1832(7):866-875. doi:10.1016/j.bbadis.2012.11.022
53. Uzman A, Lodish H, Berk A, Zipursky L, Baltimore D. Molecular Cell Biology (4th edition) New York, NY, 2000, ISBN 0-7167-3136-3. *Biochem Mol Biol Educ.* 2000;29:Section 1.2The Molecules of Life. doi:10.1016/S1470-8175(01)00023-6
54. Acerbi I, Cassereau L, Dean I, et al. Human breast cancer invasion and aggression correlates with ECM stiffening and immune cell infiltration. *Integr Biol.* 2015;7(10):1120-1134. doi:10.1039/C5IB00040H
55. Daley WP, Peters SB, Larsen M. Extracellular matrix dynamics in development and regenerative medicine. *J Cell Sci.* 2008;121(3):255-264. doi:10.1242/jcs.006064
56. Levental KR, Yu H, Kass L, et al. Matrix Crosslinking Forces Tumor Progression by Enhancing Integrin Signaling. *Cell.* 2009;139(5):891-906. doi:10.1016/j.cell.2009.10.027
57. Ortiz-Prado E, Dunn JF, Vasconez J, Castillo D, Viscor G. Partial pressure of oxygen in the

- human body: a general review. *Am J Blood Res.* 2019;9(1):1-14. <http://www.ncbi.nlm.nih.gov/pubmed/30899601>. Accessed March 30, 2020.
58. Rundqvist H, Johnson RS. Tumour oxygenation: implications for breast cancer prognosis. *J Intern Med.* 2013;274(2):105-112. doi:10.1111/JOIM.12091
 59. M N A, Mudda V, Chandra M, T J S. PHYSIOLOGY OF ACID BASE BALANCE. *J Evid Based Med Healthc.* 2014;1(17):2140-2152. doi:10.18410/jebmh/2014/308
 60. Dressman JB, Berardi RR, Dermentzoglou LC, et al. Upper Gastrointestinal (GI) pH in Young, Healthy Men and Women. *Pharm Res An Off J Am Assoc Pharm Sci.* 1990;7(7):756-761. doi:10.1023/A:1015827908309
 61. WATSON P. Intracellular trafficking pathways and drug delivery: fluorescence imaging of living and fixed cells. *Adv Drug Deliv Rev.* 2005;57(1):43-61. doi:10.1016/j.addr.2004.05.003
 62. J. Gordon Betts, Kelly A. Young, James A. Wise, Eddie Johnson, Brandon Poe, Dean H. Kruse, Oksana Korol, Jody E. Johnson, Mark Womble PD. Chapter 26.4 Acid-base balance. In: *Anatomy and Physiology.* ; 2013.
 63. Svensen C. Electrolytes and diuretics. In: *Pharmacology and Physiology for Anesthesia: Foundations and Clinical Application.* Elsevier; 2018:814-835. doi:10.1016/B978-0-323-48110-6.00042-9
 64. Lodish H, Berk A, Zipursky SL, Matsudaira P, Baltimore D, Darnell J. The Action Potential and Conduction of Electric Impulses. 2000. <https://www.ncbi.nlm.nih.gov/books/NBK21668/>. Accessed July 20, 2020.
 65. Pu F, Chen N, Xue S. Calcium intake, calcium homeostasis and health. *Food Sci Hum Wellness.* 2016;5(1):8-16. doi:10.1016/j.fshw.2016.01.001
 66. Penido MGMG, Alon US. Phosphate homeostasis and its role in bone health. *Pediatr Nephrol.* 2012;27(11):2039-2048. doi:10.1007/s00467-012-2175-z
 67. Farrugia G, Szurszewski JH. Carbon monoxide, hydrogen sulfide, and nitric oxide as signaling molecules in the gastrointestinal tract. *Gastroenterology.* 2014;147(2):303-313. doi:10.1053/j.gastro.2014.04.041

68. Rutkowski JM, Swartz MA. A driving force for change: interstitial flow as a morphoregulator. *Trends Cell Biol.* 2007;17(1):44-50. doi:10.1016/j.tcb.2006.11.007
69. Swartz MA, Fleury ME. Interstitial Flow and Its Effects in Soft Tissues. *Annu Rev Biomed Eng.* 2007;9(1):229-256. doi:10.1146/annurev.bioeng.9.060906.151850
70. Rutkowski JM, Boardman KC, Swartz MA. Characterization of lymphangiogenesis in a model of adult skin regeneration. *Am J Physiol - Hear Circ Physiol.* 2006;291(3). doi:10.1152/ajpheart.00038.2006
71. Munson JM, Shieh AC. Interstitial fluid flow in cancer: implications for disease progression and treatment. *Cancer Manag Res.* 2014;6:317-328. doi:10.2147/CMAR.S65444
72. Ng CP, Hinz B, Swartz MA. Interstitial fluid flow induces myofibroblast differentiation and collagen alignment in vitro. *J Cell Sci.* 2005;118(20):4731-4739. doi:10.1242/jcs.02605
73. Khan YS, Sajjad H. *Anatomy, Thorax, Mammary Gland.* StatPearls Publishing; 2019. <http://www.ncbi.nlm.nih.gov/pubmed/31613446>. Accessed April 22, 2020.
74. Paine IS, Lewis MT. The Terminal End Bud: the Little Engine that Could. *J Mammary Gland Biol Neoplasia.* 2017;22(2):93-108. doi:10.1007/s10911-017-9372-0
75. Gjorevski N, Nelson CM. Endogenous patterns of mechanical stress are required for branching morphogenesis. *Integr Biol.* 2010;2(9):424-434. doi:10.1039/c0ib00040j
76. Vogel V, Sheetz M. Local force and geometry sensing regulate cell functions. *Nat Rev Mol Cell Biol.* 2006;7(4):265-275. doi:10.1038/nrm1890
77. Fenner J, Stacer AC, Winterroth F, Johnson TD, Luker KE, Luker GD. Macroscopic Stiffness of Breast Tumors Predicts Metastasis. *Sci Rep.* 2015;4(1):5512. doi:10.1038/srep05512
78. Samani A, Zubovits J, Plewes D. Elastic moduli of normal and pathological human breast tissues: an inversion-technique-based investigation of 169 samples. *Phys Med Biol.* 2007;52(6):1565-1576. doi:10.1088/0031-9155/52/6/002
79. Jedrzejczak-Silicka M. History of Cell Culture. In: *New Insights into Cell Culture Technology.* InTech; 2017. doi:10.5772/66905
80. Landecker H. New times for biology: Nerve cultures and the advent of cellular life in vitro.

- Stud Hist Philos Sci Part C Stud Hist Philos Biol Biomed Sci.* 2002;33(4):667-694.
doi:10.1016/S1369-8486(02)00026-2
81. Malinin TI. Remembering Alexis Carrel and Charles A. Lindbergh. *Texas Hear Inst J.* 1996;23(1):28-35. <http://www.ncbi.nlm.nih.gov/pubmed/8680271>. Accessed April 14, 2020.
 82. Landecker H. *Culturing Life : How Cells Became Technologies*. Harvard University Press; 2007.
 83. Rous P, Jones FS. A method for obtaining suspensions of living cells from the fixed tissues, and for the plating out of individual cells. *J Exp Med.* 1916;23(4):549-556. doi:10.1084/jem.23.4.549
 84. Skloot R. *The Immortal Life of Henrietta Lacks*. Crown Publishers; 2010.
 85. Jones HW, McKusick VA, Harper PS, Wu KD. George Otto Gey. (1899-1970). The HeLa cell and a reappraisal of its origin. *Obstet Gynecol.* 1971;38(6):945-949.
 86. Hayflick L, Moorhead PS. *THE SERIAL CULTIVATION OF HUMAN DIPLOID CELL STRAINS'*. Vol 25.; 1961.
 87. Irfan Maqsood M, Matin MM, Bahrami AR, Ghasroldasht MM. Immortality of cell lines: challenges and advantages of establishment. *Cell Biol Int.* 2013;37(10):1038-1045. doi:10.1002/cbin.10137
 88. Astashkina A, Mann B, therapeutics DG-P&, 2012 undefined. A critical evaluation of in vitro cell culture models for high-throughput drug screening and toxicity. *Elsevier*. <https://www.sciencedirect.com/science/article/pii/S0163725812000022>. Accessed April 21, 2020.
 89. Pan C, Kumar C, Bohl S, Klingmueller U, Mann M. Comparative proteomic phenotyping of cell lines and primary cells to assess preservation of cell type-specific functions. *Mol Cell Proteomics.* 2009;8(3):443-450. doi:10.1074/mcp.M800258-MCP200
 90. Alge CS, Hauck SM, Priglinger SG, Kampik A, Ueffing M. Differential protein profiling of primary versus immortalized human RPE cells identifies expression patterns associated with cytoskeletal remodeling and cell survival. *J Proteome Res.* 2006;5(4):862-878. doi:10.1021/pr050420t

91. Geraghty RJ, Capes-Davis A, Davis JM, et al. Guidelines for the use of cell lines in biomedical research. *Br J Cancer*. 2014;111(6):1021-1046. doi:10.1038/bjc.2014.166
92. Lerman MJ, Lembong J, Muramoto S, Gillen G, Fisher JP. The Evolution of Polystyrene as a Cell Culture Material. *Tissue Eng Part B Rev*. 2018;24(5):359-372. doi:10.1089/ten.teb.2018.0056
93. Krüger A, Fuhrmann R, Jung F, Franke RP. Influence of the coating with extracellular matrix and the number of cell passages on the endothelialization of a polystyrene surface. *Clin Hemorheol Microcirc*. 2015;60(1):153-161. doi:10.3233/CH-151943
94. Arora M. Cell Culture Media: A Review. *Mater Methods*. 2013;3. doi:10.13070/mm.en.3.175
95. Carbon dioxide Concentration and pH Control in the Cell Culture Laboratory.
96. CO2 Incubators | Thermo Fisher Scientific - UK. <https://www.thermofisher.com/uk/en/home/life-science/lab-equipment/co2-incubators.html>. Accessed December 15, 2020.
97. Microbiological Safety Cabinets: Protecting Products and Users. <https://www.tecomak.com/product/biological-safety-cabinets/>. Accessed December 15, 2020.
98. Eisner R, Patel R. Strengthening the regulatory system through the implementation and use of a quality management system. *Rev Panam Salud Publica/Pan Am J Public Heal*. 2017;41. doi:10.26633/RPSP.2017.12
99. ISO - ISO 9000 family — Quality management. <https://www.iso.org/iso-9001-quality-management.html>. Accessed June 13, 2020.
100. Solomon J, Csontos L, Clarke D, et al. Current perspectives on the use of ancillary materials for the manufacture of cellular therapies. *Cytotherapy*. 2016;18(1):1-12. doi:10.1016/j.jcyt.2015.09.010
101. ICH Official web site : ICH. <https://www.ich.org/page/quality-guidelines>. Accessed June 13, 2020.
102. World Health Organization. Guidelines for national authorities on quality assurance for

- biological products. *WHO Tech Rep Ser No* 822. 1992. https://www.who.int/biologicals/WHO_TRS_822_A2.pdf?ua=1. Accessed June 13, 2020.
103. CFR - Code of Federal Regulations Title 21. <https://www.accessdata.fda.gov/scripts/cdrh/cfdocs/cfcfr/cfrsearch.cfm?cfrpart=610>. Accessed June 13, 2020.
 104. Atouf F, Provost NM, Rosenthal FM. *Standards for Ancillary Materials Used in Cell-and Tissue-Based Therapies FOCUS ON... REGENERATIVE MEDICINE*. Vol 11.; 2013. www.bioprocessintl.com/bpiextra. Accessed June 13, 2020.
 105. Butcher DT, Alliston T, Weaver VM. A tense situation: forcing tumour progression. *Nat Rev Cancer*. 2009;9(2):108-122. doi:10.1038/nrc2544
 106. Discher DE, Janmey P, Wang Y-L. Tissue cells feel and respond to the stiffness of their substrate. *Science*. 2005;310(5751):1139-1143. doi:10.1126/science.1116995
 107. Leipzig ND, Shoichet MS. The effect of substrate stiffness on adult neural stem cell behavior. *Biomaterials*. 2009;30(36):6867-6878. doi:10.1016/j.biomaterials.2009.09.002
 108. Birgersdotter A, Sandberg R, Ernberg I. Gene expression perturbation in vitro--a growing case for three-dimensional (3D) culture systems. *Semin Cancer Biol*. 2005;15(5):405-412. doi:10.1016/j.semcancer.2005.06.009
 109. Place TL, Domann FE, Case AJ. Limitations of oxygen delivery to cells in culture: An underappreciated problem in basic and translational research. *Free Radic Biol Med*. 2017;113:311-322. doi:10.1016/j.freeradbiomed.2017.10.003
 110. Krogh A. The supply of oxygen to the tissues and the regulation of the capillary circulation. *J Physiol*. 1919;52(6):457-474. doi:10.1113/jphysiol.1919.sp001844
 111. Allen CB, Schneider BK, White CW. Limitations to oxygen diffusion and equilibration in in vitro cell exposure systems in hyperoxia and hypoxia. *Am J Physiol - Lung Cell Mol Physiol*. 2001;281(4 25-4). doi:10.1152/ajplung.2001.281.4.11021
 112. Hutchinson L, Kirk R. High drug attrition rates--where are we going wrong? *Nat Rev Clin Oncol*. 2011;8(4):189-190. doi:10.1038/nrclinonc.2011.34
 113. Cui X, Hartanto Y, Zhang H. Advances in multicellular spheroids formation. *J R Soc*

- Interface*. 2017;14(127). doi:10.1098/rsif.2016.0877
114. Saji Joseph J, Tebogo Malindisa S, Ntwasa M. Two-Dimensional (2D) and Three-Dimensional (3D) Cell Culturing in Drug Discovery. In: *Cell Culture*. IntechOpen; 2019. doi:10.5772/intechopen.81552
 115. Fang Y, Eglen RM. Three-Dimensional Cell Cultures in Drug Discovery and Development. *SLAS Discov*. 2017;22(5):456-472. doi:10.1177/1087057117696795
 116. Kelm JM, Fussenegger M. Microscale tissue engineering using gravity-enforced cell assembly. *Trends Biotechnol*. 2004;22(4):195-202. doi:10.1016/j.tibtech.2004.02.002
 117. Wei SC, Fattet L, Tsai JH, et al. Matrix stiffness drives epithelial-mesenchymal transition and tumour metastasis through a TWIST1-G3BP2 mechanotransduction pathway. *Nat Cell Biol*. 2015;17(5):678-688. doi:10.1038/ncb3157
 118. Edmondson R, Broglie JJ, Adcock AF, Yang L. Three-dimensional cell culture systems and their applications in drug discovery and cell-based biosensors. *Assay Drug Dev Technol*. 2014;12(4):207-218. doi:10.1089/adt.2014.573
 119. Lv D, Hu Z, Lu L, Lu H, Xu X. Three-dimensional cell culture: A powerful tool in tumor research and drug discovery. *Oncol Lett*. 2017;14(6):6999-7010. doi:10.3892/ol.2017.7134
 120. Langhans SA. Three-dimensional in vitro cell culture models in drug discovery and drug repositioning. *Front Pharmacol*. 2018;9(JAN):6. doi:10.3389/fphar.2018.00006
 121. Kelm JM, Timmins NE, Brown CJ, Fussenegger M, Nielsen LK. Method for generation of homogeneous multicellular tumor spheroids applicable to a wide variety of cell types. *Biotechnol Bioeng*. 2003;83(2):173-180. doi:10.1002/bit.10655
 122. Tung YC, Hsiao AY, Allen SG, Torisawa YS, Ho M, Takayama S. High-throughput 3D spheroid culture and drug testing using a 384 hanging drop array. *Analyst*. 2011;136(3):473-478. doi:10.1039/c0an00609b
 123. Ratnayaka SH, Hillburn TE, Forouzan O, Shevkoplyas SS, Khismatullin DB. PDMS well platform for culturing millimeter-size tumor spheroids. *Biotechnol Prog*. 2013;29(5):1265-1269. doi:10.1002/btpr.1764
 124. Chen YC, Lou X, Zhang Z, Ingram P, Yoon E. High-Throughput Cancer Cell Sphere

- Formation for Characterizing the Efficacy of Photo Dynamic Therapy in 3D Cell Cultures. *Sci Rep*. 2015;5(1):1-12. doi:10.1038/srep12175
125. Sutherland RM, Inch WR, McCredie JA, Kruuv J. A multi-component radiation survival curve using an in vitro tumour model. *Int J Radiat Biol*. 1970;18(5):491-495. doi:10.1080/09553007014551401
 126. Goodwin TJ, Prewett TL, Wolf DA, Spaulding GF. Reduced shear stress: A major component in the ability of mammalian tissues to form three-dimensional assemblies in simulated microgravity. *J Cell Biochem*. 1993;51(3):301-311. doi:10.1002/jcb.240510309
 127. Ingram M, Techy GB, Saroufeem R, et al. Three-dimensional growth patterns of various human tumor cell lines in simulated microgravity of a nasa bioreactor. *Vitr Cell Dev Biol - Anim*. 1997;33(6):459-466. doi:10.1007/s11626-997-0064-8
 128. Souza GR, Molina JR, Raphael RM, et al. Three-dimensional tissue culture based on magnetic cell levitation. *Nat Nanotechnol*. 2010;5(4):291-296. doi:10.1038/nnano.2010.23
 129. Ivascu A, Kubbies M. Rapid generation of single-tumor spheroids for high-throughput cell function and toxicity analysis. *J Biomol Screen*. 2006;11(8):922-932. doi:10.1177/1087057106292763
 130. Chen W, Wong C, Vosburgh E, Levine AJ, Foran DJ, Xu EY. High-throughput image analysis of tumor spheroids: A user-friendly software application to measure the size of spheroids automatically and accurately. *J Vis Exp*. 2014;(89). doi:10.3791/51639
 131. Sirenko O, Mitlo T, Hesley J, Luke S, Owens W, Cromwell EF. High-Content Assays for Characterizing the Viability and Morphology of 3D Cancer Spheroid Cultures. *Assay Drug Dev Technol*. 2015;13(7):402-414. doi:10.1089/adt.2015.655
 132. Weiswald LB, Bellet D, Dangles-Marie V. Spherical Cancer Models in Tumor Biology. *Neoplasia (United States)*. 2015;17(1):1-15. doi:10.1016/j.neo.2014.12.004
 133. Moshksayan K, Kashaninejad N, Warkiani ME, et al. Spheroids-on-a-chip: Recent advances and design considerations in microfluidic platforms for spheroid formation and culture. *Sensors Actuators, B Chem*. 2018;263:151-176. doi:10.1016/j.snb.2018.01.223
 134. Reininger-Mack A, Thielecke H, Robitzki AA. 3D-biohybrid systems: Applications in drug screening. *Trends Biotechnol*. 2002;20(2):56-61. doi:10.1016/S0167-7799(01)01880-7

135. Kunz-Schughart LA, Freyer JP, Hofstaedter F, Ebner R. The Use of 3-D Cultures for High-Throughput Screening: The Multicellular Spheroid Model. 2004. doi:10.1177/1087057104265040
136. Caliani SR, Burdick JA. A practical guide to hydrogels for cell culture. *Nat Methods*. 2016;13(5):405-414. doi:10.1038/nmeth.3839
137. Tibbitt MW, Anseth KS. Hydrogels as extracellular matrix mimics for 3D cell culture. *Biotechnol Bioeng*. 2009;103(4):655-663. doi:10.1002/bit.22361
138. Petersen OW, Ronnov-Jessen L, Howlett AR, Bissell MJ. Interaction with basement membrane serves to rapidly distinguish growth and differentiation pattern of normal and malignant human breast epithelial cells. *Proc Natl Acad Sci U S A*. 1992;89(19):9064-9068. doi:10.1073/pnas.89.19.9064
139. Cushing MC, Anseth KS. Hydrogel cell cultures. *Science (80-)*. 2007;316(5828):1133-1134. doi:10.1126/science.1140171
140. Serban MA, Prestwich GD. Modular extracellular matrices: Solutions for the puzzle. *Methods*. 2008;45(1):93-98. doi:10.1016/j.ymeth.2008.01.010
141. Gyles DA, Castro LD, Silva JOC, Ribeiro-Costa RM. A review of the designs and prominent biomedical advances of natural and synthetic hydrogel formulations. *Eur Polym J*. 2017;88:373-392. doi:10.1016/j.eurpolymj.2017.01.027
142. Campbell D (Donald), Pethrick RA (Richard A, White JR. *Polymer Characterization : Physical Techniques*. CRC Press; 2000.
143. Polymer Characterization Lab Polymer Analysis And Characterization. <https://www.polymersolutions.com/applications/polymer-characterization/>. Accessed June 7, 2020.
144. Park KH, Kim MH, Park SH, Lee HJ, Kim IK, Chung HM. Synthesis of Arg-Gly-Asp (RGD) sequence conjugated thermo-reversible gel via the PEG spacer arm as an extracellular matrix for a pheochromocytoma cell (PC12) culture. *Biosci Biotechnol Biochem*. 2004;68(11):2224-2229. doi:10.1271/bbb.68.2224
145. Saha K, Pollock JF, Schaffer D V., Healy KE. Designing synthetic materials to control stem cell phenotype. *Curr Opin Chem Biol*. 2007;11(4):381-387.

doi:10.1016/j.cbpa.2007.05.030

146. Fan H, Hu Y, Zhang C, et al. Cartilage regeneration using mesenchymal stem cells and a PLGA-gelatin/chondroitin/hyaluronate hybrid scaffold. *Biomaterials*. 2006;27(26):4573-4580. doi:10.1016/j.biomaterials.2006.04.013
147. Xu W, Qian J, Zhang Y, et al. A double-network poly(Nε-acryloyl l-lysine)/hyaluronic acid hydrogel as a mimic of the breast tumor microenvironment. *Acta Biomater*. 2016;33:131-141. doi:10.1016/j.actbio.2016.01.027
148. Lee S, Porter M, Wasko S, et al. *Potential Bone Replacement Materials Prepared by Two Methods*.
149. Dhandayuthapani B, Yoshida Y, Maekawa T, Sakthi Kumar D. Polymeric Scaffolds in Tissue Engineering Application: A Review. *Int J Polym Sci*. 2011;2011. doi:10.1155/2011/290602
150. Balachander GM, Balaji SA, Rangarajan A, Chatterjee K. Enhanced Metastatic Potential in a 3D Tissue Scaffold toward a Comprehensive in Vitro Model for Breast Cancer Metastasis. *ACS Appl Mater Interfaces*. 2015;7(50):27810-27822. doi:10.1021/acsami.5b09064
151. Narayanan G, Vernekar VN, Kuyinu EL, Laurencin CT. Poly (lactic acid)-based biomaterials for orthopaedic regenerative engineering. *Adv Drug Deliv Rev*. 2016;107:247-276. doi:10.1016/j.addr.2016.04.015
152. Prasad A, Sankar MR, Katiyar V. State of Art on Solvent Casting Particulate Leaching Method for Orthopedic Scaffolds Fabrication. In: *Materials Today: Proceedings*. Vol 4. Elsevier Ltd; 2017:898-907. doi:10.1016/j.matpr.2017.01.101
153. Brougham CM, Levingstone TJ, Shen N, et al. Freeze-Drying as a Novel Biofabrication Method for Achieving a Controlled Microarchitecture within Large, Complex Natural Biomaterial Scaffolds. *Adv Healthc Mater*. 2017;6(21). doi:10.1002/adhm.201700598
154. Costantini M, Barbetta A. Gas foaming technologies for 3D scaffold engineering. In: *Functional 3D Tissue Engineering Scaffolds: Materials, Technologies, and Applications*. Elsevier; 2018:127-149. doi:10.1016/B978-0-08-100979-6.00006-9
155. Lannutti J, Reneker D, Ma T, Tomasko D, Farson D. Electrospinning for tissue engineering scaffolds. *Mater Sci Eng C*. 2007;27(3):504-509. doi:10.1016/j.msec.2006.05.019

156. Bishop ES, Mostafa S, Pakvasa M, et al. 3-D bioprinting technologies in tissue engineering and regenerative medicine: Current and future trends. *Genes Dis.* 2017;4(4):185-195. doi:10.1016/j.gendis.2017.10.002
157. Liu J, Yan C. 3D Printing of Scaffolds for Tissue Engineering. In: *3D Printing*. InTech; 2018. doi:10.5772/intechopen.78145
158. An J, Teoh JEM, Suntornnond R, Chua CK. Design and 3D Printing of Scaffolds and Tissues. *Engineering.* 2015;1(2):261-268. doi:10.15302/J-ENG-2015061
159. Ligon SC, Liska R, Stampfl J, Gurr M, Mülhaupt R. Polymers for 3D Printing and Customized Additive Manufacturing. *Chem Rev.* 2017;117(15):10212-10290. doi:10.1021/acs.chemrev.7b00074
160. Tamay DG, Usal TD, Alagoz AS, Yucel D, Hasirci N, Hasirci V. 3D and 4D printing of polymers for tissue engineering applications. *Front Bioeng Biotechnol.* 2019;7(JUL):164. doi:10.3389/fbioe.2019.00164
161. Gopinathan J, Noh I. Recent trends in bioinks for 3D printing. *Biomater Res.* 2018;22(1):1-15. doi:10.1186/s40824-018-0122-1
162. Jiang P, Yan C, Guo Y, et al. Direct ink writing with high-strength and swelling-resistant biocompatible physically crosslinked hydrogels. *Biomater Sci.* 2019;7(5):1805-1814. doi:10.1039/c9bm00081j
163. Yeong WY, Chua CK, Leong KF, Chandrasekaran M, Lee MW. Indirect fabrication of collagen scaffold based on inkjet printing technique. *Rapid Prototyp J.* 2006;12(4):229-237. doi:10.1108/13552540610682741
164. Quan H, Zhang T, Xu H, Luo S, Nie J, Zhu X. Photo-curing 3D printing technique and its challenges. *Bioact Mater.* 2020;5(1):110-115. doi:10.1016/j.bioactmat.2019.12.003
165. Negro A, Cherbuin T, Lutolf MP. 3D Inkjet Printing of Complex, Cell-Laden Hydrogel Structures. *Sci Rep.* 2018;8(1):1-9. doi:10.1038/s41598-018-35504-2
166. Ashammakhi N, Ahadian S, Xu C, et al. Bioinks and bioprinting technologies to make heterogeneous and biomimetic tissue constructs. *Mater Today Bio.* 2019;1:100008. doi:10.1016/j.mtbio.2019.100008

167. Chowdhury F, Li Y, Poh YC, Yokohama-Tamaki T, Wang N, Tanaka TS. Soft substrates promote homogeneous self-renewal of embryonic stem cells via downregulating cell-matrix tractions. *PLoS One*. 2010;5(12). doi:10.1371/journal.pone.0015655
168. Nguyen T V., Sleiman M, Moriarty T, Herrick WG, Peyton SR. Sorafenib resistance and JNK signaling in carcinoma during extracellular matrix stiffening. *Biomaterials*. 2014;35(22):5749-5759. doi:10.1016/j.biomaterials.2014.03.058
169. Raviraj V, Fok S, Zhao J, et al. Regulation of ROCK1 via Notch1 during breast cancer cell migration into dense matrices. *BMC Cell Biol*. 2012;13(1):1-17. doi:10.1186/1471-2121-13-12/FIGURES/8
170. Melchels FPW, Barradas AMC, Van Blitterswijk CA, De Boer J, Feijen J, Grijpma DW. Effects of the architecture of tissue engineering scaffolds on cell seeding and culturing. *Acta Biomater*. 2010;6(11):4208-4217. doi:10.1016/j.actbio.2010.06.012
171. Zeltinger J, Sherwood JK, Graham DA, Müller R, Griffith LG. Effect of pore size and void fraction on cellular adhesion, proliferation, and matrix deposition. *Tissue Eng*. 2001;7(5):557-572. doi:10.1089/107632701753213183
172. Sopyan I, Gunawan. Development of Porous Calcium Phosphate Bioceramics for Bone Implant Applications: A Review. *Recent Patents Mater Sci*. 2013;6(3):238-252. doi:10.2174/18744648113069990012
173. Heath DE, Lannutti JJ, Cooper SL. Electrospun scaffold topography affects endothelial cell proliferation, metabolic activity, and morphology. *J Biomed Mater Res Part A*. 2010;9999A(4):NA-NA. doi:10.1002/jbm.a.32802
174. Bouta EM, McCarthy CW, Keim A, Wang HB, Gilbert RJ, Goldman J. Biomaterial guides for lymphatic endothelial cell alignment and migration. *Acta Biomater*. 2011;7(3):1104-1113. doi:10.1016/j.actbio.2010.10.016
175. Drury JL, Mooney DJ. Hydrogels for tissue engineering: Scaffold design variables and applications. *Biomaterials*. 2003;24(24):4337-4351. doi:10.1016/S0142-9612(03)00340-5
176. Li R, Altreuter D, and FG-B, 1996 undefined. Transport characterization of hydrogel matrices for cell encapsulation. *Wiley Online Libr*. [https://onlinelibrary.wiley.com/doi/abs/10.1002/\(SICI\)1097-](https://onlinelibrary.wiley.com/doi/abs/10.1002/(SICI)1097-)

- 0290(19960520)50:4%3C365::AID-BIT3%3E3.0.CO;2-
 J?casa_token=ZmY23WZof74AAAAA:YIel2cEXCQ1aSBL8njUbxG4atUTbTmT7zx9Iq
 pSspXKUabfSU-t7pDiyMNesMw1ieZgk4wn97U-eZw. Accessed June 5, 2020.
177. Mi F, Kuan C, Shyu S, Lee S, Polymers SC-C, 2000 undefined. The study of gelation kinetics and chain-relaxation properties of glutaraldehyde-cross-linked chitosan gel and their effects on microspheres preparation and. *Elsevier*.
https://www.sciencedirect.com/science/article/pii/S0144861799001046?casa_token=Ysed7In8ZUwAAAAA:j40W6OM6mJqsNI6XQ8Bruxkj9BpG00s-APKYQbbJdd1pKMWutL-nQCvnbtlZra0-W_ZI_D00hA. Accessed June 5, 2020.
 178. Rödling L, Schwedhelm I, Kraus S, Bieback K, Hansmann J, Lee-Thedieck C. 3D models of the hematopoietic stem cell niche under steady-state and active conditions. *Sci Rep*. 2017;7(1). doi:10.1038/s41598-017-04808-0
 179. Ashton RS, Banerjee A, Punyani S, Schaffer D V., Kane RS. Scaffolds based on degradable alginate hydrogels and poly(lactide-co-glycolide) microspheres for stem cell culture. *Biomaterials*. 2007;28(36):5518-5525. doi:10.1016/j.biomaterials.2007.08.038
 180. Khetan S, Guvendiren M, Legant WR, Cohen DM, Chen CS, Burdick JA. Degradation-mediated cellular traction directs stem cell fate in covalently crosslinked three-dimensional hydrogels. *Nat Mater*. 2013;12(5):458-465. doi:10.1038/nmat3586
 181. Saito N, Okada T, Horiuchi H, et al. A biodegradable polymer as a cytokine delivery system for inducing bone formation. *Nat Biotechnol*. 2001;19(4):332-335. doi:10.1038/86715
 182. West JL, Hubbell JA. Polymeric biomaterials with degradation sites for proteases involved in cell migration. *Macromolecules*. 1999;32(1):241-244. doi:10.1021/ma981296k
 183. Kloxin AM, Kasko AM, Salinas CN, Anseth KS. Photodegradable hydrogels for dynamic tuning of physical and chemical properties. *Science (80-)*. 2009;324(5923):59-63. doi:10.1126/science.1169494
 184. Makadia HK, Siegel SJ. Poly Lactic-co-Glycolic Acid (PLGA) as biodegradable controlled drug delivery carrier. *Polymers (Basel)*. 2011;3(3):1377-1397. doi:10.3390/polym3031377
 185. Atala A, Mooney D. *Synthetic Biodegradable Polymer Scaffolds*.; 1997.
<https://books.google.com/books?hl=en&lr=&id=i2VJjcPJ2jYC&oi=fnd&pg=PR9&dq=+S>

- ynthetic+biodegradable+polymer+scaffolds.+Boston:+Birkhäuser:+1997.+p.+8395.&ots=HznuIKjEhx&sig=wc-A8dSwDI9wWiu4CQpfF8bNOrw. Accessed May 4, 2020.
186. Mann B, Schmedlen R, Biomaterials JW-, 2001 undefined. Tethered-TGF- β increases extracellular matrix production of vascular smooth muscle cells. *Elsevier*. https://www.sciencedirect.com/science/article/pii/S0142961200001964?casa_token=KLT4DH04tR4AAAAA:4q6XVSPqBFld49K7h1erNRMNMROBkFR9uoDpSTZTNQHVVQ0js-1bBwiiar9ADvFdV6vA4v3ibQ. Accessed May 4, 2020.
 187. Lee KY, Mooney DJ. Alginate: Properties and biomedical applications. *Prog Polym Sci*. 2012;37(1):106-126. doi:10.1016/j.progpolymsci.2011.06.003
 188. Sleeboom JFF, Eslami Amirabadi H, Nair P, Sahlgren CM, den Toonder MJM. Metastasis in context: modeling the tumor microenvironment with cancer-on-a-chip approaches. *Dis Model Mech*. 2018;11(3). doi:10.1242/dmm.033100
 189. Tirella A, La Marca M, Brace LA, Mattei G, Aylott JW, Ahluwalia A. Nano-in-micro self-reporting hydrogel constructs. *J Biomed Nanotechnol*. 2014;11(8):1401-1417. doi:10.1166/jbn.2015.2085
 190. Harrington H, Rose FRAJ, Aylott JW, Ghaemmaghami AM. Self-reporting scaffolds for 3-dimensional cell culture. *J Vis Exp*. 2013;(81):50608. doi:10.3791/50608
 191. Huch M, Koo BK. Modeling mouse and human development using organoid cultures. *Dev*. 2015;142(18):3113-3125. doi:10.1242/dev.118570
 192. de Souza N. *Organoids*.; 2018. doi:10.1038/nmeth.4576
 193. Yin X, Mead BE, Safaei H, Langer R, Karp JM, Levy O. Engineering Stem Cell Organoids. *Cell Stem Cell*. 2016;18(1):25-38. doi:10.1016/j.stem.2015.12.005
 194. Barker N, Bartfeld S, Clevers H. Tissue-resident adult stem cell populations of rapidly self-renewing organs. *Cell Stem Cell*. 2010;7(6):656-670. doi:10.1016/j.stem.2010.11.016
 195. McCracken KW, Catá EM, Crawford CM, et al. Modelling human development and disease in pluripotent stem-cell-derived gastric organoids. *Nature*. 2014;516(7531):400-404. doi:10.1038/nature13863
 196. Spence JR, Mayhew CN, Rankin SA, et al. Directed differentiation of human pluripotent

- stem cells into intestinal tissue in vitro. *Nature*. 2011;470(7332):105-110. doi:10.1038/nature09691
197. Antonica F, Kasprzyk DF, Opitz R, et al. Generation of functional thyroid from embryonic stem cells. *Nature*. 2012;491(7422):66-71. doi:10.1038/nature11525
198. Whitesides GM. The origins and the future of microfluidics. *Nature*. 2006;442(7101):368-373. doi:10.1038/nature05058
199. Wu Q, Liu J, Wang X, et al. Organ-on-a-chip: Recent breakthroughs and future prospects. *Biomed Eng Online*. 2020;19(1):1-19. doi:10.1186/s12938-020-0752-0
200. Zhang B, Korolj A, Lai BFL, Radisic M. Advances in organ-on-a-chip engineering. *Nat Rev Mater*. 2018;3(8):257-278. doi:10.1038/s41578-018-0034-7
201. Hon JDC, Singh B, Sahin A, et al. Breast cancer molecular subtypes: from TNBC to QNBC. *Am J Cancer Res*. 2016;6(9):1864-1872. <http://www.ncbi.nlm.nih.gov/pmc/articles/PMC5043099/>.
202. Li YC, Lin MW, Yen MH, et al. Programmable Laser-Assisted Surface Microfabrication on a Poly(Vinyl Alcohol)-Coated Glass Chip with Self-Changing Cell Adhesivity for Heterotypic Cell Patterning. *ACS Appl Mater Interfaces*. 2015;7(40):22322-22332. doi:10.1021/acsami.5b05978
203. Harris SG, Shuler ML. Growth of endothelial cells on microfabricated silicon nitride membranes for an In Vitro model of the blood-brain barrier. *Biotechnol Bioprocess Eng*. 2003;8(4):246-251. doi:10.1007/BF02942273
204. Zhang B, Montgomery M, Chamberlain MD, et al. Biodegradable scaffold with built-in vasculature for organ-on-a-chip engineering and direct surgical anastomosis. *Nat Mater*. 2016;15(6):669-678. doi:10.1038/nmat4570
205. Miller JS, Stevens KR, Yang MT, et al. Rapid casting of patterned vascular networks for perfusable engineered three-dimensional tissues. *Nat Mater*. 2012;11(9):768-774. doi:10.1038/nmat3357
206. Peel S, Corrigan AM, Ehrhardt B, et al. Introducing an automated high content confocal imaging approach for Organs-on-Chips. *Lab Chip*. 2019;19(3):410-421. doi:10.1039/c8lc00829a

207. Maoz BM, Herland A, Henry OYF, et al. Organs-on-Chips with combined multi-electrode array and transepithelial electrical resistance measurement capabilities. *Lab Chip*. 2017;17(13):2294-2302. doi:10.1039/c7lc00412e
208. Huh D, Matthews BD, Mammoto A, Montoya-Zavala M, Yuan Hsin H, Ingber DE. Reconstituting organ-level lung functions on a chip. *Science* (80-). 2010;328(5986):1662-1668. doi:10.1126/science.1188302
209. Ronaldson-Bouchard K, Vunjak-Novakovic G. Cell Stem Cell Review Organs-on-a-Chip: A Fast Track for Engineered Human Tissues in Drug Development. *Stem Cell*. 2018;22:310-324. doi:10.1016/j.stem.2018.02.011
210. Zhang YS, Aleman J, Arneri A, et al. From Cardiac Tissue Engineering to Heart-on-a-Chip: Beating Challenges. *Biomed Mater*. 2015;10(3):034006. doi:10.1088/1748-6041/10/3/034006
211. Badea MA, Balas M, Dinischiotu A. Biological properties and development of hypoxia in a breast cancer 3D model generated by hanging drop technique. *Cell Biochem Biophys*. 2022;80(1):63-73. doi:10.1007/S12013-021-00982-1/FIGURES/3
212. Zhao L, Xiu J, Liu Y, et al. A 3D Printed Hanging Drop Dropper for Tumor Spheroids Analysis Without Recovery. *Sci Reports 2019 91*. 2019;9(1):1-14. doi:10.1038/s41598-019-56241-0
213. Hofmann S, Cohen-Harazi R, Maizels Y, Koman I. Patient-derived tumor spheroid cultures as a promising tool to assist personalized therapeutic decisions in breast cancer. *Transl Cancer Res*. 2022;11(1):134-147. doi:10.21037/TCR-21-1577/COIF
214. Leonard F, Godin B. 3D in vitro model for breast cancer research using magnetic levitation and bioprinting method. *Methods Mol Biol*. 2016;1406:239. doi:10.1007/978-1-4939-3444-7_21
215. Valdoz JC, Johnson BC, Jacobs DJ, et al. The ECM: To Scaffold, or Not to Scaffold, That Is the Question. *Int J Mol Sci*. 2021;22(23). doi:10.3390/IJMS222312690
216. Li Y, Khuu N, Prince E, et al. Matrix Stiffness-Regulated Growth of Breast Tumor Spheroids and Their Response to Chemotherapy. *Biomacromolecules*. 2021;22(2):419-429. doi:10.1021/ACS.BIOMAC.0C01287/SUPPL_FILE/BM0C01287_SI_001.PDF

217. Sawicki LA, Ovadia EM, Pradhan L, et al. Tunable synthetic extracellular matrices to investigate breast cancer response to biophysical and biochemical cues. *APL Bioeng.* 2019;3(1):016101. doi:10.1063/1.5064596
218. Ham SL, Thakuri PS, Plaster M, et al. Three-dimensional tumor model mimics stromal - breast cancer cells signaling. *Oncotarget.* 2017;9(1):249-267. doi:10.18632/ONCOTARGET.22922
219. Singh S, Ray LA, Shahi Thakuri P, et al. Organotypic breast tumor model elucidates dynamic remodeling of tumor microenvironment. *Biomaterials.* 2020;238:119853-119853. doi:10.1016/J.BIOMATERIALS.2020.119853
220. Jiang T, Munguia-Lopez JG, Flores-Torres S, et al. Directing the Self-assembly of Tumour Spheroids by Bioprinting Cellular Heterogeneous Models within Alginate/Gelatin Hydrogels. *Sci Rep.* 2017;7(1). doi:10.1038/S41598-017-04691-9
221. Lugo-Cintrón KM, Gong MM, Ayuso JM, et al. Breast Fibroblasts and ECM Components Modulate Breast Cancer Cell Migration through the Secretion of MMPs in a 3D Microfluidic Co-Culture Model. *Cancers 2020, Vol 12, Page 1173.* 2020;12(5):1173. doi:10.3390/CANCERS12051173
222. Nagaraju S, Truong D, Mouneimne G, Nikkhah M. Microfluidic Tumor–Vascular Model to Study Breast Cancer Cell Invasion and Intravasation. *Adv Healthc Mater.* 2018;7(9). doi:10.1002/ADHM.201701257
223. Bersini S, Jeon JS, Dubini G, et al. A microfluidic 3D in vitro model for specificity of breast cancer metastasis to bone. *Biomaterials.* 2014;35(8):2454-2461. doi:10.1016/j.biomaterials.2013.11.050
224. Zervantonakis IK, Hughes-Alford SK, Charest JL, Condeelis JS, Gertler FB, Kamm RD. Three-dimensional microfluidic model for tumor cell intravasation and endothelial barrier function. *Proc Natl Acad Sci U S A.* 2012;109(34):13515-13520. doi:10.1073/PNAS.1210182109/SUPPL_FILE/SM01.MOV
225. Coecke S, Balls M, Bowe G, et al. Guidance on good cell culture practice: A Report of the Second ECVAM Task Force on good cell culture practice. *ATLA Altern to Lab Anim.* 2005;33(3):261-287. doi:10.1177/026119290503300313

226. Pamies D, Bal-Price A, Simeonov A, et al. Good cell culture practice for stem cells & stem-cell-derived models. In: *Altex*. Vol 34. Elsevier GmbH; 2017:95-132. doi:10.14573/altex.1607121
227. Pamies D, Bal-Price A, Chesné C, et al. Advanced Good Cell Culture Practice for human primary, stem cell-derived and organoid models as well as microphysiological systems. *ALTEX*. 2018;35(3):353-378. doi:10.14573/altex.1710081
228. Organisation for Economic Co-operation and Development., OECD-iLibrary - York University. *Guidance Document on Good In Vitro Method Practices (GIVIMP)*. OECD Publishing; 2018. doi:10.1787/9789264304796-en
229. Maria H, Thomas H. European Centre for the Validation of Alternative Methods (ECVAM): its role and contribution. 2008.
230. Pridgeon CS, Schlott C, Wong MW, et al. Innovative organotypic in vitro models for safety assessment: aligning with regulatory requirements and understanding models of the heart, skin, and liver as paradigms. *Arch Toxicol*. 2018;92(2):557-569. doi:10.1007/s00204-018-2152-9
231. Hartung T, de Vries R, Hoffmann S, et al. Toward good in vitro reporting standards. *ALTEX*. 2019;36(1):3-17. doi:10.14573/altex.1812191

Thesis context – Chapter 2

Breast tissue microenvironment is dynamic and undergoes changes during puberty, lactation and diseased states such as breast cancer. Physical and chemical or physico-chemical factors of tumour microenvironment also vary as the tumour progresses, however their role in breast tumour phenotypes like stemness is not yet known. **Chapter 2 - “Role of stiffness and physico-chemical properties of tumour microenvironment on breast cancer cell stemness”** is written in a research article format and explores impact of selected physico-chemical microenvironmental factors defined in Chapter 1 (ECM/matrix stiffness, ECM composition, tissue pH, and interstitial fluid flow) on breast cancer cell phenotypes. For this purpose, precise control over these factors was achieved combining them using tissue engineering methods introduced in Chapter 1. Scaffold based model was used to culture breast cancer cells in varying tissue stiffness mimicking normal breast and tumour tissue using alginate-gelatin hydrogels. These hydrogels were incubated within a milli fluidic system to introduce interstitial fluid flow within the model. Media pH was adjusted to match that of normal and tumour tissue. Ultimately this combined model was used to study impact of physico-chemical factors on primary breast tumour phenotypes- cell proliferation, cell aggregation and breast cancer stemness. The Chapter explores use of 3D *in vitro* models in engineering complex microenvironmental cues and to use such models for monitoring disease phenotypes.

Chapter 2. Role of stiffness and physico-chemical properties of tumour microenvironment on breast cancer cell stemness

Lekha Shah¹, Ayşe Latif¹, Kaye J. Williams¹, Annalisa Tirella^{1,2,*}

¹ Division of Pharmacy and Optometry, Faculty of Biology, Medicine and Health, University of Manchester, Oxford Road, M13 9PL, Manchester, United Kingdom

² BIOTech - Center for Biomedical Technologies, Department of Industrial Engineering, University of Trento, Trento, Italy

Submitted and with reviewers

*Corresponding author: BIOTech Center for Biomedical technologies, University of Trento, Via delle Regole 101, Trento 38123, Italy; annalisa.tirella@unitn.it

Abstract

Several physico-chemical properties of the breast tumour microenvironment (TME) are dysregulated during tumour progression, such as tissue stiffness, extracellular pH and interstitial fluid flow. Traditional cell culture models and animal models, although being valid models, do not provide sufficient control over these physical properties, such as tissue stiffness and composition, to further examine cause-effect relationships between them and cancer cells. Breast cancer stem cells (B-CSCs), a dynamic population within the tumour milieu, are known to affect tumour progression, metastasis and therapeutic resistance. With their emerging importance in disease physiology, it remains essential to study interactions of above-mentioned physico-chemical variables on B-CSC population.

In this work, 3D *in vitro* models with known physico-chemical properties were used to mimic normal breast and tumour pathophysiology. In particular, matrix stiffness, extracellular pH, and perfusion were controlled to study changes in proliferation, morphology and B-CSC population in two separate breast cancer cell lines (i.e. MCF-7, MDA-MB 231). Alginate-gelatin hydrogels varying in matrix stiffness (2 kPa-10 kPa) and adhesion ligand (gelatin) were perfused (500 μ L/min) up to 7 days. Physiological (pH 7.4) and tumorigenic (pH 6.5) media were also used to culture hydrogels and mimic changes in extracellular pH. We found that both cell lines have distinct responses to changes in physico-chemical factors in terms of proliferation, cell aggregates size and morphology. Most importantly, stiff and dense matrix (10 kPa) and acidic pH 6.5 impact on B-CSC dynamics by increasing stem cell content in both the tested cell lines.

Keywords: Breast cancer stem cells, tumour micro-environment, 3D *in vitro* models, matrix stiffness, perfusion models.

1. Introduction

Remodelling of the extracellular matrix (ECM) by cancer cells affects tumour progression and metastasis ¹. Conversely, variation of ECM properties, such as matrix stiffness and composition, extracellular pH (pHe) and other physico-chemical properties have also been recognised to impact tumorigenesis and metastatic formation ². To better understand changes within the tumour

microenvironment (TME), and how these contribute to tumour development, new and more comprehensive models are required.

Breast cancer stem cells (B-CSCs) are a dynamic tumour initiating cell population within the tumour milieu, with a key role in tumorigenesis, metastasis, recurrence, as well as therapeutic resistance³⁻⁶. Recently, reports on interactions of CSCs and the TME are gaining traction but yet remain poorly understood^{7,8}. In terms of characterisation of B-CSCs, Al-Hajj et al. firstly reported that patient-derived B-CSCs showed a CD44⁺/CD24^{-/low} sub-population with high tumour initiating capacity and self-renewal. Additionally this subpopulation was able to rebuild the heterogeneity of the original tumour in immunocompromised mice⁹. CD44 is a transmembrane glycoprotein with its main ligand as hyaluronic acid. Its role has been implicated in cell proliferation, increased cell survival¹⁰, and is also expressed in circulating tumour cells (CTCs) that have metastasis initiating capacity^{11,12}. Whereas, CD24 is a glycosylated membrane anchored protein mainly present on immune cells¹³. Later studies identified another marker, aldehyde dehydrogenase (ALDH), associated with stem progenitor cells, found in both normal breast as well as cancer tissue¹⁴. Co-localisation analysis of immunofluorescence stained breast cancer tissues reported that the CD44⁺/CD24⁻ B-CSC subpopulation is distinct from the ALDH⁺ one, with minimal overlap among these two groups¹⁵. Similarly, comparison of gene expression showed mainly reciprocal patterns with either mesenchymal or epithelial characteristics. The CD44⁺/CD24⁻ subpopulation had enriched mesenchymal markers like vimentin, matrix metalloproteinase-9 (MMP-9) and Zinc finger E-box-binding homeobox-1 (ZEB1), and exhibited quiescent mesenchymal phenotype further termed as mesenchymal type-cancer stem cells (M-CSCs). In contrast, the ALDH⁺ subpopulation had higher expression of epithelial associated markers like E-cadherin, claudins and occludins, which presented a proliferative epithelial phenotype, termed as epithelial type cancer stem cells (E-CSCs)¹⁵. Further, B-CSCs show plasticity and transition between these epithelial and mesenchymal states¹⁵. It remains important to understand if interactions with TME can affect B-CSCs and their plasticity.

Physico-chemical properties of TME like matrix stiffness, density, matrix composition, pHe and interstitial fluid flow are known to be dysregulated, affecting cancer risk, tumour progression and therapeutic efficiency^{16,17}. Most solid tumours like breast cancer have increased stiffness than the adjoining normal tissue, as well as a state of fibrosis known as ‘desmoplasia’¹⁸. Compression

analysis of *ex vivo* breast cancer samples showed that average elastic modulus of normal breast tissue is approximately 3 kPa, whereas for DCIS (Ductal carcinoma in situ) it is 16 kPa, proving a three to six-fold increase in stiffness for malignant tumours¹⁹. Atomic force microscopy (AFM) analysis of breast tumours observed an average of four-fold increase for invasive lesions compared to normal tissue (normal tissue 0.4-1 kPa; invasive ductal carcinoma (IDC) 2-4 kPa). Same study reported that the tissue stiffness was heterogenous throughout the tumour tissue and that increase in stiffness and collagen deposition is correlated to breast cancer stage progression from DCIS to IDC²⁰. Another factor, extracellular tumour acidosis, is caused by increased aerobic glycolysis in the TME. CEST MRI imaging of breast tumours in transgenic mice models suggest that the pHe values are in the range of 6.5-6.9 when compared to normal breast tissue pHe (typically 7.2-7.5)^{21,22}. The pHe values throughout the breast tumour are heterogenous with the core being more acidic than the tumour boundary²¹. Decrease of pHe has been linked to tumour aggressiveness²³, angiogenesis²⁴, and disruption of the cellular circadian clock²⁵. Therapies to re-equilibrate pHe within the TME were shown to inhibit spontaneous metastases in metastatic breast cancer mouse model²⁶. Interstitial fluid flow, which is a convective transport of fluid through the ECM, has effects on tissue morphogenesis, pathogenesis as well as cell mechanobiology^{27,28}. The heterogenous nature of interstitial flow makes it difficult to determine exact variations of interstitial fluid flow in the microenvironment *in vivo*, but most studies share a common conclusion that higher flow velocities are present at the tumour edge when compared to the tumour core²⁸. Mathematical models coupled with experimental data report interstitial fluid flow values in the range of 0.1 - 4 $\mu\text{m/s}$ ^{29,30}. Advanced *in vitro* models that mimic flow velocities are currently used to demonstrate its influence on cellular polarisation, proliferation, and migration. In terms of breast cancer cells, interstitial fluid flow with values such as 0.2 $\mu\text{m/s}$ ³¹ and 10 $\mu\text{m/s}$ ³² increased migration speed and invasion in three-dimensional (3D) matrices when compared to static models (without interstitial flow).

Previously, studies have focussed on factors that affect B-CSCs plasticity where expression of certain microRNAs (MIR) was associated with either of the B-CSCs state (mir-9, mir-100 is linked with M-CSC whereas mir-200, mir-93 is associated with E-CSC)³³⁻³⁵. A plausible role of the microenvironment in regulating these microRNAs and hence the B-CSC states has been suggested. However, their exact role and individual contribution is yet to be examined. Particularly, the role of physico-chemical properties on B-CSC population have not yet been deciphered due to the lack

of appropriate models. Traditional models lack physiological complexity whereas animal models provide insufficient control over these properties³⁶. To study effects of these physico-chemical cues, new approaches are required to model the TME in 3D with the required level of control over ECM properties (composition, stiffness, pH, interstitial flow)³⁷. We herein describe a new *in vitro* system to mimic variations of breast tissue homeostasis in 3D and to understand cause-effect relationship of these important physico-chemical cues on B-CSCs dynamics and phenotypes. In this work, a small library of hydrogels (alginate-gelatin) with known matrix compressive elastic moduli, varying from normal breast tissue (~2 kPa, soft) to malignant breast tissue (~10 kPa, stiff)¹⁹ was used to encapsulate two breast cancer cell lines: luminal and lower grade cell line MCF-7, and higher grade triple negative (TNBC) cell line MDA-MB-231. As alginate lacks in cell-adhesive domains, gelatin was included in hydrogel formulation to promote cell-matrix interactions and to mimic increased collagen deposition which is observed in tumours. Whereas interstitial fluid flow/perfusion was mimicked with Quasi Vivo milli-fluidic system. Variations of hydrogel stiffness, pH and fluid flow were modelled *in vitro* to mimic the breast TME at different stages of progression. The effect of TME variables (matrix stiffness, matrix composition, pH and fluid flow) was evaluated on cell proliferation, morphology and B-CSCs markers (CD44, CD24, Vimentin, E-cadherin and ALDH), as cellular heterogeneity and plasticity of B-CSCs could impact on tumour progression and specifically in forming metastases at distant sites such as bone^{4,34}.

The proposed *in vitro* models allowed independent control of TME variables to study their impact on breast cancer phenotypes. Through these models we found direct impact of physico-chemical cues on B-CSCs dynamics for the first time. These models could further open new ways of monitoring disease phenotypes, from early onset to metastatic progression, and as testing platforms for effective targeting of specific phenotypes in presence of relevant TME cues.

2. Materials and methods

2.1 Alginate-gelatin hydrogel preparation

HEPES buffered saline (HBS) was prepared by dissolving 20 mM HEPES (H4034, Sigma Aldrich UK) and 150 mM NaCl in deionized water. High-mannuronic sodium alginate (G/M ratio of 0.7, Pro-Alg, Chile) powder was reconstituted in HBS (overnight, Room temperature/RT) at a

concentration of 3% and 6% (w/v) on a shaker. Alginate solutions (aq.) were sterile filtered using a 0.22 μ m Polyethersulfone (PES) filter (SLGP033RS, MERCK) prior to cell culture use. Similarly, gelatin type A (G1890, Sigma-Aldrich, UK) was hydrated (2h, 37°C) in HBS at a concentration of 2% and 6% (w/v); and further sterile filtered with a 0.45 μ m Polyvinylidene Difluoride (PVDF) filter (SLHV033RS, MERCK) prior to use. A small library of alginate-gelatin solutions were prepared mixing different concentrations of alginate and gelatin solutions in 1:1 ratio (5 min, RT) as listed in Table 1.

Calcium chloride (CaCl₂, C/1400/53, Fischer scientific, UK) was prepared in deionized water at concentrations of 100 mM, 200 mM and 300 mM. Each solution was sterile filtered prior use (0.22 μ m PES filter) and stored at 4°C. Each alginate-gelatin solution was ionically crosslinked with CaCl₂ solutions (aq.) to form a small library of hydrogels (Table 1).

2.2 Unconfined compression tests: hydrogel stiffness

Compressive elastic moduli of hydrogels (from now on referred to as stiffness for simplicity) were determined by uniaxial compressive tests using the Texture Analyzer (TA.XT plus, Stable microsystems) equipped with 5N load cell. Compressive tests were performed using a zero-stress initial condition (i.e. configuration with no contact between the sample and the probe)³⁸. Briefly, cylindrically shaped hydrogels (Section S1) were compressed with a constant speed (0.05 mm/sec). A stress-strain plot was obtained for each samples, and the slope within the 0.05 strain interval was used to calculate the compressive modulus (kPa) of hydrogels (Section S2)^{38,39}. The measurements were performed using at least n=4 (technical replicate) samples for each group and N=2 independent and separate experiments or biological replicate. (From further on, ‘n’ will be represented as technical replicate whereas ‘N’ as biological replicate) All data are represented as mean \pm standard deviation (st.dev).

Table 1: Alginate-based hydrogels composition. A small library of alginate-hydrogels (n=18) was obtained and mechanical properties (i.e. compression modulus) further measured. Samples were physically crosslinked to control stiffness (RT, 10 min) using different concentration of Ca²⁺ (using calcium chloride solutions at concentrations of 100 mM, 200 mM and 300 mM). Alginate-hydrogels stiffness is proportional to crosslinking density. Protein content (i.e.

gelatin concentration) and density (i.e. total polymers concentration) are classified as high, medium and low. Of note: nomenclature (sample ID) for alginate-hydrogels represents the different final concentration of alginate and gelatin.

| Alginate concentration | Gelatin concentration | Protein content | Density | | Sample ID |
|-------------------------------|------------------------------|------------------------|----------------|--------|------------------|
| % (w/v) | % (w/v) | | % (w/v) | | |
| 1.5 | 1 | Low | 2.5 | Low | A1.5G1 |
| 1.5 | 2 | Medium | 3.5 | Low | A1.5G2 |
| 1.5 | 3 | High | 4.5 | Medium | A1.5G3 |
| 3 | 1 | Low | 4 | Medium | A3G1 |
| 3 | 2 | Medium | 5 | High | A3G2 |
| 3 | 3 | High | 6 | High | A3G3 |

2.3 Cell culture

2.3.1 Cell lines

Human breast adenocarcinoma cell lines MCF7 and MDA-MB-231 were selected for this study. Prior use, both cell lines were authenticated by European Collection of Authenticated Cell Cultures (ECACC, operated by Public Health England). Cells were routinely cultured in complete Dulbecco's Modified Eagle Medium (DMEM, D6546, Sigma-Aldrich, UK) media supplemented with 1% (v/v) L-glutamine (G7513, Sigma-Aldrich, UK), 10% (v/v) Fetal Bovine Serum (FBS) (F9665, Sigma-Aldrich, UK) and 1% (v/v) penicillin streptomycin (P4333). The cell lines were tested negative for mycoplasma contamination by Mycoalert mycoplasma detection kit (Lonza). Cells were discarded after they reached passage 25 for MDA-MB-231 and passage 50 for MCF-7.

2.3.2 3D *in vitro* model: Alginate-gelatin hydrogel beads

Four different hydrogels were selected based on their stiffness (i.e. soft, stiff) and gelatin concentration (i.e. low and high adhesive ligand content), and further used for 3D cell culture studies. Selected soft hydrogels were A1.5G1, A1.5G3 (crosslinked using 100 mM CaCl₂) and stiff hydrogels were A3G1, A3G3 (crosslinked using 300 mM CaCl₂). Briefly, cells were detached using trypsin for 3 minutes at 37°C and centrifuged at 600g for 3 minutes. Cell pellets were gently re-suspended in the hydrogel precursor solution (prepared as previously described) using a

MICROMAN E viscous pipette (M1000E, Gilson, UK) ensuring a single cell suspension. The cell-suspension was transferred in a sterile 1 mL syringe equipped with a 28G needle, and single droplets were ejected in a CaCl₂ solution and incubated (10 min, RT) allowing gelation to obtain spherical hydrogel beads (Figure 1C). Each bead consisted of approximately 1×10⁵ cells. To facilitate easy washing, hydrogel beads were collected using a sterile cell strainer (CSS-010-040, Biofil, UK) previously immersed in the CaCl₂ solution, and that was used to transfer the beads to HBS solution for washing⁴⁰. After two washes for 5 minutes each, the beads were finally transferred to complete cell culture media (Figure S1). Hydrogel beads were either cultured in pH 7.4 or pH 6.5 complete culture media (Section S3)

2.3.3 3D dynamic model: Quasi vivo system

Quasi vivo system (QV500) was used to mimic interstitial fluid flow and perfusion within the hydrogels. Due to complex tissue architecture *in vivo*, there is multidirectional flow from nearby blood vessels to draining lymph vessels. For the purposes of this model, we mimicked unidirectional flow from a single blood vessel to single lymph vessel with help of QV500 system. Additionally, the complex architecture of hydrogel (similar to ECM) in which the cells are encapsulated may render multidirectionality to the fluid flow, making the system more complex. The quasi vivo QV500 system (Kirkstall, UK) equipped with the Watson-Marlow 202U peristaltic pump was assembled following supplier's instruction (Fig 1G). Prior to use, the QV500 PDMS chambers along with the reservoir, tubing and luer connectors were sterilised with pure ethanol (20 min, RT) by perfusing the whole system (flow rate 2 mL/min). After 20 min, ethanol solution was removed and the system was perfused with 1× Phosphate buffered saline (PBS) sterile solution (1h, RT) and finally with complete cell culture media (overnight, 37°C, 5% CO₂). Cells embedded in hydrogel beads were transferred into individual chamber connected to their respective reservoir system (Figure 1G). Each experiment was performed with the system placed inside the incubator and with a flow rate of 500 µL/min⁴¹. The rate was decided based on previous studies that modelled flow velocities at different flow rates in QV500⁴². As per the mathematical modelling, 500 µL/min translates to velocity of 1.4 µm/s at the bottom of the chamber which is well within the physiological range (0.1- 4 µm/sec).

2.4 Cell proliferation and viability

2.5.1 Cell proliferation: Alamar blue assay

Deep Blue Cell Viability™ Kit (424701, Biolegend) was used to analyse cell proliferation at different time points (i.e. day(s) 1, 4, 7 and 14) without disrupting samples. A 10% (v/v) deep blue solution was diluted in complete cell culture media (pH 7.4) and added to each sample (refer to section S4 for additional information on sample preparation). After 2 hours, 100 µL of samples were collected and read immediately using the Synergy-2 (Biotek) plate reader (Ex 530-570 nm / Em 590-620 nm). The intensity measurements at days 4, 7 and 14 were normalised with their respective reading at day 1, for each sample. The measurements are reported as mean ± st.dev. of three independent experiments (n=3/technical replicate, N=3/biological replicate) experiments for static conditions; and as average of three independent experiments for dynamic conditions (N=3).

2.5.3 Cell viability: Live/Dead assay

Calcein-AM and ethylene homodimer (Live/Dead cytotoxicity kit L3224, ThermoFischer scientific) were diluted in sterile PBS at a final concentration of 2 µM and 4 µM, respectively. Prior image acquisition, samples at day 7 and day 14 were incubated in the dark with this solution (40 min, RT). Images were acquired using the fluorescent inverted microscope (details reported in Section 2.10) using the objective 10×.

2.6 B-CSCs and EMT Marker expression: Flow cytometry

Marker expression (i.e. CD44, CD24, CD44v6, E-cadherin and vimentin) was analysed by flow cytometry (BD Fortessa X-20). Cells cultured in 2D tissue-culture plates (TCP) plates were used as control. At each time point, cells were washed with PBS 1× and incubated with cell dissociation buffer (13151014, Gibco, 10 min, RT) to avoid disruption of membrane bound proteins during cell detachment⁴³. Cells cultured in hydrogels were recovered by dissolution of alginate beads through addition of a calcium sequestering buffer (100 mM HEPES and 500 mM Trisodium citrate dehydrate in 1× PBS) as previously described by Rios de la Rosa et al.⁴⁴. For the preparation of samples to detect cell surface markers, cell pellet (600 g, 5 min, RT) was gently resuspended in blocking buffer (5% (v/v) FBS in 1× PBS) and incubated for 30 minutes on ice. For the detection

of intracellular markers (i.e. vimentin), samples were fixed with 4% paraformaldehyde (1004968350, Sigma-Aldrich, UK, 10 min, RT), followed by n=3 washes with 1× PBS, and a final permeabilization step with 0.1% w/v Saponin (47036, Sigma-Aldrich, UK) in blocking buffer (30 min, RT). All cells were then incubated on ice with primary antibody (45 min) and secondary antibodies (30 min) at concentrations described in Table 2. Finally, for dead cell exclusion during flow cytometry measurements, all cells were incubated with 1µg/mL of 4',6-diamidino-2-phenylindole (DAPI) solution in 1× PBS (5 min, RT), then washed with 1× PBS and resuspended in 1× PBS for further measurements.

FlowJo software (v10.8.0, BD) was used to analyse data, gate single live cells and obtain measurements on median fluorescence intensity (MFI) and number of cells positive for each marker. The median intensity of the marker was normalised by its respective isotype control for every sample and then plotted as an average of N=3 independent experiments (biological replicates).

Table 2: Antibody dilutions for isotype control, primary antibodies and secondary antibody for various markers

| Marker | Isotype control | Primary antibody | Secondary antibody |
|---------------|---|---|---|
| CD44 | APC Rat IgG2b, κ Isotype Ctrl (400611, BioLegend) | APC anti-mouse/human CD44 Antibody (103012, BioLegend), | N/A |
| Dilution | <u>1:800</u> | <u>1:800</u> | N/A |
| CD24 | Alexa Fluor® 488 Mouse IgG2a, κ Isotype Ctrl Antibody (400233, BioLegend) | Alexa Fluor® 488 anti-human CD24 Antibody (311108, BioLegend) | N/A |
| Dilution | <u>1:20</u> | <u>1:20</u> | N/A |
| CD44v6 | Mouse IgG1 Negative Control antibody (MCA928, Bio-Rad) | Mouse anti Human CD44v6 (MCA1730, Bio-Rad) | BV786 Rat Anti-Mouse IgG1, (742480, BD) |
| Dilution | <u>1:10</u> | <u>1:100</u> | <u>1:150</u> |

| | | | |
|------------|---|---|---|
| E-cadherin | Mouse IgG1, kappa monoclonal (ab170190, Abcam) | Mouse IgG1 anti human E-Cadherin antibody (ab1416, Abcam) | BV786 Rat Anti-Mouse IgG1, (742480, BD) |
| Dilution | <u>1:100</u> | <u>1:100</u> | <u>1:150</u> |
| Vimentin | Rat IgG2A APC Isotype control (IC006A, R&D systems) | APC Rat anti-human Vimentin (IC2105A, R&D systems) | N/A |
| Dilution | <u>1:10</u> | <u>1:20</u> | N/A |

2.7 ALDH expression: Aldefluor assay

Aldefluor assay (Stemcell Technologies) was used to measure ALDH expression, as per the supplier's instructions. Briefly, cells (1×10^6 cells/mL) suspended in Aldefluor buffer were treated with 5 μ L of ALDH substrate Bodipy-aminoacetaldehyde (BAAA) (45 min, 37°C). For negative control, half of this mix was simultaneously treated with 5 μ L of ALDH inhibitor DEAB (1.5 mM). To exclude dead cells from measurements, cells were incubated with 7-AAD (420403, Biolegend, 10 min, RT) prior to their assessment in BD Fortessa X-20 flow cytometer. The gates for ALDH⁺ cells were sorted based on the DEAB negative control of the respective sample. As per manufacturer's protocol, the data was gated on SSC vs ALDH-488 plot to catch small population of ALDH⁺ cells. The gates were finalised such that they contain <1% population in DEAB controls. The final ALDH⁺ population was calculated by subtracting percentage of cells positive in DEAB control from those in the sample. All data were analysed using FlowJo software (v10.8.0, BD)

2.8 Analysis of cell aggregates: size and shape

Live/dead images of cells in hydrogel beads were acquired using the fluorescent inverted microscope (details reported in Section 2.10) placing each hydrogel bead between a glass slide and coverslip for the acquisition of a single focus image. ImageJ (v1.52a) was used to identify and measure the diameter and circularity of cell aggregates (approx. 200 aggregates/condition). (Refer to Section S5)

2.9 Principal component analysis

Principal component analysis (PCA) was performed on EMT marker expression (Vimentin and E-cadherin) and stemness marker positivity (CD44⁺/CD24⁻ and ALDH⁺) obtained from cells cultured in different conditions (selected TME physico-chemical cues). The data was processed using PCA analysis function on Graphpad prism (v9.2.0). Two principal components (PC1 and PC2) from the obtained analysis were selected by Kaiser's rule (>1) and used to graph the PC score plot (PC1 vs PC2).

2.10 Image acquisition and analysis

Images were acquired using the fluorescent inverted microscope (Leica DMI6000, Leica Microsystems, UK) coupled with a 5.5 Neo sCMOS camera (Andor, UK). The μ Manager software (v.1.46, Vale Lab, UCSF, USA) was used to control both microscope and camera, as well as to capture images. For acquisitions, a dry 2 \times objective (PLAN 2.5 \times /0.07, Leica) dry 10 \times objective (PL 10 \times /0.3 PH1, Leica), a dry 20 \times objective (PL 20 \times /0.5 PH2, Leica). For Live/Dead images, filter cubes I3 (Ex/Em 450/515 nm) and N2.1 (Ex/Em 515/590 nm) were used to detect calcein (live cells) ethylene homodimer (dead cells), respectively. Z-stacks were acquired with a 20 μ m z-step, and all live/dead z-stack images were post-processed using ImageJ (v1.52a) for maximum intensity projection images and to remove background noise. Percentage of live and dead cells was calculated using maximum projections (n=10 images) for each sample and at each time point.

2.11 Statistical analysis

For cell proliferation, aggregate size and circularity, and flow cytometry expression data, significance among different conditions was analysed with one-way analysis of variance (ANOVA) and significance among stiffness of hydrogel groups was analysed with two-way ANOVA using GraphPad Prism v9.1.0. P-values were set at four different significance levels: $p < 0.05$ (* $p \leq 0.05$, ** $p \leq 0.01$, *** $p \leq 0.001$, **** $p \leq 0.0001$).

3. Results

3.1 Modelling biophysical and chemical cues *in vitro*

Biophysical and chemical cues of breast TME were engineered using bottom-up tissue engineering principles and controlling: matrix stiffness and composition, pH, and fluid flow (Figure 1A). Hydrogels with varying concentrations of alginate and gelatin (Table 1) were crosslinked with different concentrations of calcium chloride (100, 200 and 300 mM) and compressive moduli tested to match stiffnesses of human breast tissue during cancer progression. Compression tests (Figure 1B) on the small library of 18 hydrogels returned stiffnesses in the range of 1.8-10 kPa (Figure 1C, 1D). It was observed that stiffness increased proportionally with alginate and calcium chloride concentration, hence with crosslinking density. An increase was also measured proportional to gelatin concentration, hence to final polymer density, but to a smaller extent when compared to crosslinking density (Figure 1C, 1D). After this analysis, four hydrogels were selected to represent different combination of stiffness (soft, stiff), adhesion ligand (low, high) and density (low, high) to investigate the role of these independent parameters in human breast cancer cells (Table 3). Of note, variation of pH in the cell culture media did not impact on swelling behaviour of selected hydrogels up to 7 days (Figure S2).

MDA-MB-231 and MCF-7 cells were encapsulated in alginate-gelatin hydrogel beads as single cell suspension, at the initial concentration of 2 million cells/mL. As observed, the encapsulated cells were homogeneously distributed within the hydrogel beads (Figure 1E, F, G) in all selected hydrogels on Day 1 (data not shown). For dynamic culture or perfused models, hydrogel beads encapsulating cells were incubated in the QV500 chamber (Figure 1H) and connected with the experimental layout as shown in Figure 1I. The beads were confined within the chamber at the used flow rate of 500 $\mu\text{L}/\text{min}$ which translates to 1.4 $\mu\text{m}/\text{s}$ flow velocity at the bottom of the chamber. The total hydrogel volume used in one experiment to 500 $\mu\text{L}/\text{chamber}$.

Table 3. Adhesion ligand density, polymer concentration and stiffness of the four selected hydrogel groups

| Sample ID Crosslinking | Adhesion ligand content | Density | Stiffness |
|--|-------------------------|---------------------------------------|-----------------------------|
| Crosslinking solution: Calcium Chloride (CaCl ₂ , M) | Gelatin concentration | Total concentration of polymers | Compressive moduli (kPa) |

| | | | |
|---------------------------------|------|--------|------------|
| A1.5G1 0.1M CaCl ₂ | Low | Low | 1.8 ± 0.2 |
| A1.5G3 0.1M CaCl ₂ | High | Medium | 2.4 ± 0.1 |
| A3G1 0.3M CaCl ₂ | Low | Medium | 6.1 ± 0.2 |
| A3G3 0.3M CaCl ₂ | High | High | 10.1 ± 0.5 |

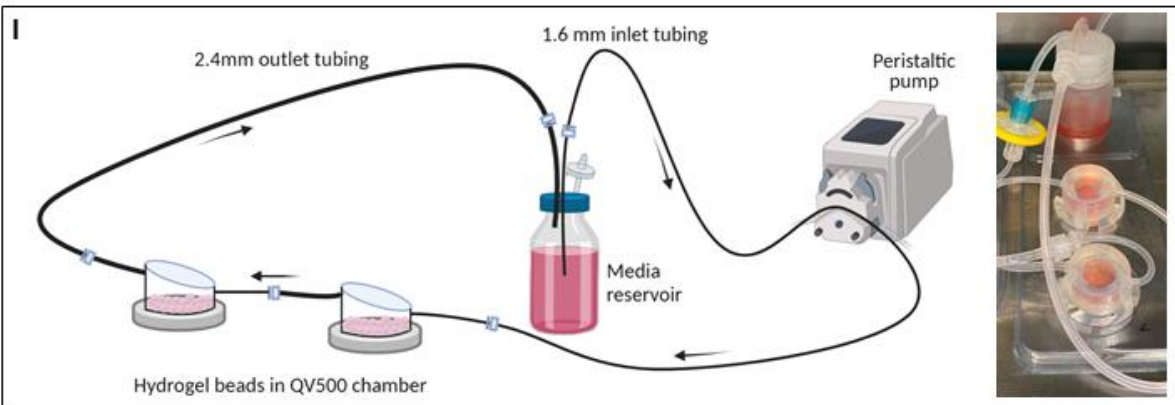
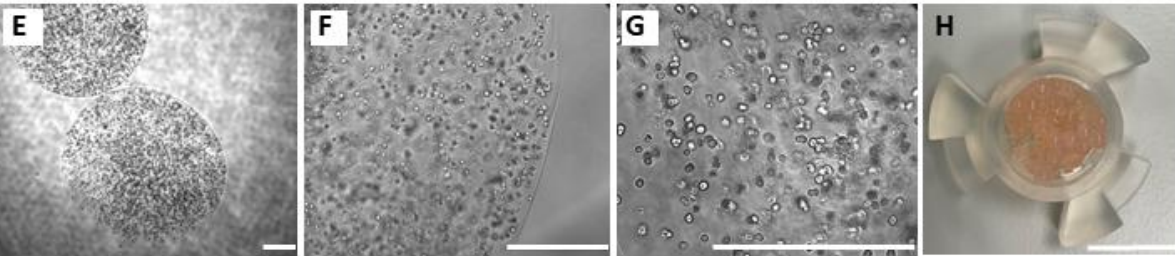
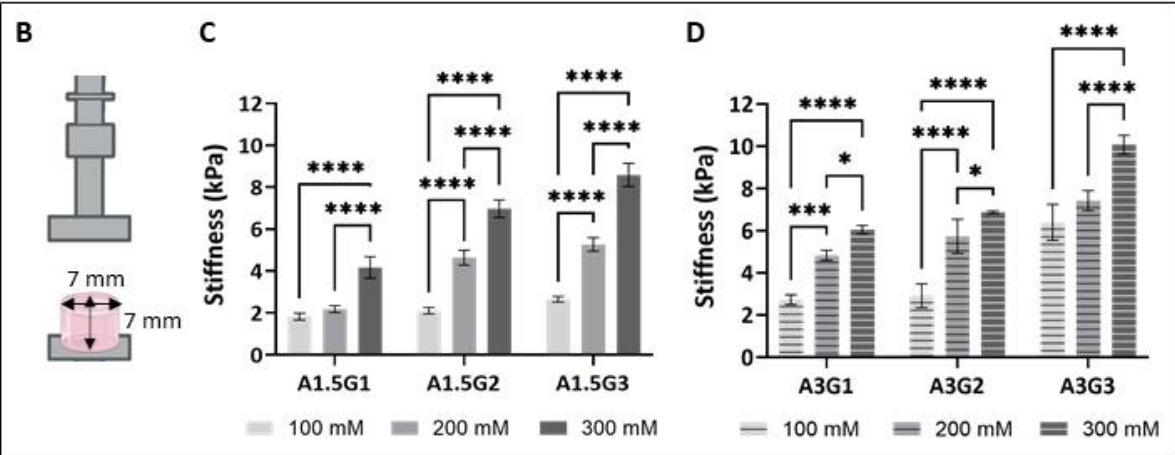
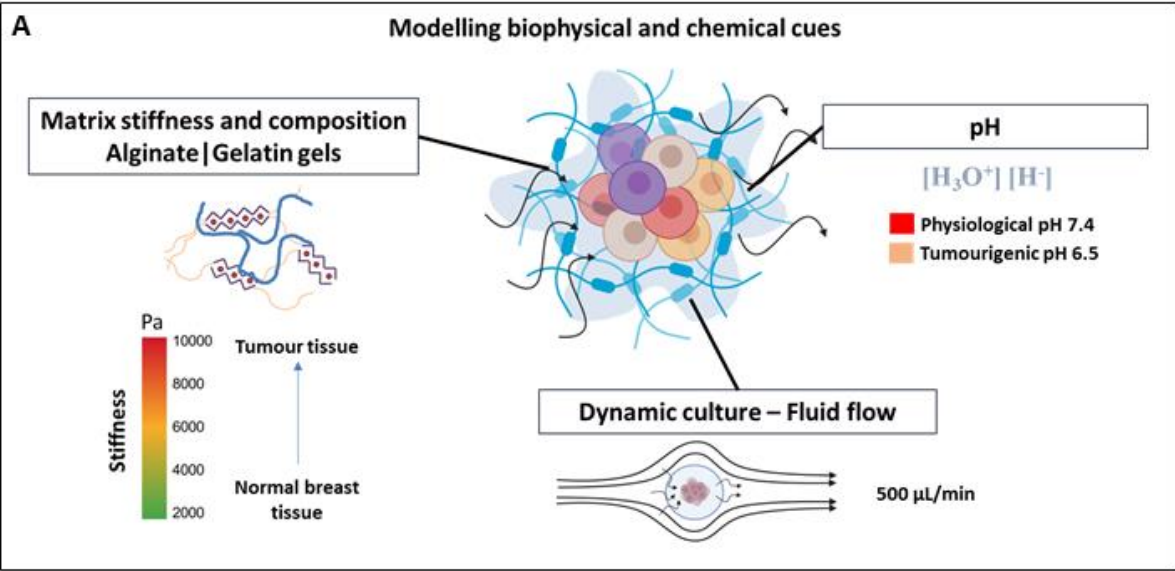


Figure 1: Representation of independent cues included in the 3D models. (A) Biophysical and chemical properties engineered in the in vitro model with varying matrix stiffness (1.8 to 10 kPa), pH (7.4 and 6.5), and fluid flow (500 μ L/min). (B-D) Mechanical properties: (B) Example of compressive test to measure hydrogels stiffness (kPa). Stiffness values of 1.5% w/v (C) and 3.0% w/v (D) alginate concentrations with varying gelatin concentrations (1% w/v and 3% w/v) and calcium chloride crosslinking solution (100 mM, 200 mM and 300 mM). Values are represented as mean of average \pm st.dev. of n=4 (technical replicate), N=2 independent experiments (biological replicate). (E-G) Examples of brightfield images of MDA-MB-231 cells encapsulated in hydrogels beads (scale bars 500 μ m) acquired with a 2 \times (E), 10 \times (F), and 20 \times (G) objective. (H) Perfusion system: hydrogel beads encapsulating cells cultured in QV-500 chamber (scale bar 10mm). (I) Schematic layout of QV500 chambers, 1.6 mm and 2.4 mm tubings, 30 mL media reservoir connected with peristaltic pump (left) along with actual image of the system (right).

3.2 MDA-MB-231 proliferation is less sensitive to varying biophysical cues than MCF-7

MCF-7 and MDA-MB-231 cells were cultured in selected hydrogels (Table 3) at either pH 7.4 or pH 6.5, with or without perfusion, for up to 14 days. To assess proliferation and cell growth, Alamar blue assay was used to measure cell metabolic activity at days 1, 4, 7 and 14 (Figure 2). Additionally, semi-quantitative assessment of cell viability was also performed by quantifying percentage of live and dead cells from images of Live/Dead assay at day 7 and day 14 (Figure S3-S6). Previous studies with alginate hydrogels have used variable end points to monitor cell growth ranging from day 3 to day 21⁴⁴⁻⁴⁶. Since we observed saturation of growth during day 7-14 interval in most groups, we stopped monitoring after day 14.

Cell proliferation data was represented as fold change relative to day 1. In static conditions and at physiological pH, MCF-7 cells exhibited a 2-3-fold growth and a significantly higher growth rate ($p < 0.01$) in lower stiffness hydrogels compared to higher stiffness ones (Figure 2A). Whereas MDA-MB-231 cells had a more quiescent (or low metabolically active) phenotype, showing a slow growth pattern with no significant differences between hydrogels (Figure 2D). This slow growth pattern was observed only when encapsulated in hydrogels and not on 2D TCP. However, majority of MDA-MB-231 cells remain viable as observed by Live/Dead images in hydrogels, reporting >85% live cells at both day 7 (Figure S4) and 14 (Figure S6) in static and pH 7.4 condition confirming a more quiescent state.

MCF-7 cultured at pHe 6.5 returned low viability at all time points (Figure 2B). Live/Dead images confirmed the presence of small group of viable cells at day 7 (Figure S3), with a large population of dead cells (>70%) increasing with culturing time (Figure S5). Whereas MDA-MB-231 cells showed sustained viability (Figure 2E) and remained viable when cultured at pHe 6.5. Live/Dead staining confirmed presence of viable cells (>80%) at both day 7 (Figure S3) and day 14 (Figure S5).

In comparison to static, perfused culture (dynamic, pHe 7.4), exhibited a 1.5-fold increase in MCF-7's growth in higher stiffness hydrogels at day 14 (Figure 2C). This was also confirmed by analysis of Live/Dead images with a higher number of viable cells (>90%) in dynamic culture compared to static culture (>70%) in all groups at day 14 (Figure S3). All hydrogels embedding MDA-MB-231 cells (dynamic, pHe 7.4) showed a slight and sustained increase in viability (Figure 2F) when compared to static culture (Figure 2E). Like MCF-7, high % of viable MDA-MB-231 cells were measured in dynamic culture (>90%) at all time points (Figure S4 and S6).

All the results of metabolic activity (Alamar blue) indicate an intrinsic proliferative phenotype for MCF-7 cells as opposed to quiescence in MDA-MB-231 cells. Viability of MDA-MB-231 cells remains high (80 - 95%) in all hydrogels and conditions, whereas MCF-7 cells returned different viability (10 - 90%) highly dependent on the physical and chemical properties of the microenvironment, with lower pHe being the parameter that reduces the cell viability drastically.

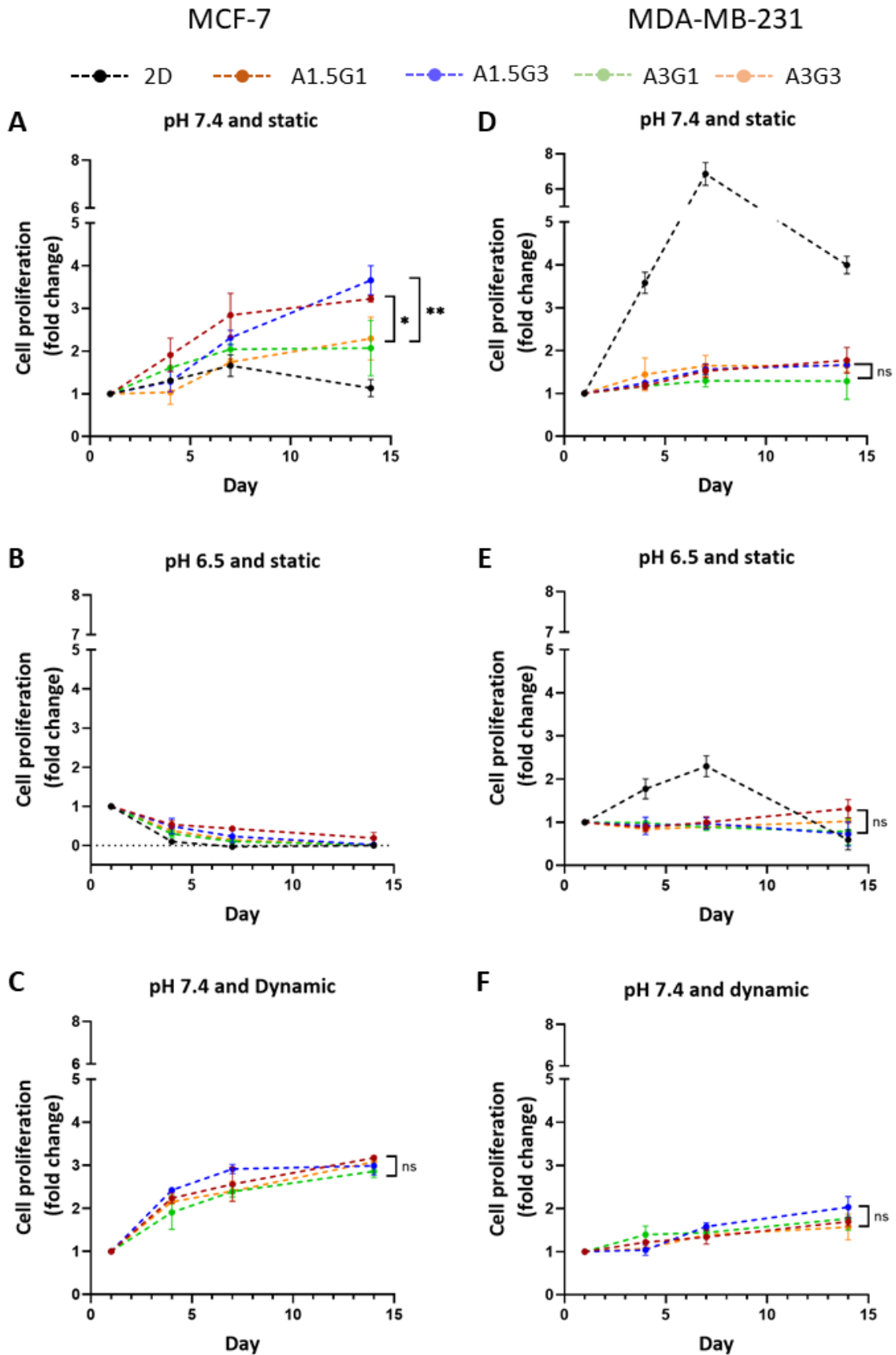


Figure 2: Breast cancer proliferation in varying TME cues. Normalised cell proliferation of MCF-7 and MDA-MB-231 cells in pHe 7.4 static culture (A, D), pHe 6.5 static culture (B, E), and pHe 7.4 dynamic culture (C, F) respectively on day 1, 4, 7, and 14. Lines represent cells cultured in 2D (control, black), A1.5G1 (brown), A1.5G3 (blue), A3G1 (green), A3G3 (orange). To better visualise relative cell growth, values reported on each graph were obtained by dividing RFU (relative fluorescence units) values by that of day 1 values at each time point. Values are represented as average and SD of n=3 (technical replicate), N=3 (biological replicate) experiments for static conditions and n=1, N=3 experiments for dynamic conditions performed on different days. P-values are set as * $p \leq 0.05$, ** $p \leq 0.01$.

3.3 Lower stiffness and perfusion permits for higher aggregate sizes in both cell lines

Unlike scaffold free technique which promotes cell-cell contact only, scaffold-based technique promotes both cell-matrix and cell-cell interactions. Depending on cellular expression of membrane proteins like integrins and cadherins, cells can prefer either matrix or intercellular interactions. Hence the two cell lines cultured in 3D alginate-gelatin hydrogel evidenced presence of both single cells and cell aggregates of mixed sizes, which varied as a function of microenvironment. Semi-quantitative analysis of cell aggregates was performed using Live stained images of cells after 14 days of culture (Figure 3B, 3C). Of note, cells did not form any aggregates when cultured in extracellular tumour acidosis conditions (i.e., pHe 6.5). Interestingly, extracellular acidic pH of 6.2 has been observed to abrogate intercellular junctions in breast cancer cell lines and promote isolated cellular morphology⁴⁷ which is what we observe in 3D hydrogels. Since aggregates were only observed when cultured at physiological pHe values (pH 7.4), both percentage of aggregates formed (Table S1) and size of aggregates were compared at day 14 in pH 7.4 (Figure 3). MDA-MB-231 cell lines showed significant increase in aggregate sizes when cultured in lower stiffness hydrogels (1.8-2.3 kPa) in both static and dynamic conditions ($p < 0.0001$) (Figure 3B). Whereas MCF-7 showed significantly increased aggregate size in lower stiffness but only in dynamic conditions (Figure 3C). Generally, dynamic culture led to increased aggregate sizes to nearly 1.2 to 1.4-fold in comparison with static culture in both cell lines, consistent with the increased proliferation rate previously observed in dynamic culture (Figure 3B, 3C). Also, MCF-7 exhibited larger aggregates than MDA-MB-231 (Figure 3B vs 3C) supporting the former's observed proliferative phenotype compared to latter's quiescent phenotype.

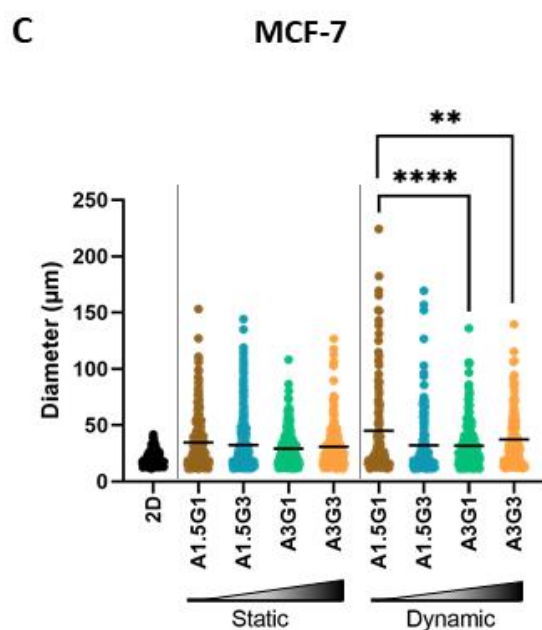
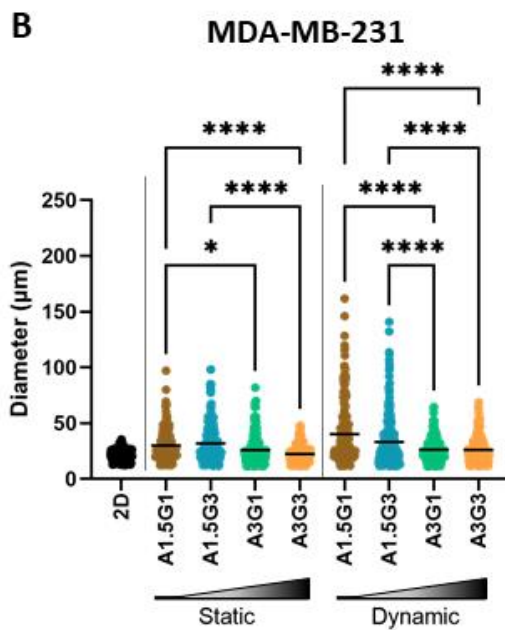
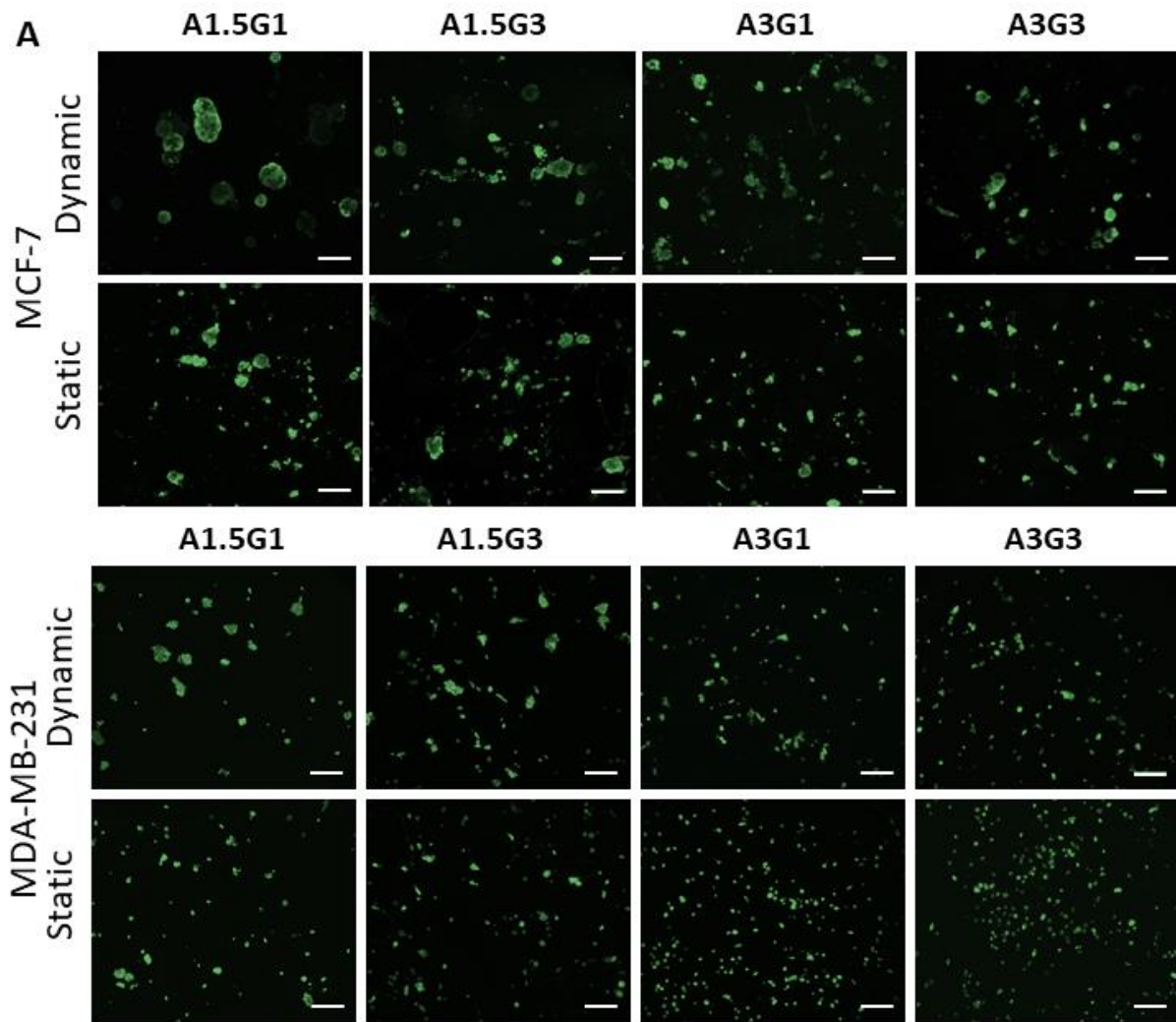


Figure 3. Breast cancer cell aggregates in varying TME cues. (A) Live cell (green) images of MCF-7 and MDA-MB-231 aggregates formed in selected four hydrogels cultured in static or dynamic conditions at physiological pHe (pH = 7.4) (Scale bars: 200 μ m). Quantification of diameter (μ m) of aggregates formed in 2D (Single cell), four hydrogel groups at pHe 7.4 in either static or dynamic condition for (B) MDA-MB 231 aggregates and (C) MCF-7 aggregates. Values are represented as dot plot and mean values for a minimum of n=200 aggregates/objects in each condition tested for both cell lines. P-values represented as *p \leq 0.05, **p \leq 0.01, ***p \leq 0.001, ****p \leq 0.0001.

Previous study with breast cancer spheroids have used aggregate shape (circularity factor) as an indicator to identify cell invasiveness within aggregates⁴⁸. Circularity is a shape descriptor with value range 0-1, where circularity = 1 is defined to be a perfect circular structure, and values < 1 indicate the extent of elongation and irregularity. Invasive cells tend to interact with matrix and form irregular shaped aggregates that protrude into the matrix (e.g Figure 4C) which was quantified through circularity parameter. The aggregates in both cell lines were analysed for their circularity (Figure 4). MDA-MB-231 aggregates showed significantly lower circularity in hydrogels with high gelatin content and lower stiffness (Figure 4E) (p<0.001). In addition, low circularity in high gelatin content was more pronounced when cells were cultured in dynamic conditions than static. As such, decrease in median circularity with increased gelatin content was almost 33% in lower stiffness groups (p<0.0001), and 16% in higher stiffness (p<0.5) (Figure 4E). However, no such change in circularity with increased gelatin content was found in MCF-7 cells, where the only significant decrease of circularity was among A1.5G3 and A3G1 groups in static culture (Figure 4F). MDA-MB-231 aggregates with low circularity have more irregular shapes (Figure 4C) than the aggregates formed by MCF-7 cells (Figure 4D), whereas MCF-7 cells had larger aggregates in general than MDA-MB-231 (Figure 4A vs Figure 4B).

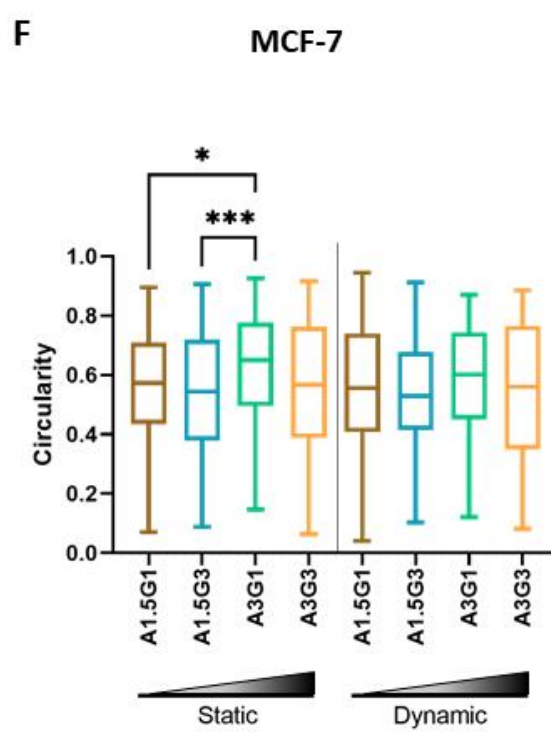
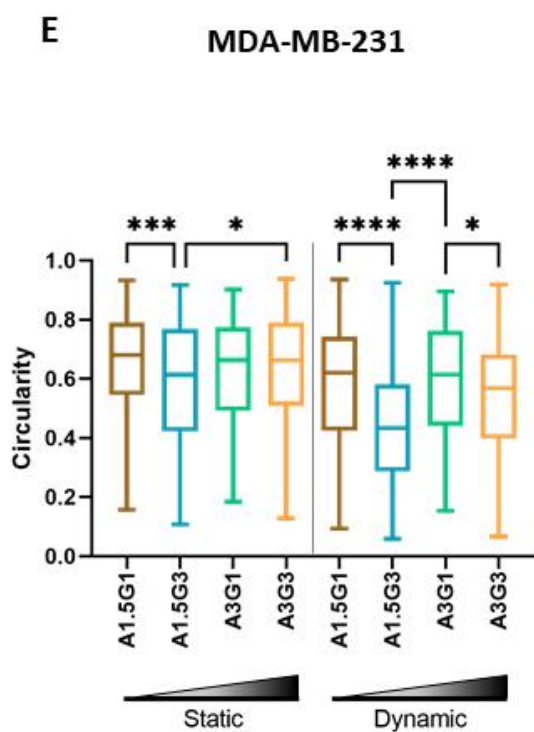
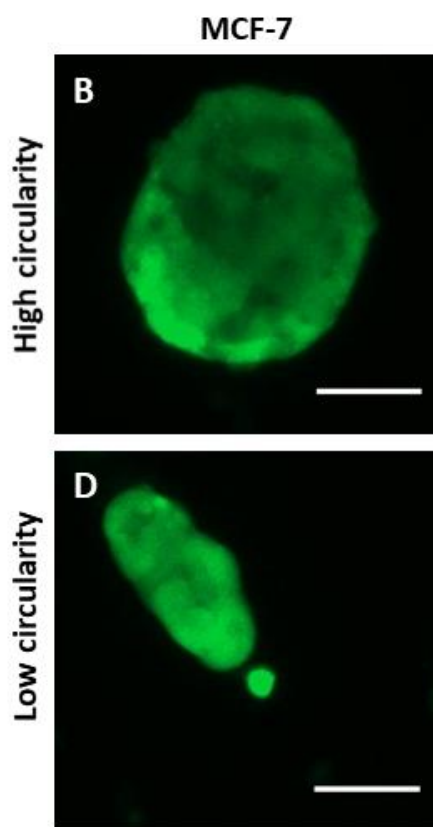
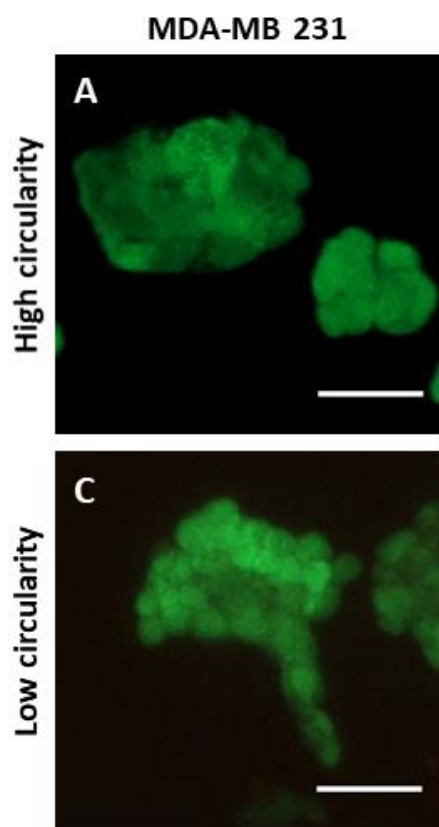


Figure 4: Breast cancer cell circularity with varying TME cues. Representative Live/Dead images of cell aggregates with high and low circularity values: MDA-MB-231 with (A) high and (C) low circularity, and MCF-7 with (B) high and (D) low circularity. (Scale bars 50 μ m). Quantification of circularity of (E) MDA-MB-231 and (F) MCF-7 cell aggregates represented as box and whiskers plot consisting of the maximum, third quartile, median, quartile and minimum values (from top to bottom) of each condition, this representation was selected to better visualise distribution of circularity for each sample. The values were obtained from quantification of a minimum of n=200 cell aggregates. P-values represented as * $p \leq 0.05$, ** $p \leq 0.01$, *** $p \leq 0.001$, **** $p \leq 0.0001$.

3.4 E-CSCs and M-CSCs marker expression in MDA-MB-231

To assess B-CSCs dynamics in response to physico-chemical cues we measured M-CSC (CD44⁺/CD24⁻, vimentin) and E-CSC markers (ALDH⁺, E-cadherin) expression through flow cytometry on day 7 of culture (Figure 5). Day 7 was chosen to study marker expression, as all conditions (pHe 7.4 static, pHe 6.5 static and pHe 7.4 dynamic) in both lines had at least 40% viable cells up until this time point. MDA-MB-231 cells are known to be mesenchymal with majority of cells being CD44⁺/CD24⁻ and high vimentin expression (>90%) and very low ALDH positivity (~3%) as observed in the cells cultured in 2D (Figure 5C-E, H-J). Interestingly, with increase in stiffness there is a significant decrease of almost 75% in CD44⁺/CD24⁻ population ($p < 0.0001$) and lower vimentin expression ($p < 0.01$) (Figure 5A, B). Of note, CD44 positivity remains unaffected but CD24 positivity increases with stiffness (Figure S7). This is coupled with slight but significant two-fold increase in ALDH positivity ($p < 0.001$) and 1.5-fold increase in E-cadherin expression ($p < 0.05$) (Figure 5F, G). Increase in hydrogel stiffness and at physiological pHe led to decreased M-CSC markers and increased E-CSC markers in MDA-MB-231 cells cultured in 3D, whereas 2D controls mainly express M-CSC markers.

On the contrary to pHe 7.4, and when cells were cultured in extracellular tumour acidosis conditions (i.e. pHe 6.5), a sustained M-CSC phenotype was confirmed in higher stiffness hydrogels with negligible decrease in CD44⁺/CD24⁻ cells and increased vimentin expression ($p < 0.5$) (Figure 5A, B). Surprisingly, E-CSC marker ALDH positivity also increased 3 to 4-fold in higher stiffness ($p < 0.0001$) (Figure 5F). Overall, acidic pHe led to sustained M-CSC phenotype and also an increase in ALDH positivity in higher stiffness compared to lower.

When MDA-MB 231 cells are perfused (pHe 7.4), CD44⁺/CD24⁻ phenotype is sustained along with vimentin expression but there is significantly less ALDH positivity (~1%) (Figure 5A, B, F). Such results suggest that perfusion (or dynamic culture conditions) might enrich M-CSCs over E-CSCs.

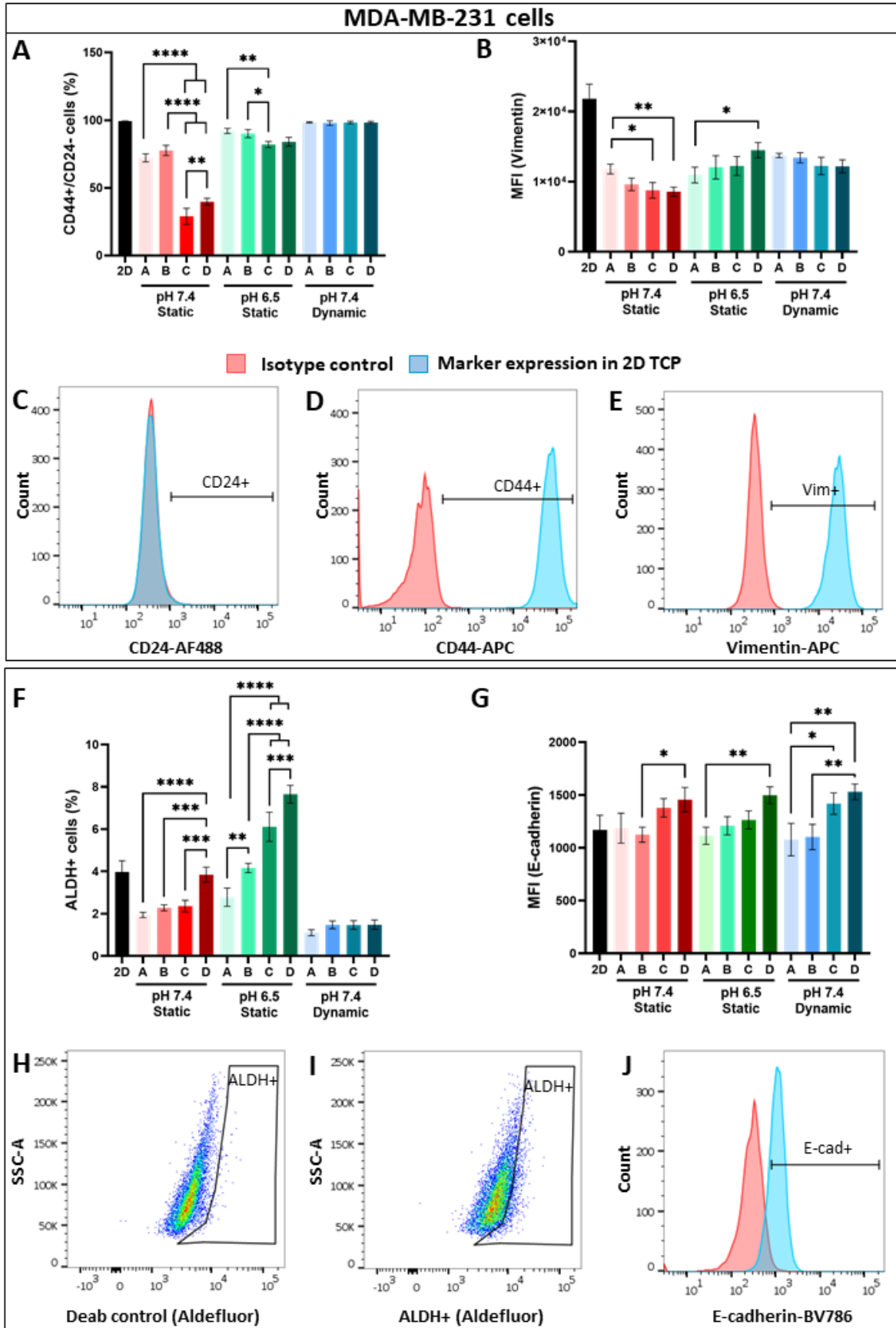


Figure 5: Flow cytometry analysis of CSC markers in MDA-MB231. Flow cytometry quantification in MDA-MB-231 cells of (A) CD44⁺/CD24⁻ cells (%), and (B) median fluorescence intensity (MFI) of Vimentin-APC (fluorescent arbitrary units, a.u.) for characterisation of M-CSCs in various conditions. Example of gating with isotype control of (C) CD24⁺, (D) CD44⁺, (E) Vimentin⁺. (F) Quantification of ALDH⁺ cells (%) and MFI of (G) Ecadherin-BV786 (a.u.) for characterisation of E-CSCs. (H) Example of gating of ALDH⁺ cells with negative DEAB control and (I) aldefluor reagent. (J) Example of gating with isotype control of E-cadherin. The labels in graphs are denoted as 2D (2D TCP plate), A (A1.5G1), B (A1.5G3), C (A3G1) and D (A3G3). The microenvironmental in which these gels are cultured is mentioned below the labels as pHe 7.4 static, pHe 6.5 static, and pHe 7.4 dynamic culture). Values are represented as mean and SD of N=3 (biological replicate) independent experiments. P-values represented as *p ≤ 0.05, **p ≤ 0.01, ***p ≤ 0.001, ****p ≤ 0.0001).

3.5 E-CSC and M-CSC marker expression in MCF-7

Similar to MDA-MB-231 we performed flow cytometry with MCF-7 cells for the same BCSC markers. MCF-7 cells are luminal type cells which are comparatively less invasive and with bulk population with epithelial characteristics. Mostly there is an absence of CD44⁺/CD24⁻ cells, no vimentin and high E-cadherin expression as observed in 2D marker expression (Figure 6C-E, H-J). Although other luminal type cells may contain low ALDH⁺ cells, Further MCF-7 have very low or negligent ALDH positivity. Hence this cell line has low stem cell pool. When cultured in pHe 7.4 static conditions, there is marked decrease of about 90% in E-cadherin expression (p<0.001) with increase in stiffness and a slight but significant increase (p<0.01) in CD44⁺/CD24⁻ (increase from ~2% positivity to ~4% positivity) (Figure 6A and 6G).

However, low pHe and high stiffness was seen to be associated with increase in ALDH⁺ from 2% to 5% (p<0.0001) accompanied with negligible E-cadherin expression (Figure 6F, 6G). Dynamic culture again shows increased CD44⁺/CD24⁻ along with a slight increase in vimentin expression (Figure 6A, 6B). Unlike MDA-MB-231 cells, this cell line exhibits no clear increase or decrease in E-CSC or M-CSC markers but rather changes in individual marker expression. Increased stiffness and acidic pHe here as well are related to slight increase in both CD44⁺/CD24⁻ and ALDH⁺ cells suggesting a role for this kind of microenvironment in increased stem cell pool.

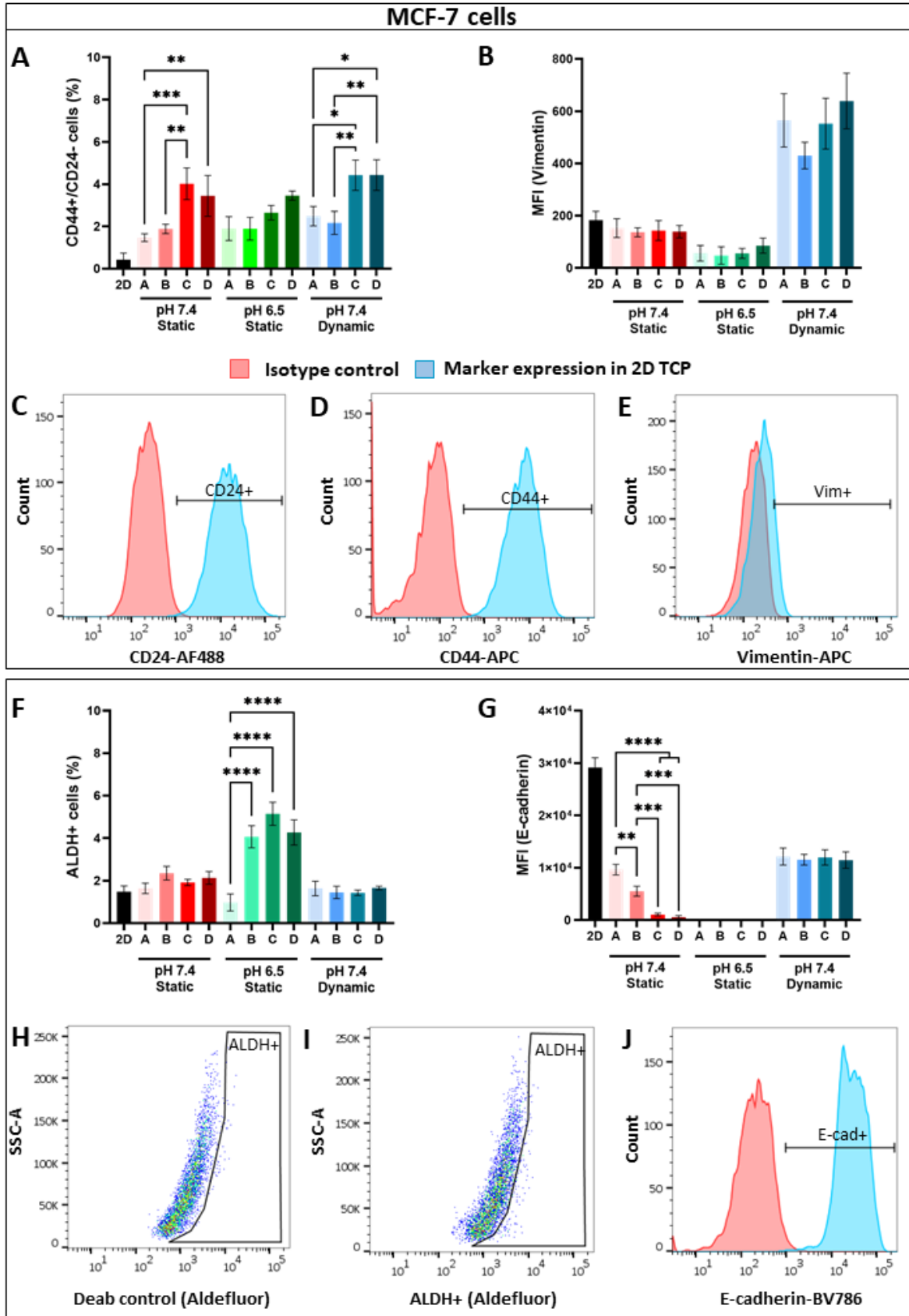


Figure 6: Flow cytometry analysis of CSC markers in MCF-7 cells. Flow cytometry quantification in MCF-7 cells of (A) CD44⁺/CD24⁻ cells (%), and (B) median fluorescence intensity (MFI) of Vimentin-APC (fluorescent arbitrary units, a.u.) for characterisation of M-CSCs in various conditions. Example of gating with isotype control of (C) CD24⁺, (D) CD44⁺, (E) Vimentin⁺. (F) Quantification of ALDH⁺ cells (%) and MFI of (G) Ecadherin-BV786 (a.u.) for characterisation of E-CSCs. (H) Example of gating of ALDH⁺ cells with negative DEAB control and (I) aldefluor reagent. (J) Example of gating with isotype control of E-cadherin. The labels in graphs are denoted as 2D (2D TCP plate), A (A1.5G1), B (A1.5G3), C (A3G1) and D (A3G3). The microenvironmental in which these gels are cultured is mentioned below the labels as pHe 7.4 static, pHe 6.5 static, and pHe 7.4 dynamic culture). Values are represented as mean and SD of N=3 (biological replicate) independent experiments. P-values represented as *p ≤ 0.05, **p ≤ 0.01, ***p ≤ 0.001, ****p ≤ 0.0001).

3.6 Principal component analysis (PCA) of B-CSC markers

These results suggest that B-CSC equilibrium is influenced by the physico-chemical characteristics of the TME. To analyse and visualise data in a comprehensive manner, PCA was used to correlate markers expression (CD44⁺/CD24⁻, ALDH⁺, vimentin and E-cadherin) with the microenvironment. To assess which physico-chemical cue most affects CSC markers, the same PC plot was presented with different colour coding based on stiffness (low and high stiffness group, Figure 7A, 7D), gelatin content (low and high gelatin, Figure 7B, 7E), or physico-chemical environment (pH 7.4 static, pH 6.5 static, pH 7.4 dynamic, Figure 7C, Figure 7F). From the PC plots, it is apparent that cells cultured in lower stiffness hydrogel cluster separately than those in high stiffness (light blue vs dark blue, Figure 7A, Figure 7D) for both the cell lines. However, no such clustering was observed when cells were cultured in different gelatin content (Figure 7B, Figure 7E). Furthermore, cells cultured in different physico-chemical factors (static/dynamic culture, pH 7.4/pH 6.5) exhibit partial clustering (red vs blue vs green, Figure 7C, Figure 7F). Interestingly, we also noticed a linear pattern of increasing hydrogel stiffness in each of these clusters (Figure 7C, Figure 7F) from point Ax (lower stiffness low gelatin) to Dx (high stiffness high gelatin), where ‘x’ represents the physico-chemical microenvironment, i.e. 1) pH 7.4 static, 2) pH 7.4 dynamic, and 3) pH 6.5 static culture. Observed clustering for both cell lines suggests that biophysical and chemical environment influences B-CSCs marker equilibrium.

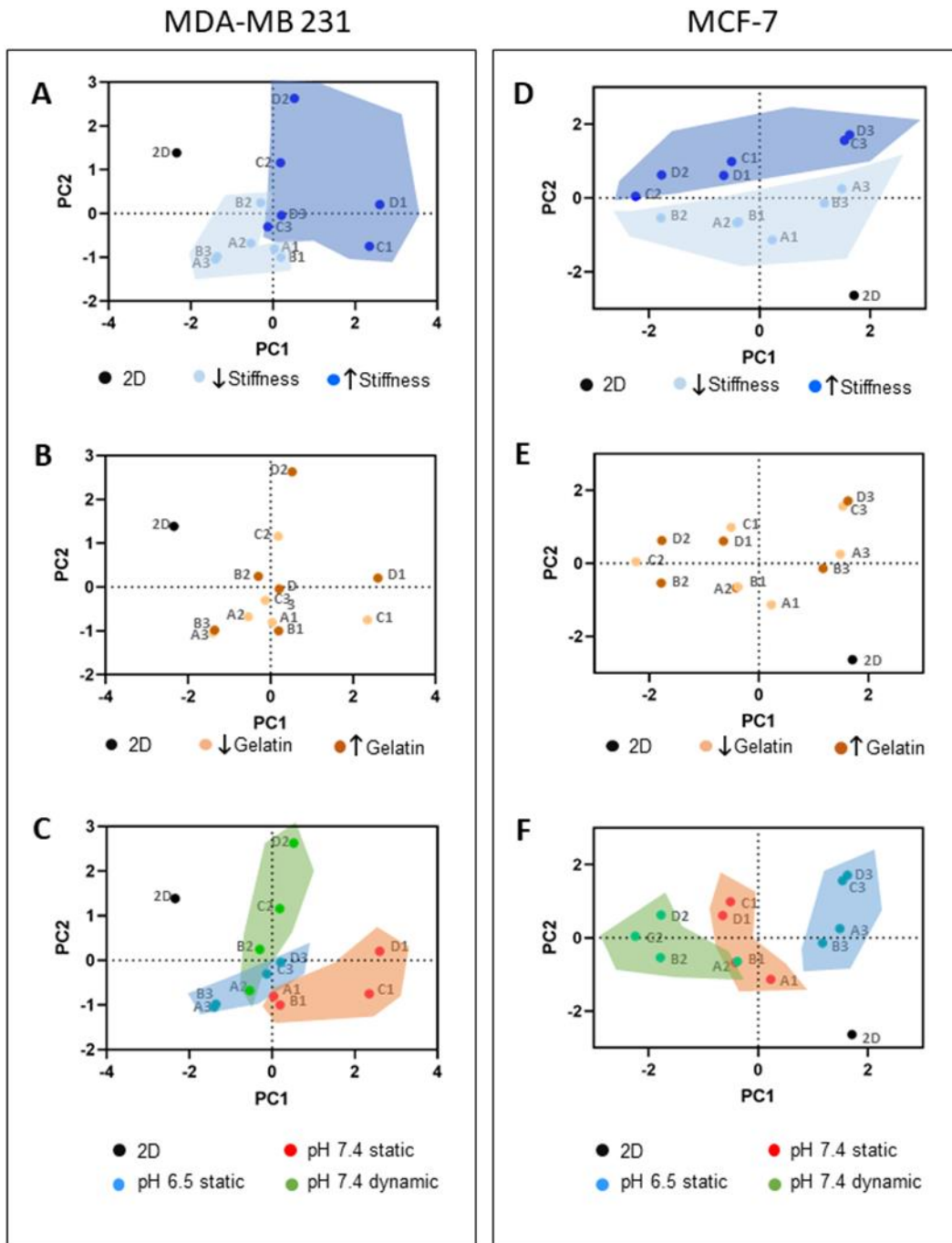


Figure 7: Principal component analysis (PCA) of B-CSC marker expression in different in vitro models presented in the study (i.e. conventional 2D pH 7.4 static, 3D pH 7.4 static, 3D pH 6.5 static and 3D pH 7.4 dynamic) for (A, B, C) MDA-MB 231 and (D, E, F) MCF-7. Data are represented by PC score plot (PC2 vs PC1) where eigenvalue for PC1 = 1.864 and PC2 = 1.258 for MDA-MB 231 and PC1 = 1.99 and PC2= 1.382 for MCF-7. Out of the four PC, only those were chosen that weighed >1 as per Kaiser’s rule for selection of PC eigen values. The plots are colour coded for: (A, D) 2D, low stiffness groups and high

stiffness groups, (B, E) 2D, low gelatin groups and high gelatin groups, and (C, F) 2D, 3D pH 7.4 static, 3D pH 6.5 static and 3D pH 7.4 dynamic culture.

4. Discussion

Traditional two-dimensional (2D) *in vitro* models have been used to study cell-cell and cell-matrix interactions from early to late-stages of cancer progression, as well as to test efficacy of treatments. However, 2D models fail to incorporate typical properties of tissues such as the three-dimensional (3D) architecture of the ECM, its physico-chemical properties, and interstitial fluid flow. Animal models have the required *in vivo* tissue complexity to study the dynamics of pathologies, being successful in mimicking most aspects of TME such as ECM, tumour stromal components, and vascularisation. However, in these models control over variations of such TME properties with required resolution cannot be easily achieved. In the past two decades, 3D *in vitro* models have been used in many applications like disease modelling^{49,50}, disease outcome⁵¹, drug discovery³⁷ and clinical applications⁵². 3D models such as spheroid culture⁵³, hydrogels (scaffolds)-based culture⁵⁴ and microphysical systems like tissue-on-a-chip⁵⁵ have tried to mimic 3D organisation, cell-matrix interactions, perfusion and other physico-chemical cues. In this study, we have also utilised 3D hydrogel-based encapsulation and milli-fluidic system to successfully control and integrate physico-chemical properties of matrix stiffness and density, matrix composition, extracellular pH and perfusion. We further used the models to understand their influence on breast cancer phenotypes that includes proliferation, cell morphology and B-CSCs dynamics.

Modelling physico-chemical TME cues

As mentioned, TME cues of matrix stiffness, pH and fluid flow are heterogenous in nature and vary vastly within the breast tumour milieu. However, due to the nature of this study we aimed at engineering specific values for TME variables, as we wanted to examine cause-effect relationship between TME cues and breast cancer phenotypes. For this purpose and to reduce confounding factors, it was necessary to have TME cues that were homogenous and constant throughout the experiment.

We characterised a small library of alginate-based hydrogels to mimic stiffness of a normal breast tissue (1- 2 kPa) and breast tumour tissue (up to a 5-fold increase in stiffness, i.e., 6-10 kPa).

Alginate-based hydrogels were selected for intrinsic bio-compatibility, better mechanical properties, ease control over gelation and structural consistency with ECM⁵⁶. Other bioactive alternatives like collagen (major ECM component), hyaluronic acid and Matrigel have been previously used in many studies for 3D encapsulation. However, pure collagen hydrogels have poor mechanical properties with higher degradation rate and are expensive to source⁵⁷. Matrigel provides cells with necessary adhesive moieties, growth factors and chemical cues but has ill-defined composition and batch-to-batch variation due to the nature of its sourcing⁵⁸. Alginate lacks adhesive moieties but with addition of gelatin (a substitute for collagen) we overcome that property partially. However, inclusion of other important ECM components like fibronectin and laminin in future models could better represent *in vivo* ECM composition to study their contribution in breast cancer phenotypes. Another reason to use alginate is easy retrieval of live cells for FACS analysis because of the gentle dissolution process. This provides better alternative than collagen or other synthetic hydrogels like peptide crosslinked polyethylene glycol that use covalent bonds and need enzymatic and mechanical degradation, reducing efficacy of cell retrieval⁵⁹. Here we used a high mannuronic alginate type because it has less intrinsic viscosity (intrinsic viscosity of high G = 7.7 dl/g, high M = 6.1 dl/g), is more manageable and leads to softer gels when compared to high guluronic alginate because of intrinsic reduction in Ca²⁺ based crosslinks^{60,61}. Additionally, the backbone of high M alginate has an open structure compared to high G which also leads to high solubility of macromolecules like albumin within the hydrogel⁶⁰. A small library of alginate-based hydrogels with controlled stiffness, density and content of adhesion motif was obtained (Table 3) and each variable was ranked low-medium-high with the ‘high’ category matching the ‘stiff, dense and highly collagenous tissue’ phenotype of tumours.

We set-up a perfusion system that includes hydrogels enabling the control over fluid perfusion and interstitial flow. As per previous mathematical modelling of flow velocities in QV500 chamber⁴², the flow rate of 500 µL/min translates to ~1.4 µm/s flow velocity at the bottom of the chamber, which is similar to average physiological range of interstitial fluid *in vivo*. This study focussed on comparison between static and perfused model hence we included a single flow rate. However, future studies could include higher flow rates (~ 4 - 10 µm/sec) to understand the role of increased fluid velocity found at the tumour boundary. Cell culture media was also formulated to mimic two values of pH from the range found *in vivo* i.e., extracellular pH of normal breast (pH 7.4) and breast tumour (pH 6.5) microenvironment. As mentioned, pH values are also heterogenous within

the breast tumour, hence it would be interesting to include other pH values (for e.g. pH 7.0) in future studies to understand role of neutral pH. As per our knowledge, this is the first report that integrates different matrix stiffness with either interstitial flow or pHe and measures its impact on breast cancer phenotypes and B-CSC dynamics.

Cell proliferation and viability

The growth rate of cell lines was affected by both their intrinsic proliferation as well as the TME cues. Particularly, growth of MCF-7 cells is more sensitive to changes in the physico-chemical microenvironment. The growth rate of MCF-7 was higher in physiological pHe and lower stiffness whereas it decreased in a more tumorigenic environment (higher stiffness, denser matrix and low pHe). In contrast, MDA-MB-231 cells showed slow and sustained growth rate in any conditions tested, exhibiting less sensitivity to changes in biophysical cues. Of note, when cultured in a perfusion system, the even distribution of nutrients and oxygen across the 3D model promoted an increased growth rate for both cell lines ⁶². Our observations are in accordance with existing literature that suggests MCF-7 spheroids are sensitive to environmental changes in nutrients supply (glucose, glutamate and pHe), and although they have intrinsically high proliferation rate, environmental perturbation hinders their growth ⁶³. MDA-MB 231s are better at acidifying their microenvironment than MCF-7, which could explain low tolerance of MCF-7 to acidic pH 6.5 ⁶⁴. MCF-7 are more 'resident' and favour growth over motility, which renders them with high intrinsic growth rate but fail to invade favourable environments to grow. Whereas MDA-MB-231 growth rate is mostly slow, constant, and independent to environment, but they have 'motile' phenotype which prioritizes motility over growth to invade areas with high resource availability ⁶³.

Cell aggregates shape and size

Both cell lines tested in the study formed cell aggregates when cultured in specific conditions, with sizes and shapes of cell aggregates varying according to microenvironment cues. Both MDA-MB-231 and MCF-7 showed larger aggregates when cultured in soft hydrogels (1.8-2 kPa), a pattern observed in both static and dynamic conditions. Previous studies on breast cancer organoids and ovarian cancer cells, reported higher spheroid sizes in lower matrix stiffness compared to higher stiffness ^{48,65,66}. Cavo et. al concluded that MCF-7 cells cultured in alginate based hydrogels formed smaller cell clusters (10-30 μm) when cultured in stiff hydrogels compared to larger

clusters (10- 200 μm) when cells were cultured in softer hydrogels⁴⁵. This and our results suggest that hydrogels with lower stiffness have a more permissible environment for cancer cell cluster growth compared to higher stiffness hydrogels. Early stages of tumour development (pre-vascularisation) have softer matrices, allowing for cell aggregation. Soft and less dense matrices allow perfusion of nutrients; hence cell growth is promoted, and clusters increase in size (as a tumour mass *in vivo*).

Shape is another parameter used to analyse cell aggregates which informs on interactions with the surrounding environment. We have used circularity as a shape parameter to investigate cell aggregates: MDA-MB-231 cells had low circularity (~ 0.6) in both soft and stiff hydrogels with high gelatin content (i.e., 3% gelatin). This effect was more pronounced in conditions with dynamic flow compared with growth in static conditions. However, this was not observed in MCF-7 with cell aggregate circularity found to be independent of stiffness and gelatin content. In previous studies, MDA-MB-231 cells clusters are reported to have grape-like structure indicative of their irregular shape and mesenchymal phenotype. A study utilising PEG based hydrogels with inclusion of RGD (fibronectin-like) and GFOGER (Collagen-like) peptides observed increased irregular cluster shapes of MDA-MB-231⁴⁸. Additionally, this effect was reversed by blocking $\beta 1$ integrin suggesting a role of integrin mediated adhesion in this phenotype⁴⁸. Infact, $\beta 1$ and $\beta 3$ integrins are known to be important in MDA-MB 231's adhesion to gelatin as well, suggesting that the observed irregularity in aggregates could be an integrin dependent phenomenon⁶⁷. When compared *in vivo*, collagen deposition in breast cancers has been correlated to increased tumour grade from DCIS to IDC and invasive phenotype²⁰. Our models also suggest that increased adhesion ligand might enhance MDA-MB-231's 'motile' phenotype' by increasing irregular shaped cell clusters. We additionally observe that perfusion enhances this effect which points out to the importance of including such biophysical cues in mimicking *in vivo* phenotypes.

B-CSC population

In this study we focussed on the widely recognised heterogenous population of B-CSCs: E-CSCs (ALDH+, high E-cadherin expression) and M-CSCs (CD44+/CD24-, high vimentin expression). There are other markers that are also implicated in B-CSC phenotype like EpCAM (CD326), CD133, Notch, ABCG2. However, due to inter and intra-heterogeneity in breast cancer it has been difficult to conclude which ones can be used as independent factors for B-CSC identification⁶⁸.

Some reports do suggest that there can be overlapping population of B-CSC markers. For instance, Notch1 expression is positively correlated with ALDH positivity in breast tumour samples, and downregulation of Notch signalling in ALDH⁺ cells inhibits growth and induces apoptosis^{69,70}. Notch1 inhibitors in TNBC also reduces overall CD44⁺/CD24^{-low} subpopulation⁷¹. Hence further studies are needed to ensure which combination of markers is the best to catch all B-CSCs. Having said that, both CD44⁺/CD24⁻ and ALDH⁺ cells are still considered most common markers for B-CSCs⁷².

Both B-CSCs subtypes (E-CSC and M-CSC) maintain their reciprocal gene expression pattern across the known molecular subtypes of breast cancer: luminal (Estrogen receptor ER+, Progesterone receptor PR+), Her2 enriched (Her2+), and basal/triple negative breast cancer (TNBC). However, their proportion varies across subtypes: ALDH⁺ B-CSCs are found enriched in Her2+ cancers and slightly in luminal ones; whereas the basal subtype has majority of CD44⁺/CD24⁻ B-CSCs^{15,34}. Additionally, B-CSCs have the plasticity to switch from one type to the other¹⁵. Hence in this study we chose a luminal subtype cell line MCF-7 (very few ALDH⁺ cells) and TNBC cell line (high CD44⁺/CD24⁻, low ALDH⁺) to study effects on different subtype.

Previously, the ALDH⁺ cells from TNBC patient derived xenografts (PDX) had higher tumour initiating capacity than the CD44⁺/CD24⁻ CSCs⁷³. In another study, subpopulations isolated from SUM149 showed increased invasive phenotype in CD44⁺/CD24⁻ than the ALDH⁺ CSCs¹⁵. In both studies, cells that were found positive for both markers (very rare population) had increased high initiating tumour capacity as well as invasive potential. While importance of heterogeneity in B-CSCs markers and phenotype has been recognised, reports are now emerging on TME's involvement in this heterogeneity. Here we observed that decreased M-CSC marker and increased E-CSC marker expression are linked with high stiffness of the encapsulating hydrogel in MDA-MB-231 cells. In contrast, in the presence of lower pH, the M-CSC population is maintained in addition to the increase in E-CSC markers with high stiffness. A similar pattern, although at a very low scale, was observed in MCF-7 cells where both ALDH⁺ and CD44⁺/CD24⁻ cells were increased in low pHe and high stiffness conditions. These results suggest that higher hydrogel stiffness coupled with acidic pHe (tumorigenic microenvironment) are associated with increased stem cell content consisting of both E-CSCs and M-CSCs. Hence these conditions might retain both tumour initiating and invasive populations of B-CSCs. Additionally, the presence of

interstitial fluid flow was observed to be associated with high CD44+/CD24- expression and low ALDH+ in both cell lines, irrespective of the hydrogel stiffness. We can deduce that the reported 3D model in this study was able to recapitulate *in vivo* breast tumour observation where most CD44+/CD24- cells were found to be located at the tumour edge (known to have high interstitial fluid flow) whereas most ALDH+ cells to be located centrally in the tumour core (known to have acidic pH) ¹⁵.

PCA further confirmed clustering of B-CSCs marker expression with biophysical (stiffness, perfusion) and chemical (pHe) cues in both of the cell lines. This analysis also highlighted a linear pattern (from lower stiffness to higher stiffness) in each of these clustered groups (Figure 8C, 8F) suggesting involvement of mechano-transduction through matrix stiffness via a proportional response. Whilst the mechanisms through which these biophysical cues affect B-CSC marker expression are not yet clear, this study presents a platform that could be used to further study these interactions.

5. Conclusions

In this study, physico-chemical cues engineered through *in vitro* modelling have shown effect on breast cancer phenotypes of cell proliferation, aggregate size and shape, and B-CSC population. With the provision to decouple and control resolution of these cues, we were able to dissect the individual effect of each independent parameter on human breast cancer cellular phenotypes. The 3D models were able to capture divergent responses of the cell lines used; MCF-7's growth had decreased whereas MDA-MB 231 retained sustained growth in tumourigenic environment (Stiff, dense ECM and acidic pHe). On the other hand, MDA-MB 231 had increased irregularity in cell clusters (invasive cells) with higher gelatin content (correlated to high ECM deposition *in vivo*). Additionally, we observe here that the most tumourigenic condition of stiff, dense matrix with pHe 6.5 showed increased proportion of both M-CSC and E-CSC subpopulation indicating increased stem cell pool in both cell lines. These models can be used to delineate mechanisms involved in these phenotypes. In future, such models can present themselves as a platform for therapeutics and drug discoveries to monitor cancer phenotypes and B-CSC population in presence of a more physiological microenvironment than the current *in vitro* models.

Acknowledgements

This work was fully funded by PhD studentship available from President's Doctoral Scholarship and the University of Manchester. The funding source was not involved in the study design, findings or recommendations mentioned in this report. The authors thank the University of Manchester Flow Cytometry Core Facility for assistance with flow cytometry protocols. The Flow Cytometry Core Facility and BD Fortessa X-20 equipment is supported in part by the University of Manchester with assistance from Arthritis UK. The authors would like to thank Miss Chen Zhao for her fruitful discussions on Alginate gel preparation.

References

1. Winkler J, Abisoye-Ogunniyan A, Metcalf KJ, Werb Z. Concepts of extracellular matrix remodelling in tumour progression and metastasis. *Nat Commun* 2020 111. 2020;11(1):1-19. doi:10.1038/s41467-020-18794-x
2. Jonietz E. Mechanics: The forces of cancer. *Nat* 2012 4917425. 2012;491(7425):S56-S57. doi:10.1038/491s56a
3. Li F, Tiede B, Massagué J, Kang Y. Beyond tumorigenesis: cancer stem cells in metastasis. *Cell Res* 2007 171. 2006;17(1):3-14. doi:10.1038/sj.cr.7310118
4. Velasco-Velázquez MA, Popov VM, Lisanti MP, Pestell RG. The Role of Breast Cancer Stem Cells in Metastasis and Therapeutic Implications. *Am J Pathol*. 2011;179(1):2. doi:10.1016/J.AJPATH.2011.03.005
5. Pavlopoulou A, Oktay Y, Vougas K, Louka M, Vorgias CE, Georgakilas AG. Determinants of resistance to chemotherapy and ionizing radiation in breast cancer stem cells. *Cancer Lett*. 2016;380(2):485-493. doi:10.1016/J.CANLET.2016.07.018
6. Rodríguez CE, Berardi DE, Abrigo M, Todaro LB, Joffé EDB de K, Fiszman GL. Breast cancer stem cells are involved in Trastuzumab resistance through the HER2 modulation in 3D culture. *J Cell Biochem*. 2018;119(2):1381-1391. doi:10.1002/JCB.26298
7. Zheng X, Yu C, Xu M. Linking Tumor Microenvironment to Plasticity of Cancer Stem

- Cells: Mechanisms and Application in Cancer Therapy. *Front Oncol.* 2021;11:2552. doi:10.3389/FONC.2021.678333/BIBTEX
8. Lau EYT, Ho NPY, Lee TKW. Cancer stem cells and their microenvironment: Biology and therapeutic implications. *Stem Cells Int.* 2017;2017. doi:10.1155/2017/3714190
 9. Al-Hajj M, Wicha MS, Benito-Hernandez A, Morrison SJ, Clarke MF. Prospective identification of tumorigenic breast cancer cells. *Proc Natl Acad Sci U S A.* 2003;100(7):3983-3988. doi:10.1073/pnas.0530291100
 10. Chen C, Zhao S, Karnad A, Freeman JW. The biology and role of CD44 in cancer progression: therapeutic implications. *J Hematol Oncol 2018 111.* 2018;11(1):1-23. doi:10.1186/S13045-018-0605-5
 11. Baccelli I, Schneeweiss A, Riethdorf S, et al. Identification of a population of blood circulating tumor cells from breast cancer patients that initiates metastasis in a xenograft assay. *Nat Biotechnol 2013 316.* 2013;31(6):539-544. doi:10.1038/nbt.2576
 12. Zöller M. CD44: can a cancer-initiating cell profit from an abundantly expressed molecule? *Nat Rev Cancer 2011 114.* 2011;11(4):254-267. doi:10.1038/nrc3023
 13. Fang X, Zheng P, Tang J, Liu Y. CD24: from A to Z. *Cell Mol Immunol 2010 72.* 2010;7(2):100-103. doi:10.1038/cmi.2009.119
 14. Ginestier C, Hur MH, Charafe-Jauffret E, et al. ALDH1 is a marker of normal and malignant human mammary stem cells and a predictor of poor clinical outcome. *Cell Stem Cell.* 2007;1(5):555. doi:10.1016/J.STEM.2007.08.014
 15. Liu S, Cong Y, Wang D, et al. Breast Cancer Stem Cells Transition between Epithelial and Mesenchymal States Reflective of their Normal Counterparts. *Stem Cell Reports.* 2014;2(1):78. doi:10.1016/J.STEMCR.2013.11.009
 16. Butcher DT, Alliston T, Weaver VM. A tense situation: forcing tumour progression. *Nat Rev Cancer.* 2009;9(2):108-122. doi:10.1038/nrc2544
 17. Emon B, Bauer J, Jain Y, Jung B, Saif T. Biophysics of Tumor Microenvironment and

- Cancer Metastasis - A Mini Review. *Comput Struct Biotechnol J*. 2018;16:279-287. doi:10.1016/J.CSBJ.2018.07.003
18. Lu P, Weaver VM, Werb Z. The extracellular matrix: a dynamic niche in cancer progression. *J Cell Biol*. 2012;196(4):395-406. doi:10.1083/jcb.201102147
 19. Samani A, Zubovits J, Plewes D. Elastic moduli of normal and pathological human breast tissues: an inversion-technique-based investigation of 169 samples. *Phys Med Biol*. 2007;52(6):1565-1576. doi:10.1088/0031-9155/52/6/002
 20. Acerbi I, Cassereau L, Dean I, et al. Human breast cancer invasion and aggression correlates with ECM stiffening and immune cell infiltration. *Integr Biol*. 2015;7(10):1120-1134. doi:10.1039/C5IB00040H
 21. Gatenby RA, Gawlinski ET, Gmitro AF, Kaylor B, Gillies RJ. Acid-Mediated Tumor Invasion: a Multidisciplinary Study. *Cancer Res*. 2006;66(10):5216-5223. doi:10.1158/0008-5472.CAN-05-4193
 22. Chen M, Chen C, Shen Z, et al. Extracellular pH is a biomarker enabling detection of breast cancer and liver cancer using CEST MRI. *Oncotarget*. 2017;8(28):45759. doi:10.18632/ONCOTARGET.17404
 23. Estrella V, Chen T, Lloyd M, Wojtkowiak J, Cornell HH, Ibrahim-Hashim A, Bailey K, Balagurunathan Y, Rothberg JM, Sloane BF, Johnson J, Gatenby RA GR. Acidity generated by the tumor microenvironment drives local invasion. *Cancer Res*. 2013;73(5):1524-1535. doi:10.1158/0008-5472.CAN-12-2796
 24. Shi Q, Le X, Wang B, Abbruzzese JL, Xiong Q, He Y XK. Regulation of vascular endothelial growth factor expression by acidosis in human cancer cells. *Oncogene*. 2001;20(28). doi:10.1038/SJ.ONC.1204500
 25. Walton ZE, Patel CH, Brooks RC, Yu Y, Ibrahim-Hashim A, Riddle M, Porcu A, Jiang T, Ecker BL, Tameire F, Koumenis C, Weeraratna AT, Welsh DK, Gillies R, Alwine JC, Zhang L, Powell JD DC. Acid Suspends the Circadian Clock in Hypoxia through Inhibition of mTOR. *Cell*. 2018;174(1):72-87.e32. doi:10.1016/J.CELL.2018.05.009

26. Robey IF, Baggett BK, Kirkpatrick ND, Roe DJ, Dosesco J, Sloane BF, Hashim AI, Morse DL, Raghunand N, Gatenby RA GR. Bicarbonate increases tumor pH and inhibits spontaneous metastases. *Cancer Res.* 2009;69(6):2260-2268. doi:10.1158/0008-5472.CAN-07-5575
27. Wagner M, Wiig H. Tumor interstitial fluid formation, characterization, and clinical implications. *Front Oncol.* 2015;5(MAY):115. doi:10.3389/FONC.2015.00115/BIBTEX
28. Munson JM, Shieh AC. Interstitial fluid flow in cancer: implications for disease progression and treatment. *Cancer Manag Res.* 2014;6:317. doi:10.2147/CMAR.S65444
29. Chary SR, Jain RK. Direct measurement of interstitial convection and diffusion of albumin in normal and neoplastic tissues by fluorescence photobleaching. *Proc Natl Acad Sci U S A.* 1989;86(14):5385-5389. doi:10.1073/PNAS.86.14.5385
30. Dafni H, Israely T, Bhujwalla ZM, Benjamin LE, Neeman M. Overexpression of vascular endothelial growth factor 165 drives peritumor interstitial convection and induces lymphatic drain: magnetic resonance imaging, confocal microscopy, and histological tracking of triple-labeled albumin. *Cancer Res.* 2002;62(22):6731-6739.
31. Polacheck WJ, Charest JL, Kamm RD, Chien S. Interstitial flow influences direction of tumor cell migration through competing mechanisms. doi:10.1073/pnas.1103581108
32. Haessler U, Teo JCM, Foretay D, Renaud P, Swartz MA. Migration dynamics of breast cancer cells in a tunable 3D interstitial flow chamber. *Integr Biol (Camb).* 2012;4(4):401-409. doi:10.1039/c1ib00128k
33. Liu S, Clouthier SG, Wicha MS. Role of microRNAs in the Regulation of Breast Cancer Stem Cells. *J Mammary Gland Biol Neoplasia.* 2012;17(1):15. doi:10.1007/S10911-012-9242-8
34. Brooks MD, Burness ML, Wicha MS. Therapeutic Implications of Cellular Heterogeneity and Plasticity in Breast Cancer. *Cell Stem Cell.* 2015;17(3):260-271. doi:10.1016/J.STEM.2015.08.014
35. Pal B, Chen Y, Bert A, Hu Y, Sheridan JM, Beck T, Shi W, Satterley K, Jamieson P,

- Goodall GJ, Lindeman GJ, Smyth GK VJ. Integration of microRNA signatures of distinct mammary epithelial cell types with their gene expression and epigenetic portraits. *Breast Cancer Res.* 2015;17(1). doi:10.1186/S13058-015-0585-0
36. Asghar W, El Assal R, Shafiee H, Pitteri S, Paulmurugan R, Demirci U. Engineering cancer microenvironments for in vitro 3-D tumor models. *Mater Today.* 2015;18(10):539-553. doi:10.1016/J.MATTOD.2015.05.002
37. Langhans SA. Three-dimensional in vitro cell culture models in drug discovery and drug repositioning. *Front Pharmacol.* 2018;9(JAN):6. doi:10.3389/fphar.2018.00006
38. Tirella A, Mattei G AA. Strain rate viscoelastic analysis of soft and highly hydrated biomaterials. *J Biomed Mater Res A.* 2014;102(10):3352-3360. doi:10.1002/JBM.A.34914
39. Tirella A, Mattei G, La Marca M, Ahluwalia A, Tirelli N. Functionalized Enzyme-Responsive Biomaterials to Model Tissue Stiffening in vitro. *Front Bioeng Biotechnol.* 2020;0:208. doi:10.3389/FBIOE.2020.00208
40. Almari B, Brough D, Harte M, Tirella A. Fabrication of Amyloid- β -Secreting Alginate Microbeads for Use in Modelling Alzheimer's Disease. *J Vis Exp.* 2019;2019(149). doi:10.3791/59597
41. Azimi T, Loizidou M, Dwek M V. Cancer cells grown in 3D under fluid flow exhibit an aggressive phenotype and reduced responsiveness to the anti-cancer treatment doxorubicin. *Sci Rep.* 2020;10(1):12020. doi:10.1038/s41598-020-68999-9
42. Mazzei D, Guzzardi MA, Giusti S, Ahluwalia A. A low shear stress modular bioreactor for connected cell culture under high flow rates. *Biotechnol Bioeng.* 2010;106(1):127-137. doi:10.1002/BIT.22671
43. Zhang B, Shan DH, Li D, et al. Different methods of detaching adherent cells significantly affect the detection of TRAIL receptors: <https://doi.org/10.1177/030089161209800619>. 2018;98(6):800-803. doi:10.1177/030089161209800619
44. Rosa JMR de la, Wubetu J, Tirelli N, Tirella A. Colorectal tumor 3D in vitro models: advantages of biofabrication for the recapitulation of early stages of tumour development.

Biomed Phys Eng Express. 2018;4(4):045010. doi:10.1088/2057-1976/AAC1C9

45. Cavo M, Fato M, Peñuela L, Beltrame F, Raiteri R, Scaglione S. Microenvironment complexity and matrix stiffness regulate breast cancer cell activity in a 3D in vitro model. *Sci Reports 2016 61.* 2016;6(1):1-13. doi:10.1038/srep35367
46. Lhuissier E, Bazille C, Aury-Landas J, et al. Identification of an easy to use 3D culture model to investigate invasion and anticancer drug response in chondrosarcomas. *BMC Cancer.* 2017;17(1):1-12. doi:10.1186/S12885-017-3478-Z/TABLES/2
47. Ralph ACL, Valadão IC, Cardoso EC, et al. Environmental control of mammary carcinoma cell expansion by acidification and spheroid formation in vitro. *Sci Reports 2020 101.* 2020;10(1):1-12. doi:10.1038/s41598-020-78989-6
48. Sawicki LA, Ovadia EM, Pradhan L, et al. Tunable synthetic extracellular matrices to investigate breast cancer response to biophysical and biochemical cues. *APL Bioeng.* 2019;3(1):016101. doi:10.1063/1.5064596
49. Huh D, Matthews BD, Mammoto A, Montoya-Zavala M, Yuan Hsin H, Ingber DE. Reconstituting organ-level lung functions on a chip. *Science (80-).* 2010;328(5986):1662-1668. doi:10.1126/science.1188302
50. Ho BX, Pek NMQ, Soh B-S. Disease Modeling Using 3D Organoids Derived from Human Induced Pluripotent Stem Cells. *Int J Mol Sci 2018, Vol 19, Page 936.* 2018;19(4):936. doi:10.3390/IJMS19040936
51. Barney LE, Dandley EC, Jansen LE, Reich NG, Mercurio AM, Peyton SR. A cell-ECM screening method to predict breast cancer metastasis †. *Integr Biol.* 2015;7:198. doi:10.1039/c4ib00218k
52. S. Franco S, Szczesna K, Iliou MS, et al. In vitro models of cancer stem cells and clinical applications. *BMC Cancer 2016 162.* 2016;16(2):23-49. doi:10.1186/S12885-016-2774-3
53. Białkowska K, Komorowski P, Bryszewska M, Miłowska K. Spheroids as a Type of Three-Dimensional Cell Cultures-Examples of Methods of Preparation and the Most Important Application. *Int J Mol Sci.* 2020;21(17):1-17. doi:10.3390/IJMS21176225

54. Nikolova MP, Chavali MS. Recent advances in biomaterials for 3D scaffolds: A review. *Bioact Mater.* 2019;4:271. doi:10.1016/J.BIOACTMAT.2019.10.005
55. Zhang B, Korolj A, Lai BFL, Radisic M. Advances in organ-on-a-chip engineering. *Nat Rev Mater.* 2018;3(8):257-278. doi:10.1038/s41578-018-0034-7
56. Lee KY, Mooney DJ. Alginate: Properties and biomedical applications. *Prog Polym Sci.* 2012;37(1):106-126. doi:10.1016/j.progpolymsci.2011.06.003
57. Sarrigiannidis SO, Rey JM, Dobre O, González-García C, Dalby MJ, Salmeron-Sanchez M. A tough act to follow: collagen hydrogel modifications to improve mechanical and growth factor loading capabilities. *Mater Today Bio.* 2021;10:100098. doi:10.1016/J.MTBIO.2021.100098
58. Aisenbrey EA, Murphy WL. Synthetic alternatives to Matrigel. *Nat Rev Mater.* 2020;5(7):539. doi:10.1038/S41578-020-0199-8
59. Caliani SR, Burdick JA. A practical guide to hydrogels for cell culture. *Nat Methods.* 2016;13(5):405-414. doi:10.1038/nmeth.3839
60. Amsden B, Turner N. Diffusion characteristics of calcium alginate gels. *Biotechnol Bioeng.* 1999;65(5):605-610. doi:10.1002/(sici)1097-0290(19991205)65:5<605::aid-bit14>3.0.co;2-c
61. Klöck G, Pfeffermann A, Ryser C, et al. Biocompatibility of mannuronic acid-rich alginates. *Biomaterials.* 1997;18(10):707-713. doi:10.1016/S0142-9612(96)00204-9
62. Pasini A, Lovecchio J, Cortesi M, et al. Perfusion Flow Enhances Viability and Migratory Phenotype in 3D-Cultured Breast Cancer Cells. *Ann Biomed Eng* 2021 499. 2021;49(9):2103-2113. doi:10.1007/S10439-021-02727-W
63. Freischel AR, Damaghi M, Cunningham JJ, et al. Frequency-dependent interactions determine outcome of competition between two breast cancer cell lines. *Sci Reports* 2021 111. 2021;11(1):1-18. doi:10.1038/s41598-021-84406-3
64. Montcourrier P, Silver I, Farnoud R, Bird I, Rochefort H. Breast cancer cells have a high

- capacity to acidify extracellular milieu by a dual mechanism. *Clin Exp Metastasis*. 1997;15(4):382-392. doi:10.1023/A:1018446104071
65. Loessner D, Stok KS, Lutolf MP, Hutmacher DW, Clements JA, Rizzi SC. Bioengineered 3D platform to explore cell–ECM interactions and drug resistance of epithelial ovarian cancer cells. *Biomaterials*. 2010;31(32):8494-8506. doi:10.1016/J.BIOMATERIALS.2010.07.064
 66. Beck JN, Singh A, Rothenberg AR, Elisseff JH, Ewald AJ. The independent roles of mechanical, structural and adhesion characteristics of 3D hydrogels on the regulation of cancer invasion and dissemination. *Biomaterials*. 2013;34(37):9486-9495. doi:10.1016/J.BIOMATERIALS.2013.08.077
 67. Beaty BT, Sharma VP, Bravo-Cordero JJ, et al. β 1 integrin regulates Arg to promote invadopodial maturation and matrix degradation. *Mol Biol Cell*. 2013;24(11):1661-1675. doi:10.1091/MBC.E12-12-0908/ASSET/IMAGES/LARGE/1661FIG7.JPEG
 68. Song K, Farzaneh M. Signaling pathways governing breast cancer stem cells behavior. *Stem Cell Res Ther* 2021 121. 2021;12(1):1-11. doi:10.1186/S13287-021-02321-W
 69. Zhong Y, Shen S, Zhou Y, et al. NOTCH1 is a poor prognostic factor for breast cancer and is associated with breast cancer stem cells. *Onco Targets Ther*. 2016;9:6865-6871. doi:10.2147/OTT.S109606
 70. Suman S, Das TP, Damodaran C. Silencing NOTCH signaling causes growth arrest in both breast cancer stem cells and breast cancer cells. *Br J Cancer*. 2013;109(10):2587-2596. doi:10.1038/BJC.2013.642
 71. Qiu M, Peng Q, Jiang I, et al. Specific inhibition of Notch1 signaling enhances the antitumor efficacy of chemotherapy in triple negative breast cancer through reduction of cancer stem cells. *Cancer Lett*. 2013;328(2):261-270. doi:10.1016/J.CANLET.2012.09.023
 72. Zhang R, Tu J, Liu S. Novel molecular regulators of breast cancer stem cell plasticity and heterogeneity. *Semin Cancer Biol*. 2022;82:11-25. doi:10.1016/J.SEMCANCER.2021.03.008

73. Liu M, Liu Y, Deng L, et al. Transcriptional profiles of different states of cancer stem cells in triple-negative breast cancer. *Mol Cancer*. 2018;17(1). doi:10.1186/S12943-018-0809-X

**Chapter 2. Role of stiffness and properties of tumour
microenvironment on breast cancer cells stemness**

Supplementary information

Supplementary figures and tables

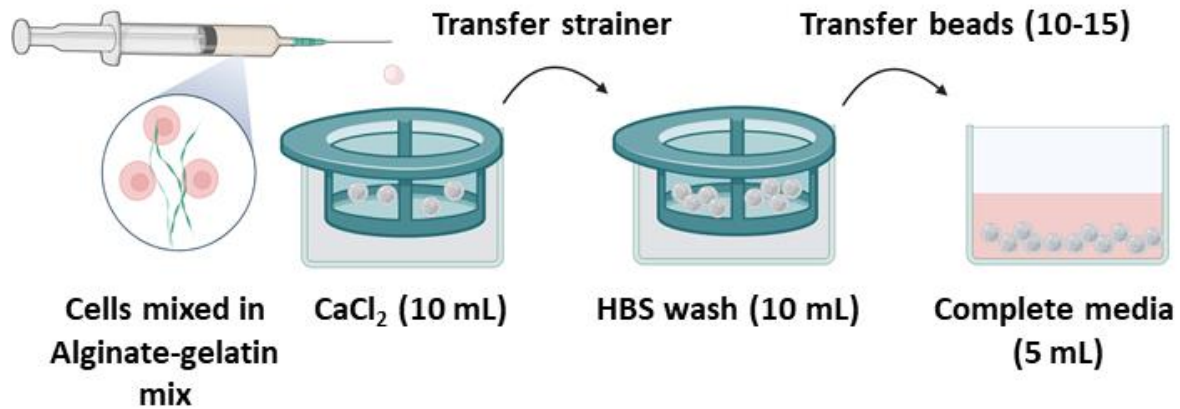


Fig. S 1: Schematic representation of alginate-gelatin beads preparation encapsulating human breast cancer cells (2×10^6 cells/mL). First a homogenous suspension of cells in alginate-gelatin solution is prepared, the cell suspension is ejected through a 27G \times 0.75" needle into a crosslinking solution (CaCl₂, 10mL) and incubated for 10 min at room temperature. Obtained beads (0.5 mL / 10-15 beads) are then washed in HBS and finally beads are transferred in a well plate. A typical experiment is set using 6-well MW with 5 mL of complete cell culture media. The MW plate is transferred to an incubator for further experiments.

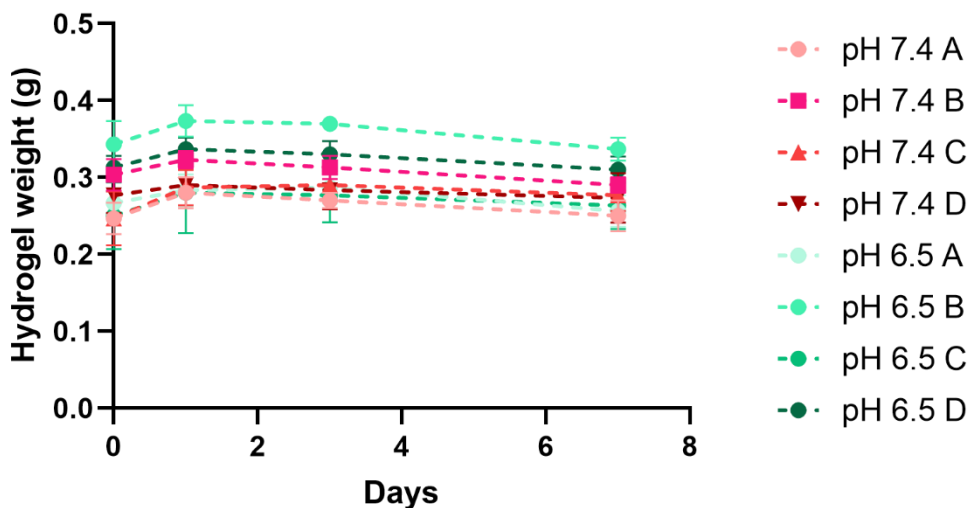


Fig. S 2: Swelling characteristics of selected four groups of hydrogels (A- A1.5G1, B- A1.5G3, C-A3G1, D- A3G3) in either pH 7.4 media or pH 6.5 media. The weight of hydrogels was measured at the specified time points over 7 days

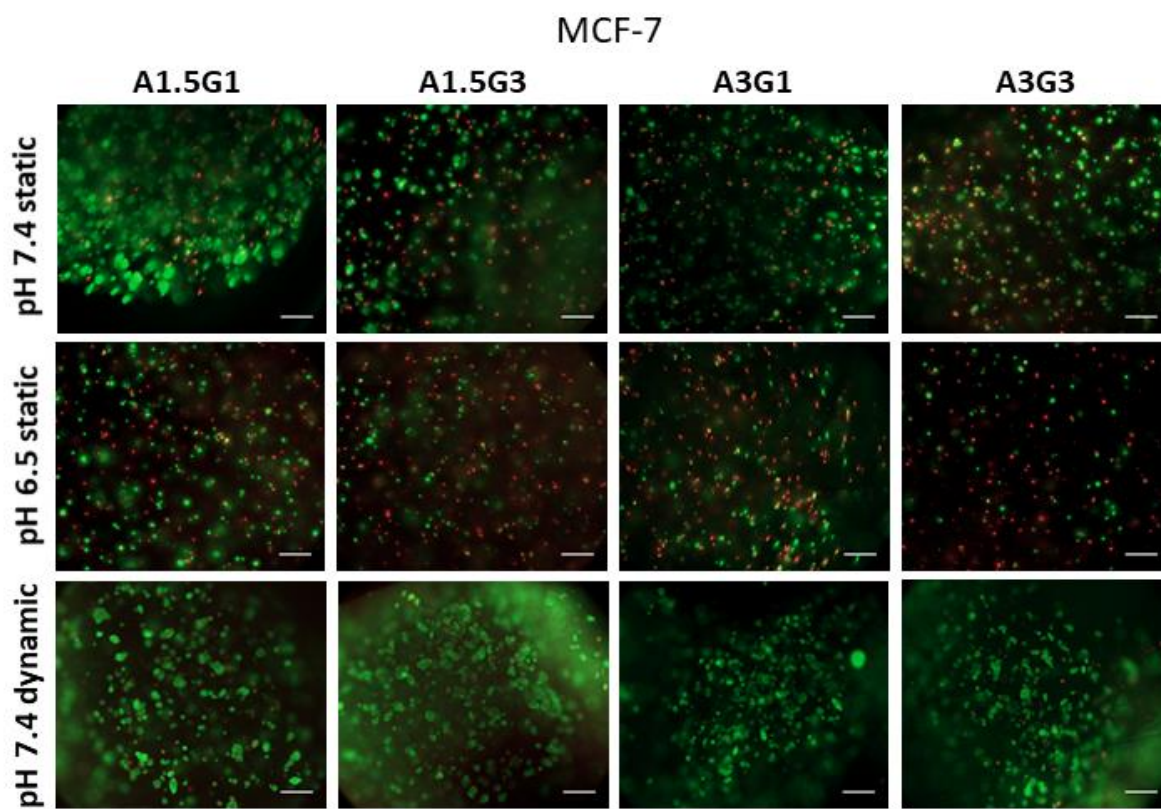


Fig. S 3: Examples of Live/Dead images at day 7: MCF-7 cells in pHe 7.4 static, pHe 6.5 static and pHe 7.4 dynamic. Scale bars 200 μ m.

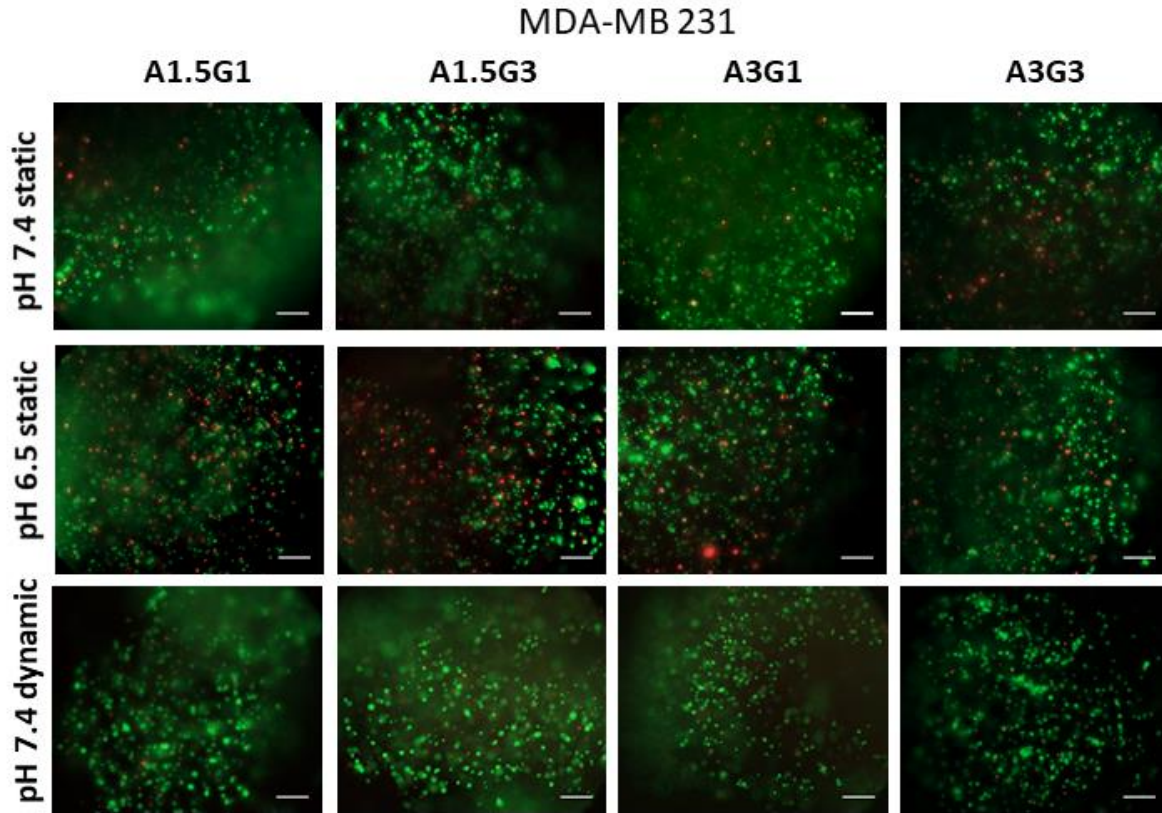


Fig. S 4: Examples of Live/Dead images at day 7: MDA-MB 231 cells in pHe 7.4 static, pHe 6.5 static and pHe 7.4 dynamic. Scale bars 200 μm .

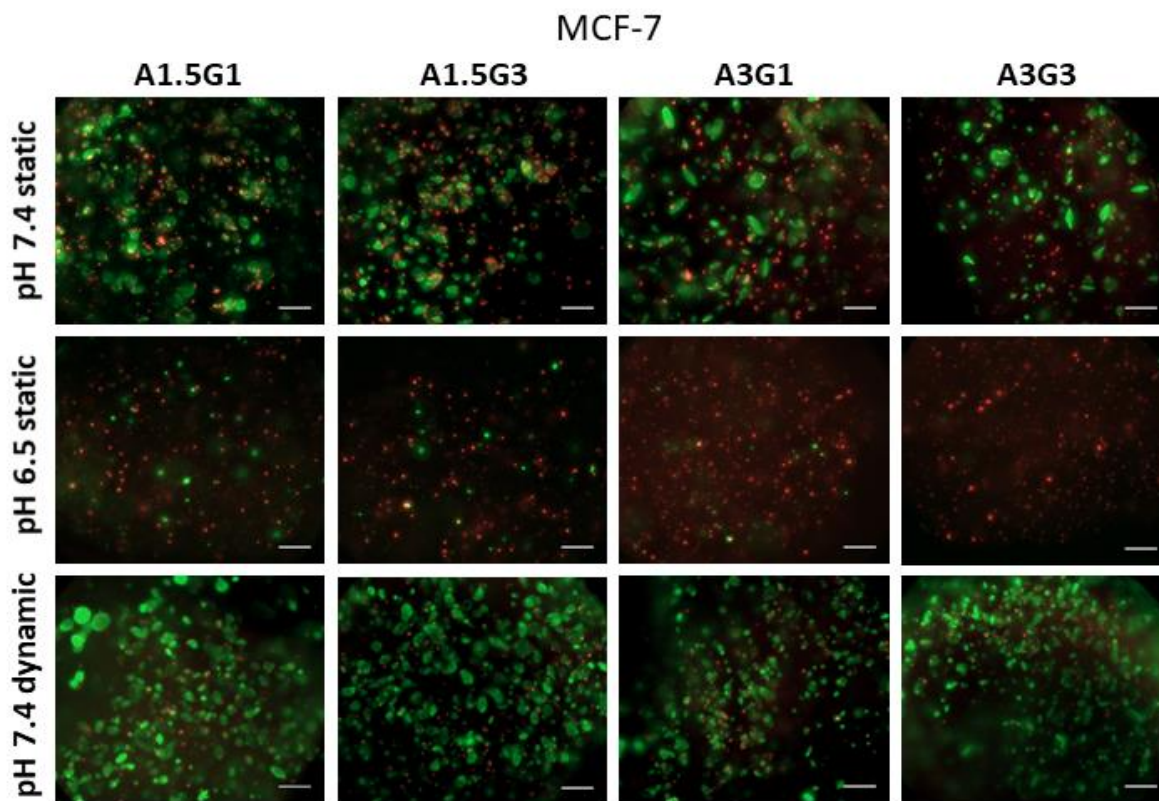


Fig. S 5: Examples of Live/Dead images at day 14: MCF-7 cells in pHe 7.4 static, pHe 6.5 static and pHe 7.4 dynamic. Scale bars 200 μm .

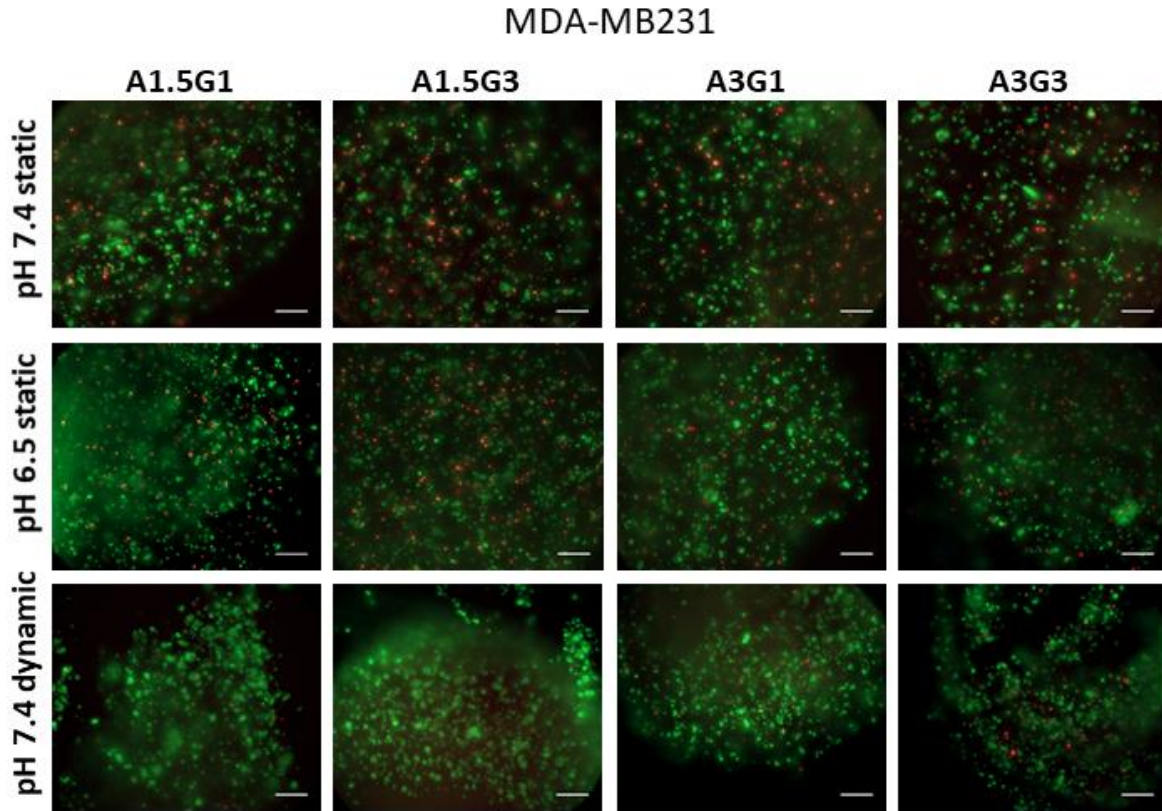


Fig. S 6: Examples of Live/Dead images at day 14: MCF-7 cells in pHe 7.4 static, pHe 6.5 static and pHe 7.4 dynamic. Scale bars 200 μm .

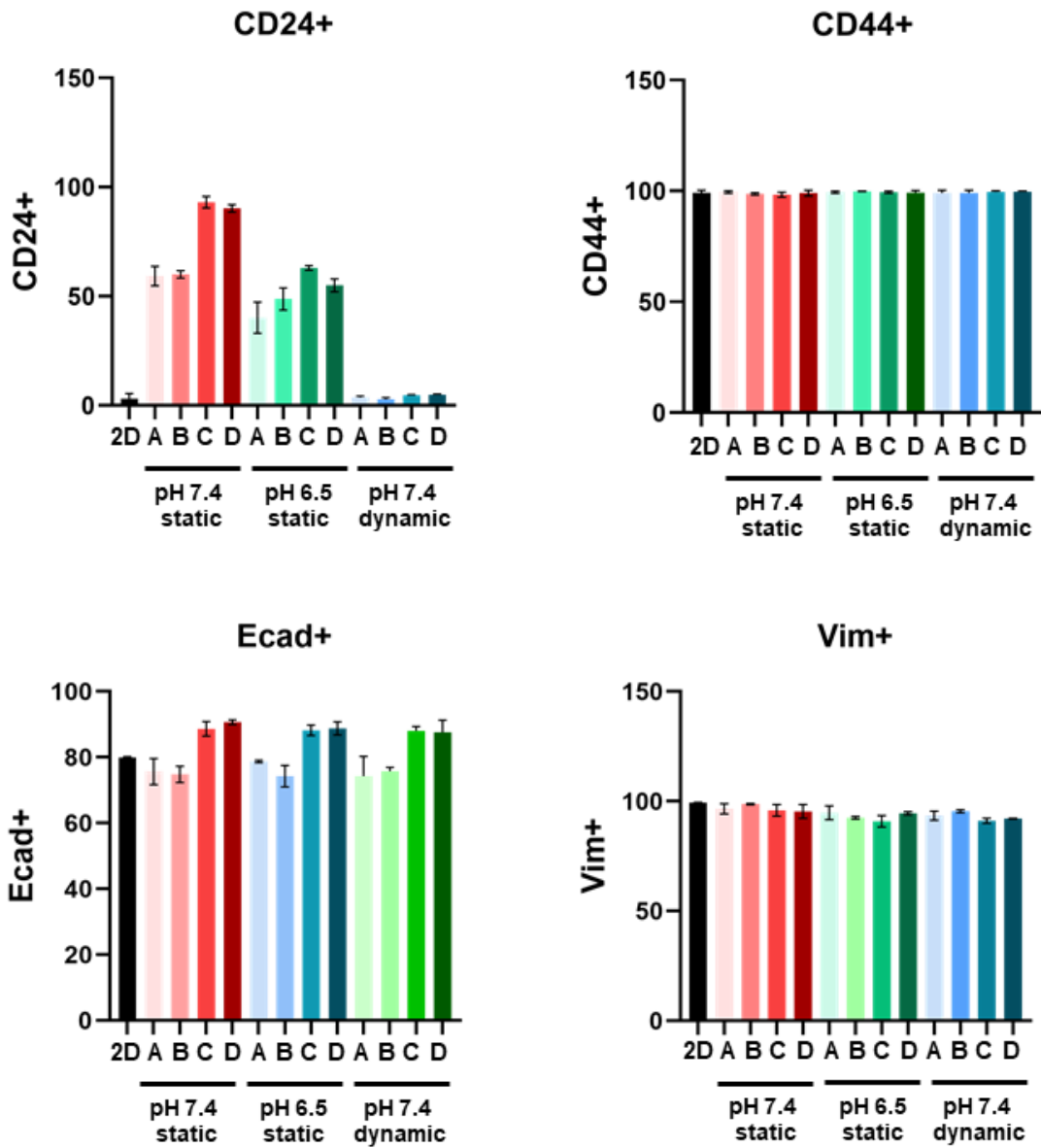


Fig. S 7: Percentage of MDA-MB 231 cells positive for CD24, CD44, E-cadherin and Vimentin cultured in four group of hydrogels (A- A1.5G1, B- A1.5G3, C-A3G1, D- A3G3) in either pHe 7.4 static, pHe 6.5 static or pHe 7.4 dynamic conditions.

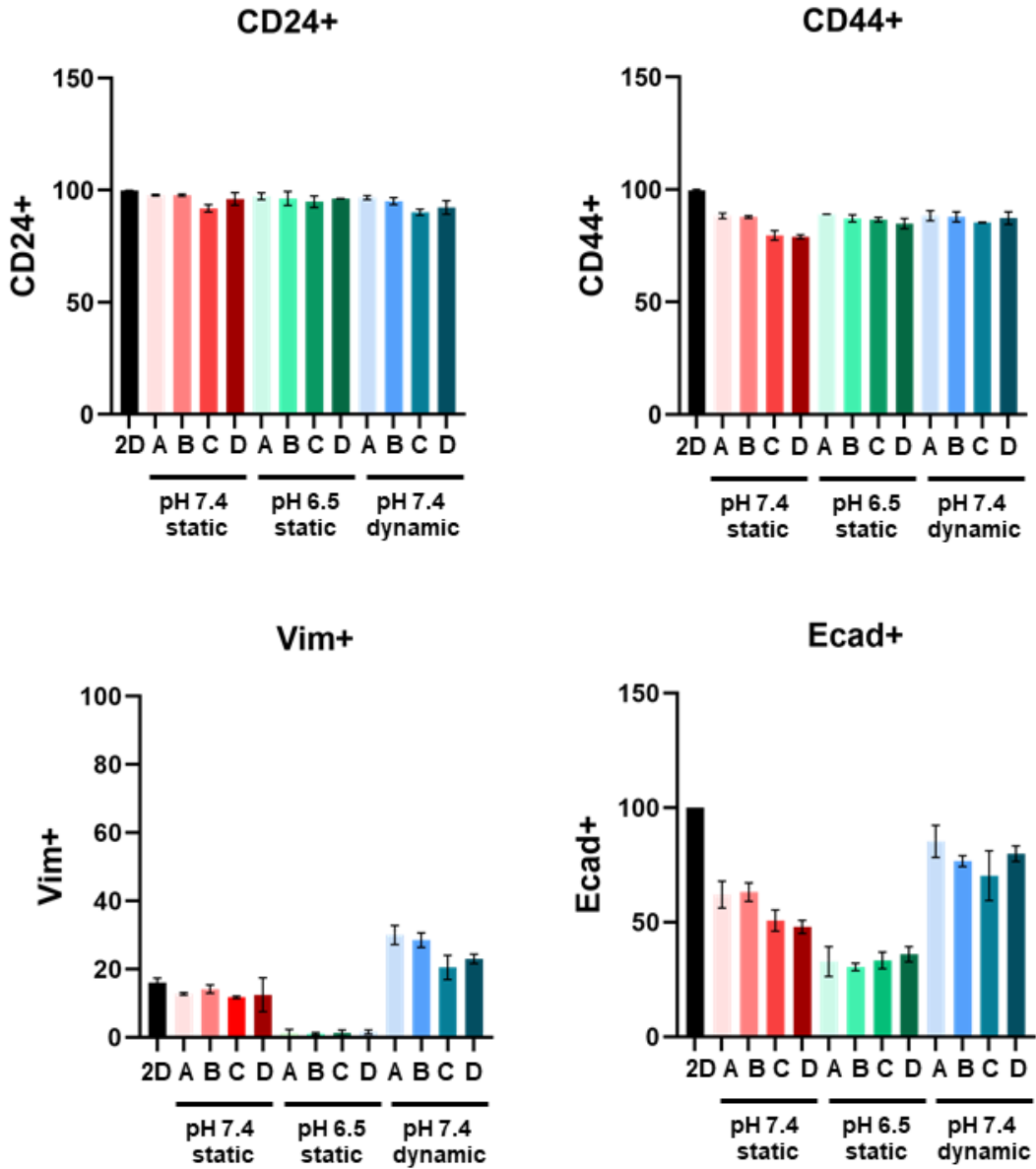


Fig. S 8: Percentage of MCF-7 cells positive for CD24, CD44, E-cadherin and Vimentin cultured in four group of hydrogels (A- A1.5G1, B- A1.5G3, C-A3G1, D- A3G3) in either pH 7.4 static, pH 6.5 static or pH 7.4 dynamic conditions.

Table S1. Percentage of cell aggregates formed when cells are cultured in different hydrogels at static or dynamic conditions

| Cell line Physicochemical cues | MDA-MB 231 Cell aggregates (%) | MCF-7 Cell aggregates (%) |
|-----------------------------------|-----------------------------------|------------------------------|
| Static A1.5G1 | 44.63 | 51.83 |
| Static A1.5G3 | 46.97 | 41.80 |
| Static A3G1 | 29.53 | 43.14 |
| Static A3G3 | 18.45 | 45.03 |
| Dynamic A1.5G1 | 57.45 | 42.18 |
| Dynamic A1.5G3 | 46.97 | 32.92 |
| Dynamic A3G1 | 35.57 | 45.41 |
| Dynamic A3G3 | 33.57 | 51.92 |

Supplementary protocol

S1. Preparation of cylindrical hydrogels for mechanical tests

Cylindrical-shaped hydrogel samples were prepared to determine the stiffness of each alginate-gelatin hydrogel composition used in this study. Briefly, alginate-gelatin mix was added to cylindrical mould of 7 mm in diameter and 7 mm height (tip holder). The holder was incubated at 4°C for 1 hour allowing thermal gelation for shape retention. These gels were transferred to a calcium chloride bath allowing physical gelation for 10 minutes (Ca²⁺ crosslinking with alginate chains). Obtained hydrogel samples were washed twice with HBS for 5 minutes at RT to remove any unbound calcium ion. A total of 18 different hydrogels with controlled crosslinking density were prepared using combination of alginate and gelatin concentrations (summarized in table 1) in 100 mM, 200 mM and 300 mM CaCl₂.

S2. Quantification of compressive moduli

The stress (Pa) was calculated for each dataset dividing the measured force (N) by each sample's contact surface area (m², determined prior each test). The initial length (l₀) of each sample was determined and the displacement of the probe to deform the samples was measured to calculate the deformed length of the sample (l, mm). This value was then used to calculate the strain of each sample from collected displacement data as (l – l₀)/ (l₀). A stress-strain plot was obtained for each

sample, and the slope within the 0.05 strain interval was used to calculate the compressive modulus (kPa) of hydrogels.

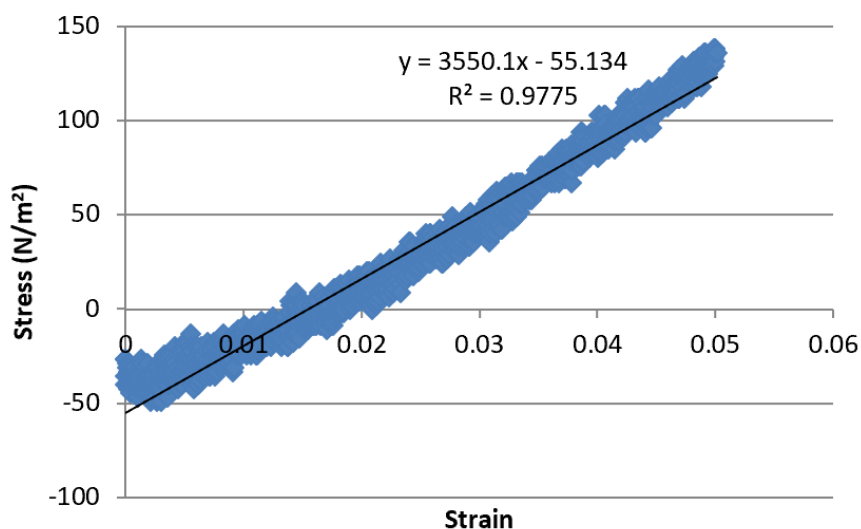


Fig. S 9. An example of Stress (N/m^2) vs strain curve for A3G1 hydrogel. Only 0.05 (or 5%) of strain interval was used to capture the linear range and to calculate the slope i.e Compressive modulus of hydrogel

S3. 3D cell culture: preparation of cell culture media with controlled pH

The pH value of complete DMEM was adjusted to match the reported values of physiological and tumour microenvironments, respectively reported as 7.4 and 6.5²⁸. High glucose DMEM powder (D7777, Sigma Aldrich, UK) was used to prepare a 1× DMEM (aq.) solution, buffered using 25 mM HEPES (pKa = 7.31 at 37°C) and 25 mM PIPES (P1851, Sigma-Aldrich, UK, pKa = 6.33 at 37°C). Solutions of 0.1 M NaOH (J/7620/15, Fisher scientific) and 0.1 M HCl (J/4320/15, Fisher scientific) were used to adjust the pH to 7.4 or 6.5³⁰. After pH adjustment, the media was sterile filtered using the 0.2 μm rapid-flow filter unit (566-0020, Thermo Scientific); the sterile media was stored at 4°C for 4-5 weeks, then discarded. Both pH adjusted media were supplemented with 10% (v/v) FBS and 1% (v/v) L-glutamine prior to use

S4. Sample preparation for Cell proliferation assay

For 3D model in static conditions, cells were cultured in selected alginate-gelatin hydrogels at an initial cell seeding density of 2×10^6 cells/mL. To maintain equal number of cells in all conditions, each well in a 96 well plate contained a 10 μL bead with $\sim 20,000$ cells/bead. At each time point, the cell culture media was gently removed from each well without disrupting the beads. 200 μL of working deep blue solution were gently pipetted into each well, and incubated for 2 hours (37°C,

5% CO₂). After 2 hours, a volume of 100 µL of sample was taken from each well and transferred to a 96 well plate for further reading with the plate reader.

For 3D model in dynamic culture, the flow direction was reversed at each time point to collect media back into the reservoir, followed by removal of cell culture media from the reservoir. After disconnecting the system 1 mL of deep blue solution was directly added to each QV500 chamber without disrupting the hydrogel beads encapsulating cells. The QV500 chambers were placed in incubator (37°C, 5% CO₂) for 2 hours, then 100 µL of the reduced solution was transferred to 96 well plate for further measurements.

S5. Image quantification for cell aggregate size and shape

To identify aggregates as objects, the image of live cells was first processed with thresholding the signal and then converting it to binary. The identified objects were selected by ‘create selection’ feature. Area and shape descriptors of selected cell aggregates were measured using the ‘Analyze particles’ plug-in (Image J, v1.52a): ‘circularity’ was used to describe cell aggregates, to determine the similarity between each object and a circle (i.e., a value of 1.0 indicates a perfect circle, a value of 0.0 indicates an elongated shape).

Thesis context – Chapter 3

Chapter 2 focussed on engineering primary breast tumour site and studying primary breast tumour phenotypes whereas further chapters explore “breast to bone metastasis”. For studying bone metastasis, the first step was to establish a bone *in vitro* model that can mimic bone mechanical properties and tissue architecture. **Chapter 3 – “Additively manufactured BaTiO₃ composite scaffolds: A novel strategy for load bearing bone tissue engineering applications”** is a published research article that studies composite poly-caprolactone (PCL) based scaffolds in developing bone *in vitro* model. PCL is an FDA approved and biocompatible polymer widely used in fabricating hard polymeric scaffolds (described in Chapter 1) and can mimic bone tissue stiffness. Since bone is a highly porous tissue, additive manufacturing or 3D printing technique is advantageous in PCL fabrication as the technique offers homogenous and constant pore size. However, pristine PCL lacks bioactive compounds that can interact with cells. Addition of bioceramics like hydroxyapatite (HA) has been successfully used as HA is a common calcium-based mineral found naturally in the bone ECM. Chapter 3 explores addition of another bioceramic, barium titanate (BaTiO₃) a piezoelectric material with the ability to carry electric charge similar to *in vivo* bone tissue, with potential to enhance osteoblasts proliferation and differentiation. So far, BaTiO₃ has not been combined with 3D printed PCL scaffolds. Hence this chapter compares known PCL composite (PCL HA) with the new PCL BaTiO₃ and study their response compared to pristine PCL (a gold standard in bone tissue engineering) in terms of osteoblast proliferation and potential for bone ECM generation by cells.

Experiments related to mechanical characterisation and dielectric properties of PCL scaffolds reported in this study pave the potential use of these scaffolds in load bearing purposes and after *in vivo* implantation. However, same properties are also advantageous in preclinical *in vitro* models because they render the models with tissue like mechanical features, which is known to affect cellular phenotypes. Although the PCL composite scaffolds herein described have a direct application to repair large bone defects with a load bearing purpose, we also explored their use as *in vitro* bone tissue replicate, further explored in Chapter 4 for studying bone metastasis.

Chapter 3. Additively manufactured BaTiO₃ composite scaffolds: A novel strategy for load bearing bone tissue engineering applications

Elena Mancuso^{1,*}, Lekha Shah², Swati Jindal¹, Cecile Serenelli¹, Zois Michail Tsikriteas³,
Hamideh Khanbareh³, Annalisa Tirella^{2,*}

¹ Nanotechnology and Integrated Bio-Engineering Centre (NIBEC), Ulster University, Shore Road, BT37 0QB Newtownabbey, United Kingdom

² Division of Pharmacy and Optometry, School of Health Sciences, Faculty of Biology, Medicine and Health (FMBH), University of Manchester, Oxford Road, M13 9PT, Manchester, United Kingdom

³ Department of Mechanical Engineering, University of Bath, BA2 7AY Bath, United Kingdom

Mater Sci Eng C Mater Biol Appl., (2021), 126, 112192.

DoI: 10.1016/j.msec.2021.112192

*Corresponding author:

Nanotechnology and Integrated Bio-Engineering Centre (NIBEC), Ulster University, Shore Road, BT37 0QB Newtownabbey, United Kingdom; e.mancuso@ulster.ac.uk

Division of Pharmacy and Optometry, School of Health Sciences, Faculty of Biology, Medicine and Health (FMBH), University of Manchester, Oxford Road, M13 9PT, Manchester, United Kingdom; annalisa.tirella@manchester.ac.uk

Abstract

Piezoelectric ceramics, such as BaTiO₃, have gained considerable attention in bone tissue engineering applications thanks to their biocompatibility, ability to sustain a charged surface as well as improve bone cells' adhesion and proliferation. However, the poor processability and brittleness of these materials hinder the fabrication of three-dimensional scaffolds for load bearing tissue engineering applications. For the first time, this study focused on the fabrication and characterisation of BaTiO₃ composite scaffolds by using a multi-material 3D printing technology. Polycaprolactone (PCL) was selected and used as dispersion phase for its low melting point, easy processability and wide adoption in bone tissue engineering. The proposed single-step extrusion-based strategy enabled a faster and solvent-free process, where raw materials in powder forms were mechanically mixed and subsequently fed into the 3D printing system for further processing.

PCL, PCL/hydroxyapatite and PCL/BaTiO₃ composite scaffolds were successfully produced with high level of consistency and an inner architecture made of seamlessly integrated layers. The inclusion of BaTiO₃ ceramic particles (10% wt.) significantly improved the mechanical performance of the scaffolds (54 ± 0.5 MPa) compared to PCL/hydroxyapatite scaffolds (40.4 ± 0.1 MPa); moreover, the presence of BaTiO₃ increased the dielectric permittivity over the entire frequency spectrum and tested temperatures. Human osteoblasts Saos-2 were seeded on scaffolds and cellular adhesion, proliferation, differentiation and deposition of bone-like extracellular matrix were evaluated. All tested scaffolds (PCL, PCL/hydroxyapatite and PCL/BaTiO₃) supported cell growth and viability, preserving the characteristic cellular osteoblastic phenotype morphology, with PCL/BaTiO₃ composite scaffolds exhibiting higher mineralisation (ALP activity) and bone-like extracellular matrix deposition (osteocalcin and collagen I) by cells. The single-step multi-material additive manufacturing technology used for the fabrication of electroactive PCL/BaTiO₃ composite scaffolds holds great promise for sustainability (reduced material waste and manufacturing costs) and it importantly suggests PCL/BaTiO₃ scaffolds as promising candidates for varied applications such as preclinical bone *in vitro* models or load bearing bone tissue engineering applications to solve unmet clinical needs.

Keywords: barium titanate, PCL, composite scaffolds, bone tissue engineering, additive manufacturing, extrusion-based technology.

1. Introduction

Unlike in other tissues, most bone injuries are able to heal spontaneously, thanks to the self-regeneration ability of human bone and without the need for further treatment [1,2]. However, in complex conditions such as critical size bone defects, or in cases where the regenerative process is compromised (i.e. atrophic non-unions, avascular necrosis and osteoporosis), additional reconstructive intervention is necessary. To overcome the shortcomings of traditional strategies (i.e. autografts, allografts and xenografts), tissue engineering emerged as a promising approach for the management of bone defects [3–6]. Such engineered tissue with matched *in vivo* mechanical properties can also be used as *in vitro* bone models for preclinical needs such as platforms for preliminary cancer therapeutics.

Inspired by the composition of native bone, which is primarily made up of collagen fibrils and hydroxyapatite (HA) crystals (naturally occurring mineral form of calcium apatite found in bones), the use of composite materials has received great attention towards the development of bone tissue engineering scaffolds. Typical composite biomaterials fit to this purpose are polymeric matrix (e.g. polycaprolactone (PCL), polylactic acid (PLA)) filled with bioactive ceramic particles, including tricalcium phosphate (TCP) and HA [7–10]. With this strategy, the already excellent characteristics of polymers to reproduce bone tissue features, such as processability and mechanical properties, are further improved with the inclusion of the bioactive ceramic phase to better mimic natural bone composition [7–10].

Moreover, electrical effects have been recently shown to play an important role in bone growth, remodelling and fracture healing [11]. Natural bone exhibits an electrical potential in response to mechanical stimuli due to its inherent piezoelectric property [12], manufacturing strategies to obtain composite scaffolds including bioactive materials capable of mimicking such property would pose a step stone to restore critical size bone defects. Among piezoelectric ceramics (i.e. lithium niobate, potassium sodium niobate and lithium-doped potassium sodium niobate), barium titanate (BaTiO_3) represents the most investigated lead-free piezoceramic [13]. In addition to its good biocompatibility and intrinsic capacity to sustain a charged surface, BaTiO_3 has shown great

ability to improve bone cells' adhesion and proliferation [12,14]. In a study by Li et al., the incorporation of BaTiO₃ nanoparticles into randomly oriented poly-(l-lactic acid) (PLLA) electrospun scaffolds enhanced the osteogenic differentiation of bone marrow mesenchymal stem cells (MSCs) [15]. Etherami et al. found that the piezoelectric effect of highly porous BaTiO₃ scaffolds, produced through the conventional foam replication method and then coated with gelatine/HA, greatly improved the proliferation, differentiation, and extracellular matrix deposition of osteoblast-like cells [16]. Also, BaTiO₃ particles filled into a PCL/calcium sulfate whisker (15 wt%) matrix were used to prepare ternary composites. Even though the piezoelectric coefficient of the ternary composite decreased in comparison to the PCL/ BaTiO₃, the presence of the calcium sulphate whisker contributed to enhance by 50% the flexural strength of the resulting composite and in the range of human cancellous bone [17].

Despite the fact that combination of polymers and ceramics have successfully addressed many of the limitations deriving from the use of single-phase biomaterials, scaffolds produced by conventional technologies still suffer from several shortcomings. Mainly they lack adequate control in terms of porosity and pore sizes, as well as mechanical properties and material composition throughout the structure. Also, they are inherently incapable to mimic complex architectures and with highly level of reproducibility for patient-specific applications [18,19]. Additionally, conventional biomanufacturing (i.e., solution electrospinning, freeze-drying, solvent casting) for the processing of composite materials often involves the use of organic solvents, whose inherent harmful effects further challenge their subsequent biological performances [15,17].

The design, architecture, porosity and fabrication methods are all crucial features that, together with biomaterial physico-chemical properties, contribute to the successful performance of a scaffold for bone tissue engineering and *in vivo* like mechanical properties[20,21]. Additive manufacturing (AM) techniques (described in Chapter 1, Section 3.3), including binder jetting and fused deposition modelling (FDM), enable the design and fabrication of patient-specific substitutes with precise structural configurations [22–24] with higher degree of porosity and pore interconnectivity than conventional technologies [18,19]. Moreover, in the last decade AM technologies have greatly contributed to the design of bone tissue scaffolds with integrated and tailorable functionalities (including biochemical, electrical and mechanical) [25]. Recent studies have explored the development of composite scaffolds containing specific micro/nano-fillers, and

which allow scaffolds to become bioactive [26,27], perform a specific function in response to an external stimulus (i.e., heat, light, magnetic field or pH) as well as change their shape or colour [28–31].

Although great achievements have been attained, the challenges in the processing of ceramic-based materials are still greatly hampering the manufacturing of 3D composite scaffolds with functional properties. In a recent study by Polley et al., BaTiO₃/HA composite scaffolds have been produced via binder jetting 3D printing. Although a good degree of customisation was achieved, along with a highly interconnected porous structure (open porosity = 50%), and piezoelectric properties comparable to human bone, due to their inherent brittleness the composite scaffolds showed very limited ability to withstand mechanical loadings (compressive strength of 150 ± 120 kPa) [32].

Furthermore, the processing and formulation of the raw materials often increase the complexity of the product development cycle as well as the manufacturing costs. Scaffolds produced by binder jetting generally require a final sintering step, which is necessary to consolidate the mechanical integrity of the printed structure. Whereas, FDM technologies require the additional extrusion step to produce a composite filament, which is then used to produce 3D scaffolds [33]. Lately, several studies, including some of the authors, have demonstrated the advantages in using multi-material extrusion-based AM technology as emergent manufacturing approach for the production of composites scaffolds [9,34–37]. Although, to the best of our knowledge, only limited research has been conducted so far to exploit this environmentally friendly and versatile strategy for the manufacture of biodegradable composites based on piezoelectric materials.

Given the existing evidence that piezoelectric characteristics of BaTiO₃ have positive effects on natural bone formation pathways [12,14], and to enable its wider adoption in load bearing tissue engineering applications, in this study we focused on the fabrication, characterisation and biological validation of composite PCL scaffolds incorporating BaTiO₃ particles. PCL was selected as polymeric matrix material due to its thermoelastic behaviour, low melting point and ease of processing, remarkable mechanical strength, biocompatibility, as well as being an FDA approved biodegradable polymer. The physico-chemical, mechanical and electrical properties of the additively manufactured PCL/BaTiO₃ scaffolds were assessed and compared against pure PCL and PCL/HA. BaTiO₃ was compared to HA as ‘HA’ is most commonly used ceramic for bone tissue engineering purposes because of its natural occurrence in bone. The addition of BaTiO₃

ceramic particles increased both the mechanical performance and the dielectric permittivity, with decreased dielectric loss in the composite scaffolds. All tested scaffolds supported the adhesion of human osteoblasts (i.e. Saos-2), with increased proliferation and extracellular matrix deposition in both PCL/HA and PCL/BaTiO₃ scaffolds up to 28 days. In particular, after incubation with mineralisation media, calcium phosphate and osteocalcin deposition were observed in both composite scaffolds; the increased deposition of collagen I in PCL/BaTiO₃ scaffolds may suggest this configuration as more suitable for bone tissue engineering applications.

2. Materials and methods

2.1 Design and manufacturing of 3D scaffolds

PCL powder ($M_w = 40,000\text{--}50,000$, $M_n = 45,000$ and particle size $<600\ \mu\text{m}$) was purchased from Polyscience Europe (Germany), BaTiO₃ powder ($D_{90} = 4.0\ \mu\text{m}$) was purchased from Ferro Ltd. (UK), and sintered HA was supplied by the Biomaterials Innovation and Development Centre of Riga Technical University (Riga, Latvia) and produced as reported in [9].

Scaffold manufacturing (Figure 1A) was performed as previously described [9,34]. For composite scaffolds, the powder-based materials were homogeneously mixed with 10% wt. ceramic content, as reported in Table 1. Previously, inclusion of 20% ceramic (HA) content in PCL lead to white spots in SEM images (as opposed to smooth surface of 10%) indicating inhomogeneous mixing due to increased ceramic content, hence 10% wt. was finalised for these scaffolds [9]. The powder was placed into heated metal cartridges and extruded following optimised parameters through a blunt tip needle (0.4 mm inner diameter) and by using a commercial 3D Bioplotter extrusion system (EnvisionTEC, Germany). 3D porous cylindrical models (3 and 6 mm height, 7 mm diameter) were designed in Solid Edge™ 3D software, then the Computer-aided design (CAD) model was uploaded into Perfactory Software Suite (EnvisionTEC, Germany) and sliced to obtain 420 μm slicing thickness (Figure 1B). Cylindrical specimens were printed continuously, with a spacing of 0.8 mm between strands and an offset between each layer equal to half of the strands' distance (Figure 1C).

Table 1. Summary of processing conditions used to fabricate polymeric PCL scaffolds, PCL/HA and PCL/BaTiO₃ composite scaffolds.

| <i>Sample</i> | <i>Composition (wt %)</i> | <i>Printing Temperature (°C)</i> | <i>Printing Pressure (bar)</i> | <i>Printing speed (mm/s)</i> | <i>Pre/Post Flow (s)</i> |
|------------------------------|---------------------------|----------------------------------|--------------------------------|------------------------------|--------------------------|
| <i>PCL</i> | 100 | 130 | 6 | 0.6 | 0.75/0.10 |
| <i>PCL/HA</i> | 90/10 | 130 | 6.5 | 0.5 | 0.75/0.10 |
| <i>PCL/BaTiO₃</i> | 90/10 | 125 | 5.5 | 0.7 | 0.75/0.10 |

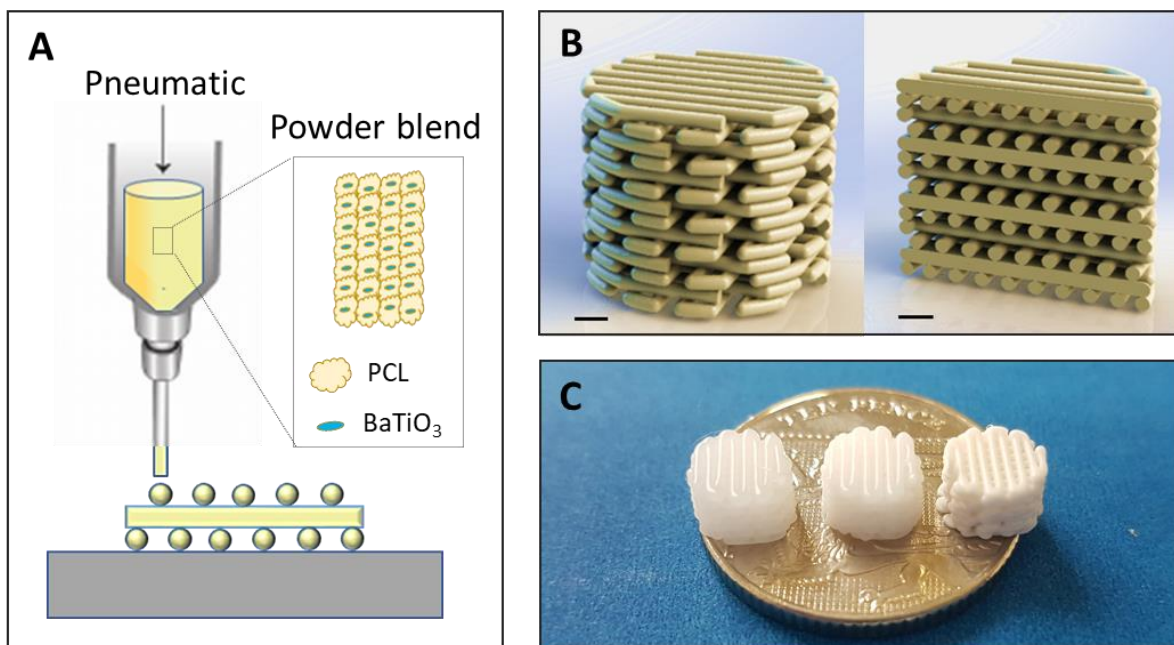


Figure 1. Manufacturing of polymeric and composite scaffolds: (A) Schematic representation of the extrusion-based additive manufacturing process; (B) CAD model of the scaffold 3D volume and corresponding cross section (scale bar = 1 mm); (C) representative image of the final 3D printed PCL (left), PCL/HA (centre) and PCL/BaTiO₃ (right) scaffolds.

2.2 Physicochemical characterisation and mechanical properties evaluation

2.2.1 Attenuated Total Reflectance Fourier Transform Infrared Spectroscopy (ATR-FTIR)

The composition of raw materials was analysed via Attenuated Total Reflectance Fourier Transform Infrared Spectroscopy (ATR-FTIR) using a Nicolet iS5 (Thermo Scientific, UK) system, equipped with an iD5 ATR diamond crystal window. FTIR spectra were recorded in the range of 400 – 4000 cm^{-1} .

2.2.2 Thermogravimetric analysis (TGA)

In order to assess the ceramic content in the extruded filaments after printing as well as their thermal behaviour upon heating, thermogravimetric analysis (TGA) was performed. The analyses were performed in nitrogen atmosphere by using a TGA2 METTLER TOLEDO™ instrument with a resolution of 1 μg and weighing accuracy of 0.005%. All the samples (PCL, PCL/HA and PCL/BaTiO₃), with an initial weight of ~ 15 mg, were tested in the range of temperature between 50 and 600°C at a heating rate of 10°C/min.

2.2.3 Imaging: Scanning Electron Microscopy (SEM) and Micro-Computed Tomography (micro-CT)

The microstructure of the printed composite scaffolds and the dimension of the printed strands was measured using images acquired by Scanning Electron Microscopy (Hitachi FE-SEM SU5000) at voltage of 3.0 kV and working distance between 5 and 8 mm. In addition to this, the 3D architecture of the scaffolds and the distribution of the bioceramic phases were evaluated by using a micro-Computed Tomography (micro-CT) scanner (Skyscan 1275, Bruker, Belgium) equipped with a source voltage of 40 kV and a current of 250 μA , setting the pixel detector resolution to 10 μm . All the scaffolds were scanned with a 49 ms exposure in a 360 scan with 0.2° increment to improve image quality and reduce noise. For image reconstruction, the Bruker NRecon Software (Bruker, Belgium) was used with 15% beam hardening reduction and no ring artefact reduction. The overall porosity of the scaffolds was calculated theoretically from the CAD design as reported by Moroni et al. [38], and also experimentally through the actual dimensions of the specimens (n=3) measured from the 2D sections, and by using the Bruker CTAn software.

2.2.4 Mechanical properties

The mechanical properties or stiffness of the scaffolds were measured via uniaxial compressive tests. For this purpose, cylindrical samples were printed with diameter of 7 mm and thickness of 6 mm (a total of 12 layers). Tests were performed using a universal testing machine (Instron 5500S, Instron, UK) equipped with a 500 N load cell. The uniaxial testing was conducted at a constant loading rate of 0.5 mm/min and maximum loading of 490 N. All the specimens (n=5) were subjected to a preload of 2 N before starting of the test. All tests were performed on dry samples at room temperature. The modulus was calculated from the linear range of the stress–strain curve for each sample. All experimental data are presented as mean \pm standard deviation (SD).

2.3 Dielectric and piezoelectric properties

The electrical response of the printed composite scaffolds was examined through impedance spectroscopy using a 1260A Impedance/Gain-Phase Analyzer (Solartron Analytical, UK). The fabricated composites were tested in the frequency range from 0.1 Hz to 100 kHz at room temperature (RT) and 40°C. A poling study was performed using a Corona poling set-up and the effect of time, temperature, and the electric field strength on the poling efficiency of the composites was studied. Firstly, poling was performed at room temperature by varying the applied voltage (5 kV, 10 kV, 15 kV and 20 kV) for 5 hours in each individual voltage. Afterwards, the composites were poled with an applied potential of 20 kV at increasing applied temperatures (40°C, 45°C, 50°C and 55°C), while held for 5 hours at each individual one. The d₃₃ values of the composites were recorded after each poling step using a d₃₃ Berlincourt piezometer supplied by Piezotest at 97 Hz. The polarisation-electric field (P-E) hysteresis loops were recorded using the Sawyer-Tower circuit at 100 Hz and room temperature with a high-voltage amplifier (Precision RT66C Ferroelectric Tester) supplied by Radiant Technologies.

2.4 *In vitro* cell studies

2.4.1 Cell culture

Human bone osteosarcoma Saos-2 cell line was kindly provided by Dr Olga Tsikou (The University of Manchester) and maintained in McCoy's 5A media (M9309, Sigma-Aldrich, UK) supplemented with 15% v/v FBS (10500064, Gibco, UK) and 1% v/v penicillin-streptomycin

(P0781, Sigma-Aldrich, UK). Cells were cultured in standard cell culture conditions (37°C, 5% CO₂), passaged when reached confluency and kept at a cell density of 3×10^5 cells/cm². Prior use, Saos-2 were tested Mycoplasma negative by Mycoalert mycoplasma detection kit (Lonza, UK). All the experiments were performed with Saos-2 from passage 11 to passage 20, then cells were discarded.

2.4.2 Scaffold cell seeding and mineralisation protocol

Scaffolds were sterilised prior to cell seeding as previously described [9]. All the following steps were performed in a class II biological safety cabinet. Briefly, scaffolds were immersed in 70% v/v ethanol (aq.) and incubated for 20 minutes at RT; scaffolds were washed three times with 1× PBS. The scaffolds were placed in a non-TC treated sterile 48 well plate and further exposed to UV-C light for 30 minutes each side. After sterilisation, 2×10^5 Saos-2 cells were suspended in 50 µL volume of complete media and gently pipetted on the top of each scaffold. Scaffolds were incubated for 30 minutes (37°C, 5% CO₂) allowing cell adhesion, then a volume of 400 µL of complete media was gently pipetted in each well covering the whole scaffold. Cell culture media was replaced after 4 days, and after 7 days of culture (37°C, 5% CO₂), the culture media was changed to Osteoblast mineralisation media (C-27020, PromoCell) to induce mineralisation and changed thereafter every 4 days and until the end point (i.e. day 28).

2.4.3 Proliferation assay

Cell proliferation was quantified by Alamar blue assay using Deep blue cell viability reagent (424702, BioLegend, UK). Briefly, at each time point, cell culture media was removed from each well and replaced with a 400 µL volume of 10% v/v deep blue viability reagent in complete media. Cells were incubated for 2 hours (37°C, 5% CO₂), then a volume of 200 µL was transferred to a 96 well plate and the fluorescence was measured using a plate reader (Ex 530-570 nm /Em 590-620 nm, Synergy-2, Biotek, UK). After each time point, a 400 µL volume of complete fresh media was added to each well, avoiding any interference in future readings. Of note and prior to each measurement, the scaffolds were transferred to a new sterile well plate to measure proliferation of cells on the scaffold only. Experiments were performed in triplicate for each time point and type of scaffold tested and repeated for biological duplicate. For each scaffold and time point, data are presented as mean ± SD (n=2, N=3).

2.4.4 Alkaline phosphatase activity (ALP) assay

At selected time points, cells were fixed with 4% v/v formaldehyde solution (1004968350, Sigma-Aldrich UK) for 10 minutes followed by washes with 1× PBS. The cells were then permeabilised with a solution of 0.1% v/v Triton-X in 1× PBS for 15 minutes and finally washed three times with 1× PBS. Cellular alkaline phosphatase activity (ALP) was quantified for each type of scaffold tested (n=3) using ALP Diethanolamine activity kit (AP0100, Sigma-Aldrich, UK) following manufacturer's instructions. Briefly, after permeabilization, a 1 mL volume of ALP reaction buffer was added to the scaffolds. A 0.67 M pNPP substrate solution was prepared in ultrapure water and a 1 µL volume of this solution was added to the scaffolds, previously immersed in ALP buffer. Scaffolds were incubated for 15 minutes at 37°C. The enzymatic activity was immediately measured with absorbance readings at 405 nm (Synergy-2 plat reader, Biotek, UK). Readings were converted to units/mL using a calibration curve obtained by measuring known amounts of ALP enzyme (U/mL) using the same method previously described and in the range of 0.15 U/mL and 10 U/mL. Finally, ALP activity was normalised to cell number, with each U/mL values divided by the cell proliferation reading (Alamar blue) measured for the corresponding scaffolds. For each scaffold and time point, data are presented as mean ± SD (n=2, N=3).

2.4.5 Alizarin-red staining and deposited calcium quantification

To quantify calcium deposition, scaffolds were fixed with 4% v/v formaldehyde solution at selected time points (day 21, day 28, n=2, N=3). After fixation, scaffolds were washed with ultrapure water and then incubated with Alizarin-red staining solution (TMS-008-C, Sigma-Aldrich, UK) for 15 minutes at room temperature on a plate shaker. Excess stain was removed by additional washes (n=3) with ultrapure water, then scaffolds were washed with acetone (n=1) and left to dry at room temperature. To quantify the reacted and deposited alizarin stain on the scaffolds, a 2 mL volume of 0.2M NaOH:MeOH (1:1) solution was added to dissolve the stain for each scaffold, then a volume of 200 µL was transferred to another well-plate and measured by absorbance reading at 405 nm (Synergy-2 plate reader, Biotek, UK). A calibration curve obtained from known concentration of Alizarin red stain (mM) in 0.2M NaOH:MeOH was used to calculate the deposited calcium. For each scaffold and time point, data are presented as mean ± SD (n=2, N=3).

2.4.6 Immunofluorescence staining and image acquisition

The morphology of Saos-2 cells on scaffolds was analysed by immunofluorescence staining using DAPI (Thermofisher, UK) and Alexa Fluor™ 488 Phalloidin (A12379, Thermofisher, UK) for nucleus and F-actin, respectively. Briefly, each scaffold was fixed with 4% v/v paraformaldehyde for 10 minutes and permeabilised with 0.1% Triton-X for 10 minutes at RT. After washes the scaffolds were incubated with a mix of DAPI (1 µg/mL) and Phalloidin (1:80) in 1× PBS for 30 minutes at RT and in the dark. Samples were washed three times with 1× PBS and stored immersed in 1× PBS at 4°C in the dark.

Collagen I and osteocalcin immunofluorescence staining were performed on the scaffolds to detect any deposition of extracellular matrix after 28 days of culture. For this staining, scaffolds were fixed with 4% v/v paraformaldehyde for 5 min at RT, washed three times with 1× PBS and then incubated with blocking buffer (1% w/v BSA in 1× PBS) for 1 hour at RT to avoid non-specific antibody binding. Scaffolds were washed with 1× PBS, and then incubated with Osteocalcin monoclonal antibody (1:500 dilution in 1× PBS, MA1-82975, Thermofisher, UK) and Collagen-I polyclonal antibody (1:250 dilution in 1× PBS, PA5-95137, Thermofisher, UK) overnight (16 h) at 4°C. After three washes with blocking buffer, samples were incubated with a solution of secondary antibodies Goat anti-rabbit 488 (1:2000 dilution in 1× PBS, A-11008, Thermofisher, UK) and Goat anti-mouse 594 (1:2000 dilution in 1× PBS, A-11005, Thermofisher, UK) for 30 minutes at RT following manufacturers instruction. Samples were washed three times with blocking buffer and stored immersed in 1× PBS at 4°C in the dark.

Images of scaffolds were acquired using the fluorescent inverted microscope (Leica DMI6000, Leica Microsystems, UK) coupled with a 5.5 Neo sCMOS camera (Andor, UK). The µManager software (v.1.46, Vale Lab, UCSF, USA) was used to control both microscope and camera, as well as to capture images. For acquisitions, a dry 10× objective (PL 10x/0.3 PH1, Leica), a dry 20× objective (PL 20x/0.5 PH2, Leica) and a dry 63× objective (PL 63x/0.9 PH2, Leica) with filter cubes (A4, I3 and N2.1) was used. All images were post-processed to remove background noise using ImageJ v1.49p.

2.5 Statistical Analysis

For the mechanical analysis, differences between groups were determined by using a Paired t-test using a level of statistical significance (p) < 0.05. All experimental data are presented as mean \pm SD.

For all cellular experiments, data are presented as average of at least three (N=3) independent experiments \pm SD, unless otherwise stated. For further references, technical replicate are denoted as ‘n’ and biological replicate as ‘N’). One-way analysis of variance (ANOVA) with Brown-Forsythe and Welch was performed using GraphPad Prism v9.1.0, as to analyse the significant differences among results for cell proliferation, ALP and Alizarin Red quantification. Probabilities were set at four different significance levels: $p < 0.05$ (* $p \leq 0.05$, ** $p \leq 0.01$, *** $p \leq 0.001$, **** $p \leq 0.0001$).

Paired t-test was used to compare the same scaffold at two time points for Alizarin Red stain quantification since they were related and dependent. The p-values obtained are mentioned under the representative figure.

3. Results and Discussion

3.1 Physicochemical and mechanical characterisation

ATR-FTIR analysis is an infrared based spectroscopy technique that gives information about chemical composition and chemical interactions (characteristic bonds like C-H or C=O etc) among liquid and solid polymers. A material has its own signature peaks that defines combination of different chemical bonds within its composition. This technique was performed on raw materials in order to confirm the presence of HA and BaTiO₃ inorganic phases into the mixed PCL-based powders by comparing their spectroscopic graph peaks. As reported in Figure 2A, both the PCL/HA and PCL/ BaTiO₃ spectra showed the characteristic bands of PCL (Figure 2A, black line); specifically the C-H stretching (2943 and 2865 cm⁻¹), the C=O carbonyl group at 1720 cm⁻¹, the CH₂ deformation band 1165-1468 cm⁻¹, the backbone C—O and C—C stretching of the crystalline phase 1293 cm⁻¹, and the C—O—C symmetric and asymmetric band at 1239 cm⁻¹, 1164 cm⁻¹, 1107 cm⁻¹, 1047 cm⁻¹ were detected [39]. Moreover, in the PCL/HA spectra (Figure 2A, red line) the characteristic peaks of pure HA were observed as: the O-H and (PO₄)₃ groups and respectively at

560, 600 and 1041 cm^{-1} [40]. The PCL/BaTiO₃ spectra (Figure 2A, blue line) showed the Ti-O stretching vibration peak at 559 cm^{-1} and the distinctive shape of BaTiO₃ spectrum (Figure 2A, green line), which confirmed the presence of this phase into the PCL/BaTiO₃ composite material [41]. Although the inorganic phases were incorporated at smaller amount (10% wt.) within the composite material, it was possible to detect their distinctive peaks via FTIR analysis.

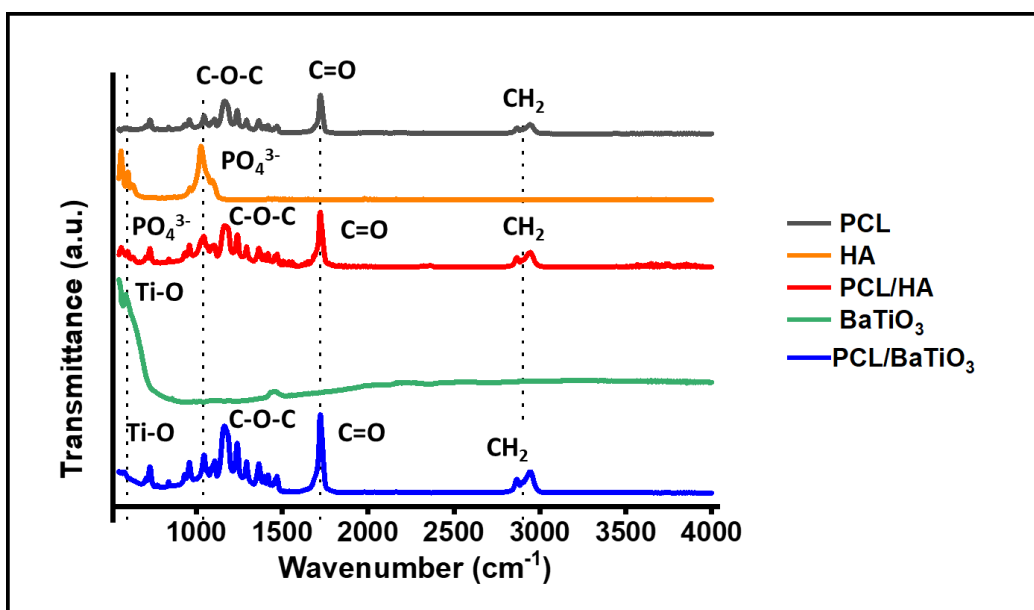


Figure 2. FTIR spectra comparing PCL (black), HA powder (orange), BaTiO₃ powder (green), PCL/HA composite powder (red) and PCL/BaTiO₃ composite powder (blue).

TGA analysis is used to determine a material's thermal stability and its fraction of volatile components by monitoring the weight change that occurs as a sample is heated at a constant rate. The analysis was performed to evaluate the behaviour upon heating of the extruded materials and if the amount of bioceramics incorporated within them affect their thermal stability (Figure 3). Single step degradation and a pronounced mass loss was observed for all the samples (Figure 3A). According to the analysis, a structural decomposition started at temperature above 250°C, thus confirming the stability of all the compositions during the printing process. Both composite materials shown a slightly higher temperature requirement for degradation in comparison to pure PCL, with the 50% of the weight loss occurring at 385°C, 395°C and 405°C for the PCL, PCL/HA and PCL/BaTiO₃ respectively. After 550°C the remaining mass in the composite samples was relatively constant and content close to the theoretical value of 10% wt. (10.05 ± 1.3 % wt. for

PCL/HA and 12.5 ± 1.9 % wt. for PCL/BaTiO₃ scaffolds). Also, as shown by the TGA first derivatives curves (Figure 3B) the presence of the inorganic phases contributed to a slight shift in the maximum peaks towards higher temperatures, indicating the effect of the bioceramic particles in delaying the materials' degradation rate [42].

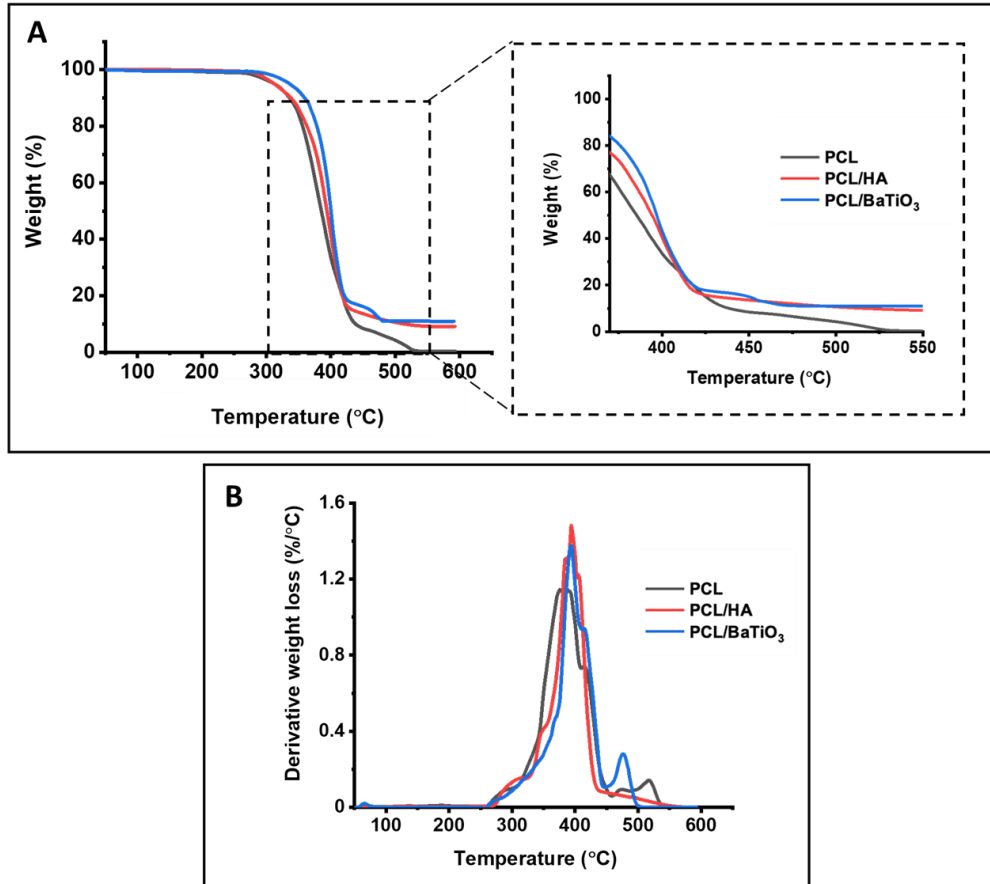


Figure 3. Thermal characterization of the samples after extrusion: **(A)** TGA thermograms and the zoom of the selected area indicating the remaining mass in each sample, and **(B)** TGA first derivative curves of PCL (black), PCL/HA (red) and PCL/BaTiO₃ (blue).

Scaffold morphology is known to greatly affect *in vitro* cell behaviour, with pore size, pores interconnectivity and surface characteristics, playing the most important role in promoting cell–scaffold interactions such as cell adhesion and migration, as well as proliferation [22,43]. SEM observations of the 3D printed scaffolds at low magnification (Figure 4) showed the shifted pattern design and the resulting interconnected macro-porosity, matching the CAD design across all the scaffolds and proving the suitability of the printing process. A uniform strand diameter was

measured across all groups, with an average strand diameter approximately 31 μm bigger than the theoretical target value (400 μm). This behaviour, observed across all the materials used in this study, is typical of viscoelastic polymer-based biomaterial inks, and due to its expansion upon extrusion from the nozzle [44]. At higher magnification (1000X) it was possible to appreciate the presence of uniformly distributed micro-pores on all the scaffolds. Moreover, no agglomeration or clumping of the ceramic particles was detected in any of the high-magnification images of the composite-based samples, supporting good mixing of the two materials prior printing. Back scattered electrons (BSE) are high-energy electrons used to obtain high-resolution images that show the distribution of various elements that make up a sample. BSE mode confirmed presence of ceramics within composite PCL/HA and PCL/BaTiO₃ at high resolution compared to a homogenous image of pristine PCL.

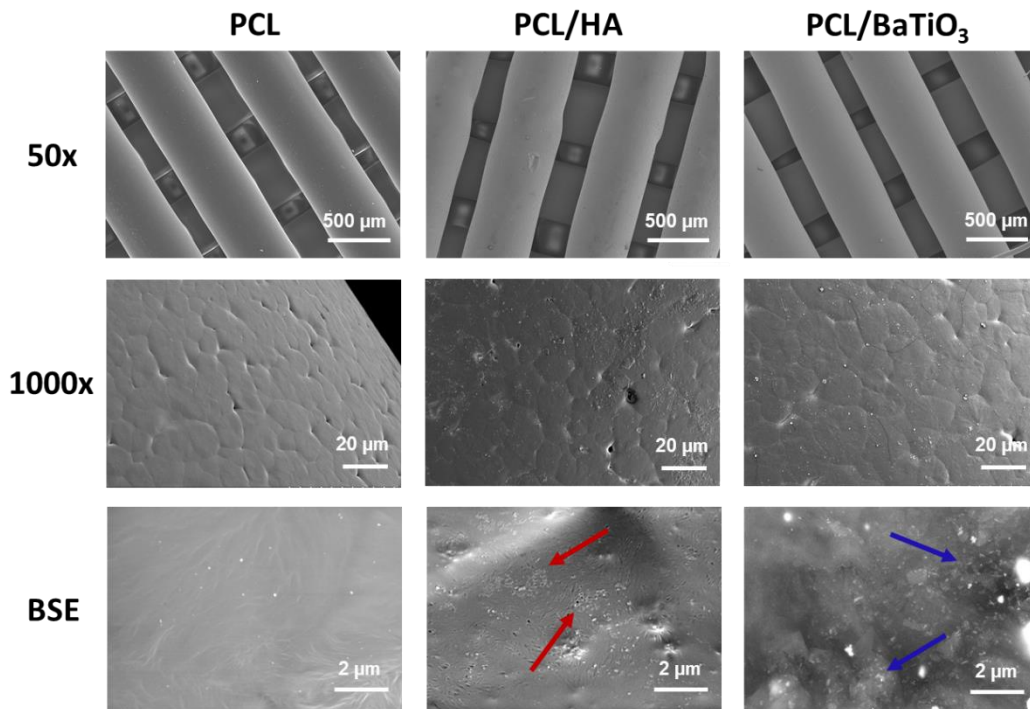


Figure 4. SEM morphological evaluation of the 3D printed scaffolds at different magnifications showing strands and surface. Images acquired with the Backscattered Electron (BSE) mode evidenced the presence of HA (red arrows) and BaTiO₃ (blue arrows) particles. All images were captured using a top-view scan.

Micro-CT analysis was performed to evaluate the overall scaffolds' architecture, as well as the inner structure of the 3D printed scaffolds. As pore size and scaffold architecture impacts on cellular phenotypes, it is preferable to have uniform characteristics to have homogenous cellular

phenotypes. The CAD designed repeating lattice structure renders the scaffold with uniform pore size, architecture and interconnected porosity. As shown in Figure 5, the micro-CT reconstructions of all scaffolds evidenced a uniform geometry and a consistent structural integrity along with a high fidelity to the CAD model dimensions. Regular pore size and defined circular cross-sections of the printed filament was observed in the cross-sectional reconstructions across all the groups (Figure 5B, 4E, 4H). From these datasets, it is also evidenced the uniform distribution of the ceramic phase in the PCL matrix for the composite-based scaffolds, further supporting the appropriate mixing step of the raw materials [45]. Experimental data derived from the micro-CT reconstructions also supported the assessment of the 3D scaffolds' porosity.

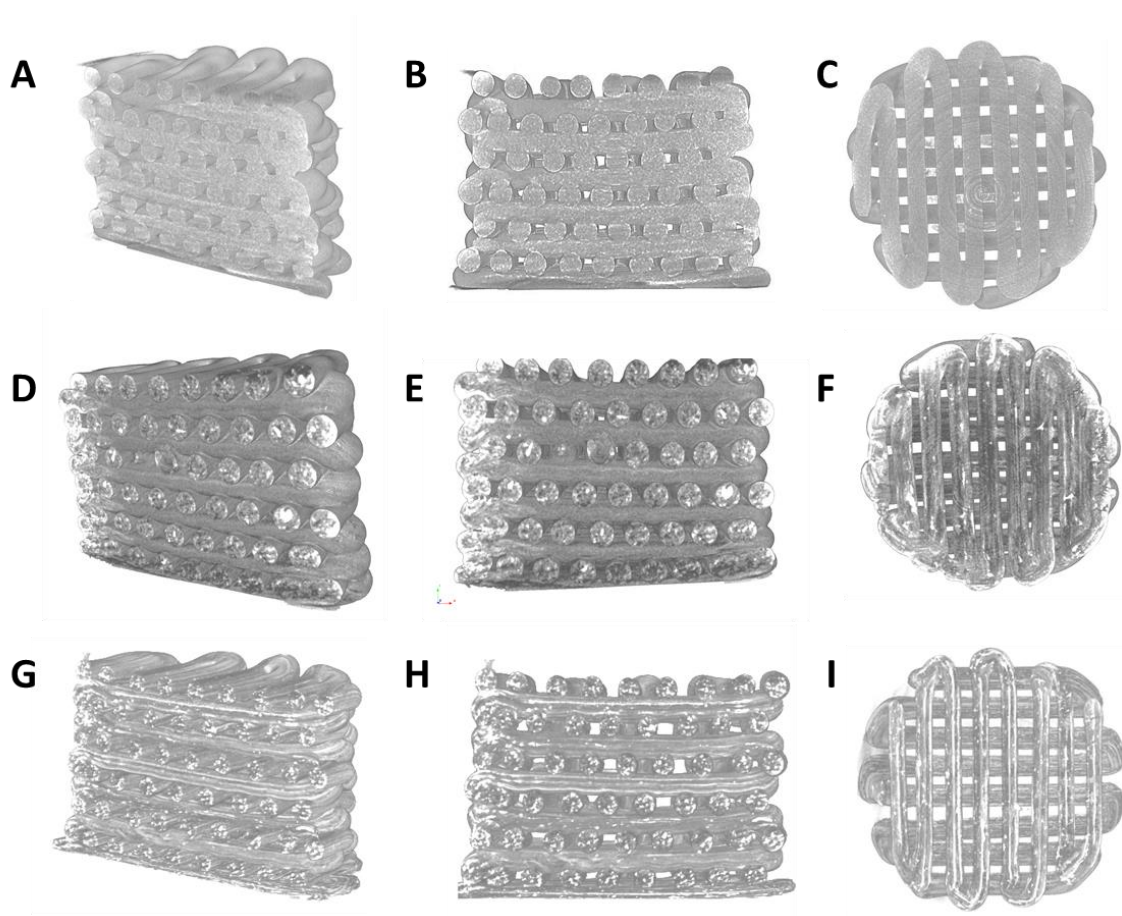


Figure 5. Micro-CT reconstruction of PCL (A-C), PCL/HA (D-F) and PCL/BaTiO₃ (G-I) scaffolds. Cross sections (A-B, D-E, G-H) evidence the high-fidelity of printed scaffold towards the CAD model. All scaffolds show circular printed strand, homogeneous across the XY plane. Top view (C, F, I) showing the cylindrical shape of all scaffolds, as well as alignment of printed layers.

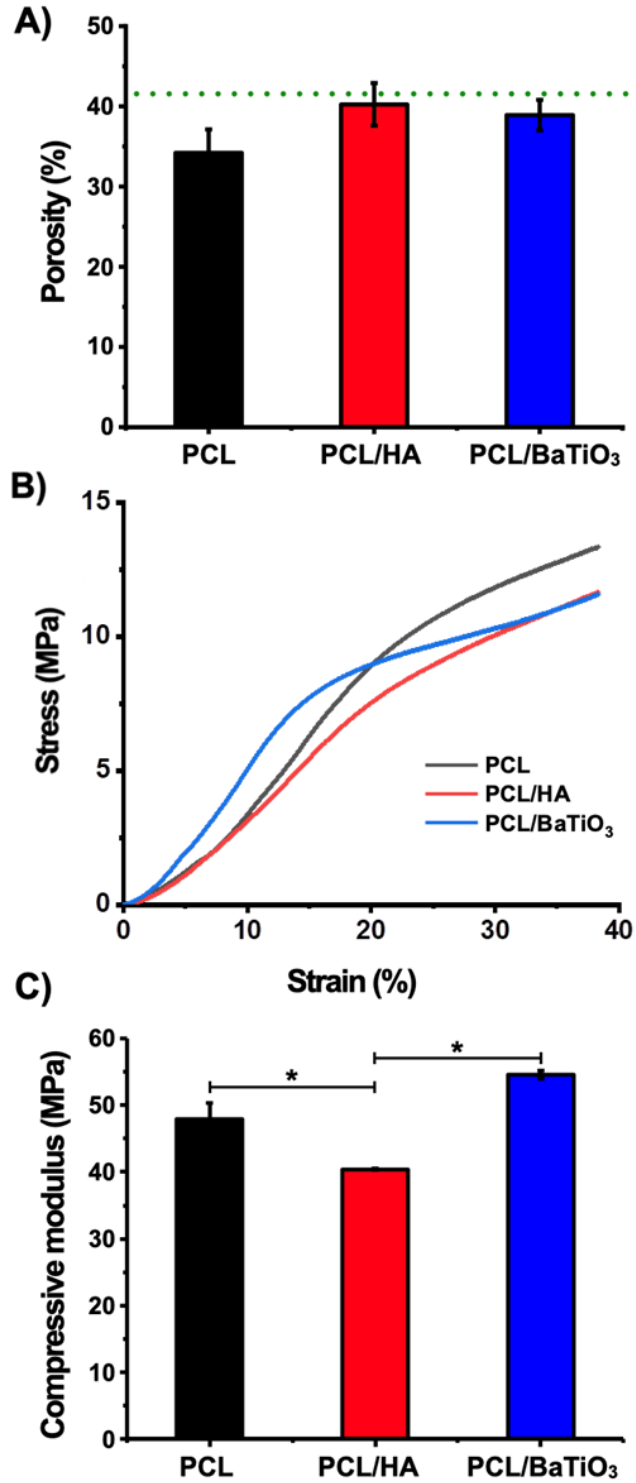


Figure 6. (A) Porosity values derived from micro-CT scans of the 3D scaffolds (n=3) and theoretical porosity (green dotted line; results are presented as mean \pm SD). (B) Example of the engineering stress-strain curves of PCL (black), PCL/HA (red) and PCL/BaTiO₃ (blue). All

samples were compressed approximately until 40% strain. (C) Compressive Modulus of each scaffold. The compressive modulus was calculated in the 0-10% strain interval; results represent mean \pm SD (n = 5), p < 0.05

As shown in Figure 6A all the printed samples displayed similar porosity values, which were found between 35% and 45%, as expected theoretically (41.6%) and within the range of porosity of human cancellous bone [46]. Notably, no statistical difference was observed across samples. Obtained results prove the suitability of the extrusion-based approach towards the manufacturing of composite scaffolds with highly interconnected structures and reproducible architectures.

Mechanical performances represent a key requirement for bone scaffolds, particularly in load bearing applications, as they need to match the host tissue mechanical characteristics and withstand physiological forces imposed on the structure [6,20,43]. In this study, the mechanical properties of the scaffolds were measured using cylindrical samples (diameter 7 mm, thickness 6 mm) tested under uniaxial compressive loading to investigate the role of the bioceramic phase included in the polymeric matrix. Figure 6B shows representative stress-strain curves of PCL (black), PCL/HA (red) and PCL/BaTiO₃ (blue) scaffolds. All the tested scaffolds showed a stress-strain response characterised by an initial linear elastic region up to 10% compression strain, followed by densification and the eventual rupture of the samples at approx. 40% strain. As shown in Figure 6C the inclusion of BaTiO₃ particles into the polymeric matrix led to a composite structure with significantly improved mechanical performance when compared to pure PCL and PCL/HA composite scaffolds. This outcome might be attributed to the particles acting as strain absorbers within the polymeric matrix [47,48]. According to the published literature focusing on 3D printed scaffolds, in addition to the design features (including shape, size pore size and strand dimension), it is reported that physicochemical properties play a crucial role towards their mechanical performance [19,46,49]. While several studies have reported that the incorporation of inorganic fillers (up to 10% wt.) improves composite scaffold mechanical properties [50,51], there are as much demonstrating their adverse effect [9,36]. Considering the characteristics of the scaffolds produced in this study and with reference to the reproducibility in terms of strand dimensions, high fidelity to the CAD model and the similar porosity values across all the groups, it is likely that the increased compressive modulus measured in the PCL/BaTiO₃ scaffolds is the result of the actual material composition, irrespective of the geometrical features. In particular, the higher density of

BaTiO₃ (6 g/cm³) in comparison to HA powder (~ 3 g/cm³) could be responsible for the higher compressive modulus. Our results suggest that the inclusion of 10% wt. of BaTiO₃ particles enhanced the mechanical properties of the PCL/ BaTiO₃ composite scaffolds, fabricated for the first time via a single-step additive manufacturing technology and in comparison to ceramic-based composites manufactured using binder jetting 3D printing [32].

3.2 Electroactive properties

Figure 7A-C present the room temperature dielectric permittivity, AC conductivity and dielectric loss plots of the printed composite scaffolds as a function of frequency. Figure 7D-F show the dielectric permittivity, AC conductivity and dielectric loss at 40°C, respectively. The dielectric properties are investigated at RT and 40°C as the poling study has been performed at these two temperatures. As observed in Figure 7A and Figure 7D, the inclusion of both HA and BaTiO₃ particles increase the relative permittivity with respect to pristine PCL scaffolds, with PCL/BaTiO₃ scaffolds showing the highest permittivity values over the entire frequency spectrum at both tested temperatures. This is in agreement with the reported dielectric behaviour of PCL/BaTiO₃ composites [52].

Relative permittivity values of all scaffolds at both RT and 40°C increase with decrease of the applied frequency as the dipoles attain sufficient time to reorientate in the direction of the electric field [53]. A strong electrode polarisation is observed at low frequencies, which reduces with increasing frequencies as expected for dielectric polymers and particulate composites [54]. However, at RT, the increase of PCL/HA's permittivity values do not follow the same trend as PCL and PCL/BaTiO₃ samples, PCL/HA exhibits lower slope in the low frequency region ($f < 10$ Hz) than the other two types of samples leading in lower values of permittivity than pristine PCL. This is likely due to a strong adhesion between the HA particles and the polymer chain leading to immobilization of the macromolecular chain or even entanglement which in turn reduces the dielectric response of the polymer to the applied electric field, thus decreasing the permittivity [55,56]. The BaTiO₃ particles on the other hand do not show this adverse effect and effectively increase the dielectric permittivity of PCL even at the relatively low weight fractions used in this study.

The measured AC conductivity at RT (Figure 7.B) and 40°C (Figure 7.E) shows the presence of flat, dispersive, and linear regions as a function of frequency, in agreement with the reported behaviour for PCL in literature [52]. The dielectric loss factor ($\tan(\delta)$) behaviour of the composites as a function of frequency measured at RT (Figure 7.C) and 40°C (Figure 7.F) showed an increase in dielectric loss is in accordance with the increase in real permittivity at low frequencies. The phenomenon observed in the high-frequency region ($f > 10,000$ Hz) can be attributed to interfacial polarisation occurring at the interface of the crystalline and the amorphous phase of the PCL polymer due to ionic motions [53] and it seems to be more intense in the composite scaffolds compared to the pristine PCL. This is due to the fact that in the composite scaffolds, interfaces are formed between polymer matrix and ceramic inclusions as well as the crystalline and the amorphous phase of the polymer.

The poling study performed at RT and 40°C, for up to 5 hours at the varying electric field of 5, 10, 15 and 20 kV/mm resulted in d_{33} values lower than 0.1 pC/N, indicating the effect of low fraction of the ferroelectric phase.

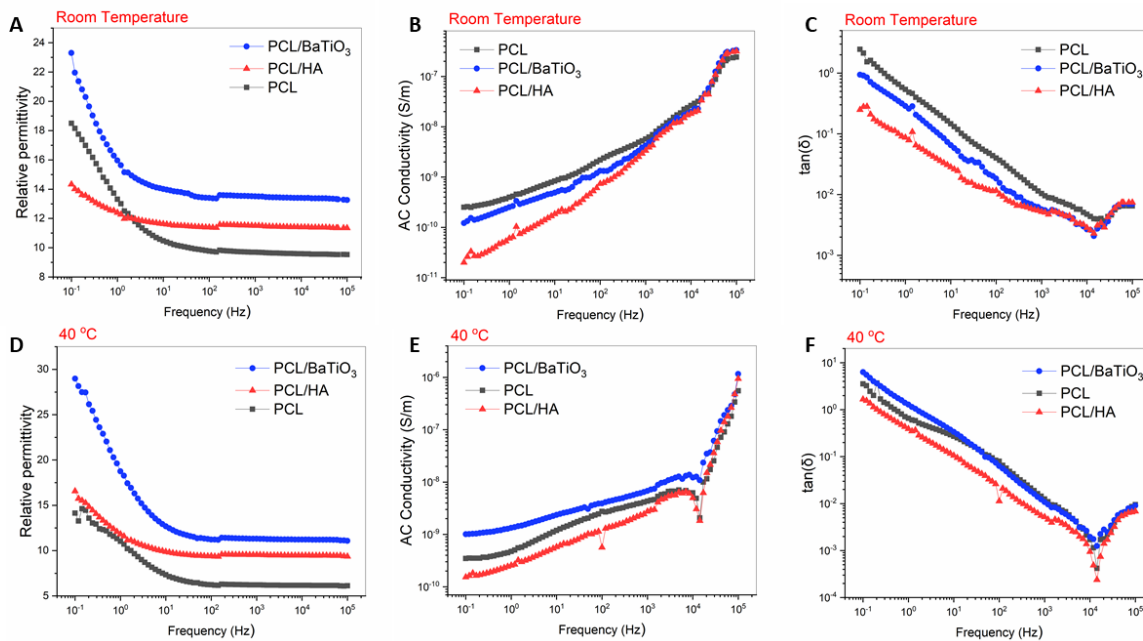


Figure 7. Dielectric response of scaffolds: **(A)** Real part of dielectric permittivity, **(B)** AC conductivity (S/m) and **(C)** Loss tangent ($\tan\delta$) as a function of frequency (Hz) for the PCL (black), PCL/HA (red) and PCL/BaTiO₃ (blue) composites at RT, **(D)** Real part of dielectric permittivity, **(E)** AC conductivity (S/m)

and (F) Loss tangent ($\tan\delta$) as a function of frequency (Hz) for the PCL (black), PCL/HA (red) and PCL/BaTiO₃ (blue) composites at 40 °C.

3.3 *In vitro* evaluation of the 3D printed scaffolds

3.3.1 Cytocompatibility

Saos-2 cell lines were chosen as an osteoblast model to test preliminary cytocompatibility and osteogenic potential of polymeric and composite scaffolds. Another alternative, immortalised osteoblast cell lines are not easily available and the available ones such as hFOB have issues like need for lower ambient temperature (33 °C) as their growth is unstable at 37 °C. In addition to being easily available, Saos-2 cells have been previously used in *in vitro* models for their osteogenic potential and mineralisation capability mimicking human osteoblasts [57,58]. Since the intended application of these scaffolds was for *in vitro* purposes only, we chose Saos-2 cells for preliminary results. However, as per future applications inclusion of primary osteoblasts will be considered.

Proliferation results show steady increase in cellular proliferation from day 1 to day 14 in all the scaffolds tested (Alamar blue viability assay, Figure 8A), with increased proliferation rate in composite scaffolds from day 14 to day 28. Of note, cells have higher proliferation rate in PCL/BaTiO₃ scaffolds compared to pristine PCL and comparable to PCL/HA. Mineralisation media was added at day 7 to give cells time to adhere and grow within scaffolds first. It was observed that earlier addition of mineralisation media hampers growth of cells later in the scaffolds (data not shown). Infact, slower rate of proliferation from day 7 to day 14 could be attributed to the change in media from normal to mineralisation inducing media as cells would be acclimatising to the new chemical cues

Figure 8B shows uniform adhesion of Saos-2 cells after 28 days of culture on the scaffolds' strands, with no difference observed between pristine PCL and composite scaffolds (PCL/HA and PCL/BaTiO₃), as expected. Noticeably, Saos-2 cells were more uniformly adhered onto PCL/BaTiO₃ scaffolds when compared to PCL and PCL/HA scaffolds.

Moreover, images show similar Saos-2 cells alignment in PCL and PCL/BaTiO₃ scaffolds, with higher cell density and distinctive alignment in PCL/BaTiO₃ scaffolds visible at all the magnification. Morphology of Saos-2 cells cultured varied on different scaffolds and is better

appreciated at higher magnifications (staining nuclei and F-actin, Figure 8B). Saos-2 cells on pristine PCL and PCL/BaTiO₃ scaffolds are more elongated with spindle-like morphologies and higher attachments to the scaffolds' surface, whereas Saos-2 cells on PCL/HA scaffolds are less aligned and with a rather circular shape. Altogether, both proliferation and morphology show that PCL/BaTiO₃ showed higher cytocompatibility compared to pristine PCL and PCL/HA scaffolds, and confirms, suggesting a more functional osteoblast phenotype as also reported in literature [59,60].

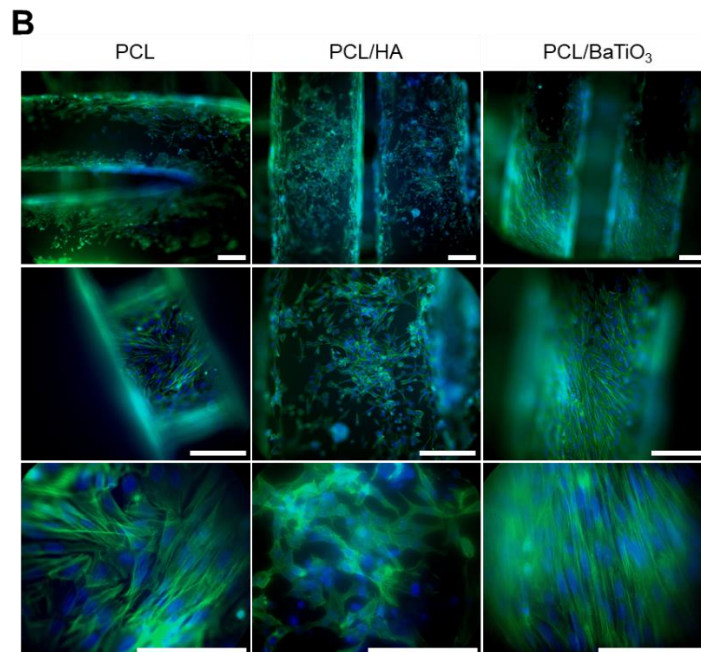
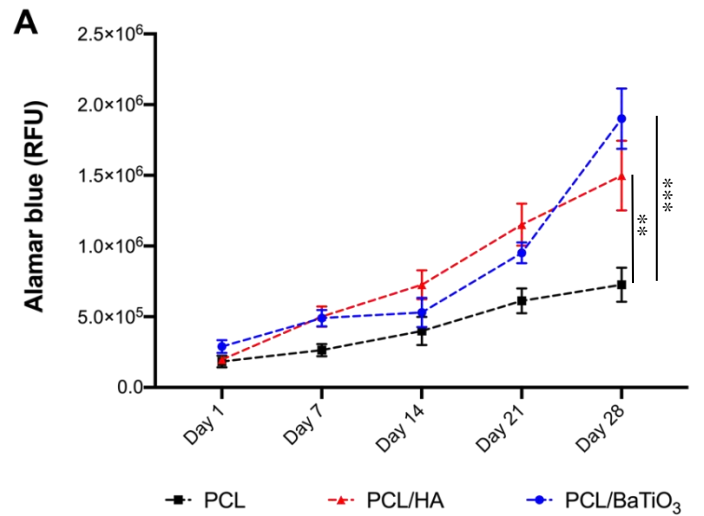


Figure 8. (A) Proliferation assay of Saos-2 cell lines when cultured in PCL (black), PCL/HA (red) and PCL/BaTiO₃ (blue) scaffolds. Cell proliferation was measured by Alamar blue fluorescence at different time points and up to day 28 showing higher proliferation in both PCL/HA and PCL/BaTiO₃ composite scaffolds compared to pristine PCL scaffolds at day 28. Statistical analysis at day 28 using One-way ANOVA returned: PCL vs PCL/BaTiO₃ p-value < 0.001 (**), PCL vs PCL/HA p-value < 0.05 (*), and no significance between PCL/HA vs PCL/BaTiO₃. Data are presented as mean ± SD (n=2, N=3). (B) Morphology of Saos-2 cell lines in PCL, PCL/HA and PCL/BaTiO₃ scaffolds. Immunostained images of Saos-2 cells at day 28 in tested 3D composite scaffolds. Nucleus stained is by DAPI (blue) and actin stained by Phalloidin alexa fluor 488 (green) and imaged at different magnification using inverted microscope. Scale bars 200 μm.

3.3.2 Osteogenic potential and mineralisation

The osteogenic potential was tested by measuring cellular ALP activity, extracellular matrix deposition and mineralisation. Osteoblast culture maturation has been known to occur in three stages: first stage is characterised by growth, second stage by extracellular deposition of collagen and high ALP activity, and the third stage which marks complete maturation is characterised by matrix mineralisation (calcium phosphate and osteocalcin deposition) [61,62].

The addition of mineralisation media induces culture maturation to the third stage and hence the decrease in ALP activity is observed with consequent increase in calcium deposition (Figure 9). Until the addition of mineralisation media at day 7, ALP activity as measured by the phosphatase activity on the pNPP substrate showed higher levels in PCL/BaTiO₃ scaffolds, demonstrating better osteogenic potential (Figure 9A) when compared to PCL and PCL/HA scaffolds. Calcium deposition measured by alizarin stain and its quantification ((Figure 8B) showed increasing trend from day 21 to day 28 in both composite scaffolds (i.e. PCL/HA, PCL/BaTiO₃), indicating that the inclusion of the bioceramic phases increases the level of mineralization of Saos-2 cells on the scaffold [63,64].

Immunofluorescent staining images confirm the deposition of osteogenic extracellular matrix by Saos-2 cells, with the presence of Collagen-I (green) and osteocalcin (red) detected after 28 days of culture in the presence of mineralisation media (Figure 10). Of note, scaffolds were fixed with PFA only and not permeabilised to stain only extracellular components and avoid detection of intracellular components. However, intracellular signal was still detected and observed in acquired

images, and could be explained due to loss of membrane integrity during the fixation process as reported in other studies [65,66]. A punctuated extracellular staining is visible close to cells (Figure 10), demonstrating that the surface characteristics of tested scaffolds preserve the osteoblastic phenotype with deposition of bone-like extracellular matrix onto the scaffolds. In particular, the presence of osteocalcin deposition indicates culture maturation and validates mineralisation capacity of Saos-2 cells in all scaffolds, with no clear difference across the three compositions tested. Collagen I is also deposited in all the scaffolds, with a slight increase in signal observed in PCL/BaTiO₃ composite scaffolds (PCL/HA < PCL ≤ PCL/BaTiO₃). In this study, immunofluorescence imaging gave a preliminary qualitative analysis for presence of bone ECM on these scaffolds. However, additional analysis like collagen and osteocalcin mRNA expression when cells are cultured on different scaffolds can give a better quantitative conclusion as to which scaffolds are better in terms of inducing ECM deposition.

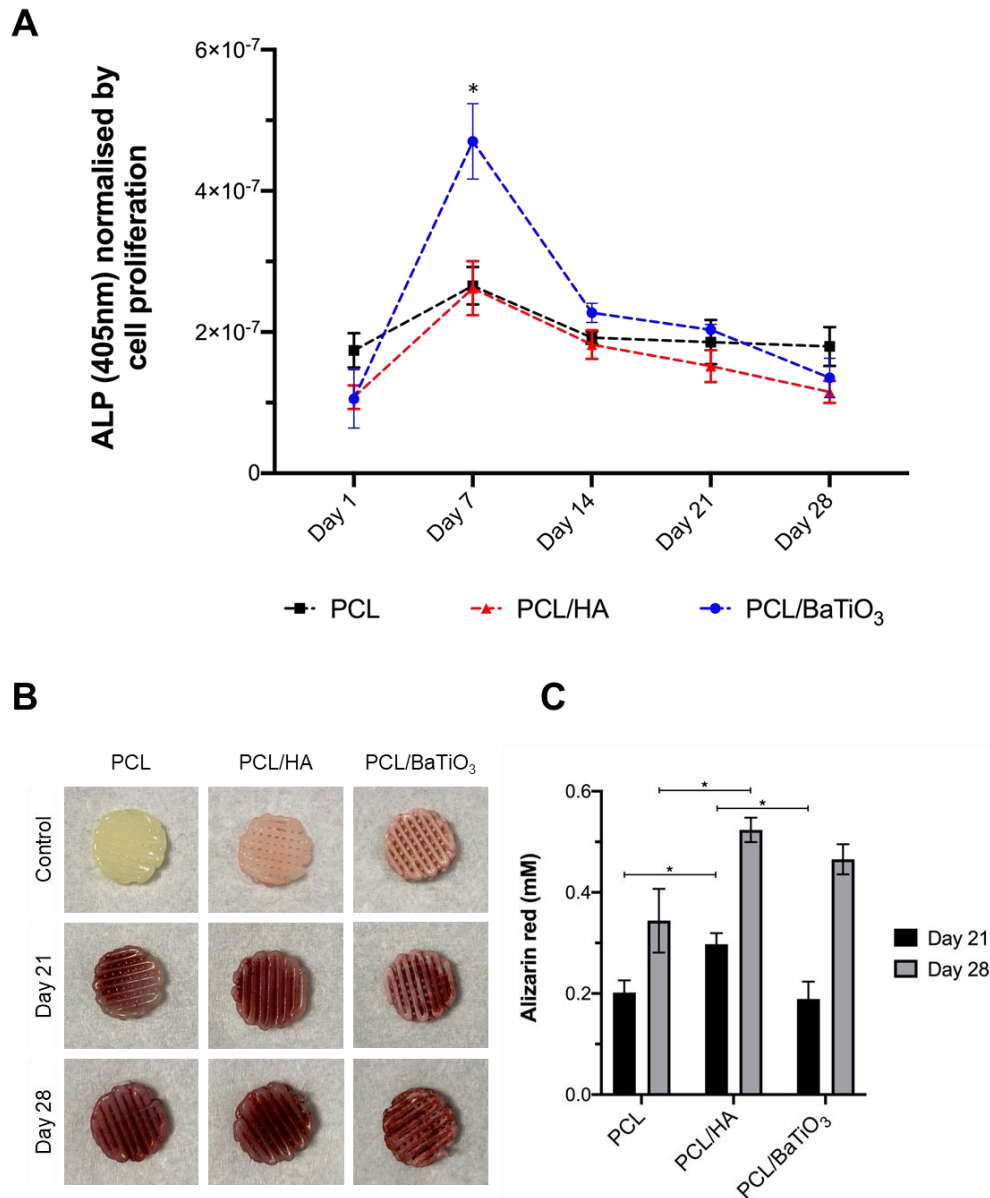


Figure 9. Osteogenic activity of Saos-2 cells in PCL, PCL/HA and PCL/BaTiO₃ scaffolds. **(A)** Alkaline phosphatase activity (ALP) of Saos-2 cells cultured in scaffolds at different time points and up to 28 days. The phosphatase activity was read at 405 nm. Statistics One-way ANOVA between PCL vs PCL/BaTiO₃ and PCL/HA vs PCL/BaTiO₃ p-value < 0.05 (*), no significance was measured at all the other time points. **(B)** Images of Alizarin stain on 3D scaffolds after 21 and 28 days of culture to highlighting calcium deposition by Saos-2 cells over time. **(C)** Quantification of Alizarin stain by absorbance readings at 405 nm. Data are presented as mean ± SD (n=2, N=3). One-way ANOVA statistics is displayed in the figure, with significance levels p < 0.05 (*). Additional statistical analysis between each scaffold and at different

time points (paired t-test) returned $p = 0.045(*)$ for pristine PCL scaffolds, $p = 0.0107(**)$ for PCL/HA scaffolds, and $p = 0.0019 (**)$ for PCL/BaTiO₃ scaffolds.

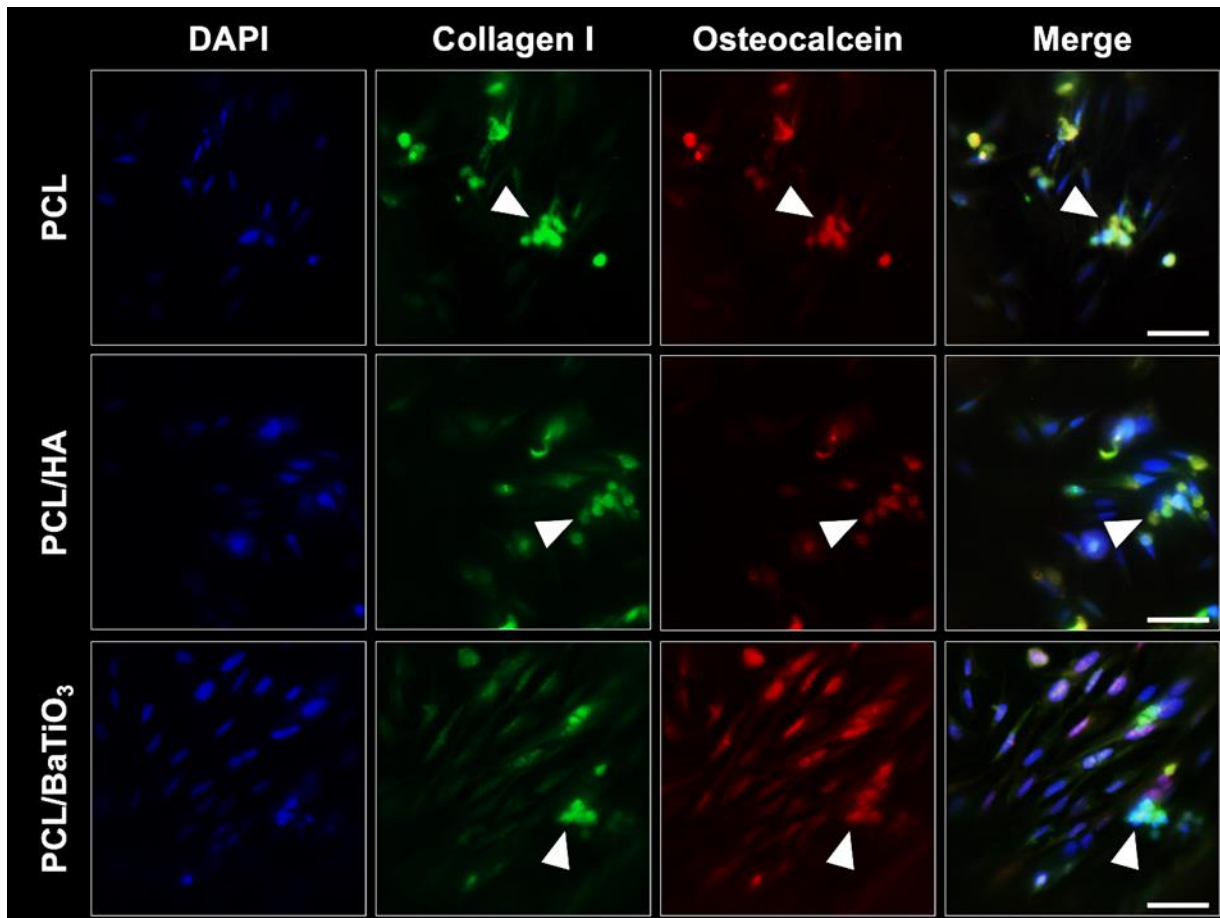


Figure 10. Collagen and osteocalcein deposition by Saos-2 cells in PCL, PCL/HA and PCL/BaTiO₃ scaffolds after 28 days of culture. Fluorescent images of nucleus (blue), collagen I (green), and osteocalcein (red) and composite image to detect difference in extracellular matrix deposition in tested scaffolds. Scale bars: 50 μm .

4. Conclusions

Electroactive biomaterials have been demonstrated to play a significant role on natural bone pathway. In this work, for the first time PCL/BaTiO₃ composite scaffolds were produced by using a single-step extrusion-based 3D printing technology. Scaffolds with an interconnected structure and a high level of integrity among the inner layers were successfully manufactured, as demonstrated by the morphological analysis. Compressive moduli of PCL/BaTiO₃ scaffolds was

better than PCL/HA which is considered the ‘gold standard’ in terms of composite scaffolds. Whereas its porosity values were found in the range of human cancellous bone and comparable to PCL/HA. Significantly, the inclusion of 10% wt. BaTiO₃ particles into the polymeric matrix improved dielectric permittivity and decreased the dielectric loss. The bioactive surface of these scaffolds promoted Saos-2 osteoblast cells adhesion and proliferation comparable to that of PCL/HA. Additionally, ALP activity was observed to be highest among all groups with successful ECM deposition of osteocalcin and collagen I.

Overall, these results have highlighted the potential of multi-material additive manufacturing as promising technology towards the processing of composite electroactive biomaterials and their use in bone tissue engineering applications. This strategy holds great promise for sustainability by reducing material waste, the stages of the product development cycle and finally the manufacturing costs associated. Initiated by this study, future work will be performed to further investigate the use of higher concentration of BaTiO₃ particles into the polymeric matrix to closely mimic bone tissue properties, and the role of electrical stimulation on cellular response to obtain a functional bone tissue unit.

Acknowledgements

The authors would like to thank Dr John Kelly (Ulster University, UK) for the support with the mechanical characterization, Dr Olga Tsikou (The University of Manchester, UK) for the provision of Saos-2 cells, and both Dr Līga Stīpniece and Dr Kristīne Šalma-Ancāne (Riga Technical University, Latvia) for having supplied the HA powder. This work was financially supported by Ulster University (Research Challenge Fund, 2018 competition) and The North West Centre for Advanced Manufacturing (NW CAM) Project, a European Union’s INTERREG VA Programme, managed by the Special EU Programmes Body (SEUPB). The views and opinions in this document do not necessarily reflect those of the European Commission or the Special EU Programmes Body (SEUPB). If you would like further information about NWCAM please contact the lead partner, Catalyst, for details.

References

- [1] A.S. Brydone, D. Meek, S. Maclaine, Bone grafting, orthopaedic biomaterials, and the clinical need for bone engineering, *Proc Inst Mech Eng H*. 224 (2010) 1329–1343. <https://doi.org/10.1243/09544119JEIM770>.
- [2] A.R. Amini, C.T. Laurencin, S.P. Nukavarapu, Bone Tissue Engineering: Recent Advances and Challenges, *Crit Rev Biomed Eng*. 40 (2012) 363–408. <https://www.ncbi.nlm.nih.gov/pmc/articles/PMC3766369/> (accessed February 3, 2021).
- [3] H.C. Pape, A. Evans, P. Kobbe, Autologous bone graft: properties and techniques, *J Orthop Trauma*. 24 Suppl 1 (2010) S36-40. <https://doi.org/10.1097/BOT.0b013e3181cec4a1>.
- [4] S. Stevenson, Enhancement of fracture healing with autogenous and allogeneic bone grafts, *Clin Orthop Relat Res*. (1998) S239-246. <https://doi.org/10.1097/00003086-199810001-00024>.
- [5] R. Dimitriou, E. Jones, D. McGonagle, P.V. Giannoudis, Bone regeneration: current concepts and future directions, *BMC Med*. 9 (2011) 66. <https://doi.org/10.1186/1741-7015-9-66>.
- [6] J. Henkel, M.A. Woodruff, D.R. Epari, R. Steck, V. Glatt, I.C. Dickinson, P.F.M. Choong, M.A. Schuetz, D.W. Hutmacher, Bone Regeneration Based on Tissue Engineering Conceptions — A 21st Century Perspective, *Bone Research*. 1 (2013) 216–248. <https://doi.org/10.4248/BR201303002>.
- [7] G. Turnbull, J. Clarke, F. Picard, P. Riches, L. Jia, F. Han, B. Li, W. Shu, 3D bioactive composite scaffolds for bone tissue engineering, *Bioact Mater*. 3 (2017) 278–314. <https://doi.org/10.1016/j.bioactmat.2017.10.001>.
- [8] E.M. Gonçalves, F.J. Oliveira, R.F. Silva, M.A. Neto, M.H. Fernandes, M. Amaral, M. Vallet-Regí, M. Vila, Three-dimensional printed PCL-hydroxyapatite scaffolds filled with CNTs for bone cell growth stimulation, *Journal of Biomedical Materials Research Part B: Applied Biomaterials*. 104 (2016) 1210–1219. <https://doi.org/10.1002/jbm.b.33432>.
- [9] D. Pierantozzi, A. Scalzone, S. Jindal, L. Stipniece, K. Šalma-Ancāne, K. Dalgarno, P. Gentile, E. Mancuso, 3D printed Sr-containing composite scaffolds: Effect of structural design and

material formulation towards new strategies for bone tissue engineering, *Composites Science and Technology*. 191 (2020) 108069. <https://doi.org/10.1016/j.compscitech.2020.108069>.

[10] H. Kemppi, M.A. Finnilä, G.S. Lorite, M. Nelo, J. Juuti, M. Kokki, H. Kokki, J. Räsänen, A. Mobasheri, S. Saarakkala, Design and development of poly-L/D-lactide copolymer and barium titanate nanoparticle 3D composite scaffolds using breath figure method for tissue engineering applications, *Colloids and Surfaces B: Biointerfaces*. 199 (2021) 111530. <https://doi.org/10.1016/j.colsurfb.2020.111530>.

[11] K. Kapat, Q.T.H. Shubhra, M. Zhou, S. Leeuwenburgh, Piezoelectric Nano-Biomaterials for Biomedicine and Tissue Regeneration, *Advanced Functional Materials*. 30 (2020) 1909045. <https://doi.org/10.1002/adfm.201909045>.

[12] B. Tandon, J.J. Blaker, S.H. Cartmell, Piezoelectric materials as stimulatory biomedical materials and scaffolds for bone repair, *Acta Biomaterialia*. 73 (2018) 1–20. <https://doi.org/10.1016/j.actbio.2018.04.026>.

[13] M. Acosta, N. Novak, V. Rojas, S. Patel, R. Vaish, J. Koruza, G.A. Rossetti, J. Rödel, BaTiO₃-based piezoelectrics: Fundamentals, current status, and perspectives, *Applied Physics Reviews*. 4 (2017) 041305. <https://doi.org/10.1063/1.4990046>.

[14] A.H. Rajabi, M. Jaffe, T.L. Arinzeh, Piezoelectric materials for tissue regeneration: A review, *Acta Biomaterialia*. 24 (2015) 12–23. <https://doi.org/10.1016/j.actbio.2015.07.010>.

[15] Y. Li, X. Dai, Y. Bai, Y. Liu, Y. Wang, O. Liu, F. Yan, Z. Tang, X. Zhang, X. Deng, Electroactive BaTiO₃ nanoparticle-functionalized fibrous scaffolds enhance osteogenic differentiation of mesenchymal stem cells, *Int J Nanomedicine*. 12 (2017) 4007–4018. <https://doi.org/10.2147/IJN.S135605>.

[16] A. Ehterami, M. Kazemi, B. Nazari, P. Saraeian, M. Azami, Fabrication and characterization of highly porous barium titanate based scaffold coated by Gel/HA nanocomposite with high piezoelectric coefficient for bone tissue engineering applications, *J Mech Behav Biomed Mater*. 79 (2018) 195–202. <https://doi.org/10.1016/j.jmbbm.2017.12.034>.

- [17] J. Liu, X. Hu, H. Dai, Z. San, F. Wang, L. Ren, G. Li, Polycaprolactone/calcium sulfate whisker/barium titanate piezoelectric ternary composites for tissue reconstruction, *Advanced Composites Letters*. 29 (2020) 2633366X19897923. <https://doi.org/10.1177/2633366X19897923>.
- [18] I. Jun, H.-S. Han, J.R. Edwards, H. Jeon, Electrospun Fibrous Scaffolds for Tissue Engineering: Viewpoints on Architecture and Fabrication, *Int J Mol Sci*. 19 (2018). <https://doi.org/10.3390/ijms19030745>.
- [19] M.P. Nikolova, M.S. Chavali, Recent advances in biomaterials for 3D scaffolds: A review, *Bioact Mater*. 4 (2019) 271–292. <https://doi.org/10.1016/j.bioactmat.2019.10.005>.
- [20] G.L. Koons, M. Diba, A.G. Mikos, Materials design for bone-tissue engineering, *Nature Reviews Materials*. 5 (2020) 584–603. <https://doi.org/10.1038/s41578-020-0204-2>.
- [21] P. Chocholata, V. Kulda, V. Babuska, Fabrication of Scaffolds for Bone-Tissue Regeneration, *Materials (Basel)*. 12 (2019). <https://doi.org/10.3390/ma12040568>.
- [22] A.-V. Do, B. Khorsand, S.M. Geary, A.K. Salem, 3D Printing of Scaffolds for Tissue Regeneration Applications, *Adv Healthc Mater*. 4 (2015) 1742–1762. <https://doi.org/10.1002/adhm.201500168>.
- [23] P. Ahangar, M.E. Cooke, M.H. Weber, D.H. Rosenzweig, Current Biomedical Applications of 3D Printing and Additive Manufacturing, *Applied Sciences*. 9 (2019) 1713. <https://doi.org/10.3390/app9081713>.
- [24] S.-S.D. Carter, P.F. Costa, C. Vaquette, S. Ivanovski, D.W. Hutmacher, J. Malda, Additive Biomanufacturing: An Advanced Approach for Periodontal Tissue Regeneration, *Ann Biomed Eng*. 45 (2017) 12–22. <https://doi.org/10.1007/s10439-016-1687-2>.
- [25] H. Qu, Additive manufacturing for bone tissue engineering scaffolds, *Materials Today Communications*. 24 (2020) 101024. <https://doi.org/10.1016/j.mtcomm.2020.101024>.
- [26] D. Liu, W. Nie, D. Li, W. Wang, L. Zheng, J. Zhang, J. Zhang, C. Peng, X. Mo, C. He, 3D printed PCL/SrHA scaffold for enhanced bone regeneration, *Chemical Engineering Journal*. 362 (2019) 269–279. <https://doi.org/10.1016/j.cej.2019.01.015>.

- [27] J.L. Dávila, M.S. Freitas, P. Inforçatti Neto, Z.C. Silveira, J.V.L. Silva, M.A. d'Ávila, Fabrication of PCL/ β -TCP scaffolds by 3D mini-screw extrusion printing, *Journal of Applied Polymer Science*. 133 (2016) n/a-n/a. <https://doi.org/10.1002/app.43031>.
- [28] A. Gelmi, C.E. Schutt, Stimuli-Responsive Biomaterials: Scaffolds for Stem Cell Control, *Advanced Healthcare Materials*. 10 (2021) 2001125. <https://doi.org/10.1002/adhm.202001125>.
- [29] L.C. Hsiao, A.Z.M. Badruddoza, L.-C. Cheng, P.S. Doyle, 3D printing of self-assembling thermoresponsive nanoemulsions into hierarchical mesostructured hydrogels, *Soft Matter*. 13 (2017) 921–929. <https://doi.org/10.1039/C6SM02208A>.
- [30] R.D. Santis, A. Gloria, T. Russo, U. D'Amora, S. Zeppetelli, A. Tampieri, T. Herrmannsdörfer, L. Ambrosio, A route toward the development of 3D magnetic scaffolds with tailored mechanical and morphological properties for hard tissue regeneration: Preliminary study, *Virtual and Physical Prototyping*. 6 (2011) 189–195. <https://doi.org/10.1080/17452759.2011.631324>.
- [31] D.G. Tamay, T. Dursun Usal, A.S. Alagoz, D. Yucel, N. Hasirci, V. Hasirci, 3D and 4D Printing of Polymers for Tissue Engineering Applications, *Front. Bioeng. Biotechnol.* 7 (2019). <https://doi.org/10.3389/fbioe.2019.00164>.
- [32] C. Polley, T. Distler, R. Detsch, H. Lund, A. Springer, A.R. Boccaccini, H. Seitz, 3D Printing of Piezoelectric Barium Titanate-Hydroxyapatite Scaffolds with Interconnected Porosity for Bone Tissue Engineering, *Materials*. 13 (2020) 1773. <https://doi.org/10.3390/ma13071773>.
- [33] C. Chen, X. Wang, Y. Wang, D. Yang, F. Yao, W. Zhang, B. Wang, G.A. Sewvandi, D. Yang, D. Hu, Additive Manufacturing of Piezoelectric Materials, *Advanced Functional Materials*. 30 (2020) 2005141. <https://doi.org/10.1002/adfm.202005141>.
- [34] S.M. Bittner, B.T. Smith, L. Diaz-Gomez, C.D. Hudgins, A.J. Melchiorri, D.W. Scott, J.P. Fisher, A.G. Mikos, Fabrication and mechanical characterization of 3D printed vertical uniform and gradient scaffolds for bone and osteochondral tissue engineering, *Acta Biomaterialia*. 90 (2019) 37–48. <https://doi.org/10.1016/j.actbio.2019.03.041>.

- [35] S.M. Bittner, J.L. Guo, A. Melchiorri, A.G. Mikos, Three-dimensional printing of multilayered tissue engineering scaffolds, *Materials Today*. 21 (2018) 861–874. <https://doi.org/10.1016/j.mattod.2018.02.006>.
- [36] K.K. Gómez-Lizárraga, C. Flores-Morales, M.L. Del Prado-Audelo, M.A. Álvarez-Pérez, M.C. Piña-Barba, C. Escobedo, Polycaprolactone- and polycaprolactone/ceramic-based 3D-bioprinted porous scaffolds for bone regeneration: A comparative study, *Materials Science and Engineering: C*. 79 (2017) 326–335. <https://doi.org/10.1016/j.msec.2017.05.003>.
- [37] N. Ashammakhi, S. Ahadian, C. Xu, H. Montazerian, H. Ko, R. Nasiri, N. Barros, A. Khademhosseini, Bioinks and bioprinting technologies to make heterogeneous and biomimetic tissue constructs, *Materials Today Bio*. 1 (2019) 100008. <https://doi.org/10.1016/j.mtbio.2019.100008>.
- [38] L. Moroni, J.R. de Wijn, C.A. van Blitterswijk, 3D fiber-deposited scaffolds for tissue engineering: Influence of pores geometry and architecture on dynamic mechanical properties, *Biomaterials*. 27 (2006) 974–985. <https://doi.org/10.1016/j.biomaterials.2005.07.023>.
- [39] M. Neufurth, X. Wang, S. Wang, R. Steffen, M. Ackermann, N.D. Haep, H.C. Schröder, W.E.G. Müller, 3D printing of hybrid biomaterials for bone tissue engineering: Calcium-polyphosphate microparticles encapsulated by polycaprolactone, *Acta Biomaterialia*. 64 (2017) 377–388. <https://doi.org/10.1016/j.actbio.2017.09.031>.
- [40] M. Porta, C. Tonda-Turo, D. Pierantozzi, G. Ciardelli, E. Mancuso, Towards 3D Multi-Layer Scaffolds for Periodontal Tissue Engineering Applications: Addressing Manufacturing and Architectural Challenges, *Polymers*. 12 (2020) 2233. <https://doi.org/10.3390/polym12102233>.
- [41] X. Jin, D. Sun, M. Zhang, Y. Zhu, J. Qian, Investigation on FTIR spectra of barium calcium titanate ceramics, *J Electroceram*. 22 (2009) 285–290. <https://doi.org/10.1007/s10832-007-9402-1>.
- [42] K. Chrissafis, D. Bikiaris, Can nanoparticles really enhance thermal stability of polymers? Part I: An overview on thermal decomposition of addition polymers, *Thermochimica Acta*. 523 (2011) 1–24. <https://doi.org/10.1016/j.tca.2011.06.010>.

- [43] H. Qu, H. Fu, Z. Han, Y. Sun, Biomaterials for bone tissue engineering scaffolds: a review, *RSC Adv.* 9 (2019) 26252–26262. <https://doi.org/10.1039/C9RA05214C>.
- [44] H. Yuk, X. Zhao, A New 3D Printing Strategy by Harnessing Deformation, Instability, and Fracture of Viscoelastic Inks, *Advanced Materials.* 30 (2018) 1704028. <https://doi.org/10.1002/adma.201704028>.
- [45] A. Zimmerling, Z. Yazdanpanah, D.M.L. Cooper, J.D. Johnston, X. Chen, 3D printing PCL/nHA bone scaffolds: exploring the influence of material synthesis techniques, *Biomaterials Research.* 25 (2021) 3. <https://doi.org/10.1186/s40824-021-00204-y>.
- [46] A. Di Luca, A. Longoni, G. Criscenti, C. Mota, C. van Blitterswijk, L. Moroni, Toward mimicking the bone structure: design of novel hierarchical scaffolds with a tailored radial porosity gradient, *Biofabrication.* 8 (2016) 045007. <https://doi.org/10.1088/1758-5090/8/4/045007>.
- [47] Q.M. Li, I. Magkiriadis, J.J. Harrigan, Compressive Strain at the Onset of Densification of Cellular Solids, *Journal of Cellular Plastics.* 42 (2006) 371–392. <https://doi.org/10.1177/0021955X06063519>.
- [48] A. Ali, A. Andriyana, Properties of multifunctional composite materials based on nanomaterials: a review, *RSC Advances.* 10 (2020) 16390–16403. <https://doi.org/10.1039/C9RA10594H>.
- [49] L. Zhang, G. Yang, B.N. Johnson, X. Jia, Three-dimensional (3D) printed scaffold and material selection for bone repair, *Acta Biomaterialia.* 84 (2019) 16–33. <https://doi.org/10.1016/j.actbio.2018.11.039>.
- [50] L. Tian, Z. Zhang, B. Tian, X. Zhang, N. Wang, Study on antibacterial properties and cytocompatibility of EPL coated 3D printed PCL/HA composite scaffolds, *RSC Advances.* 10 (2020) 4805–4816. <https://doi.org/10.1039/C9RA10275B>.
- [51] F. Olate-Moya, L. Arens, M. Wilhelm, M.A. Mateos-Timoneda, E. Engel, H. Palza, Chondroinductive Alginate-Based Hydrogels Having Graphene Oxide for 3D Printed Scaffold Fabrication, *ACS Appl. Mater. Interfaces.* 12 (2020) 4343–4357. <https://doi.org/10.1021/acsami.9b22062>.

- [52] A. Bagchi, S.R.K. Meka, B.N. Rao, K. Chatterjee, Perovskite ceramic nanoparticles in polymer composites for augmenting bone tissue regeneration, *Nanotechnology*. 25 (2014) 485101. <https://doi.org/10.1088/0957-4484/25/48/485101>.
- [53] V.J. Hegde, O. Gallot-Lavallée, L. Heux, Dielectric study of Polycaprolactone: A biodegradable polymer, in: 2016 IEEE International Conference on Dielectrics (ICD), 2016: pp. 293–296. <https://doi.org/10.1109/ICD.2016.7547602>.
- [54] F. Kremer, A. Schönhal, eds., *Broadband Dielectric Spectroscopy*, Springer-Verlag, Berlin Heidelberg, 2003. <https://doi.org/10.1007/978-3-642-56120-7>.
- [55] O. Vryonis, D.L. Anastassopoulos, A.A. Vradis, G.C. Psarras, Dielectric response and molecular dynamics in epoxy-BaSrTiO₃ nanocomposites: Effect of nanofiller loading, *Polymer*. 95 (2016) 82–90. <https://doi.org/10.1016/j.polymer.2016.04.050>.
- [56] T. Tanaka, M. Kozako, N. Fuse, Y. Ohki, Proposal of a multi-core model for polymer nanocomposite dielectrics, *IEEE Transactions on Dielectrics and Electrical Insulation*. 12 (2005) 669–681. <https://doi.org/10.1109/TDEI.2005.1511092>.
- [57] E.M. Czekanska, M.J. Stoddart, R.G. Richards, J.S. Hayes, In search of an osteoblast cell model for in vitro research, *European Cells and Materials*. 24 (2012) 1–17. <https://doi.org/10.22203/eCM.v024a01>.
- [58] M. Prideaux, A.R. Wijenayaka, D.D. Kumarasinghe, R.T. Ormsby, A. Evdokiou, D.M. Findlay, G.J. Atkins, SaOS2 osteosarcoma cells as an in vitro model for studying the transition of human osteoblasts to osteocytes, *Calcified Tissue International*. 95 (2014) 183–193. <https://doi.org/10.1007/s00223-014-9879-y>.
- [59] W.E.G. Müller, E. Tolba, H.C. Schröder, B. Diehl-Seifert, T. Link, X. Wang, Biosilica-loaded poly(ϵ -caprolactone) nanofibers mats provide a morphogenetically active surface scaffold for the growth and mineralization of the osteoclast-related SaOS-2 cells, *Biotechnology Journal*. 9 (2014) 1312–1321. <https://doi.org/10.1002/biot.201400277>.
- [60] N. Ayobian-Markazi, T. Fouroutan, M.J. Kharazifar, Comparison of cell viability and morphology of a human osteoblast-like cell line (SaOS-2) seeded on various bone substitute

materials: An in vitro study, *Dent Res J (Isfahan)*. 9 (2012) 86–92. <https://doi.org/10.4103/1735-3327.92959>.

[61] G.S. Stein, J.B. Lian, A.J. Van Wijnen, J.L. Stein, M. Montecino, A. Javed, S.K. Zaidi, D.W. Young, J.Y. Choi, S.M. Pockwinse, Runx2 control of organization, assembly and activity of the regulatory machinery for skeletal gene expression, *Oncogene*. 23 (2004) 4315–4329. <https://doi.org/10.1038/sj.onc.1207676>.

[62] A. Rutkovskiy, K.-O. Stensløkken, I.J. Vaage, Osteoblast Differentiation at a Glance, *Medical Science Monitor Basic Research*. 22 (2016) 95–106. <https://doi.org/10.12659/msmbr.901142>.

[63] S.-W. Tsai, W.-X. Yu, P.-A. Hwang, Y.-W. Hsu, F.-Y. Hsu, Fabrication and Characteristics of PCL Membranes Containing Strontium-Substituted Hydroxyapatite Nanofibers for Guided Bone Regeneration, *Polymers (Basel)*. 11 (2019). <https://doi.org/10.3390/polym11111761>.

[64] Q. Zhang, Y. Ji, W. Zheng, M. Yan, D. Wang, M. Li, J. Chen, X. Yan, Q. Zhang, X. Yuan, Q. Zhou, Electrospun Nanofibers Containing Strontium for Bone Tissue Engineering, *Journal of Nanomaterials*. 2020 (2020) e1257646. <https://doi.org/10.1155/2020/1257646>.

[65] R. Thavarajah, V.K. Mudimbaimannar, J. Elizabeth, U.K. Rao, K. Ranganathan, Chemical and physical basics of routine formaldehyde fixation, *Journal of Oral and Maxillofacial Pathology*. 16 (2012) 400–405. <https://doi.org/10.4103/0973-029X.102496>.

[66] R. Cheng, F. Zhang, M. Li, X. Wo, Y.W. Su, W. Wang, Influence of Fixation and Permeabilization on the Mass Density of Single Cells: A Surface Plasmon Resonance Imaging Study, *Frontiers in Chemistry*. 7 (2019) 588. <https://doi.org/10.3389/fchem.2019.00588>.

Thesis context – Chapter 4

The developed 3D *in vitro* model for breast tissue in Chapter 2 and bone tissue in Chapter 3 were combined together in Chapter 4 – “**Invasion and Secondary site colonisation as a function of *in vitro* primary tumour matrix stiffness**” to study breast cancer invasion and metastasis to bone. The aim of this chapter was to understand influence of primary tumour stiffness conditioning on secondary site colonisation. For this purpose, cells grown and conditioned in varying stiffness of alginate-gelatin gels were examined for their migratory, invasive and bone/PCL scaffolds colonisation.

When combined, Chapter 2 and Chapter 4 managed to study impact of physico-chemical cues on a range of primary tumour phenotypes as well as secondary site response. Here, *in vitro* models made it possible to isolate influence of primary tumour microenvironment from secondary site ECM characteristics on breast cancer cell response. Such models can further be used for monitoring disease phenotypes *in vitro* and future platforms for studying therapeutic efficacy.

Chapter 4. Invasion and Secondary site colonisation as a function of *in vitro* primary tumour matrix stiffness

Lekha Shah¹, Ayşe Latif¹, Kaye J. Williams¹, Elena Mancuso³, Annalisa Tirella^{1,2,*}

¹Division of Pharmacy and Optometry, Faculty of Biology, Medicine and Health, University of Manchester, Oxford Road, M13 9PL, Manchester, United Kingdom

² BIOTech - Center for Biomedical Technologies, Department of Industrial Engineering, University of Trento, Trento, Italy

³ Nanotechnology and Integrated Bio-Engineering Centre (NIBEC), Ulster University, Shore Road, BT37 0QB, Newtownabbey, United Kingdom

Manuscript in preparation

*Corresponding author: BIOTech Center for Biomedical technologies, University of Trento, Via delle Regole 101, Trento 38123, Italy; annalisa.tirella@unitn.it

Abstract

Increase of breast tissue stiffness have been implicated in increased breast cancer risk and is also correlated to cancer progression from ductal carcinoma in situ (DCIS) to Invasive ductal carcinoma (IDC). To better understand the cause-effect relationship of tissue stiffness on breast cancer cells metastatic potential, we fabricated three-dimensional (3D) models to mimic the breast and the bone tissue *in vitro*. First model used alginate-based hydrogels allowing precise control over stiffness and composition of extracellular matrix, varying stiffness in the range of 2-10 kPa and adhesion ligand (aka gelatin). Effect of primary tumour matrix stiffness on human breast cancer cells (MDA-MB 231) was analysed testing various aspects of the metastatic cascade like cell adhesion, migration, 3D invasion and secondary site metastasis through *in vitro* assays. The second model used 3D printed PCL-composite scaffolds which were remodelled using Saos-2 cells that deposited bone ECM on these scaffolds. After a decellularization step, the scaffolds were assembled with alginate gelatin gels and used to obtain a novel breast-to-bone *in vitro* model. The increased stiffness of hydrogel resulted in higher migration and 3D collagen invasion of MDA-MB 231 cells. Additionally, PTHrP expression and IL-6 release both of which are implicated in bone metastatic cascade were observed to be higher when cells from higher stiffness are cultured in bone ECM enriched PCL scaffolds. These models pave the way for understanding disease mechanisms by incorporating important TME cues like tissue stiffness and present as future platforms for monitoring metastatic disease phenotypes and therapeutic efficacy

Keywords

Hydrogel stiffness, biohybrid scaffolds, breast to bone metastasis, engineered *in vitro* models, invasive potential.

1. Introduction

Dynamic communication between cells and extracellular matrix (ECM) governs tissue structure and function. However, this homeostasis is dysregulated in cancer wherein tumour cells and cancer associated fibroblasts actively remodel the ECM, leading to increased deposition, crosslinking and linearisation of fibrillar components such as collagen^{1,2}. This leads to a change in biomechanical and biochemical nature of the ECM with implications on its physical properties, for instance increased matrix stiffness and dense tissue architecture, as well as chemical changes such as modified or over-expressed cell adhesion motifs³. Biomechanical changes like tumour breast tissue stiffness have been reported to be 3-6 times stiffer than normal tissue (Compressive moduli – 3 kPa normal tissue, 15 kPa tumour tissue), and are used clinically to detect breast cancer⁴. Due to their long-term nature which are shared across patients, tissue stiffening and ECM changes are more reliable markers than other dynamic cellular changes, acquiring a significant importance in solid cancer progression⁵. As a matter of facts, what is now known is that modified ECM cues are implicated in cell fate⁶, cancer stemness⁷, cancer progression³, metastasis⁸ and therapeutic response in tumour tissue^{9,10}.

Many on-going studies are investigating ECM's mechano-transduction effects on breast cancer progression. For example, a stiffness increase from 200 Pa to 5000 Pa in peptide crosslinked polyacrylamide gels was observed to perturb mammary acini formation by inducing unhindered growth and polarity loss in mammary epithelial cells¹¹. This effect was shown to be induced by cytoskeletal changes such as force mediated integrin aggregation and focal adhesion formation¹¹. Stiff matrices were also observed to affect genome wide expression changes in non-malignant breast epithelial cells and found to develop malignant phenotype by altering chromatin accessibility of genes¹². However, very few studies illustrate effects of primary tumour stiffness, and ECM properties, on invasion and metastasis to a secondary site.

Bone is the most common site for breast cancer metastasis (~60-70%) followed by lung, liver and brain¹³. Breast cancer metastasis to a secondary site like bone involves a change in ECM composition, which in contrast to breast's collagenous matrix, consists of ~60% inorganic matrix (majorly hydroxyapatite/HA) and ~40% organic matrix (majorly collagenous)¹⁴. Highly vascular trabecular bone, which is a preferred site for bone metastasis¹⁵, has high porosity and a

heterogeneous tissue stiffness that ranges from 4-80 MPa¹⁶, whereas normal breast and tumour tissue are comparatively dense with tissue stiffness ranging from 3-16 kPa⁴. When a subpopulation of circulatory breast tumour cells encounters bone ECM, they start a cascade of vicious bone metastatic cycle. An important first step of this cycle is when tumour cells release Parathyroid Hormone related Protein (PTHrP) in response to increased extracellular calcium¹⁷ and Transforming Growth Factor- β (TGF- β)¹⁸ in the bone ECM. Tumour secreted cytokines such as Interleukin-6 (IL-6)¹⁹ along with PTHrP²⁰ instructs osteoblasts to release Receptor Activator of Nuclear factor Kappa-B Ligand (RANKL) and consequently stimulate osteoclast activity. This forms osteolytic bone lesions that further release trapped calcium and TGF- β to induce cancer cell signalling, hence completing the cycle.

Increase of primary matrix stiffness is recorded in many solid tumours, and cells mechanically conditioned to such TME maintain such phenotype even after removal of mechanical stimuli^{21,22}. This is of particular relevance at later stages of tumour progression i.e. invasion and metastasis which involve leaving the primary tumour site and invading spaces with different ECM properties. To better understand how metastasis are formed, it is important to firstly answer how primary tumour ECM properties can condition cells and dictate their response to secondary site ECM. In this scenario, 3D *in vitro* models can provide an opportunity to model ECM changes with required precision as well as decouple components (e.g., chemical, physical) to understand their individual contribution. In this study, key aspects of breast and bone tissue ECM were engineered namely matrix composition, stiffness, density, porosity, and architecture to study breast to bone metastasis. We previously demonstrated effects of matrix stiffness and composition on breast cancer stemness with alginate-gelatin hydrogels (Chapter 2). Here we use selected hydrogels to mimic normal breast tissue stiffness of 2 kPa and tumour tissue stiffness of 6-10 kPa, varying also the concentration of gelatin to change composition and density of hydrogels. On the other hand, bone ECM was modelled using biohybrid 3D polycaprolactone (PCL) scaffolds. Composite PCL scaffolds containing inorganic compounds such as hydroxyapatite (HA), Strontium HA (SrHA) and Barium Titanate (BaTiO₃) were previously shown to have stiffness and porosity matching the values of trabecular bone^{23,24}, being 40-55 MPa and 35-45% respectively. To increase biocompatibility and physiological relevance of composite PCL scaffolds, Saos-2 were cultured within these scaffolds, and decellularization procedures were optimised to retain mineralised ECM

deposited by them. These decellularized scaffolds later termed as ‘biohybrid PCL scaffolds’ were selected to be used as bone secondary metastatic site.

To understand effects of breast tumour ECM, adhesion, migration and invasive potential of human breast cancer cells (MDA-MB 231) pre-conditioned for 7 days in selected alginate-gelatin hydrogels with different stiffnesses and compositions were tested. We found that high stiffness conditioned cells had higher migratory and invasive potential.

Then, breast-to-bone invasion models were used to assess MDA-MB 231 cells metastatic potential to bone using biohybrid PCL scaffolds. Breast to bone metastatic cascade involves extravasating/localising to a favourable metastatic site (Seed and soil hypothesis ²⁵) followed by remodelling of secondary site for further colonisation. To model breast to bone metastasis, two systems were standardised to focus on localisation and on remodelling the matrix. The indirect migration model looked at the response of breast cancer cells to secondary site ECM. The direct migration system instead was used to assess invasion and capacity of breast cancer cells to migrate to the bone-mimicking site.

This work demonstrates the proportional relation between increase of migration, invasion, PTHrP and IL-6 expression in MDA-MB 231 cells with stiffness of hydrogels used to pre-condition cells. Additionally, this work reminds the necessity to use physiologically relevant 3D *in vitro* models able to mimic several aspects of tumour microenvironment allowing the detection of cellular events directing biological processes (e.g., extravasation, migration, invasion). Such models are not intended to replace other models, but to support and better understand the complex metastatic cascade, aiming at the identification of new therapeutic modalities (e.g. mechano-therapeutics) and accelerate their translation to the clinic.

2. Methodology

2.1 General Cell culture

Human breast adenocarcinoma cell line MDA-MB 231 (ATCC) and breast cancer bone homing cell line MDA-IV (kindly provided by Prof Ingunn Holen, University of Sheffield, Sheffield, UK) were cultured in Dulbecco’s Modified Eagle Medium (DMEM, D6546, Sigma-Aldrich, UK)

media supplemented with 1% (v/v) L-glutamine (G7513, Sigma-Aldrich, UK), 10% (v/v) Fetal Bovine Serum (FBS, F9665, Sigma-Aldrich, UK) and 1% (v/v) Penicillin-Streptomycin (P4333, Sigma-Aldrich, UK). Human osteosarcoma cell line Saos-2 (kindly provided by Dr Olga Tsikou, The University of Manchester, Manchester, UK) were cultured in McCoy's 5A media (M9309, Sigma-Aldrich, UK), supplemented with 15% (v/v) FBS and 1% (v/v) Penicillin-Streptomycin.

All cell lines were tested negative for mycoplasma contamination by Mycoalert mycoplasma detection kit (LT07-318, Lonza) prior use. Unless otherwise specified, all cell culture experiments were performed in a humidified 5% (v/v) CO₂ air atmosphere at 37 °C in complete medium. Cells were discarded upon reaching passage number 25.

2.2 3D cell culture: encapsulation in alginate-gelatin hydrogel beads

2.2.1 Preparation of hydrogel precursors and crosslinking solutions

Four different combination of alginate and gelatin hydrogel precursor solutions (A1.5G1, A1.5G3, A3G1 and A3G3) were selected and prepared as previously described (Chapter 2, Section 2.1) to match stiffness and composition of normal and tumour breast cancer tissue. Briefly, sodium alginic acid (G/M ratio of 0.7, Pro-Alg, Chile) was dissolved in HEPES buffered saline (HBS), at a concentration of 3 % and 6%. Obtained alginate solutions (aq.) were sterile filtered with 0.22µm PES filter. Gelatin type A (G1890, Sigma-Aldrich, UK) was dissolved in HEPES buffered saline (HBS), at a concentration of 2 % and 6%. Gelatin solutions (aq.) were sterile filtered with 0.45µm PVDF filter. Hydrogel precursor solutions were prepared by mixing different combination of alginate and gelatin solutions at selected concentrations in 1:1 volume ratio (final concentrations reported in Table 1). This mix was thoroughly homogenised with a vortex at room temperature for 5 min.

Calcium chloride (CaCl₂, C/1400/53, Fischer scientific, UK) was prepared in deionized water at concentrations of 100 mM, 200 mM and 300 mM. Each solution was sterile filtered prior use (0.22 µm PES filter) and stored at 4°C.

2.2.2 3D breast cancer models: alginate-gelatin hydrogels

MDA-MB 231 cell pellet containing 2×10^6 cells was re-suspended in 1 mL of alginate-gelatin solution (aq.) using the MICROMAN E viscous pipette (M1000E, Gilson, UK) and ensuring a homogeneous single cell suspension. The cell-suspension was transferred in a sterile 1 mL syringe equipped with a 28G needle. A beaker was filled with sterile CaCl_2 solution (Table 1), the cell suspension was ejected through the nozzle drop-wise, generated hydrogel beads were incubated in the CaCl_2 solution (aq.) allowing gelation (10 min, Room Temperature/RT). Spherical alginate-gelatin beads encapsulating cells were recovered from the gelling solution using a cell strainer, washed twice with sterile HBS solution, and finally immersed in complete cell culture media and transferred in the incubator.

Table 1. Final concentrations of Alginate, gelatin and calcium chloride in preparation of Alginate-gelatin gels

| Sample ID | Final concentration alginate (w/v) % | Final concentration gelatin (w/v) % | Calcium chloride solution (mM) |
|-----------|--------------------------------------|-------------------------------------|--------------------------------|
| So-L | 1.5 | 1 | 100 |
| So-H | 1.5 | 3 | 100 |
| St-L | 3 | 1 | 300 |
| St-H | 3 | 3 | 300 |

2.2.3 Cell recovery: hydrogels dissolution

Recovery of viable encapsulated cells in alginate-gelatin hydrogels was obtained by gentle dissolution of alginate beads by incubation with a calcium sequestering buffer solution (10 min, RT). The dissolution buffer was prepared dissolving 100 mM HEPES (H4034, Sigma-Aldrich, UK) and 500 mM Trisodium citrate dehydrate (W302600-K, Sigma-Aldrich, UK) in $1 \times$ phosphate buffered solution (PBS, D8537, Sigma-Aldrich, UK). The dissolution buffer was sterile filtered with a $0.22 \mu\text{m}$ PES filter prior use.

2.3 3D bone models: PCL-based scaffold

3D PCL-based scaffolds (PCL, PCL HA, PCL BaTiO₃ and PCL SrHA) were manufactured as previously described^{23,24} by using a 3D-Bioplotter system (EnvisionTEC, Gladbeck; Germany). Briefly, the dispersion phase (10 % w/w) of each composite formulation was mechanically mixed with the polymeric phase at room temperature. Subsequently, about 4g of the raw materials in powder form was introduced into a stainless-steel cartridge and processed as single extruded filament using a 22G nozzle, and according to the printing conditions reported in table 1. In order to increase pore interconnectivity, porous cylindrical (7 mm diameter) scaffolds were produced with a shifted architecture, made using a laydown pattern of 0/90° and an offset distance equal to half the distance between strands.

Table 2. Optimised printing parameters for 3D scaffolds

| Sample ID | Temperature (°C) | Pressure (bar) | Speed (mm/s) | Pre-Flow (s) | Post-Flow (s) |
|------------------------|------------------|----------------|--------------|--------------|---------------|
| PCL | 130 | 6 | 0.6 | 0.45 | 0.1 |
| PCL HA | 130 | 6.5 | 0.6 | 0.75 | 0.1 |
| PCL BaTiO ₃ | 125 | 5.5 | 0.7 | 0.75 | 0.1 |
| PCL SrHA | 130 | 6.2 | 0.6 | 0.75 | 0.1 |

2.3.1 PCL scaffolds: bone scaffold

Composite PCL scaffolds were sterilised as previously described in Mancuso *et al.*²³. Sterile scaffolds were transferred to a 48 multi-well (MW) plate, 2×10⁵ Saos-2 cells (previously re-suspended in 50 µL of complete media) were gently pipetted on the top of each scaffold. Scaffolds were incubated allowing cell adhesion (37°C, 5% CO₂, 30 min), then 400 µL of fresh complete media was added in each well covering the whole scaffold. After seven days of culture (37°C, 5% CO₂), the culture media was changed to osteoblast mineralisation media (C-27020, PromoCell, UK) to induce mineralisation and changed thereafter every four days until the end point (i.e., day 28).

2.3.2 Decellularization of PCL scaffolds: biohybrid bone scaffolds

PCL scaffolds were decellularized via a combination of mechanical and chemical methods^{26,27}, with all steps performed in sterile conditions. After 28 days of culture (end point), scaffolds were washed twice with sterile distilled water and frozen at -80°C in water overnight. Scaffolds were thawed (RT, 2 h), and the freeze-thaw cycle was repeated twice to complete cell lysis. Following the mechanical decellularization step, scaffolds were washed twice with HBS and then incubated with sterile 1 mg/mL DNase (11284932001, Roche) solution diluted in HBS (37°C, 1 h) to remove any residual nuclear debris. Incubation with 0.05% (w/v) SDS solution in HBS (RT, 15 min) to remove any further remaining debris. Before further cell culture experiments, scaffolds were washed (n=3) with HBS (RT, 5 min) to remove any residual reagents.

2.4 Alginate-gelatin hydrogels and PCL scaffold: breast to bone model

2.4.1 Indirect migration model

The indirect migration model was designed as manually seeding pre-conditioned breast cancer cells on biohybrid bone scaffolds. Prior this step, MDA-MB 231 cells were cultured in selected alginate-gelatin hydrogels (Table 1) for 7 days, allowing conditioning in distinctive conditions mimicking breast tumour microenvironments (Fig 1A). After the pre-conditioning step, MDA-MB 231 cells were retrieved from alginate-gelatin beads using the dissolution buffer. As control, MDA-MB 231 (non-conditioned) and MDA-IV cells (non-conditioned) were cultured on standard tissue culture plastic (TCP) wells, detached with trypsin (T3924, Sigma-Aldrich, UK) following standard protocols (37°C, 3 min). All recovered cells were centrifuged at 600 g and re-suspended in complete media, then seeded directly on biohybrid scaffold at a seeding density of 1×10^5 /scaffold, and on TCP wells at density of 2×10^4 cells/cm² as additional control group (Fig 1A). As mentioned in the introduction, trapped TGF- β in bone is released by osteolysis and is involved in bone metastasis *in vivo*. To make up for this released TGF- β in our model, TGF- β was added externally. Hence, for all the mentioned conditions, experiments were performed with complete cell culture media or with supplementation of 5 ng/mL TGF- β (100-21, Peprotech). For all the conditions, cells were cultured (37°C, 5% v/v CO₂) for 7 days in complete DMEM medium, changing the media every 2 days.

2.4.2 Direct migration model

The direct migration model was designed to mimic the migration of breast cancer cells from primary (breast) to the secondary site (bone), aka from hydrogels to biohybrid scaffolds (Fig 1B). Briefly, cells were retrieved from hydrogels after 7 days using the dissociation buffer and re-encapsulated in the same hydrogel at a density of 2×10^6 cells/mL. 200 μ L of cell-hydrogel suspension was gently pipetted on top of the decellularized PCL scaffold in a 48 MW plate followed by incubation at 4°C (15 min) to allow physical gelation of gelatin and obtain cylindrical shaped hydrogels encapsulating pre-conditioned cells. Then 200 μ L of CaCl₂ (aq.) was added to the well allowing ionic alginate crosslinking (RT, 10 min). The combined scaffold was washed with HBS (n=3) and then supplemented with complete media (DMEM). Cells were incubated up to 7 days and cell culture media was replaced every day.

2.5 Cell proliferation assay

Alamar blue assay carried out with Deep Blue Cell Viability™ Kit (424701, Biolegend) was used to analyse proliferation of MDA MB 231 and MDA-IV cells in PCL scaffolds at day 1, 3 and 7. Briefly, cell culture media was gently removed from each well, 400 μ L of deep blue solution (10% v/v Deep blue viability reagent in complete cell culture media) was added to each well and incubated for 2 hours (37°C, 5% v/v CO₂). Then, 200 μ L of cell culture media was taken from each well, transferred to a 96 well plate, and immediately measured with Synergy-2 (Biotek) plate reader (Ex 530-570 nm / Em 590-620 nm). The measurements are reported as mean \pm standard deviation of (n=2, N=3) experiments.

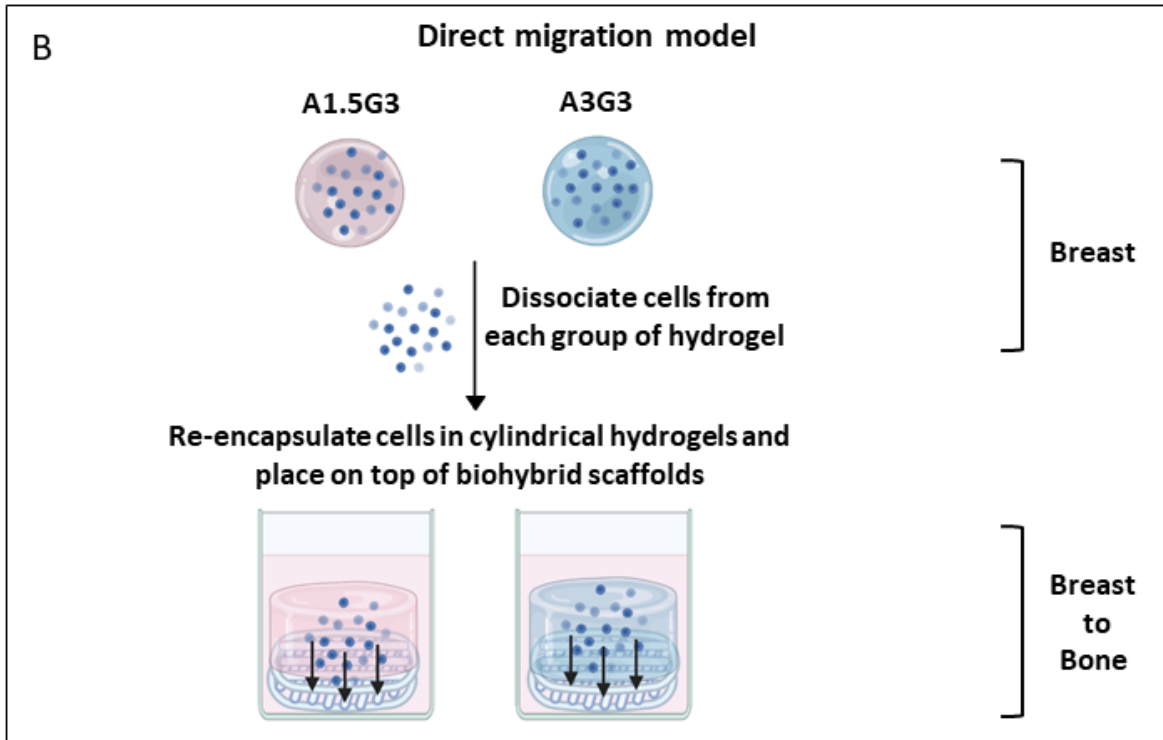
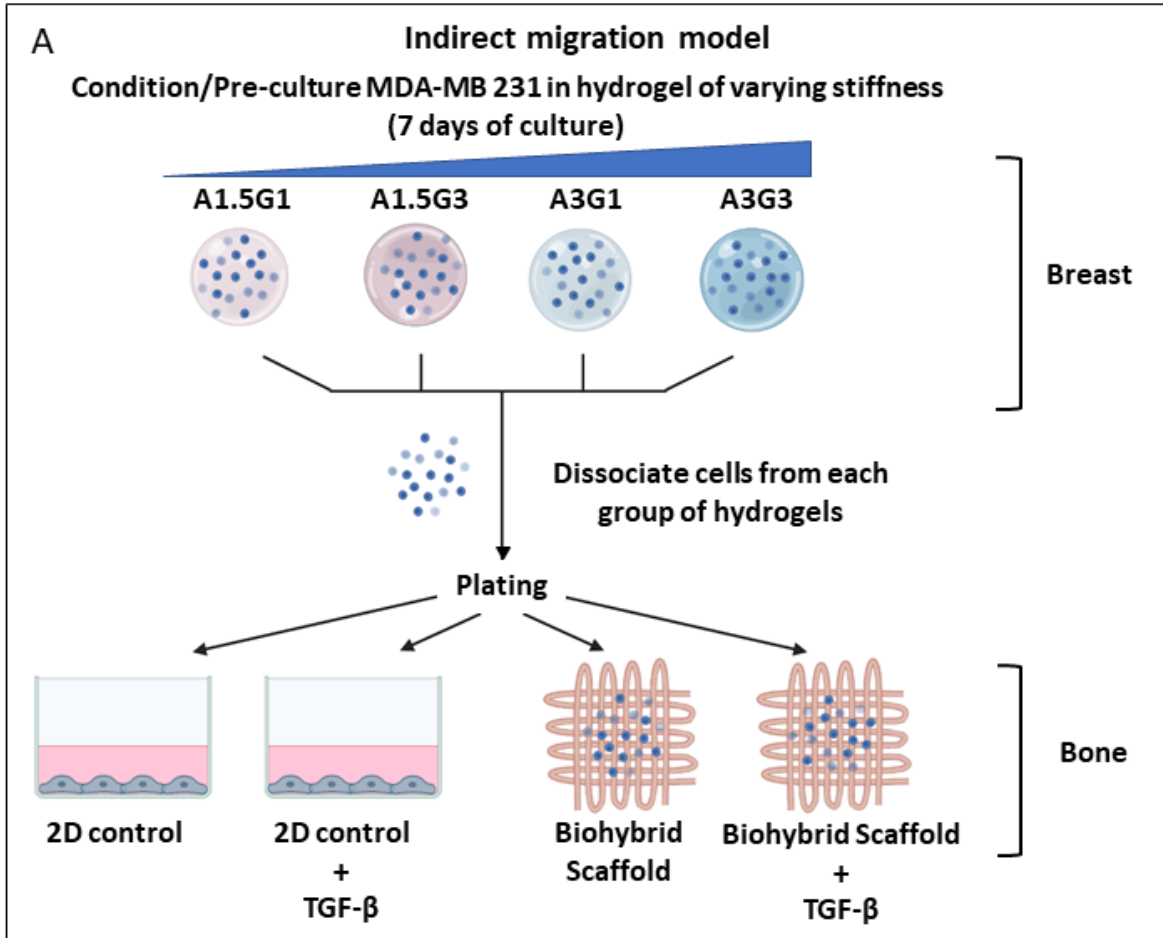


Figure 1: Schematic layout of experimental plan for indirect (A) and direct migration (B).

2.6 Adhesion/ Cell spreading assay

8-well chambers slides (80826, Ibbidi) were coated with collagen according to manufacturer's protocol. Briefly, each chamber was coated with 35 $\mu\text{g}/\text{mL}$ Collagen type I (sterile, 50201, Ibbidi) diluted in 17.5 mM acetic acid and incubated (RT, 1 h). Collagen solution was slowly removed, and chambers were washed with sterile PBS (n=1). Similarly, fibronectin (F2006, Sigma) was diluted in sterile PBS and used at a concentration of 20 $\mu\text{g}/\text{mL}$ (RT, 1h). After incubation, fibronectin solution was removed and chambers were washed with sterile PBS (n=1). After washing, both collagen and fibronectin coated chambers were left to air dry in sterile conditions (RT, 30 min).

Cells pre-conditioned in selected hydrogels (7 days) were recovered using the dissociation buffer and seeded on uncoated (control), collagen or fibronectin coated surfaces at a density of 1×10^4 cells/ cm^2 . After 45 minutes of incubation (37°C, 5% CO_2), cells were fixed with 4% paraformaldehyde (PFA) and incubated (RT, 30 min) with 1 $\mu\text{g}/\text{mL}$ DAPI in PBS (D954, Sigma-Aldrich, UK) and a 1: 50 Phalloidin Alexa-568 in methanol (A12380, Invitrogen). The experiment was performed N=2 independent experiment

2.7 Scratch assay

MDA-MB 231 cells preconditioned in hydrogels (different stiffnesses, 7 days) were recovered, seeded in 6-well plate at a density of 4×10^5 cells/well and transferred to the incubator (37°C, 5% v/v CO_2) allowing cell adhesion (24 h). A scratch was then performed in each well using a sterile 200 μL tip, each well was washed with cell culture media to remove any cellular debris. Cells were supplemented with low serum media (1% v/v FBS in DMEM with 1% v/v L-glutamine and 1% v/v PenStrep) to reduce cell proliferation^{28,29}. Images of the scratch were acquired after 0, 24 and 48 h. The experiments were performed in duplicates and for N=3 independent experiment.

2.8 Invasion assay

Silicon inserts (80406, Ibidi) were cut in 4x4 mm pieces placed at the centre of each well (8-well chambers, Ibidi) to create a cell free space (Figure S1A). Collagen (50201, Ibidi) pre-gel mix was prepared following the supplier's instruction: collagen was diluted to a final concentration of 1 mg/mL in 10× DMEM (D2429, Sigma-Aldrich) and sterile water, the pH was adjusted to 7.2-7.4 using sterile 1 M NaOH (12963614, Fischer scientific) and 7.5% NaHCO₃ solution (S8761, Sigma-Aldrich). MDA-MB 231 cells were gently re-suspended in the collagen pre-gel solution at a density of 7.5×10^5 cells/mL. Immediately, 200 μL of cells-collagen mix was pipetted outside the silicon insert and incubated allowing collagen gelation (37°C, 5% CO₂, 30 min). The central insert was removed and 50 μL of 1 mg/ml collagen solution were pipetted to fill the space with cell-free collagen hydrogel. The whole setup was further incubated to complete gelation (37°C, 5% CO₂, 20 min).

After gelation, encapsulated cells were stained with Cytopainter red (ab138893, Abcam). Briefly, cells were incubated with 1X dye diluted in cell culture media for 1 hour in the incubator and washed twice with 1X PBS followed by addition of cell culture media only. The assay was imaged at day 0 and day 3.

2.10 PThrP expression

PThrP expression was detected from cell lysates at day 7 using the Human PTHrP Elisa kit (E-EL-H1478, Elabscience). MDA-MB 231 cells were first trypsinized from the either scaffolds or well plates (37C, 5 min), then recovered using fresh media. Cells were centrifuged (500g, 3 min), the pellet was incubated (4C, 5 min) in 200 μL of lysis buffer composed of 1X RIPA buffer (ab156034, Abcam), Complete mini protease inhibitor cocktail tablet (11836170001, Roche) and 1 μM Phenylmethylsulfonyl fluoride (PMSF). After 5 minutes on ice, the cell lysate was centrifuged (4C, 2000g, 10 min) and supernatant collected for further ELISA analysis. Sandwich ELISA was performed as per supplier's manual. The blank OD values (lysate buffer only) obtained at 450nm were subtracted from sample and standard's OD values and pg/mL values of samples were calculated using the standard calibration curve. BCA protein assay (23228, Thermo Scientific) was used to measure the lysate concentration for each sample. Finally, the obtained PThrP

concentrations were further normalised by their respective lysate concentration, obtaining PTHrP pg/mg of protein values. Obtained values are plotted as Mean \pm SD of (N=3) three independent experiments.

2.11 IL-6 release quantification

For each sample, fresh media was changed on day 6 and collected on day 7 (24 hours later). Briefly, media was centrifuged (RT, 10 min, 1000g) and the supernatant collected and used to detect IL-6 release. ELISA (human IL-6 Kit, 550799, BD OptEIA™) was performed according to supplier's instruction, with fresh complete media used as blank. The amount of IL-6 (pg/mL) was determined from the standard calibration curve of known standard IL-6 concentration. Obtained concentrations were normalised against their respective cell proliferation data (Section 2.5) measured at day 7. Obtained values are plotted as mean \pm SD of three independent experiments (N=3).

2.12 Image acquisition and analysis

Images were acquired using the fluorescent inverted microscope (Leica DMI6000, Leica Microsystems, UK) coupled with a 5.5 Neo sCMOS camera (Andor, UK), and equipped with: 2 \times objective (PLAN 2.5 \times /0.07, Leica), dry 10 \times objective (PL 10 \times /0.3 PH1, Leica), dry 20 \times objective (PL 20 \times /0.5 PH2, Leica), dry 63 \times objective (PL 63 \times /0.9 PH2, Leica), and filter cubes (A4, I3 and N2.1). The μ Manager software (v.1.46, Vale Lab, UCSF, USA) was used to control both microscope and camera, as well as to capture images.

2.12.1 Adhesion assay

Cells were imaged with the 20 \times dry objective with filter cubes A4 and N2.1. Images were analysed with ImageJ (v1.49p) for object identification and measure the cell spread area. Overall, nearly 200 cells from two independent experiment were analysed per condition and area of each cell was plotted in group for each condition.

2.12.2 Scratch assay

Brightfield images using the 10× dry objective of the scratch and taken at different time points (24h, 48h). The area of scratch invaded by cells was calculated using ImageJ by measuring the combined cellular area in the scratch over time. The data is plotted as Mean ± SD of (n=2, N=3) independent experiments.

2.12.2 3D collagen invasion assay

Cells were imaged using the 2× objective and N2.1 filter cube, at different time points (day 0 and day 3). In order to measure invasion on the overall volume, z-stacks (z-step of 50 μm) were acquired, and the maximum projection of each sample was analysed with ImageJ. For the analysis, maximum projections were converted to binary, and the total area stained in the acellular collagen hydrogel at day 3 was measured for each condition. The data is plotted as Mean ± SD of (n=2, N=3) independent experiments

2.13 Statistical analysis

For adhesion, migration and invasion assay, significance among different conditions was analysed with one-way analysis of variance (ANOVA). For PTHrP and IL-6 analysis significance among conditions were analysed by Two-way ANOVA using GraphPad prism v9.1.0. P-values were set at four different significance levels: * $p \leq 0.05$, ** $p \leq 0.01$, *** $p \leq 0.001$, **** $p \leq 0.0001$.

3. Results and Discussion

3.1 Conditioning MDA-MB 231 with high stiffness leads to increased migratory and invasive phenotype

In our previous study (Chapter 2), we demonstrated the effect of stiffness and composition of alginate-gelatin hydrogels on stem cell marker expression using two breast cancer cell lines: MDA-MB 231 and MCF-7. Compared to MCF-7, MDA-MB 231 which are triple negative breast cancer cell line (TNBC), are well known for their invasive potential and are commonly used as a model to study bone metastasis^{30,31}. TNBC are hormone insensitive and much more aggressive, therapeutic resistant than other breast cancer subtypes³². Hence in this study, MDA-MB 231 were selected and used to understand role of ECM properties in various aspects of metastatic potential

which could be used for further targeting of metastasis. We examined effect of stiffness and composition of hydrogels on MDA-MB 231's invasive and migratory phenotypes using three experiments: adhesion ability (2D cell spread assay, paragraph 2.6), migration ability (2D scratch assay, paragraph 2.7) and invasion (3D collagen invasion assay, paragraph 2.9). In all experiments, MDA-MB 231 cells were allowed to adapt to the microenvironment (i.e. hydrogels) for 7 days: cells were encapsulated in alginate-gelatin hydrogels with known stiffness and composition (Table 2).

Table 3: Hydrogel composition of the four selected alginate-gelatin hydrogels varying compressive moduli (stiffness) and concentration of gelatin (adhesion ligand content). Sample ID are named with a combination of their properties: Soft (So, stiffness < 3 kPa), Stiff (St, stiffness > 6 kPa), low adhesion ligand (L, 1% w/v gelatin), high adhesion ligand (H, 3% w/v gelatin). Compressive moduli of selected hydrogels were measured in Chapter 2.

| Sample ID | Hydrogel composition | Adhesion ligand | Stiffness |
|-----------|--|--|---------------------------|
| | Crosslinking solution, Calcium Chloride (CaCl ₂ , mM) | Gelatin concentration (1% w/v, 3% w/v) | Compressive modulus (kPa) |
| So-L | A1.5G1 100 CaCl ₂ | Low | 1.8 ± 0.2 |
| So-H | A1.5G3 100 CaCl ₂ | High | 2.4 ± 0.1 |
| St-L | A3G1 300 CaCl ₂ | Low | 6.1 ± 0.2 |
| St-H | A3G3 300 CaCl ₂ | High | 10.1 ± 0.5 |

Adhesion assay examined cellular adhesion and extent of membrane protrusion, both of which precede migratory and invasive phenotype. Substrate adhesion was examined by plating preconditioned MDA-MB 231 cells on non-coated, collagen and fibronectin coated plates (Figure 2A-D). The number of cells that attached to the substrate (adhesion) didn't vary significantly among groups of conditioned cells in all the substrates tested. Individual cell spread area of conditioned cells exhibited no differences amongst them on non-coated and collagen coated plates. On the contrary, cells preconditioned in St-H hydrogels (high stiffness, high gelatin) showed

increased spread area in fibronectin coated plates (Figure 2A, 1D). In this model, both high stiffness and composition of hydrogels are responsible for changes in cells' adhesion capacity.

Parallel to previous findings, MDA-MB 231 cells conditioned in stiff hydrogels (compressive modulus > 6 kPa) covered the scratch area significantly faster at both days than the ones from softer hydrogels (compressive modulus < 3 kPa) as shown in (Figure 3A, B, C). Cells conditioned in So-L vs St-L hydrogels showed 30% increase ($p < 0.01$) and So-H vs St-H showed 40% increase in covering the scratch area ($p < 0.0001$) at Day 2 (Figure 3C). Within high stiffness groups, cells cultured in St-H showed increased migration capacity than St-L ($p \leq 0.001$, Figure 3C). These results suggest a primary role of stiffness in this phenotype with gelatin content affecting cell migration capacity only when coupled with high stiffness.

Invasive potential in 3D was quantified measuring the cells ability to invade pristine collagen hydrogels. Again, MDA-MB 231 cells previously cultured in selected alginate-gelatin hydrogels were resuspended in collagen at known concentration and migration towards acellular collagen hydrogels was observed over time. To measure invasion, MDA-MB 231 cells were stained with Cytopainter red, as this staining is retained only by cells initially encapsulated in the gel. In this way, daughter cells proliferated in collagen were removed from the counting, distinguishing invasion from proliferation (Figure S1B, 4A). After three days, cells from stiffer hydrogels (St-L and St-H) invaded the area 1.5 times more than the ones from softer hydrogels (So-L and So-H, Figure 4B). We did not observe any correlation between the amount of gelatin in hydrogels and cells' invasive potential (Figure 4), as no statistical difference was observed when comparing hydrogels with similar stiffness and increased gelatin content (So-L vs So-H, St-L vs St-H). On the contrary, and as expected, cells from stiffer hydrogels have higher invasive potential compared to cells from softer hydrogels (So-L vs St-L, $p \leq 0.01$; So-H vs St-H, $p \leq 0.05$).

This study suggests that preconditioning cells in environments with different stiffnesses plays a major role in directing MDA-MB 231 migratory and invasive phenotypes, whereas this correlation was not evidenced at different adhesion ligand concentrations. While this study only elucidates effects of gelatin-related adhesion motifs, inclusion of other ECM components like fibronectin, laminin, and hyaluronic acid could better illustrate contributions of ECM composition on migration and invasion capacity.

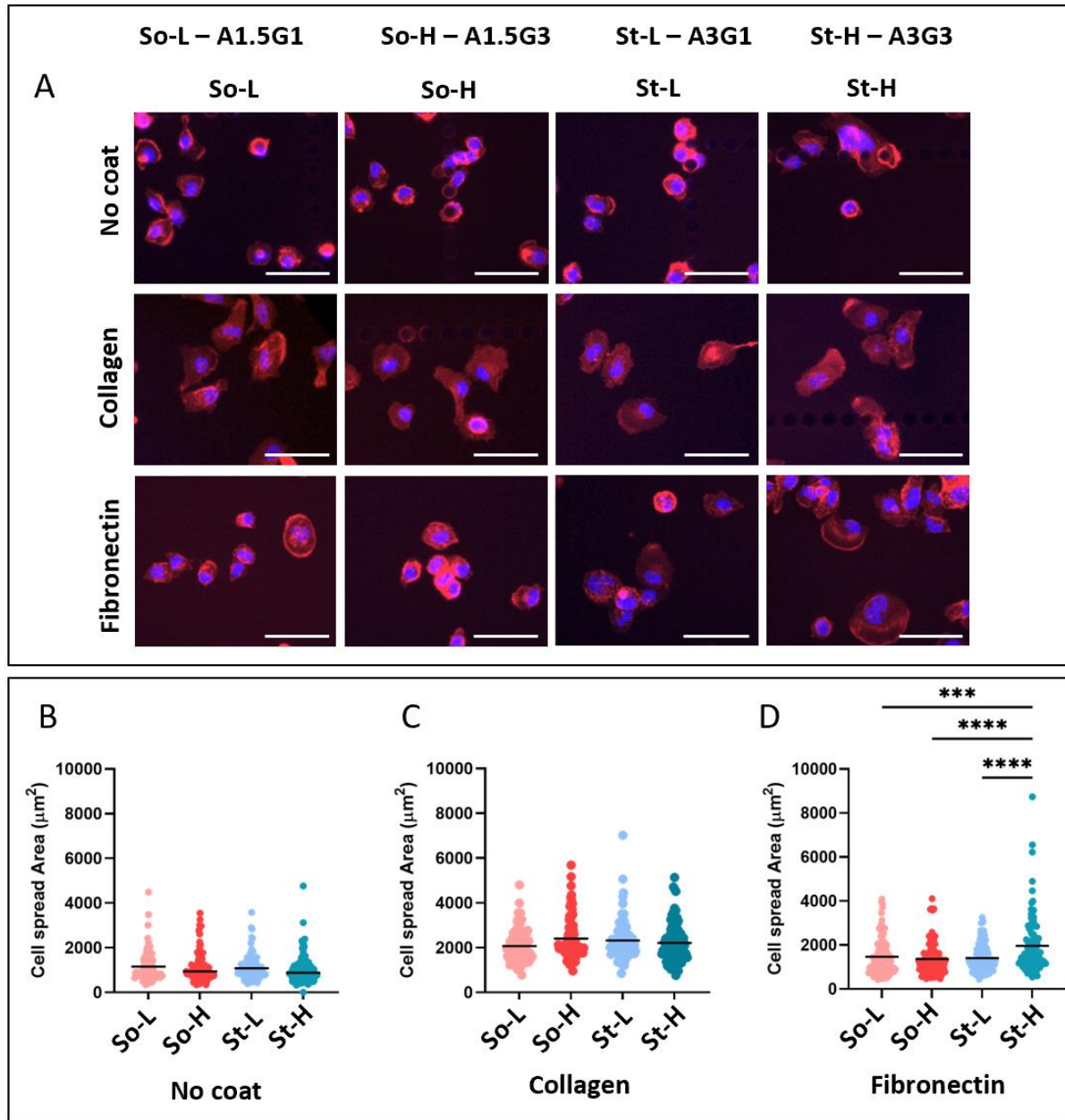


Figure 2. Cellular adhesion on stiffness conditioned cells. Cell spread area assessed on non-coated, collagen and fibronectin covered plates. **A)** Immunofluorescent images of MDA-MB 231 cells stained with DAPI (nuclei, blue) and Phalloidin (F-Actin, red) conditioned in the selected four alginate-gelatin hydrogels on non-coated, collagen-coated or fibronectin-coated surfaces (Scale bars: 100 μm). Dot-plot representations of individual cell area and mean of at least $n=100$ cells of: **B)** non-coated, **C)** Collagen-coated, and **D)** and Fibronectin-coated. P-values represented as $*p \leq 0.05$, $**p \leq 0.01$, $***p \leq 0.001$, $****p \leq 0.0001$).

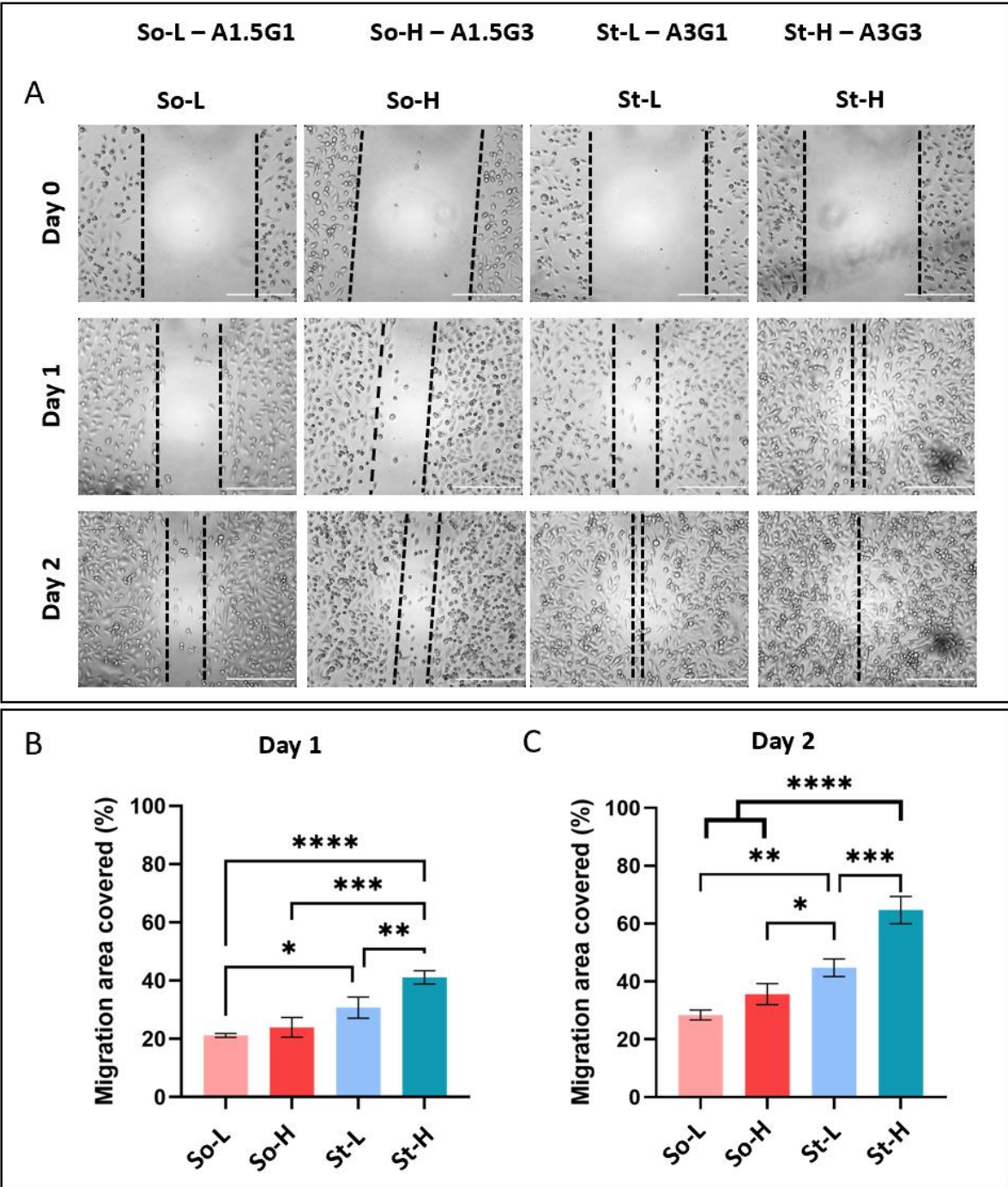


Figure 3. Migration assay of stiffness conditioned cells. Scratch assay performed on stiffness conditioned cells: **A**) Brightfield images of the scratch assay performed on cells conditioned in selected four hydrogels at day 0, day 1 and day 2 (Scale bars- 500 μ m). Graphical representation of scratch area (μ m²) covered by migratory cells represented as % in comparison to blank area at day 0: **B**) at day 1 and **C**) at day 2. The data

is represented as mean and SD of n=2 wells, N=3 independent experiments. P-values represented as *p ≤ 0.05, **p ≤ 0.01, ***p ≤ 0.001, ****p ≤ 0.0001).

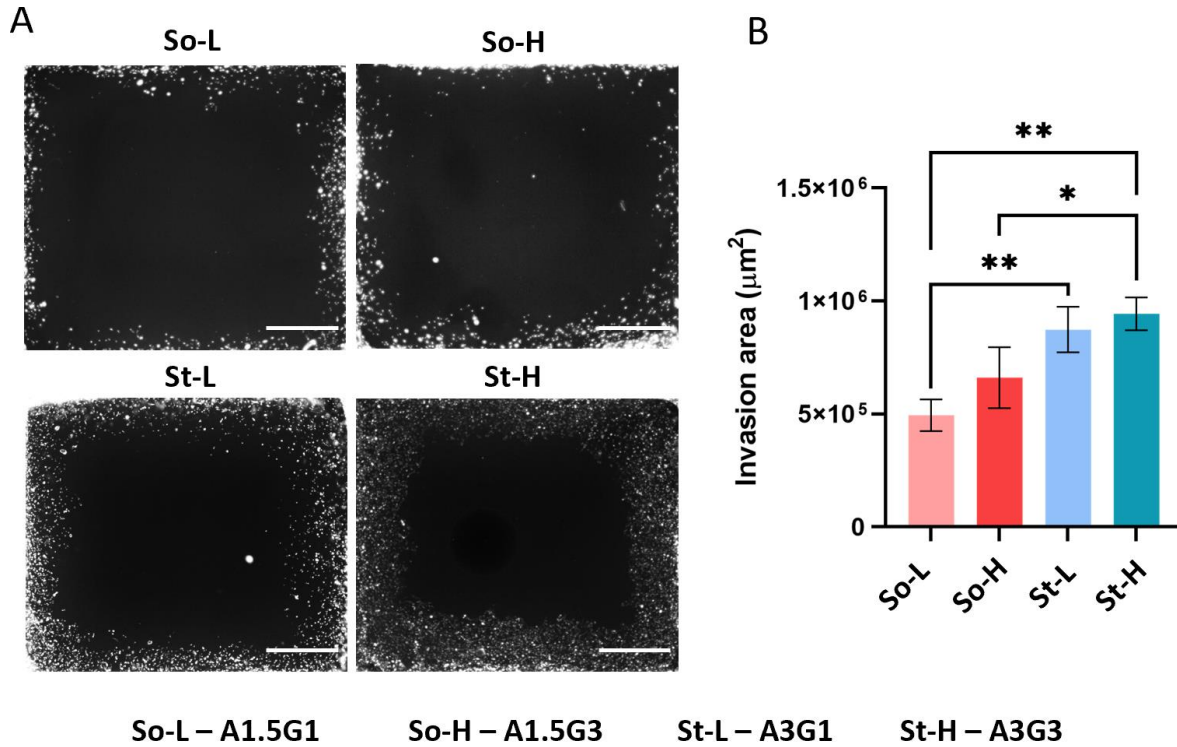


Figure 4. Invasion assay of stiffness conditioned cells. 3D collagen invasion assay of stiffness conditioned cells. **A)** Cropped images of the acellular collagen hydrogel area showing invasion of MDA-MB 231 pre-conditioned in alginate-gelatin hydrogels at day 3 to showcase impact of alginate-gelatin hydrogels on cell invasive potential (Scale bars: 1000 μm). Whole image of the well is shown in Figure S1B. **B)** Binary images of cropped area obtained after post-processing were used to calculate the invaded area (μm²) and represented as mean ± SD of n=1 and N=3 independent experiments. P-values represented as *p ≤ 0.05, **p ≤ 0.01, ***p ≤ 0.001, ****p ≤ 0.0001).

3.2 Decellularized PCL scaffolds to mimic bone ECM

PCL scaffolds are known to retain ECM deposited by cells cultured on them after decellularization^{26,27}. Here, we compared osteogenic potential of composite PCL scaffolds and evaluated their ECM retaining ability after decellularization (Figure 5A). We selected four PCL-composite scaffolds (i.e. PCL, PCL HA, PCL SrHA and PCL BaTiO₃) to mimic bone tissue properties^{23,24}. The

scaffolds were printed with the same 3D structure and characterised in terms of composition, strand dimension and mechanical properties^{23,24}. All PCL-composite scaffolds were cultured up to 28 days with Saos-2 allowing deposition of bone-ECM. Decellularization of scaffolds was performed to assess A) the capacity to retain ECM-deposited, and B) the feasibility to remove cells from scaffolds in sterile condition and allowing for their use as metastatic site in other experiments (Figure 5A). SaOs-2 cells were chosen as human osteoblast model because of their resemblance to osteoblastic properties especially matrix production and calcium deposition under mineralising conditions³³⁻³⁵. Osteoblasts maturation was quantified in all PCL-based scaffolds up to 28 days using: cell proliferation, ALP activity, calcium deposition (Alizarin stain) and ECM deposition (collagen and osteocalcin IF stain)³⁶. Proliferation data suggests higher compatibility of composite PCL scaffolds (PCL HA, PCL SrHA, PCL BaTiO₃) when compared to pristine PCL ones (Figure S2A). PCL BaTiO₃ scaffolds were found to induce highest amount of ALP in Saos-2 cells when compared to other scaffolds (Figure S2B); moreover, both PCL HA and PCL BaTiO₃ scaffolds lead to increased calcium deposition by Saos-2 cells (alizarin stain, Fig S3). IF stain confirmed deposition of both collagen and osteocalcin, suggesting comparable deposition of both ECM proteins by SaOs-2 on all scaffolds tested by day 28 (Fig S4).

The ability to use decellularized PCL scaffolds and to create sterile biohybrid PCL scaffolds (i.e. composite bone-mimicking scaffolds enriched in bone mineralised matrix) was assessed as criteria to use such biohybrid scaffolds in other *in vitro* experiments. In fact, biohybrid PCL scaffolds could act as a more physiologically relevant *in vitro* secondary site for breast cancer. The decellularization steps were optimised for all PCL-based scaffolds (Supplementary Information, Fig S5), and the incubation with 1 mg/mL of DNase to lyse nuclear debris after mechanical disruption of cells was found critical to completely remove any residual of Saos-2 cells (Figure S5, 5B). The capability to retain deposited ECM was tested quantifying the amount of collagen and osteocalcin in decellularized scaffolds (IF staining, Figure 5B). Pristine PCL, PCL HA and PCL SrHA scaffolds retained both collagen and osteocalcin; whereas PCL BaTiO₃ showed a minimal ECM protein with negligible staining detected (Figure 5B). Calcium deposition after decellularization was measured using Alizarin stain, observing a minimal reduction of calcium in all scaffolds tested. Of note, the highest calcium amount detected was in PCL HA scaffolds (Figure 5C). Pristine PCL scaffolds and PCL BaTiO₃ scaffolds lost around 30% of previously quantified calcium deposition, which is possible due to the decellularization process. Both PCL HA and PCL

SrHA scaffolds were instead able to retain more calcium (about 10% reduction with respect to Saos-2 colonised scaffolds). Of note, Alizarin stain also recognises intracellular calcium, hence the reduction observed after decellularization could be attributed also to loss of intracellular calcium. From the results, PCL HA scaffold was selected as secondary metastatic scaffold as the one able to retain the highest amount of calcium and deposited ECM, which will from now on referred to as biohybrid PCL HA scaffold.

Preparation of Biohybrid PCL scaffolds

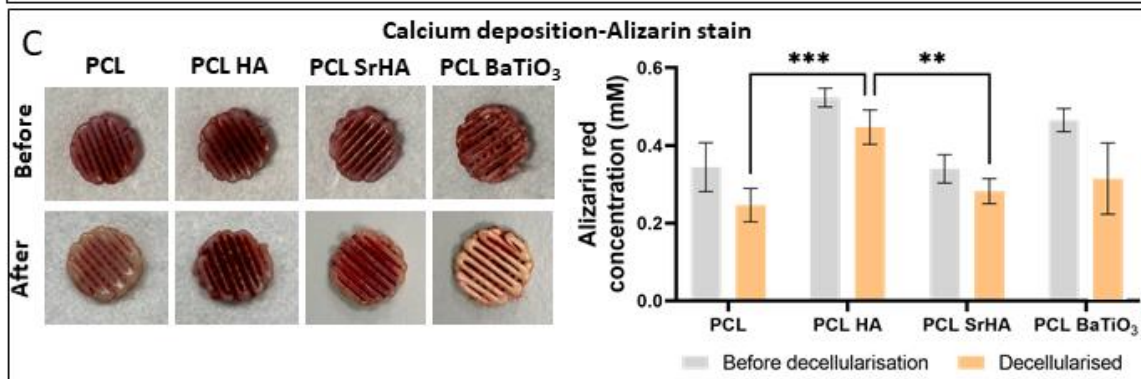
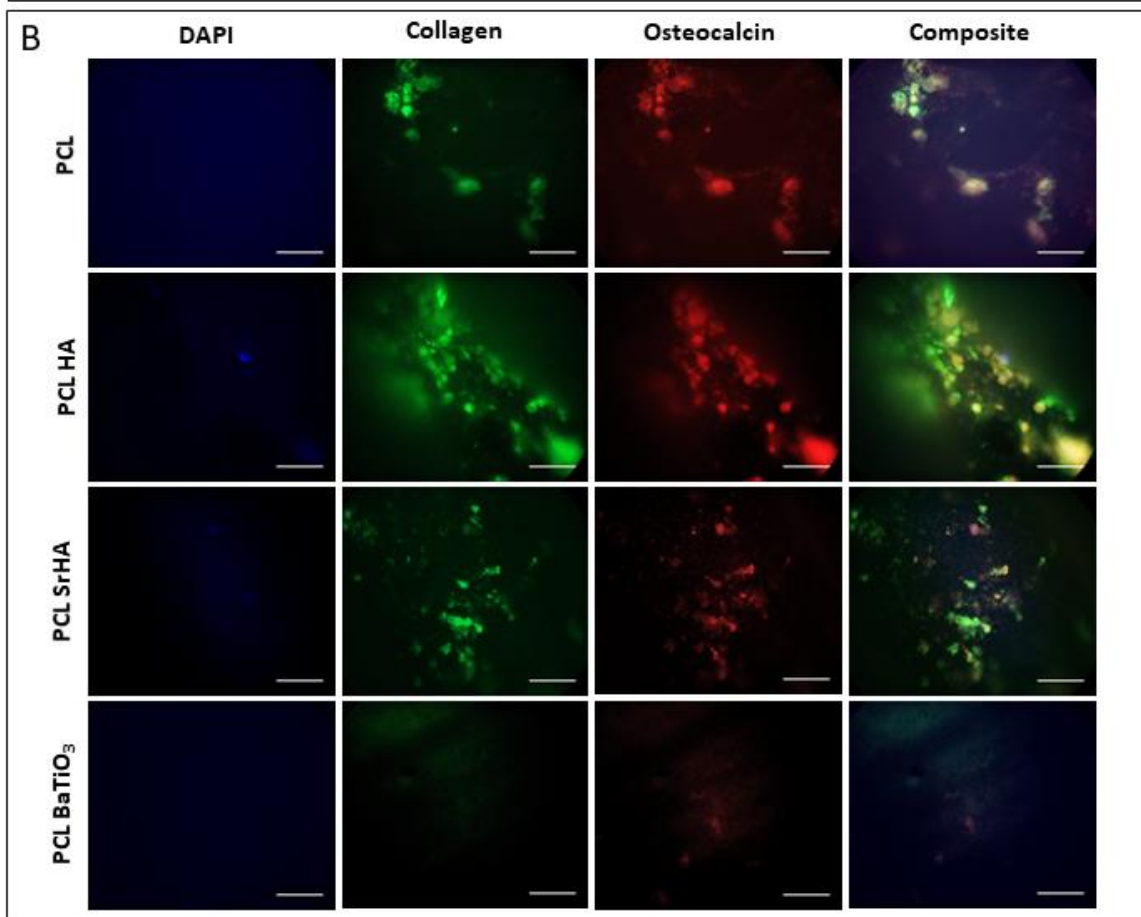
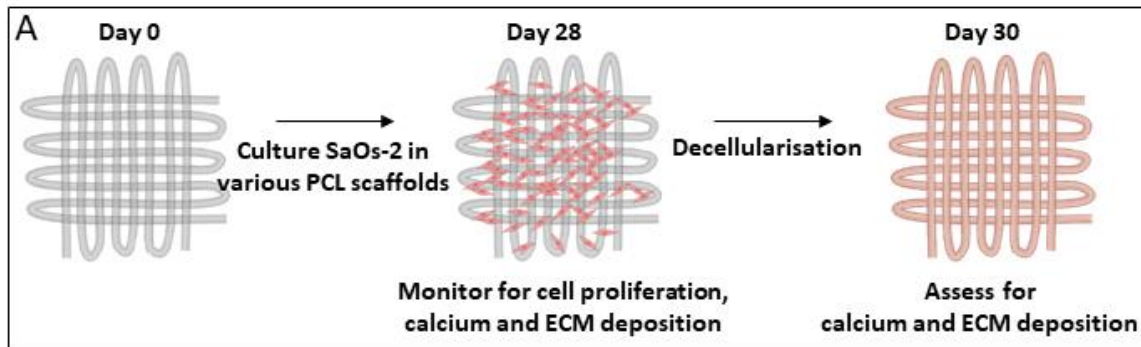


Figure 5. Biohybrid PCL scaffolds. Characterisation of decellularized composite PCL scaffolds to mimic bone ECM. **A)** Schematic representation of preparation of decellularized scaffolds and their characterisation. **B)** Immunofluorescent images of nucleus (blue), collagen (green) and osteocalcin (red) of stained PCL-based scaffolds after decellularization steps (Scale bars: 50 μm). **C)** Images of PCL-based scaffolds stained with Alizarin stain before and after decellularization and Alizarin stain concentration (mM) from scaffolds before and after decellularization. Values are represented as mean and SD of N=3 independent experiments. P-values represented as * $p \leq 0.05$, ** $p \leq 0.01$, *** $p \leq 0.001$, **** $p \leq 0.0001$).

3.3 Indirect migration of MDA-MB 231 and MDA-IV cells in biohybrid scaffolds

We have shown that conditioning MDA-MB 231 cells in different microenvironments (alginate-gelatin hydrogels, 7 days) of varying stiffness and adhesion motifs concentration could impact on invasive potential and migratory phenotypes of breast cancer cells (Figure 1-3). These results are preliminary indications suggesting to further assess metastatic potential of MDA-MB 231 and their capacity to invade a secondary bone site. In this study, two models were used to study the breast to bone metastasis. First was ‘Indirect migration model’, obtained by manually retrieving MDA-MB 231 cells from alginate-gelatin hydrogels and seeding them onto biohybrid PCL HA scaffold. This model was designed to focus on the response of breast cancer cells to bone ECM irrespective of their bone localising potential. As a control, non-conditioned MDA-MB 231 and MDA-IV (i.e. bone homing variant of MDA-MB 231) were cultured on biohybrid PCL HA scaffold to compare responses to conditioned cells. Response was quantified by examining cell proliferation, and osteolytic factor PTHrP and IL-6 expression up to 7 days of culture. To study the role of bone microenvironment growth factors like TGF- β , which are released in response to increased osteoclast activity in bone metastasis, the supplementation of 5 ng/ml TGF- β was used as additional variable of the model (Figure 6).

PTHrP expression as measured by ELISA at day 7 of culture showed overall increased expression in cells plated on biohybrid PCL HA scaffolds than the controls (i.e. 2D TCP plates), confirming that exposure to bone specific ECM is essential to induce PTHrP expression (Figure 6A), first key step in bone metastasis cycle. Interestingly MDA-MB 231 cells cultured on biohybrid PCL HA scaffolds showed proportional expression of PTHrP with stiffness of hydrogels (preconditioning step); two-fold increase was observed when comparing stiffer conditioned groups than softer

($p < 0.0001$ for So-L vs St-L, $p < 0.001$ for So-H vs St-H) (Figure 6A, 6C). The same trend (proportional PTHrP expression with stiffness) was observed in the presence of TGF- β ($p < 0.0001$ for So-L vs St-L and So-H vs St-H). Overall, the presence of TGF- β lead to an increased PTHrP expression in biohybrid PCL HA scaffolds (Figure 5C). Of note, no correlation of PTHrP expression with stiffness was observed when MDA-MB 231 were cultured on TCP and regardless the presence of TGF- β in the cell culture media. This trend suggests the active role of A) the primary site and cellular adaptation to the stiffness of the microenvironment and B) the composition of the secondary site in promoting osteolytic activity. These results support the need to use models representing better the characteristics of tissues (i.e. 3D/scaffolds) rather than conventional models (i.e. 2D/TCP surfaces) as they mimic microenvironment of the pathology. This can further help in understanding specific biological processes to support animal and clinical studies.

IL-6 release was assessed in similar manner as PTHrP expression. In groups without TGF- β supplementation, IL-6 release increased two-fold with high stiffness conditioning in the scaffolds but remained constant in TCP (Figure 6B). However, unlike PTHrP, IL-6 released by cells plated on scaffolds was less compared to that of TCP with the only exception of St-H group that matched its TCP counterpart (Figure 6B, C). Surprisingly, with TGF- β supplementation IL-6 release was reduced among all groups. The values almost remained constant in both TCP and scaffolds for conditioned and non-conditioned cells (Figure 6B, C).

In summary, MDA-MB 231 cells intrinsically express less PTHrP as seen in TCP plates but they have the potential to increase expression in response to stiffness conditioning from primary tumour and exposure to bone ECM (secondary site). On the other hand, MDA-MB 231 seem to release IL-6 at higher concentration intrinsically but it is observed to be fine-tuned by stiffness conditioning when exposed to bone ECM.

TGF- β interactions also align with previous studies, where a clear relationship of increased PTHrP expression induced by TGF- β in breast to bone metastasis is established^{18,37}; and no correlation with IL-6 expression in the same context. Studies done in other model systems report complex and mixed crosstalk between TGF- β and IL-6. In intestinal epithelial cells, TGF- β dampens IL-6 signalling by decreasing expression of IL-6 receptor but reports no direct effect on its expression³⁸. In biliary tract cancer, they work synergistically to induce EMT and chemotherapy resistance

³⁹. Other possibilities could include concentration dependent effect of TGF- β which might report a different response on IL-6 at either lower or higher concentrations. Both TGF- β ⁴⁰ and IL-6 ⁴¹ have pleiotropic effects which makes their interaction complex, hence further investigation is needed to draw solid conclusions within this model.

No significant difference in MDA-MB 231 proliferation (day 3, day 7) in biohybrid PCL HA scaffolds was observed between conditioned and non-conditioned cells (Figure S6A). However, the presence of TGF- β induced an increase in proliferation, proportional with alginate-gelatin stiffness during the preconditioning. Of note, MDA-IV cells growth was found similar to MDA-MB 231 preconditioned in the stiffer and high gelatin content hydrogel (Figure S6B).

Results show that the indirect model can recreate initial steps of bone metastatic cycle, and in particular the release of osteolytic factors by cancer cells in response to bone ECM. Of note, cell proliferation and colonisation come at a later stage of the metastatic cycle and rely on complex interactions with other components such as cell types (e.g. osteoblasts, osteoclasts, etc.) and tissue vascularisation. An in-depth understanding of metastatic onsets could be achieved by including relevant bone cells in the model, enabling to capture significant interactions and hence recreate *in vivo* phenotypes.

Indirect migration

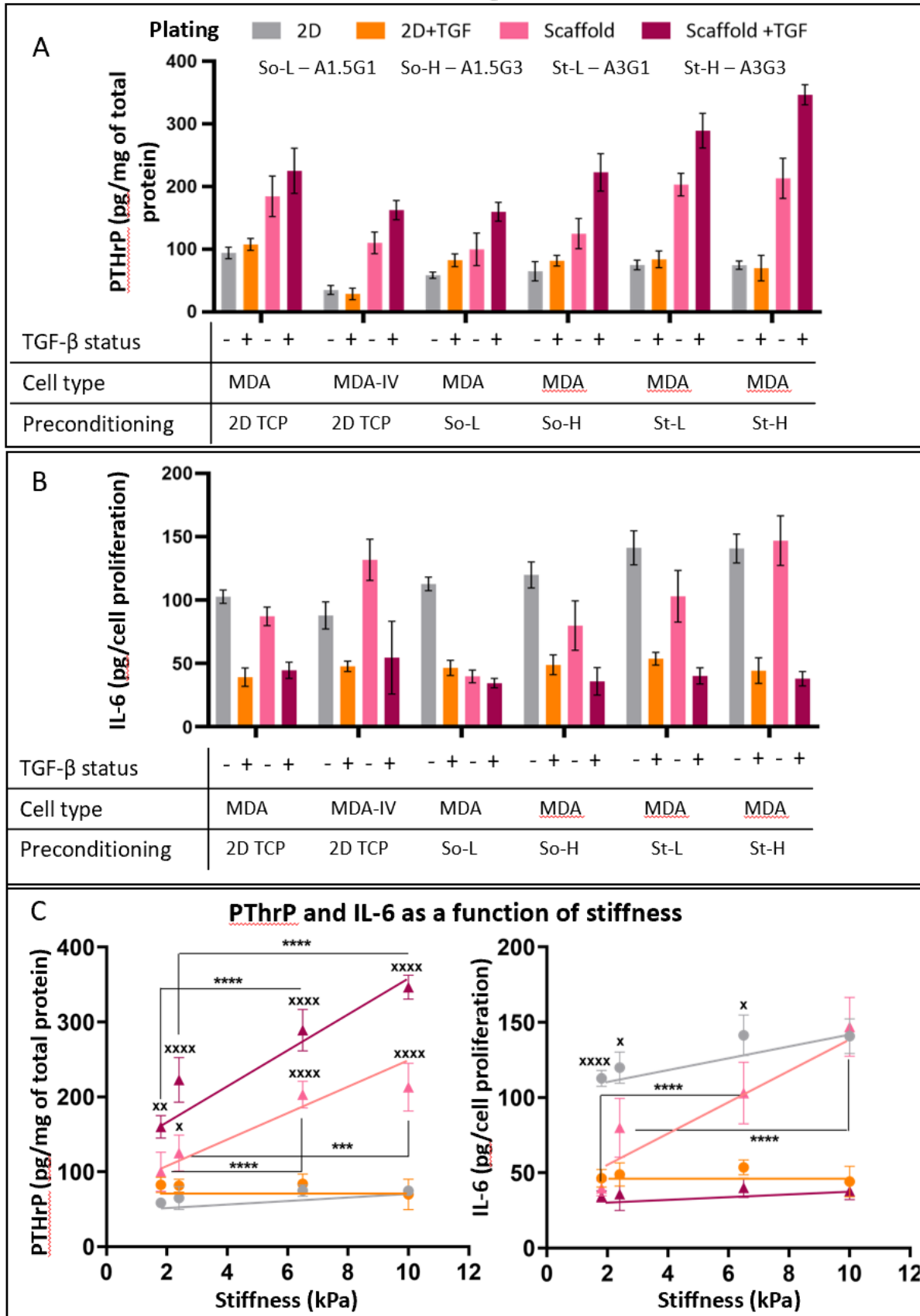


Figure 6. PTHrP expression and IL-6 release in indirect migration assay. (A) PTHrP expression and (B) IL-6 release quantified in MDA-MB 231 (referred to as MDA) and bone homing MDA-IV cells plated on either TCP plates (**Grey** -without TGF- β , and **Orange** -with TGF- β) or biohybrid PCL HA scaffolds (**Pink** -without TGF- β and **Purple** -with TGF- β). MDA-MB 231 cells were pre-conditioned in TCP plates or four groups of alginate-gelatin hydrogels as mentioned below each graph. The values are represented as mean and SD of n=2 scaffolds and N=3 independent experiments. Same data of PTHrP expression and IL-6 release in MDA-MB 231 represented as a function of stiffness values (kPa) of hydrogels in which they were pre-conditioned (C). P-values represented as *p \leq 0.05, **p \leq 0.01, ***p \leq 0.001, ****p \leq 0.0001).

3.4 Direct migration of MDA-MB 231 and MDA-IV from hydrogels to biohybrid scaffolds

The Direct migration model was set-up with alginate-gelatin hydrogels containing breast cancer cells (primary site) placed on top of biohybrid PCL scaffolds (secondary site), and to study the localisation / migration of cells into the bone ECM. This model was tested with two hydrogel groups that varied in stiffness but with similar gelatin concentration (i.e. So-H and St-H), since stiffness was the primary parameter dictating MDA-MB 231 response in the indirect model. Both MDA-MB 231 and MDA-IV cells were re-encapsulated in selected hydrogels and cultured on top of biohybrid PCL scaffolds to study migration to the secondary site (Figure 7).

To assess migration, at the endpoint (day 7) biohybrid PCL scaffolds were separated from hydrogels, measuring only the number of viable cells migrated in the scaffolds using the Deep blue viability assay. Results were observed to be similar between MDA-MB 231 and bone homing MDA-IV cells, where higher number of cells migrated from softer hydrogel than stiff hydrogel (So-H > St-H, Figure S7). This seems contradictory to the invasion and migration studies (Section 3.1) where high stiffness conditioning led to increased migration and invasion. Literature supports both these observations, where invasion of cancer cell is high within softer alginate gels⁴², but when cultured in a separate collagen gel, cancer cells conditioned in stiff matrix can invade more than soft matrix²². The possible explanation could be that stiff and dense matrix can constrict migration but when such conditioned cells reach surrounding soft/less dense matrix, they have higher potential to invade.

Interestingly, when PTHrP expression was measured in migrated MDA-MB 231 cells, St-H group showed 1.4-fold increased expression than So-H ($p < 0.05$) (Figure 7A). IL-6 release was measured to be 8-fold higher in stiffer hydrogels (St-H vs So-H, $p < 0.0001$) (Figure 7B). This suggests that while less cells migrated from high stiffness gels, they have higher expression of osteolytic factors and might possibly lead to higher metastatic load. This aligns with a similar study for breast to bone metastasis, which examined effect of *in vitro* stiffness conditioning of breast cancer cells on *in vivo* bone metastasis in mouse model. It reported progressive osteolysis as well as increased osteolytic lesions when high stiffness conditioned cells were injected (intra ventricular injection) in mouse model compared to low stiffness conditioned cells²².

Overall, this study and our models suggest high primary tumour stiffness is linked with increased osteolysis. Particularly in our models, expression of osteolytic factors could be a better indicator of future bone metastatic load than migration of cells.

3.5 Response of MDA-IV cells in ‘Direct’ and ‘Indirect’ model

MDA-IV cells, a bone homing variant of MDA-MB 231, are known to exclusively metastasize to bone *in vivo* but show no difference in their colonisation efficiency with respect to parental/original MDA-MB 231⁴³. In MDA-IV cells, intrinsic PTHrP (culture in 2D TCP) expression was found to be overall reduced in comparison to parental MDA-MB 231 cell line (Figure 6A). Although PTHrP expression in MDA-IV increased when cultured in biohybrid PCL scaffolds and with TGF- β supplementation, paralleling what was observed with the parental cell line (Figure 6A) and confirming that bone ECM induces expression of osteolytic factors in this cell line as well. Surprisingly in direct model, PTHrP expression showed low expression and no significant changes among stiffness conditioning (Figure 7A). These results could suggest that while PTHrP is an important factor in bone colonisation, it might not be as important to localise to the bone. In fact, studies on patient tumours indicate that positive PTHrP expression in primary tumour is linked to lower bone metastasis as well as patient survival^{44,45}. This could explain why MDA-IV cells have intrinsically low PTHrP expression than parental MDA-MB 231 when tested *in vitro*.

Intrinsic IL-6 release from MDA-IV was similar to that of MDA-MB-231 when cultured in conventional models (TCP, 2D). Indirect models showcased that levels of IL-6 increased in scaffolds and were similar to the response of MDA-MB 231 in highest stiffness (St-H, Figure 6B).

This pattern was also repeated in direct models, where IL-6 release was found to have 2-fold increase in higher stiffness (Figure 7B). These results suggest that IL-6 might be important in both localisation and in remodelling of bone ECM. Even parental MDA-MB 231 showcased stiffness related high fold change of IL-6 (eight times) than PTHrP (1.4 times) in direct model. This aligns with what is reported in literature on the importance of IL-6 cytokine in initiation of invasion and metastasis^{46,47}. Also IL-6 importance in bone metastasis and osteolytic activity has been documented^{19,48}.

With results from direct and indirect models, we could de-couple two different properties of breast to bone metastasis: localisation and osteolytic/remodelling potential. The different expression patterns of PTHrP and IL-6 in MDA-IV as compared to parental MDA-MB 231 and in direct and indirect models, gives insights in function of two factors in either bone localising or bone remodelling.

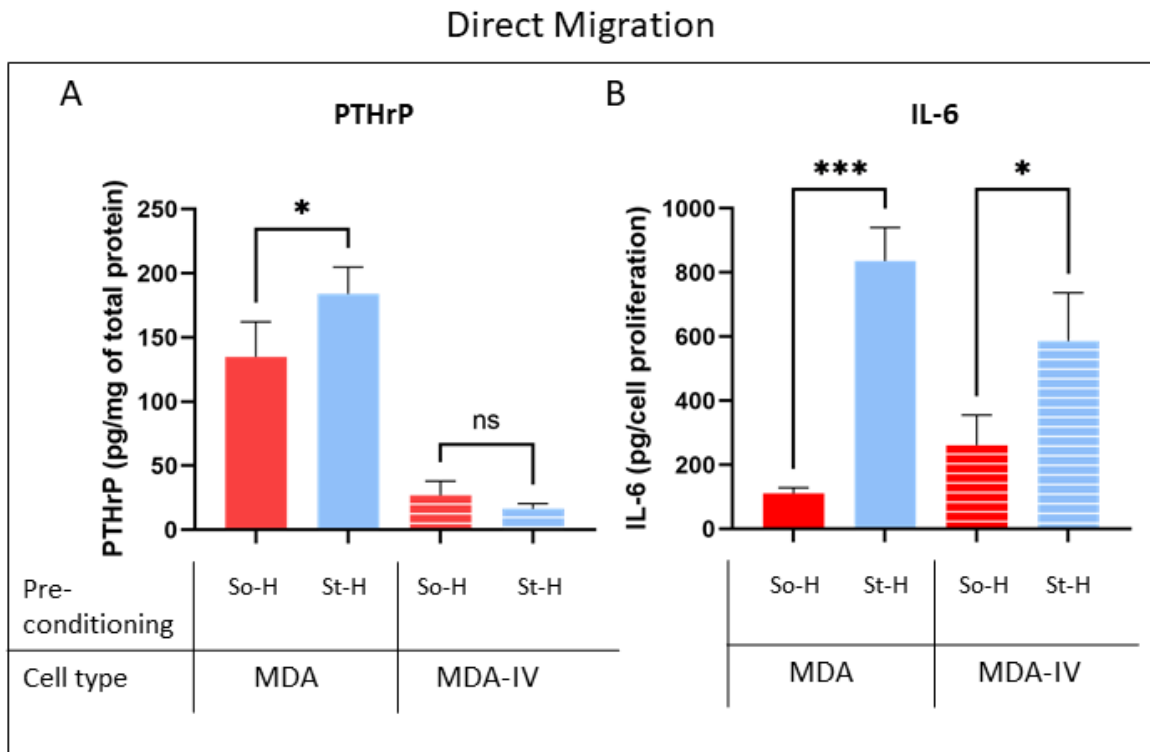


Figure 7. PTHrP and IL-6 quantification in Direct Migration model. (A) Bar graphs representing PTHrP expression and (B) IL-6 release in MDA-MB 231 (referred to as MDA in the graph) and MDA-IV cells. Results are normalised against the number of cells that have migrated to the biohybrid PCL HA scaffolds from So-H or St-H hydrogels. Data is represented as mean and SD of n=2 scaffolds and N=3

independent experiments. P-values represented as * $p \leq 0.05$, ** $p \leq 0.01$, *** $p \leq 0.001$, **** $p \leq 0.0001$). Overall, both models reveal information about separate aspects of bone metastasis i.e bone localisation vs bone remodelling. The information from indirect model focusses on breast cancer cell response to bone ECM and might predict the potential of these cells to develop into a full-blown metastasis. Whereas direct model might reveal more about bone localisation ability. With further validation from other cell lines and patient samples it would be possible to build on this hypothesis and confirm if the models can be used to predict these phenotypes.

Conclusions

Interactions between ECM and cancer cells direct phenotypes and matrix remodelling during tumour progression. Engineering the microenvironment *in vitro* and designing new models could be useful in isolating specific pattern or ECM components, to better understand biological processes. In this study we used two models to understand cell-ECM interactions at a fundamental level, and to predict metastatic potential (e.g., migration, invasion). Using specific 3D *in vitro* models, we were able to elucidate effects of primary tumour matrix stiffness and gelatin-related adhesion motifs on various dimensions of metastasis (i.e., adhesion, migration, 3D invasion, 3D metastatic site response). Stiffer primary tumour microenvironments (compressive moduli > 6 kPa) were found to be essential in inducing migratory and invasive phenotypes in MDA-MB 231 cells. In this study we then modelled aspects of breast-to-bone metastasis, combining two distinctive 3D *in vitro* models: one matching human breast cancer tissue, the other matching bone ECM properties. Two layouts were set-up to model breast to bone metastasis, focusing on bone localisation vs bone remodelling. The Indirect migration model showcased that both primary tumour stiffness and secondary site ECM composition are essential in regulating expression of osteolytic factors PTHrP and IL-6, and hence could affect osteolytic bone remodelling. Increased osteolytic potential in bone metastatic site is linked to stiffer primary tumour microenvironments. With direct model we evidenced that high stiffness is linked to high IL-6 activity an important factor for metastasis initiation as well as osteolysis.

Overall, with help of engineered *in vitro* models, and in accordance with previous studies, we were able to prove that high primary tumour stiffness is linked to increased migration, invasion and

osteolytic factors expression in breast cancer cells. Moreover, decoupling different parameters within these models, we were able to elucidate effect of both primary tumour ECM and secondary site ECM in breast to bone metastasis.

Further inclusion of primary cells (from patient tumours of known metastatic status) in developed *in vitro* models would validate their use in future for predicting bone metastasis and also as a platform to test therapeutic efficacy.

References

1. Cox TR, Erler JT. Remodeling and homeostasis of the extracellular matrix: implications for fibrotic diseases and cancer. *Dis Model Mech.* 2011;4(2):165. doi:10.1242/DMM.004077
2. Yuzhalin AE, Lim SY, Kutikhin AG, Gordon-Weeks AN. Dynamic matrisome: ECM remodeling factors licensing cancer progression and metastasis. *Biochim Biophys Acta Rev cancer.* 2018;1870(2):207-228. doi:10.1016/J.BBCAN.2018.09.002
3. Winkler J, Abisoye-Ogunniyan A, Metcalf KJ, Werb Z. Concepts of extracellular matrix remodelling in tumour progression and metastasis. *Nat Commun.* 2020;11(1):5120. doi:10.1038/s41467-020-18794-x
4. Samani A, Zubovits J, Plewes D. Elastic moduli of normal and pathological human breast tissues: an inversion-technique-based investigation of 169 samples. *Phys Med Biol.* 2007;52(6):1565-1576. doi:10.1088/0031-9155/52/6/002
5. Zhang SX, Liu L, Zhao W. Targeting Biophysical Cues: a Niche Approach to Study, Diagnose, and Treat Cancer. *Trends in Cancer.* 2018;4(4):268-271. doi:10.1016/J.TRECAN.2018.02.006
6. Lopez JI, Mouw JK, Weaver VM. Biomechanical regulation of cell orientation and fate. *Oncogene* 2008 2755. 2008;27(55):6981-6993. doi:10.1038/onc.2008.348
7. Nallanthighal S, Heiserman JP, Cheon DJ. The Role of the Extracellular Matrix in Cancer Stemness. *Front Cell Dev Biol.* 2019;7:86. doi:10.3389/FCELL.2019.00086/BIBTEX
8. Di Martino JS, Akhter T, Bravo-Cordero JJ. Remodeling the ECM: Implications for Metastasis and Tumor Dormancy. *Cancers (Basel).* 2021;13(19). doi:10.3390/CANCERS13194916
9. Denys H, Braems G, Lambein K, et al. The extracellular matrix regulates cancer progression and therapy response: implications for prognosis and treatment. *Curr Pharm Des.* 2009;15(12):1373-1384. doi:10.2174/138161209787846711
10. Henke E, Nandigama R, Ergün S. Extracellular Matrix in the Tumor Microenvironment and

- Its Impact on Cancer Therapy. *Front Mol Biosci.* 2020;6:160. doi:10.3389/FMOLB.2019.00160/BIBTEX
11. Paszek MJ, Zahir N, Johnson KR, et al. Tensional homeostasis and the malignant phenotype. *Cancer Cell.* 2005;8(3):241-254. doi:10.1016/J.CCR.2005.08.010
 12. Stowers RS, Shcherbina A, Israeli J, et al. Matrix stiffness induces a tumorigenic phenotype in mammary epithelium through changes in chromatin accessibility. *Nat Biomed Eng.* 2019;3(12):1009. doi:10.1038/S41551-019-0420-5
 13. Chen MT, Sun HF, Zhao Y, et al. Comparison of patterns and prognosis among distant metastatic breast cancer patients by age groups: a SEER population-based analysis. *Sci Reports 2017 71.* 2017;7(1):1-8. doi:10.1038/s41598-017-10166-8
 14. Lin X, Patil S, Gao YG, Qian A. The Bone Extracellular Matrix in Bone Formation and Regeneration. *Front Pharmacol.* 2020;11. doi:10.3389/FPHAR.2020.00757
 15. Fornetti J, Welm AL, Stewart SA. Understanding the Bone in Cancer Metastasis. *J Bone Miner Res.* 2018;33(12):2099-2113. doi:10.1002/JBMR.3618
 16. Syahrom A, Abdul Kadir MR, Abdullah J, Öchsner A. Mechanical and microarchitectural analyses of cancellous bone through experiment and computer simulation. *Med Biol Eng Comput.* 2011;49(12):1393-1403. doi:10.1007/S11517-011-0833-0
 17. Sanders JL, Chattopadhyay N, Kifor O, Yamaguchi T, Butters RR, Brown EM. Extracellular Calcium-Sensing Receptor Expression and Its Potential Role in Regulating Parathyroid Hormone-Related Peptide Secretion in Human Breast Cancer Cell Lines*. *Endocrinology.* 2000;141(12):4357-4364. doi:10.1210/endo.141.12.7849
 18. Yin JJ, Selander K, Chirgwin JM, et al. TGF- β signaling blockade inhibits PTHrP secretion by breast cancer cells and bone metastases development. *J Clin Invest.* 1999;103(2):197. doi:10.1172/JCI3523
 19. Palmqvist P, Persson E, Conaway HH, Lerner UH. IL-6, Leukemia Inhibitory Factor, and Oncostatin M Stimulate Bone Resorption and Regulate the Expression of Receptor Activator of NF- κ B Ligand, Osteoprotegerin, and Receptor Activator of NF- κ B in Mouse

- Calvariae. *J Immunol.* 2002;169(6):3353-3362. doi:10.4049/JIMMUNOL.169.6.3353
20. Thomas RJ, Guise TA, Yin JJ, et al. Breast cancer cells interact with osteoblasts to support osteoclast formation. *Endocrinology.* 1999;140(10):4451-4458. doi:10.1210/ENDO.140.10.7037
 21. Matte BF, Kumar A, Placone JK, et al. Matrix stiffness mechanically conditions EMT and migratory behavior of oral squamous cell carcinoma. 2019. doi:10.1242/jcs.224360
 22. Watson AW, Grant AD, Parker SS, et al. Breast tumor stiffness instructs bone metastasis via maintenance of mechanical conditioning. *Cell Rep.* 2021;35(13):109293. doi:10.1016/J.CELREP.2021.109293
 23. Mancuso E, Shah L, Jindal S, et al. Additively manufactured BaTiO₃ composite scaffolds: A novel strategy for load bearing bone tissue engineering applications. *Mater Sci Eng C.* 2021;126:112192. doi:10.1016/J.MSEC.2021.112192
 24. Pierantozzi D, Scalzone A, Jindal S, et al. 3D printed Sr-containing composite scaffolds: Effect of structural design and material formulation towards new strategies for bone tissue engineering. *Compos Sci Technol.* 2020;191:108069. doi:10.1016/j.compscitech.2020.108069
 25. Paget S. The distribution of secondary growths in cancer of the breast. 1889. *Cancer Metastasis Rev.* 1989;8(2):98-101.
 26. Dikici BA, Reilly GC, Claeysens F. Boosting the Osteogenic and Angiogenic Performance of Multiscale Porous Polycaprolactone Scaffolds by In Vitro Generated Extracellular Matrix Decoration. *ACS Appl Mater Interfaces.* 2020;12(11):12510. doi:10.1021/ACSAMI.9B23100
 27. Nayak B, Balachander GM, Manjunath S, Rangarajan A, Chatterjee K. Tissue mimetic 3D scaffold for breast tumor-derived organoid culture toward personalized chemotherapy. *Colloids Surfaces B Biointerfaces.* 2019;180:334-343. doi:10.1016/j.colsurfb.2019.04.056
 28. Rodriguez LG, Wu X, Guan JL. Wound-Healing Assay. *Methods Mol Biol.* 2005;294:23-29. doi:10.1385/1-59259-860-9:023

29. Pires BRB, Mencialha AL, Ferreira GM, et al. NF-kappaB Is Involved in the Regulation of EMT Genes in Breast Cancer Cells. *PLoS One*. 2017;12(1):e0169622. doi:10.1371/JOURNAL.PONE.0169622
30. Dai X, Cheng H, Bai Z, Li J. Breast Cancer Cell Line Classification and Its Relevance with Breast Tumor Subtyping. *J Cancer*. 2017;8(16):3131. doi:10.7150/JCA.18457
31. Bellahcène A, Bachelier R, Detry C, Lidereau R, Clézardin P, Castronovo V. Transcriptome analysis reveals an osteoblast-like phenotype for human osteotropic breast cancer cells. *Breast Cancer Res Treat* 2006 1012. 2006;101(2):135-148. doi:10.1007/S10549-006-9279-8
32. Anders C, Carey LA. Understanding and Treating Triple-Negative Breast Cancer. *Oncology (Williston Park)*. 2008;22(11):1233. /pmc/articles/PMC2868264/. Accessed May 26, 2022.
33. McQuillan DJ, Richardson MD, Bateman JF. Matrix deposition by a calcifying human osteogenic sarcoma cell line (SAOS-2). *Bone*. 1995;16(4):415-426. doi:10.1016/8756-3282(95)90186-8
34. Prideaux M, Wijenayaka AR, Kumarasinghe DD, et al. SaOS2 osteosarcoma cells as an in vitro model for studying the transition of human osteoblasts to osteocytes. *Calcif Tissue Int*. 2014;95(2):183-193. doi:10.1007/s00223-014-9879-y
35. Czekanska EM, Stoddart MJ, Richards RG, Hayes JS. In search of an osteoblast cell model for in vitro research. *Eur Cells Mater*. 2012;24:1-17. doi:10.22203/eCM.v024a01
36. Rutkovskiy A, Stensløkken K-O, Vaage IJ. Osteoblast Differentiation at a Glance. *Med Sci Monit Basic Res*. 2016;22:95-106. doi:10.12659/msmbr.901142
37. Chiechi A, Waning DL, Stayrook KR, Buijs JT, Guise TA, Mohammad KS. Role of TGF- β in breast cancer bone metastases. *Adv Biosci Biotechnol*. 2013;4(10C):15-30. doi:10.4236/abb.2013.410A4003
38. Walia B, Wang L, Merlin D, Sitaraman S V. TGF- β down-regulates IL-6 signaling in intestinal epithelial cells: Critical role of SMAD-2. *FASEB J*. 2003;17(14):1-20. doi:10.1096/FJ.02-1211FJE

39. Yamada D, Kobayashi S, Wada H, et al. Role of crosstalk between interleukin-6 and transforming growth factor-beta 1 in epithelial–mesenchymal transition and chemoresistance in biliary tract cancer. *Eur J Cancer*. 2013;49(7):1725-1740. doi:10.1016/J.EJCA.2012.12.002
40. Veldhoen M, Stockinger B. TGFβ1, a ‘Jack of all trades’: the link with pro-inflammatory IL-17-producing T cells. *Trends Immunol*. 2006;27(8):358-361. doi:10.1016/J.IT.2006.06.001
41. Kishimoto T. Interleukin-6: discovery of a pleiotropic cytokine. *Arthritis Res Ther*. 2006;8(Suppl 2):S2. doi:10.1186/AR1916
42. Pebworth MP, Cismas SA, Asuri P. A Novel 2.5D Culture Platform to Investigate the Role of Stiffness Gradients on Adhesion-Independent Cell Migration. *PLoS One*. 2014;9(10):110453. doi:10.1371/JOURNAL.PONE.0110453
43. Nutter F, Holen I, Brown HK, et al. Different molecular profiles are associated with breast cancer cell homing compared with colonisation of bone: evidence using a novel bone-seeking cell line. *Endocr Relat Cancer*. 2014;21(2):327-341. doi:10.1530/ERC-13-0158
44. Henderson MA, Danks JA, Moseley JM, et al. Parathyroid Hormone-Related Protein Production by Breast Cancers, Improved Survival, and Reduced Bone Metastases. *JNCI J Natl Cancer Inst*. 2001;93(3):234-237. doi:10.1093/JNCI/93.3.234
45. Henderson MA, Danks JA, Slavin JL, et al. Parathyroid hormone-related protein localization in breast cancers predict improved prognosis. *Cancer Res*. 2006;66(4):2250-2256. doi:10.1158/0008-5472.CAN-05-2814
46. Dethlefsen C, Højfeldt G, Hojman P. The role of intratumoral and systemic IL-6 in breast cancer. *Breast Cancer Res Treat*. 2013;138(3):657-664. doi:10.1007/S10549-013-2488-Z
47. Jayatilaka H, Phillip JM. Targeting metastasis through the inhibition of interleukin 6 and 8. <https://doi.org/102217/bmt-2019-0002>. 2019;8(1):BMT20. doi:10.2217/BMT-2019-0002
48. Ara T, DeClerck YA. Interleukin-6 in Bone Metastasis and Cancer Progression. *Eur J Cancer*. 2010;46(7):1223. doi:10.1016/J.EJCA.2010.02.026

**Chapter 4. Invasion and Secondary site colonisation as a function of
in vitro primary tumour matrix stiffness**

Supplementary information

Supplementary figures

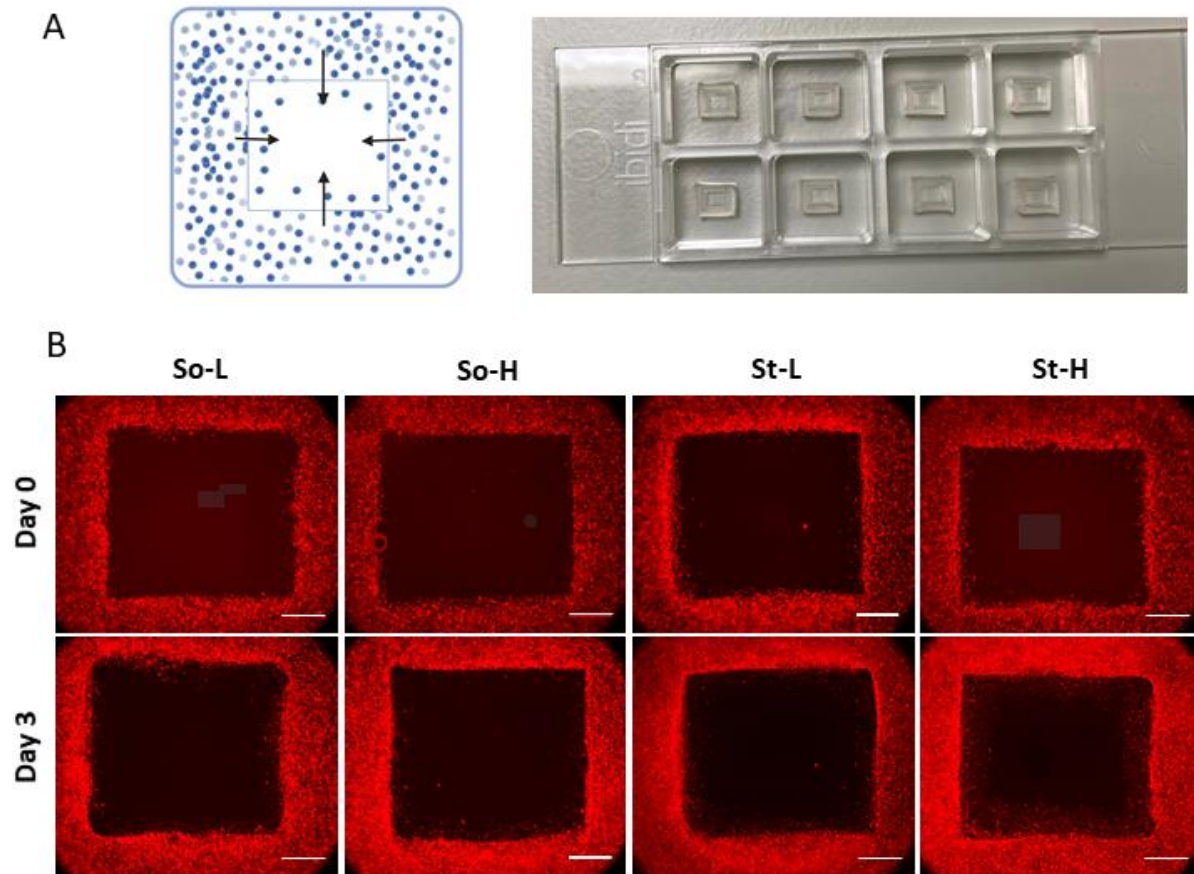


Fig. S 1. 3D Collagen invasion assay. (A) Schematic of invasion assay and representative image of inserts in 8-well imaging slides. (B) Cells stained with Cytopainter red were imaged at day 0 and day 3 of the assay (Scale bar- 1000 μm). Cells conditioned within four hydrogel groups of So-L, So-H, St-L and St-H were used in this assay. Insets and brightened image of day 3 invasion in acellular region showed in figure 4.

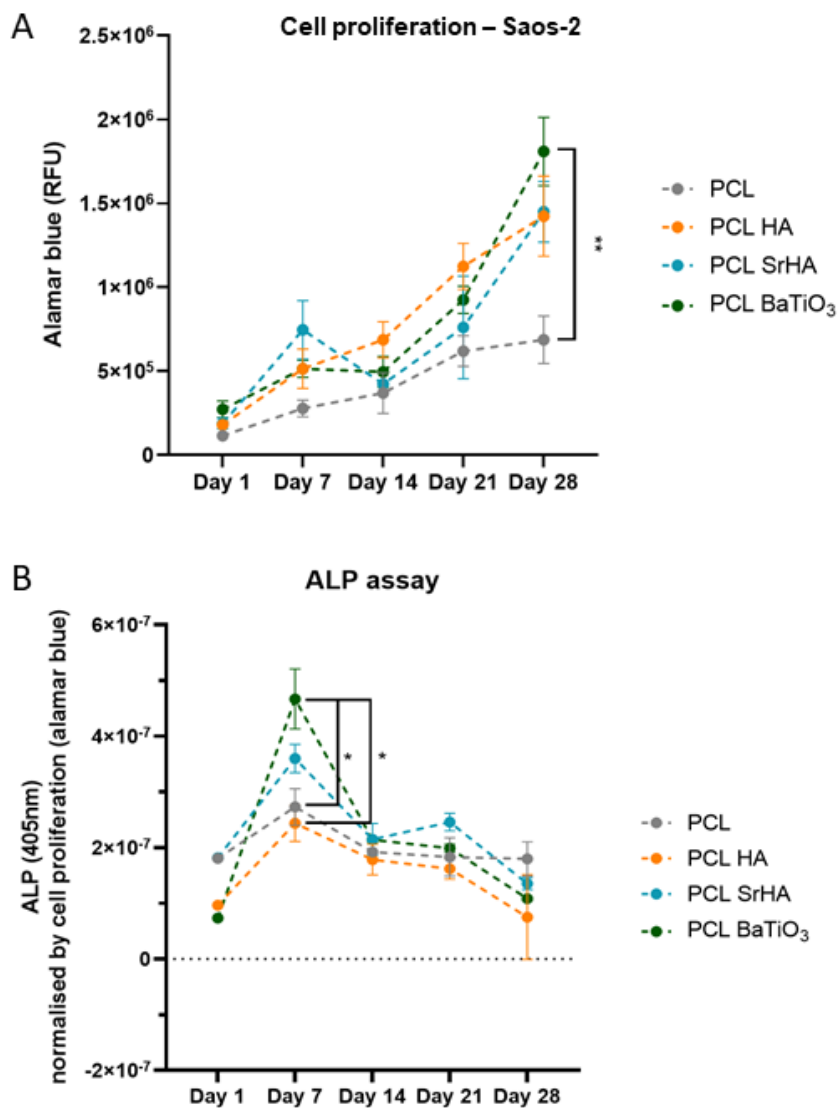


Fig. S 2: Proliferation and ALP activity. (A) Saos-2 proliferation as measured by Alamar blue assay and (B) ALP activity measured in Saos-2 cells when cultured in composite PCL scaffolds- PCL, PCL HA, PCL SrHA and PCL BaTiO₃. Data is plotted as a line graph from day 1 to day 28 with a 7-day interval (average and SD of three independent experiments). P-values represented as * $p \leq 0.05$, ** $p \leq 0.01$, *** $p \leq 0.001$, **** $p \leq 0.0001$

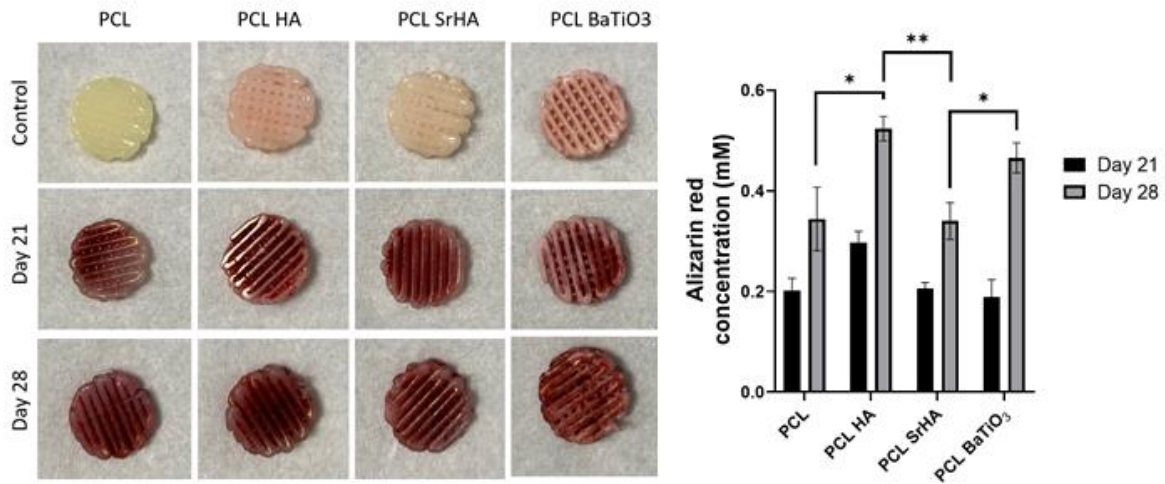


Fig. S 3. Calcium deposition analysis. PCL composite scaffolds stained with Alizarin stain on day 21 and day 28 of culture with Saos-2 cells (left). Control consisted of staining scaffolds with no cells cultured. Quantification of Alizarin stain on day 21 and day 28 and data represented as average and SD of three independent experiments (right). P-values represented as * $p \leq 0.05$, ** $p \leq 0.01$, *** $p \leq 0.001$, **** $p \leq 0.0001$

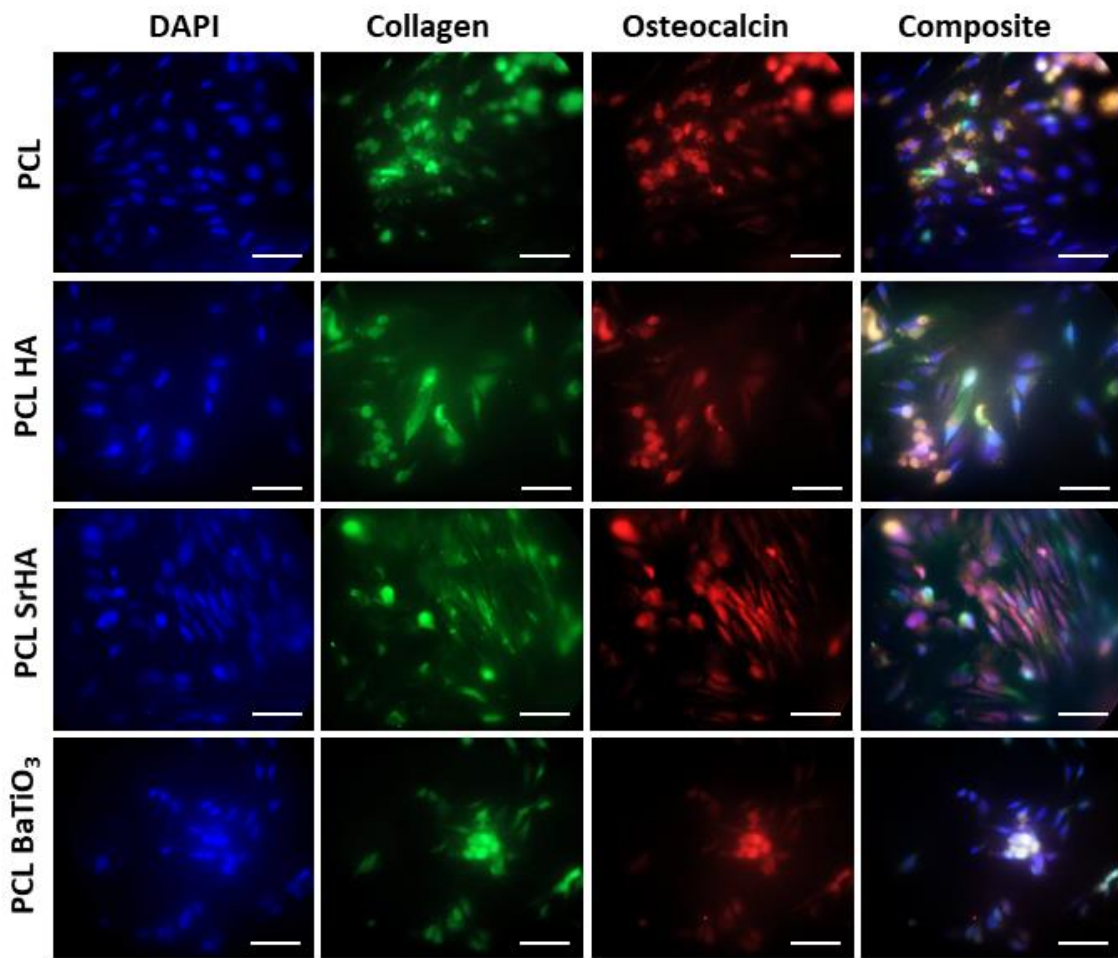


Fig. S 4. Collagen and osteocalcin deposition. Saos-2 cells were stained with DAPI, Collagen Ab and osteocalcin Ab on day 28 of culture in composite PCL scaffolds (Scale bar- 50 μm). The presence of punctate staining near nucleus of cells is considered to be ECM deposited by cells.

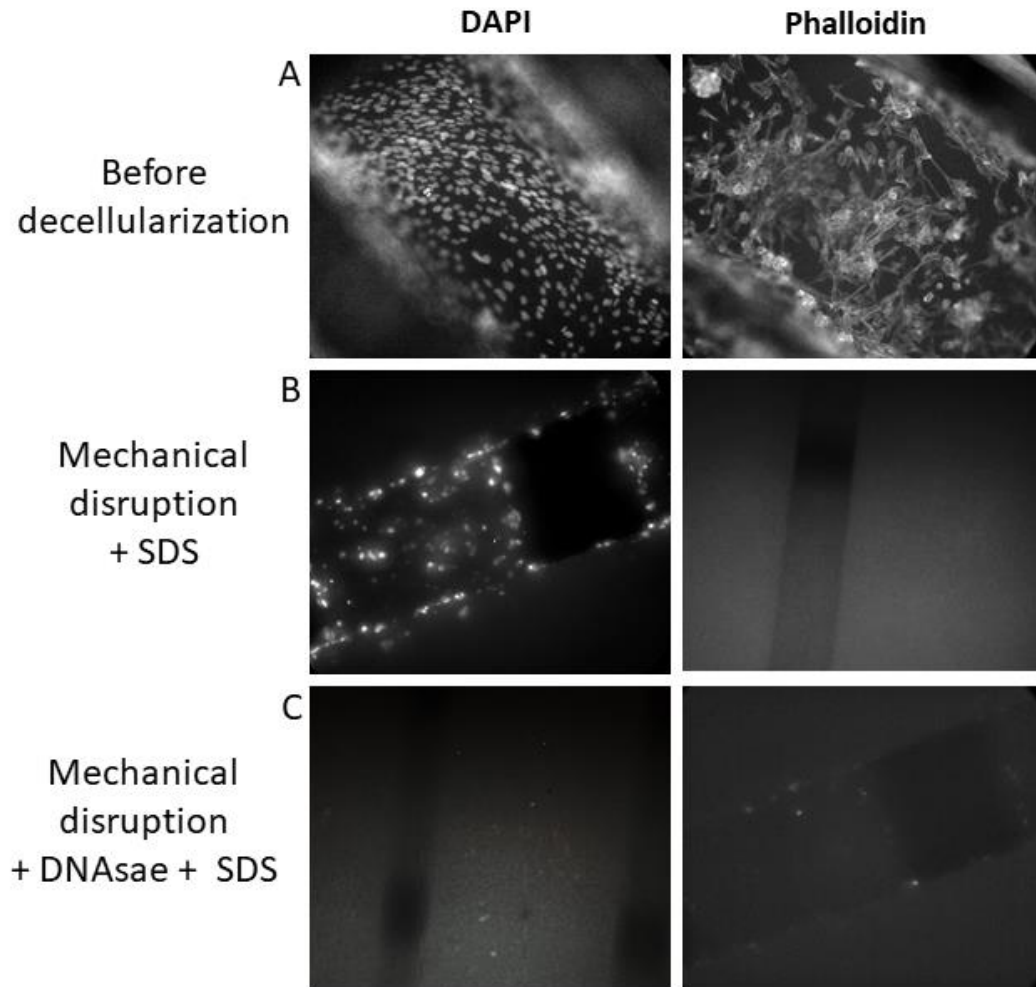


Fig. S 5. Standardisation of decellularization process in composite PCL scaffolds. DAPI and Phalloidin stained PCL scaffolds (A) before decellularization, (B) after mechanical lysis of cells and 0.05% SDS wash, and (C) after mechanical lysis with SDS and 1mg/mL DNase.

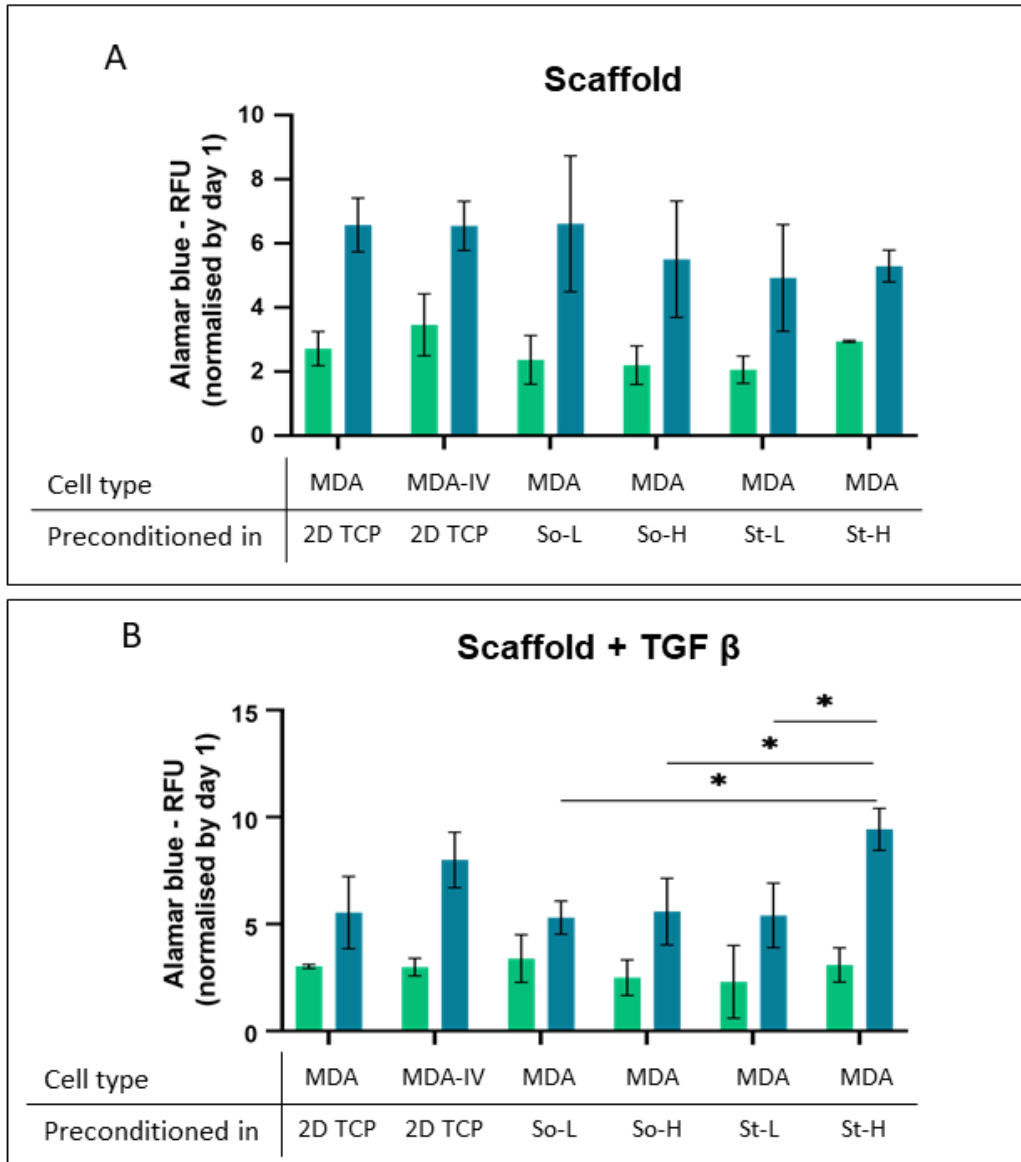


Fig. S 6. Indirect model - Cell proliferation of breast cancer cells in biohybrid PCL scaffolds. Alamar blue assay readings on day 3 (green) and day 7 (blue) of MDA-MB 231 (represented as ‘MDA’) and MDA-IV cells pre-conditioned in either 2D TCP plates or alginate-gelatin hydrogels and plated on **(A)** Scaffolds and **(B)** Scaffolds + 5ng/mL TGF- β . Data is represented as average and SD of three independent experiments (right). P-values represented as * $p \leq 0.05$.

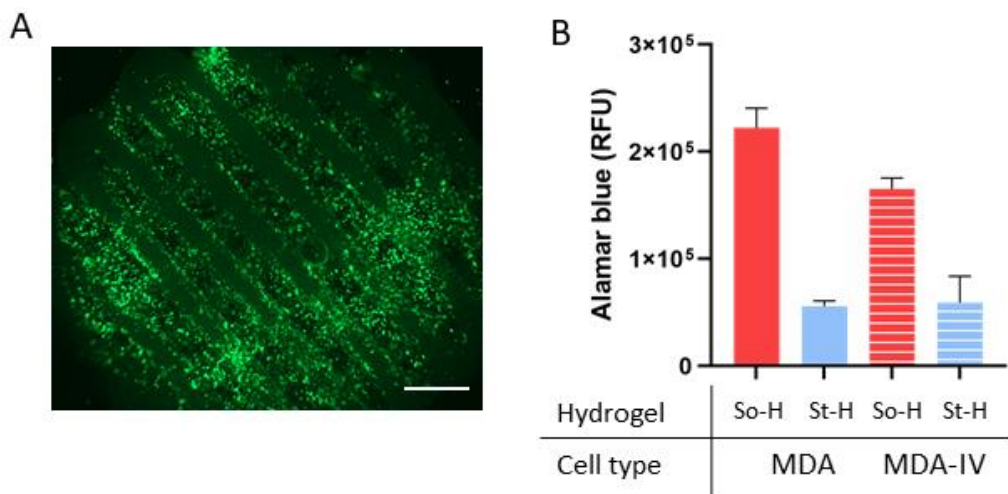


Fig. S 7. Migration quantified in ‘direct migration’ model. (A) Cells migrated from alginate hydrogels to biohybrid scaffolds stained with green Live stain (ethylene homodimer) at day 7 (Scale bar- 1000 μm). (B) Quantification of migrated cells (MDA or MDA-IV) from So-H or St-H hydrogels to biohybrid PCL scaffold with Alamar blue assay at Day 7.

Supplementary protocols

Characterisation of PCL scaffolds

S1. Alizarin stain analysis:

Calcium deposition was quantified using the Alizarin red stain. Briefly, scaffolds were fixed with 4% v/v formaldehyde solution at selected time points (day 21, day 28, $n = 2$, $N = 3$) or after decellularisation. After fixation, scaffolds were washed with ultrapure water and then incubated with Alizarin-red staining solution (TMS-008-C, Sigma-Aldrich, UK) for 15 min at room temperature on a plate shaker. Excess stain was removed by additional washes ($n = 3$) with ultrapure water, then scaffolds were washed with acetone ($n = 1$) and left to dry at room temperature. To quantify the reacted and deposited alizarin stain on the scaffolds, a 2 mL volume of 0.2 M NaOH:MeOH (1:1) solution was added to dissolve the stain for each scaffold, then a volume of 200 μL was transferred to another well-plate and measured by absorbance reading at 405 nm (Synergy-2 plate reader, Biotek, UK). A calibration curve obtained from known concentration of Alizarin red stain (mM) in 0.2 M NaOH:MeOH was used to calculate the

deposited calcium. For each scaffold and time point, data are presented as mean \pm SD (n = 2, N = 3).

S2. Collagen I and osteocalcin immunofluorescence (IF) staining:

Staining was performed on the scaffolds to detect any deposition of extracellular matrix after 28 days of culture and after decellularization of scaffolds. For this staining, scaffolds were fixed with 4% v/v paraformaldehyde for 5 min at RT, washed three times with 1 \times PBS and then incubated with blocking buffer (1% w/v BSA in 1 \times PBS) for 1 h at RT to avoid non-specific antibody binding. Scaffolds were washed with 1 \times PBS, and then incubated with Osteocalcin monoclonal antibody (1:500 dilution in 1 \times PBS, MA1-82975, Thermofisher, UK) and Collagen-I polyclonal antibody (1:250 dilution in 1 \times PBS, PA5-95137, Thermofisher, UK) overnight (16 h) at 4 °C. After three washes with blocking buffer, samples were incubated with a solution of secondary antibodies Goat anti-rabbit 488 (1:2000 dilution in 1 \times PBS, A-11008, Thermofisher, UK) and Goat anti-mouse 594 (1:2000 dilution in 1 \times PBS, A-11005, Thermofisher, UK) for 30 min at RT following manufacturers instruction. Samples were washed three times with blocking buffer and stored immersed in 1 \times PBS at 4 °C in the dark.

S3. ALP assay:

At selected time points, cells were fixed with 4% v/v formaldehyde solution (1004968350, Sigma-Aldrich UK) for 10 min followed by washes with 1 \times PBS. The cells were then permeabilised with a solution of 0.1% v/v Triton-X in 1 \times PBS for 15 min and finally washed three times with 1 \times PBS. Cellular alkaline phosphatase activity (ALP) was quantified for each type of scaffold tested (n = 3) using ALP Diethanolamine activity kit (AP0100, Sigma-Aldrich, UK) following manufacturer's instructions. Briefly, after permeabilization, a 1 mL volume of ALP reaction buffer was added to the scaffolds. A 0.67 M pNPP substrate solution was prepared in ultrapure water and a 1 μ L volume of this solution was added to the scaffolds, previously immersed in ALP buffer. Scaffolds were incubated for 15 min at 37 °C. The enzymatic activity was immediately measured with absorbance readings at 405 nm (Synergy-2 plat reader, Biotek, UK). Readings were converted to units/mL using a calibration curve obtained by measuring known amounts of ALP enzyme (U/mL) using the same method previously described and in the range of 0.15 U/mL and 10 U/mL. Finally, ALP activity was normalised to cell number, with each U/mL values divided by the cell proliferation

reading (Alamar blue) measured for the corresponding scaffolds. For each scaffold and time point, data are presented as mean \pm SD (n = 2, N = 3).

Final discussion and conclusions

TME is a complex combination of cellular and non-cellular components whose importance in tumour progression is gaining attention. However, most of its components are intertwined together, making it difficult to understand contribution of each to tumour phenotypes. The work presented in this thesis has demonstrated use of 3D *in vitro* models as a way for: 1) modelling and decoupling physico-chemical cues of TME and 2) examining effect of these physico-chemical properties on breast tumour progression. Novelty of this work lies in the fact that multiple TME cues (matrix stiffness, matrix composition, tissue porosity, extracellular pH and interstitial fluid flow) were integrated in models described in **Chapter 2**, **Chapter 3** and **Chapter 4**, and at the same time also dissecting their importance in various dimensions of breast cancer progression (tumour growth, shape and size, CSC population, migration, invasion and bone secondary site metastasis). Hence, the work done in this study is discussed in two parts: 1) Modelling important aspects of tissue microenvironment to mimic breast and bone separately; and 2) Examining the impact of these microenvironmental cues on breast cancer phenotypes.

1) Modelling TME cues.

Breast and bone have varied tissue properties in terms of matrix stiffness, density, composition and porosity. During the metastatic cascade, breast cancer cells not only migrate from breast to bone, but also respond to distinct microenvironments of these tissues. Hence the aim of this thesis was to mimic various aspects of breast and bone tissue to study breast to bone metastasis. For the primary breast cancer model, we chose a scaffold-based approach so as to study the contribution of TME's non-cellular components. The physico-chemical cues (i.e. matrix stiffness, density and composition, pH and interstitial fluid flow) of normal breast and tumour tissue were modelled using alginate-gelatin hydrogels which were cultured in a perfusion system. Varying alginate crosslinking by calcium ions concentration enabled precise control over the resultant stiffness, being in the required range of 1-10 kPa (*In vivo* Normal breast tissue- 1-3 kPa, tumour tissue- 10-15 kPa). Inclusion of gelatin in the hydrogel as viscous/dissipative component, not interacting with alginate crosslinking, decoupled mechanical stiffness from collagen related adhesion motifs. On the other hand, tumour associated acidic extracellular pH was mimicked by maintaining pH of cell culture media at 6.5 vs normal physiological pH of 7.4. Interstitial fluid flow which is a result of movement of interstitial fluid due to lymphatic drainage in tissues, was mimicked by continuous

flow of media in a millifluidic chamber at a rate of 500 $\mu\text{L}/\text{min}$ or flow velocity of 1.4 $\mu\text{m}/\text{s}$ ¹, which is within physiological interstitial fluid flow range (0.1 - 4 $\mu\text{m}/\text{s}$). Compared to scaffold free 3D models, the model described in this study was able to successfully incorporate many aspects of tumour physiology like cell-ECM interactions, mechanical stress and perfusion. However, with added dimensions there is a need for standardised protocols that can precisely recreate models for cellular assays. With inclusion of techniques like 3D printing and hydrogel encapsulator devices, the size of Alginate-gelatin beads can be controlled for better scalability. In comparison to microfluidic devices, millifluidic ones provide larger sample content which is necessary for assays such as flow cytometry. At the same, millifluidic models are not appropriate for real time imaging as they lack thin channels, which is a feature of microfluidic models and important for high resolution imaging. Hence as per our application, millifluidic chambers were appropriate.

For the bone tissue engineering, Saos-2 cells were cultured in composite 3D printed PCL scaffolds that mimicked cancellous bone tissue stiffness and porosity. These scaffolds were decellularised to retain ECM deposited by Saos-2 cells to further use them as *in vitro* models for bone metastasis. Saos-2 are osteoblastic osteosarcoma cell lines and their resemblance to osteoblastic ECM deposition and mineralisation has been documented². However, future inclusion of primary osteoblasts and osteoclasts could render the model more physiologically relevant.

Finally, two systems were used to study breast to bone metastasis, assembling breast and bone scaffolds differently. Indirect migration model was designed and tested by culturing MDA-MB 231 cells pre-conditioned in breast TME (i.e. alginate hydrogels), onto the biohybrid scaffolds. This model was designed to capture initial response of breast cells to bone microenvironment. The direct migration model was purposely designed and tested to study migration of cells from alginate-gelatin hydrogels (aka breast, primary site) to the scaffolds (bone, secondary site). In this model, invasive breast cancer cells are more likely to reach and invade the bone scaffolds, hence this system enables to capture better biological processes important in bone metastasis localisation. In fact, metastasis is a process that involves numerous other steps with intravasation into circulatory system and extravasating to various secondary sites. With tissue engineering techniques like Tissue-on-a-chip or Organ-on-a-chip, it is possible to further integrate breast and bone tissue by connecting scaffolds in a perfusion system. As described in Chapter 1 (section 3.7), microfluidic breast cancer models have tried to mimic processes such as intravasation and

extravasation separately ^{3,4}. However, models still lack to mimic the whole metastatic cascade in a single device. In that terms, our model was able to link primary and secondary site, and most importantly showcased the influence of primary tumour conditioning on secondary site phenotypes. To further improve our model, there is scope for the integration of scaffolds described in this study within a single microfluidic device (Alginate-gelatin hydrogels and PCL scaffolds) hence better represent and study metastasis.

In this thesis, while some TME cues were modelled, there is still scope for the inclusion of others, such as hypoxia. Hypoxia is a characteristic hallmark of solid tumour and is also implicated in angiogenesis, metastasis and treatment resistance ⁵. Apart from that, oxygen content of breast and bone tissue is different, with bone being hypoxic than breast. The models designed and tested in the thesis have the possibility to be included and incubated in hypoxic chambers (typically used to control the levels of atmospheric oxygen in the range of 0.5-18 %). Due to limited available time, it was not possible to perform such experiments during the PhD thesis. Another possibility to further expand the thesis is by including interstitial fluid pressure, which is built up in the tumour due to excess leaky vasculature but poor lymphatic drainage ^{6,7}. Modifications of the perfusion system used in the thesis (eg. one-way luer valves) allows to increase the fluid pressure in the culturing chambers matching pressures found *in vivo* (3 mmHg – 19 mmHg) ⁸.

2) Effect of TME cues on breast cancer progression

We explored effects of primary tumour TME on breast cancer cells at both primary tumour site and secondary site of bone. We managed to study primary breast tumour phenotypes and compare responses of lower grade luminal subtype MCF-7 from that of aggressive TNBC subtype MDA-MB 231. These models suggests that MCF-7's growth is reduced in presence of harsh tumorigenic environment (Stiffer matrix and acidic pH) whereas MDA-MB 231 sustains growth in all conditions tested, as expected. Also, in invasive MDA-MB 231 cell lines, high gelatin content in hydrogels induced formation of irregular shaped cell clusters. We have included in this study only two cell lines. To draw more significant conclusions on the effect of TME variables on cells, the inclusion of other breast cancer cell lines or primary tumour cells from patients would better inform if these models could differentiate in aggressiveness of cells by gauging their resilience to different TME dysregulation.

Most importantly, this is the first study that explores different stem cell population in response to physico-chemical TME dysregulation. Overall stem cell pool increased in both cell lines in acidic pH with high tumour stiffness, clearly showing that tumorigenic microenvironment increases stemness in primary tumour. In addition, MDA-MB 231 has increased E-CSC as well as M-CSC populations when cultured in tumorigenic model. In a previous study, E-CSC population was shown to have high tumour initiating capacity and M-CSC had high invasion capacity. Here tumorigenic environment pushes the system to have both populations, probably increasing tumour aggressiveness. Overall, this model helps in easy monitoring of stem cell population in presence of relevant TME cues, which can make them a better model for understanding stem cell dynamics, disease prognosis and drug efficacy studies. The use of primary cells could help in better predicting outcomes and have the potentiality to screen effects of therapies towards more personalized treatments.

For studying effects of primary tumour on secondary site we only examined effect of matrix stiffness and composition of the primary tumour. High matrix stiffness was found to condition MDA-MB 231 cells making them more migratory and invasive. Importantly, high stiffness pre-conditioned cells had increased expression of osteolytic factors PTHrP and IL-6 when cultured in biohybrid bone scaffolds, suggesting that behaviour of cells in secondary site can be shaped by their primary tumour microenvironment. It can additionally suggest that such conditioned cells might have a higher change of progressing into a full-blown metastasis. Furthermore, biohybrid PCL scaffolds were able to capture initial steps of breast to bone metastasis, especially breast cancer's osteolytic response to bone ECM. Again, validation with the use of patients derived cells in this model, could help to better understand progression of disease and potentially tailor better treatments. On the same note, inclusion of primary tumour cells with known bone metastasis outcomes within the model could better inform on the osteolytic potential (e.g., starting with PTHrP expression) in bone scaffolds, and then compare this to other possible metastatic sites such as lung, liver or brain tissues.

In summary, this study modelled and integrated important TME cues *in vitro* to understand their effects on breast tumour phenotypes. With future integration of other cues and paralleled with validation of cells phenotypes using primary cells from patients with known outcome, these

models could have a great potential to become screening platforms for disease prognosis, as well as testbeds for drug efficacy studies.

Future work and perspective

In vitro platforms have a potential to replace or reduce animal models for preclinical studies that involve studying disease mechanism, predicting disease prognosis, as drug discovery platforms and even for personalised treatment options. As mentioned before, first steps to achieve this is by mimicking important aspects of the pathology and secondly by validating their potential with wide range of patient samples. In terms of future direction, engineering 3D models on both these fronts is necessary to achieve an ideal *in vitro* system. Some of the future work that can be done with our model is described here.

1. Alginate-gelatin hydrogels were able to mimic most aspects of native ECM but they lack whole repertoire of ECM components, such as fibronectin, laminin etc, which are implicated in breast tumour physiology. For this alginate gels can be functionalized to covalently link with peptides mimicking fibronectin (RGDS) and laminin (IKVAV) and provide necessary biochemical signalling from these components ⁹.
2. Instead of using individual primary osteoblasts and osteoclasts, bone-marrow derived mesenchymal stem cells (BM-MSCs) can be used in the PCL scaffolds. Osteo-differentiation by addition of osteogenic specific media to BM-MSCs can provide a varied population of differentiated osteoblasts and osteoclasts ⁴. The ECM and growth factors released by such cells will be more physiologically relevant than only a single cell culture.
3. Use of microfluidic devices and tissue-on-a-chip model to combine breast hydrogels and bone scaffolds could make the integration closer to *in vivo* conditions. Individual extravasation ⁴ and intravasation ¹⁰ models have been developed which can be combined on a single chip. However, both these models only use collagen for both breast and bone tissue which lacks the contribution from matrix stiffness, ECM architecture and mechanical stress. Inclusion of hydrogels and scaffolds described in this model can be a step further for physiological relevance. With development of liver, lung and brain scaffolds there is a possibility to combine breast tissue with all four preferable metastatic sites – bone, liver, lungs and brain. For proof-of-concept, recent organ-on-a-chip studies have successfully integrated four organ system on

a single device. Heart, liver, skeletal muscle and nervous system were integrated together to study therapeutic dose toxicity on these organs ¹¹. It was found that when integrated together, the engineered tissues were able to sustain each other for 28 days without serum supplementation. With further development and standardisation of such systems, metastasis-on-a-chip models could be integrated to predict metastasis and organ tropism, and also as a platform to therapeutically target metastasis.

4. Partial pressure of oxygen is another characteristic feature of each tissue which is dysregulated during cancer. There are several ways of including hypoxia in 3D cancer models. Firstly, hypoxic cabinets are able to control the environmental oxygen and the *in vitro* systems can be placed inside to receive a particular amount of oxygen. However, this makes the system less flexible as different tissue types have different oxygen needs, which can hinder development of a multiorgan system on a single device. Microfluidic devices can present solutions to individual oxygen content where separate gas channels can be placed adjacent to each tissue module ¹². Individual gas channels can provide controlled and specific amount of oxygen to each tissue type on a single device. Alternatively, a channel for oxygen scavenging chemicals like Na_2SO_4 can be placed next to each tissue module where concentration of Na_2SO_4 can decide oxygen content ¹².
5. Tumour tissue is known to be heterogenous in terms of features like matrix stiffness or presence of growth factors. 3D printing techniques and photo-responsive hydrogels can provide dynamic variation of features like matrix stiffness, enzymatic activity and growth factor presentation. Compared to conventional hydrogels that involve modifications to the bulk material to mimic the static aspects of the cellular microenvironment, dynamic hydrogels possess possibility to alter chemical and physical properties with external stimuli, to better mimic the dynamics of the *in vivo* cellular microenvironment. For instance, hydrogels can be functionalized with photo-labile linking groups that are activated by two-photon irradiation and release specific volumes of growth factors within the 3D hydrogel ¹³. This can create customised growth factor patterns and concentration gradients important for processes such as migration, intravasation and extravasation. With similar technique, alginate hydrogels stiffness can be temporally and spatially modulated by light-triggered release of calcium or a chelator from liposomes ¹⁴.

6. While model building is important, the other aspect that takes precedence is validation with patient samples and multiple cell lines. With respect to this study, biohybrid PCL scaffolds can be validated as preclinical model for predicting bone metastasis by using patient samples of known metastatic status (i.e bone vs non-bone metastasis) and compared for their colonisation and osteolytic factor expression.

In summary, the ideal *in vitro* system would take into consideration the factors mentioned above. However, these systems are still a long way from being the preferred preclinical model for disease evaluation and drug studies. There are factors like complete recreation of immune components present in *in vivo* models that *in vitro* models lack. Future methodologies and techniques might help in further development of such models.

The findings of this study present the importance of physico-chemical cues or non-cellular components of TME in breast cancer progression. Due to their presence in most types of solid cancers, novel therapies are focussing on targeting these cues in conjunction with current drug therapies. For instance, mechano-responsive cell system (MRCS) uses mesenchymal stem cells that are responsive to high mechanical stiffness and can be engineered to locally activate drugs and specifically target cancer microenvironment¹⁵. Acidic pH has also been targeted to increase drug efficacies in *in vivo* tumours. Sodium bicarbonate supplementation in mouse models has been shown to increase extracellular tumoural pH which further reduces metastatic potential and increases responsiveness to certain drugs^{16,17}. Described models that mimic these essential cues, could become a preclinical platform for testing efficacy of such novel therapies and potentially tailor new therapies for personalized medicine / enhanced patients' outcomes. Due to the simplicity, but mainly the highest degree of control, with which TME cues can be integrated and decoupled in comparison to *in vivo* models, these *in vitro* models can serve as a preliminary platform to delineate basis of such therapies. In addition, they have better potential to transform into high throughput systems than other *in vivo* alternatives.

In summary, there are various avenues that can be explored with *in vitro* models, that were described in this thesis. With advancements in materials functionalization, manufacturing, harmonization of methods and inclusion of quality checks in the development of *in vitro* models, better preclinical models including patients' cells would help in better understand progression of

the disease and identify effective treatments, limiting the use of animals as standard preclinical models in the near future.

References

1. Mazzei D, Guzzardi MA, Giusti S, Ahluwalia A. A low shear stress modular bioreactor for connected cell culture under high flow rates. *Biotechnol Bioeng*. 2010;106(1):127-137. doi:10.1002/BIT.22671
2. Czekanska EM, Stoddart MJ, Richards RG, Hayes JS. In search of an osteoblast cell model for in vitro research. *Eur Cells Mater*. 2012;24:1-17. doi:10.22203/eCM.v024a01
3. Jeon JS, Bersini S, Gilardi M, et al. Human 3D vascularized organotypic microfluidic assays to study breast cancer cell extravasation. *Proc Natl Acad Sci U S A*. 2015;112(1):214-219. doi:10.1073/pnas.1417115112
4. Bersini S, Jeon JS, Dubini G, et al. A microfluidic 3D invitro model for specificity of breast cancer metastasis to bone. *Biomaterials*. 2014;35(8):2454-2461. doi:10.1016/j.biomaterials.2013.11.050
5. Muz B, Puente P de la, Azab F, Azab AK. The role of hypoxia in cancer progression, angiogenesis, metastasis, and resistance to therapy. *Hypoxia*. 2015;3:83. doi:10.2147/HP.S93413
6. Baxter LT, Jain RK. Transport of fluid and macromolecules in tumors. I. Role of interstitial pressure and convection. *Microvasc Res*. 1989;37(1):77-104. doi:10.1016/0026-2862(89)90074-5
7. Boucher Y, Salehi H, Witwer B, Harsh GR, Jain RK. Interstitial fluid pressure in intracranial tumours in patients and in rodents. *Br J Cancer*. 1997;75(6):829-836. doi:10.1038/BJC.1997.148
8. Azimi T, Loizidou M, Dwek M V. Cancer cells grown in 3D under fluid flow exhibit an aggressive phenotype and reduced responsiveness to the anti-cancer treatment doxorubicin. *Sci Rep*. 2020;10(1):12020. doi:10.1038/s41598-020-68999-9
9. Neves MI, Moroni L, Barrias CC. Modulating Alginate Hydrogels for Improved

- Biological Performance as Cellular 3D Microenvironments. *Front Bioeng Biotechnol.* 2020;8:665. doi:10.3389/FBIOE.2020.00665/BIBTEX
10. Nagaraju S, Truong D, Mouneimne G, Nikkhah M. Microfluidic Tumor–Vascular Model to Study Breast Cancer Cell Invasion and Intravasation. *Adv Healthc Mater.* 2018;7(9). doi:10.1002/ADHM.201701257
 11. Oleaga C, Lavado A, Riu A, et al. Long-Term Electrical and Mechanical Function Monitoring of a Human-on-a-Chip System. *Adv Funct Mater.* 2019;29(8):1805792. doi:10.1002/ADFM.201805792
 12. Byrne MB, Leslie MT, Gaskins HR, Kenis PJA. Methods to study the tumor microenvironment under controlled oxygen conditions. *Trends Biotechnol.* 2014;32(11):556. doi:10.1016/J.TIBTECH.2014.09.006
 13. Tam RY, Smith LJ, Shoichet MS. Engineering Cellular Microenvironments with Photo- and Enzymatically Responsive Hydrogels: Toward Biomimetic 3D Cell Culture Models. 2017. doi:10.1021/acs.accounts.6b00543
 14. Stowers RS, Allen SC, Suggs LJ, Anseth KS. Dynamic phototuning of 3D hydrogel stiffness. *Proc Natl Acad Sci U S A.* 2015;112(7):1953-1958. doi:10.1073/PNAS.1421897112/SUPPL_FILE/PNAS.201421897SI.PDF
 15. Zhang SX, Liu L, Zhao W. Targeting Biophysical Cues: a Niche Approach to Study, Diagnose, and Treat Cancer. *Trends in Cancer.* 2018;4(4):268-271. doi:10.1016/J.TRECAN.2018.02.006
 16. McCarty MF, Whitaker J. Manipulating tumor acidification as a cancer treatment strategy. *Altern Med Rev.* 2010;15(3):264-272.
 17. Robey IF, Baggett BK, Kirkpatrick ND, Roe DJ, Dosesco J, Sloane BF, Hashim AI, Morse DL, Raghunand N, Gatenby RA GR. Bicarbonate increases tumor pH and inhibits spontaneous metastases. *Cancer Res.* 2009;69(6):2260-2268. doi:10.1158/0008-5472.CAN-07-5575

----- End of thesis -----